

Interfacial, compositional and morphological engineering for single- and multi-junction perovskite solar cells

Citation for published version (APA):

Wang, J. (2020). *Interfacial, compositional and morphological engineering for single- and multi-junction perovskite solar cells*. [Phd Thesis 1 (Research TU/e / Graduation TU/e), Chemical Engineering and Chemistry]. Technische Universiteit Eindhoven.

Document status and date:

Published: 10/12/2020

Document Version:

Publisher's PDF, also known as Version of Record (includes final page, issue and volume numbers)

Please check the document version of this publication:

- A submitted manuscript is the version of the article upon submission and before peer-review. There can be important differences between the submitted version and the official published version of record. People interested in the research are advised to contact the author for the final version of the publication, or visit the DOI to the publisher's website.
- The final author version and the galley proof are versions of the publication after peer review.
- The final published version features the final layout of the paper including the volume, issue and page numbers.

[Link to publication](#)

General rights

Copyright and moral rights for the publications made accessible in the public portal are retained by the authors and/or other copyright owners and it is a condition of accessing publications that users recognise and abide by the legal requirements associated with these rights.

- Users may download and print one copy of any publication from the public portal for the purpose of private study or research.
- You may not further distribute the material or use it for any profit-making activity or commercial gain
- You may freely distribute the URL identifying the publication in the public portal.

If the publication is distributed under the terms of Article 25fa of the Dutch Copyright Act, indicated by the "Taverne" license above, please follow below link for the End User Agreement:

www.tue.nl/taverne

Take down policy

If you believe that this document breaches copyright please contact us at:

openaccess@tue.nl

providing details and we will investigate your claim.

Interfacial, Compositional and Morphological Engineering for Single- and Multi-junction Perovskite Solar Cells

PROEFSCHRIFT

ter verkrijging van de graad van doctor aan de Technische Universiteit Eindhoven, op
gezag van de rector magnificus prof.dr.ir. F.P.T. Baaijens, voor een commissie
aangewezen door het College voor Promoties, in het openbaar te verdedigen op
donderdag 10 december 2020 om 16:00 uur

door

Junke Wang

geboren te Hunan, China

Dit proefschrift is goedgekeurd door de promotoren en de samenstelling van de promotiecommissie is als volgt:

voorzitter:	prof.dr. F. Gallucci
1 ^e promotor:	prof.dr.ir. R.A.J. Janssen
copromotor:	dr.ir. M.M. Wienk
leden:	prof.dr. H.J. Snaith (University of Oxford)
	prof.dr. M.A. Loi (Rijksuniversiteit Groningen)
	prof.dr.ir. W.M.M. Kessels
	prof.dr. E. Garnett (AMOLF en Universiteit van Amsterdam)

Het onderzoek of ontwerp dat in dit proefschrift wordt beschreven is uitgevoerd in overeenstemming met de TU/e Gedragscode Wetenschapsbeoefening.

Interfacial, Compositional and Morphological
Engineering for Single- and Multi-junction
Perovskite Solar Cells

Junke Wang

Printed by: Gildeprint, Enschede

A catalogue record is available from the Eindhoven University of Technology Library

ISBN: 978-90-386-5171-2

The research described in this thesis has been financially supported by the European Research Council under the European Union's Seventh Framework Programme (FP/2007–2013)/ERC Grant Agreement No. 339031, the Ministry of Education, Culture and Science (Gravity program 0.24.001.035), and the Spinoza prize of the Dutch Research Council (NWO).

Table of contents

Chapter 1 Introduction	1
1.1 Solar energy and photovoltaics (PV).....	2
1.2 Perovskite semiconductors	3
1.3 Device architecture of perovskite solar cells.....	4
1.4 Deposition methods of perovskite films.....	8
1.5 Characterization of perovskite solar cells	10
1.6 Shockley-Queisser limit and multijunction solar cells.....	13
1.7 Outline	16
1.8 References	19
Chapter 2 Insights into fullerene passivation of SnO₂ electron transport layers in perovskite solar cells	25
2.1. Introduction	26
2.2 Device performance of planar <i>n-i-p</i> perovskite solar cells.....	28
2.3 Morphology and crystallinity of perovskite films	35
2.4 Fullerene profile at the interface	36
2.5 PCBM-dimer layers.....	40
2.6 Conclusions	44
2.7 Experimental section	45
2.8 References	48
Chapter 3 Understanding the film formation kinetics of sequential deposited narrow-bandgap Pb–Sn hybrid perovskite films	51
3.1 Introduction	52
3.2 Formation kinetics of Pb–Sn perovskite films	53
3.3 Structural properties of Pb–Sn perovskite films.....	59
3.4 Performance of Pb–Sn perovskite solar cells	65

3.5 Conclusions	71
3.6 Experimental Section	71
3.7 References	76
Chapter 4 Interconnecting layers for all-perovskite tandem solar cells	79
4.1 Introduction	80
4.2 SALD-SnO ₂ for all-perovskite tandem solar cells	82
4.3 Optimization for all-perovskite tandem solar cells	84
4.4 Photovoltaic performance of all-perovskite tandem solar cells	89
4.5 Conclusions	91
4.6 Experimental section	91
4.7 References	95
Chapter 5 16.8% monolithic all-perovskite triple-junction solar cells.....	97
5.1 Introduction	98
5.2 Formation of wide/mid/narrow bandgap perovskite films	99
5.3 ICLs for all-perovskite triple-junction solar cells	102
5.4 Photovoltaic performance of all-perovskite triple-junction solar cells	103
5.5 Conclusions	109
5.6 Experimental section	109
5.7 References	110
Chapter 6 Ultrathin hole transport layers for efficient narrow-bandgap perovskite solar cells.....	111
6.1 Introduction	112
6.2 Small molecule organic thin films.....	115
6.3 Device performance based on small molecule HTL	116
6.4 Ultrathin HTLs for narrow-bandgap PSCs.....	120
6.5 Conclusions	123
6.6 Experimental section	123

6.7 References	126
Summary	129
Curriculum Vitae	133
List of Publications.....	134
Acknowledgments.....	137

Chapter 1

Introduction

Abstract

Solar technology is on its way to becoming a pivotal contributor to the future energy supply because of its accessibility and predictability. Solar energy is directly converted into electricity using a photovoltaic cell. The pursuit of low production cost and high device performance has led to the development of various types of solar cells. This chapter gives a brief introduction to traditional and new-generation solar cell technologies. Novel perovskite semiconductors are discussed with focuses on their structural and optoelectronic properties. The advancement of perovskite-based solar cells is presented in parallel to the evolution of device architectures. Moreover, different solution-processing techniques are compared with an emphasis on their impact on the film formation dynamics. After introducing the performance metrics for solar cells, the fundamental efficiency loss of single-junction solar cells is discussed. The potential of perovskite-based multijunction solar cells is highlighted, and some recent developments of the interconnecting layers are reviewed.

1.1 Solar energy and photovoltaics (PV)

Developing clean, accessible, and renewable energy sources are of critical importance for the next generations in the context of climate change and energy shortage.¹ Among all forms of energy resources on earth, the ubiquitous sunlight would be a pivotal contributor to future energy consumption due to its vast abundance and zero-carbon emission.^{2,3} By using a photovoltaic (PV) cell, solar energy is directly converted into electricity, which can be exported through the power grid or restored in chemical fuels.⁴ Since the first report on a 6% silicon *p-n* junction photocell in 1954,⁵ the laboratory power conversion efficiency (PCE) of crystalline silicon (c-Si) has now reached 26.7%.⁶ Meanwhile, c-Si modules have shown PCEs of ~20% at a production scale, with a moderate price of ~\$0.25 W⁻¹. To date, over 90% of the global PV market is based on c-Si, which has become the fastest-growing renewable energy technology, reaching a total capacity of 627 gigawatts by the end of 2019.⁷⁻⁹

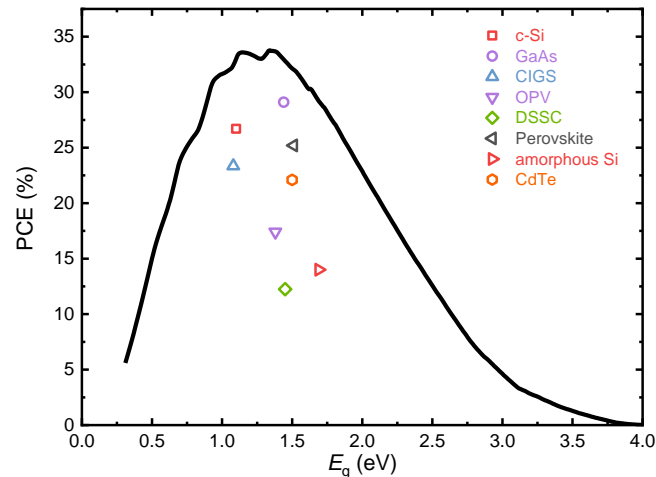


Figure 1.1 The maximum power conversion efficiencies as a function of optical bandgaps for a solar cell operated under the standard AM1.5G spectral irradiance.¹⁰ The record efficiencies of different types of solar cells are marked with symbols.⁶

Further improving the solar cell performance and reducing the production costs are needed to enable the terawatt-scale PV industry in the coming decades.¹¹ Half the cost of a c-Si module is attributed to the high purity material.¹ Due to the indirect bandgap of silicon semiconductors, a thick silicon wafer (~200 μm) is required for sufficient light absorption, resulting in a large amount of material waste during manufacturing and heavy modules for installation.¹ On the other hand, the PCE of single-junction c-Si is already approaching its theoretical limit (Figure 1.1), which makes it very challenging to improve the cost-efficiency of c-Si technology.¹² In comparison, thin-film solar cells based on direct-bandgap III–V

semiconductors can be made with a much thinner photo-active layer ($\sim 1 \mu\text{m}$). Owing to the excellent material quality and suitable bandgap, the state-of-the-art gallium arsenide (GaAs) device has achieved a record PCE of 29.1%, very close to the theoretical Shockley-Queisser PCE limit of 33% for single-junction solar cells.⁶ However, the requirements of intricate and expensive deposition processes of such semiconductors prohibit their large-scale applications.¹³

In the past decades, research interests have been focused on new PV technologies, including dye-sensitized solar cell (DSSC),¹⁴ organic photovoltaic (OPV),¹⁵ and quantum dot solar cell (QDSC)¹⁶ for their low-cost, lightweight, and solution processability. These features enable high-throughput manufacturing techniques such as roll-to-roll coating.¹⁷ However, their sub-optimal performance reported to date,⁶ i.e., 12.3% for DSSC, 17.4% for OPV, and 16.6% for QDSC prohibit their grid-scale applications. Recently, organic-inorganic hybrid perovskite semiconductors offer new avenues for the development of low-cost and high-efficiency solar cells, with rapid advances in the PCE from 3.8% to a record of 25.2% within a decade.^{6,18}

1.2 Perovskite semiconductors

Perovskite, named after a mineralogist Lev Perovski, is a nomenclature for any material adopting the same crystal structure as calcium titanium oxide (CaTiO_3).¹⁹ Such materials can be described by the formula ABX_3 , where X is an anion, and A and B are different cations (Figure 1.2). The crystal structure is stable when the ionic radii of A (R_A), B (R_B), and X (R_X) satisfy the Goldschmidt tolerance factor $0.81 < t < 1.11$ and octahedral factor $0.44 < \mu < 0.90$, where $t = (R_A + R_X)/[\sqrt{2}(R_B + R_X)]$ and $\mu = R_B/R_A$, respectively.²⁰ This allows a myriad of oxide- and halide-based perovskite materials with distinct optical and electronic properties.²¹ Developed in 1972, the archetypal organic-inorganic hybrid metal halide $\text{CH}_3\text{NH}_3\text{MX}_3$ (M = Pb or Sn, X = I, Br, or Cl) was known for its potential in transistors and light-emitting diodes in the mid-1990s.²²⁻²⁴ In 2009, Miyasaka and co-workers first reported the use of $\text{CH}_3\text{NH}_3\text{PbX}_3$ (X = Br and I) as light sensitizers in DSSCs and showed a promising PCE of 3.8%.²⁵ Since then, metal halide perovskites have been under the spotlight of the PV research community for their exceptional optoelectronic properties.

Compositional engineering has suggested several components that are suitable to form photo-active perovskite phases.²⁶ In general, the A site is a monovalent cation, which is methylammonium (MA^+), formamidinium (FA^+), or cesium (Cs^+); the B site is a divalent cation, which can be lead (Pb^{2+}) or tin (Sn^{2+}); and X is the halide anion, which is iodide (I^-), bromide (Br^-), or chloride (Cl^-).²⁶ Interestingly, the optical bandgap of perovskite can be easily tuned by

changing its composition.²⁷ Starting from a conventional 1.5 eV MAPbI₃, the perovskite bandgap is gradually increased to 2.3 eV when replacing I with Br, and further to 3.1 eV by using Cl.²⁷ Meanwhile, an anomalous bandgap behavior is observed when mixing Pb- (1.5 eV) with Sn-based (1.3 eV) compounds, providing the narrowest bandgap of ~1.2 eV between 50% and 80% Sn-content.²⁸ Such a broad bandgap tunability offers a great promise for developing perovskite-based multijunction solar cells (see in Section 1.6).¹²

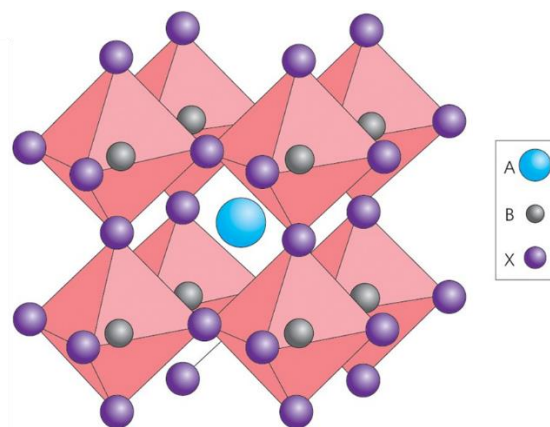


Figure 1.2 Illustration of a cubic perovskite crystal structure.²⁰ Reprinted by permission from Springer Nature.

Remarkably, metal halide perovskites exhibit a direct bandgap and an even stronger optical absorption than some III–V semiconductors, which allows the usage of below 1 μm thin films to harvest most of the above-bandgap photons.^{20,29} Such materials also show a large dielectric constant, suggesting that photo-generated excitons can easily dissociate into free carriers at room temperature and thereby generating a high photocurrent.²⁹ Besides, perovskite crystallites have shown a high defect tolerance, together with high carrier mobility as well as long diffusion lengths ($>1 \mu\text{m}$) for both electrons and holes.³⁰ As a result, the non-radiative recombination rate is significantly reduced, which results in a small difference between open-circuit voltage (V_{oc}) of the solar cells and their effective bandgap potential (E_g/q).³¹ In contrast to traditional semiconductors, these prominent features are also found in polycrystalline perovskite films with small grains ($<1 \mu\text{m}$), thus providing great flexibility in fabricating high-quality perovskite films.²⁰

1.3 Device architecture of perovskite solar cells

As mentioned above, perovskite was first utilized as a dye-sensitizer by self-organizing on a mesoporous TiO₂ film.²⁵ It was infiltrated in a liquid electrolyte containing an iodide/triiodide redox couple. The meso-TiO₂ was crucial for the fast extraction of electrons,

whereas the liquid electrolyte collected holes. The initial DSSCs showed PCEs of 3.8% and 6.5%.^{25,32} Later, the liquid electrolyte was found to dissolve perovskite compounds and was replaced by a more stable, solid-state 2,2',7,7'-tetrakis[*N,N*-di(methoxyphenyl)amino]-9,9'-spirobifluorene (Spiro-OMeTAD) as the hole transport layer (HTL), with reported cell efficiencies up to 10%.³³ Since then, most of the record-breaking perovskite solar cells (PSCs) were achieved in a similar mesoscopic structure: fluorine-doped tin oxide (FTO)/compact TiO₂/meso-TiO₂/perovskite/HTL/Au (Figure 1.3a).^{34,35} However, meso-TiO₂ requires a high-temperature (≥ 450 °C) sintering, which is not compatible with the large-scale processing on flexible plastic substrates.^{36,37}

By replacing TiO₂ with insulating Al₂O₃ in mesostructured devices, Snaith and co-workers have shown that the perovskite layer alone can act as both a light absorber and a charge transporter.³³ This allows the fabrication of planar-structured PSCs without using meso-TiO₂ and thereby high-temperature processing.³⁸ Planar PSCs are divided into *p-i-n* and *n-i-p* structures (Figure 1.3b and c), in which the intrinsic perovskite absorber (*i*) is deposited either on a *p*-type HTL or an *n*-type electron transport layer (ETL).³⁷ To date, PCEs of ~23% have been achieved in both planar structures, which are comparable to that of mesostructured devices.^{39,40}

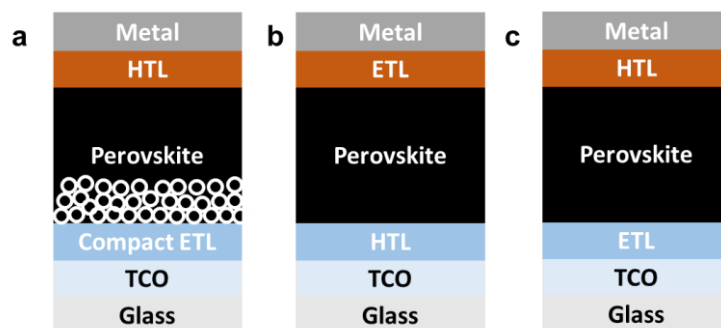


Figure 1.3 (a) Mesoporous and planar (b) *p-i-n* and (c) *n-i-p* device structure of perovskite solar cells.

A judicious selection of charge transport materials is crucial for the high efficiency and long-term stability of PSCs. The (front) transport layers should be optically transparent to ensure sufficient light reaching the photo-active layer.⁴¹ They should provide a favorable energetic alignment with the perovskite, thus enabling a fast charge extraction process while retaining a low potential energy drop.⁴² They should possess high charge mobility such that free carriers can be efficiently collected at both electrodes.³⁶ Besides, the transport layers need to be intrinsically stable and compact to protect the perovskite layer from degradation.⁴³ Furthermore, manipulating defect states at the transport layer/perovskite interfaces is essential to mitigate

non-radiative recombination and ionic charge accumulation, both are responsible for the V_{oc} drop and hysteresis effect in the current density–voltage (J – V) characteristics of PSCs (see in Section 1.5).^{42,44}

In n - i - p PSCs, Spiro-OMeTAD and poly[bis(4-phenyl)(2,4,6-trimethylphenyl)amine] (PTAA) are the most commonly used HTLs for their ease of solution process and high device performance. However, both organic HTLs are expensive and require hygroscopic dopants such as lithium bis(trifluoromethanesulfonyl)imide (Li-TFSI), 4-*tert*-butylpyridine (tBP) to improve their hole mobility, which accelerates device degradation under ambient conditions.⁴² Numerous dopant-free organic HTLs have also been investigated, yet the reported efficiencies are relatively low compared to that of Spiro-OMeTAD.⁴⁵ In comparison, low-cost inorganic HTLs exhibit much higher hole mobilities and excellent stability.⁴² However, most of the polar solvents used for solution processing such inorganic materials can degrade the underlying perovskite layer. Grätzel and co-workers have developed a fast solvent removal method to deposit a compact copper thiocyanate (CuSCN) layer on the perovskite film. Combined with a reduced graphene oxide layer at the CuSCN/Au interface, the authors demonstrated a PCE of 20.4% with excellent operational stability.⁴⁶

N -type semiconducting metal oxides are the most used ETLs in the n - i - p device structure.⁴⁷ Compared to other metal oxides, TiO_2 has relatively low electron mobility and a conduction band misalignment with the state-of-the-art mixed-cation perovskite materials, which creates an energetic barrier at the interface and lowers the device performance.⁴⁸ Besides, TiO_2 can be photo-activated under ultraviolet (UV) illumination, which will trigger the oxidation of I^- and eventually decompose the perovskite material by releasing CH_3NH_2 or HI.⁴³ Similarly, ZnO has much higher electron mobility and is commonly used in OPV devices; however, its basicity causes instability of perovskite material during thermal annealing.⁴⁹ Recently, SnO_2 has received tremendous attention as the ETL for n - i - p PSCs.⁴¹ Compared to TiO_2 , SnO_2 has been shown to provide excellent UV stability, higher electron mobility, and a better energy level alignment with many perovskite materials.⁴¹ Using SnO_2 nanoparticles, You and co-workers have achieved a high PCE of 23.32% in planar n - i - p devices.³⁹

Notably, metal oxides are easy to form imperfections that are correlated with deep trap states and affect interfacial charge carrier dynamics of PSCs.⁵⁰ Depending on the preparation methods, the number of trap states can vary drastically, which makes the modification or surface passivation of such metal oxides crucial for the device performance.⁴¹ Typically, self-assembled monolayers such as fullerene and its derivatives are commonly used at the ETL/perovskite

interface.⁵¹ Such modification layers can effectively block defects at the metal oxide surface and enhance electron mobility.⁵⁰ As for the elemental doping method, Tan and co-workers have demonstrated high PCEs of 22.2% by using SnO₂-KCl composite as the ETL.⁵² They found that both K⁺ and Cl⁻ ions can passivate the ETL/perovskite contact, while K⁺ ions further diffuse through the perovskite layer and passivate the grain boundaries.

For planar *p-i-n* PSCs, poly(3,4-ethylenedioxythiophene):polystyrene sulfonate (PEDOT:PSS) is widely used as the HTL for its high conductivity and low-temperature solution processability.⁴³ However, PEDOT:PSS has a relatively low work function of ≈ 5.0 eV and can be further reduced by *N,N*-dimethylformamide (DMF) to ≈ 4.5 eV when spin coating the perovskite precursor solution on top.^{53,54} The large energy offset between the valence band maximum (VBM) of perovskites and the work function of PEDOT:PSS can lead to significant exciton quenching at the interface and potential energy loss in the PSCs.⁵⁵ Besides, hygroscopic and acidic PEDOT:PSS can adversely react with the perovskite layer, which limits the thermal stability of PSCs.⁵⁶ To date, most of the high-efficiency *p-i-n* PSCs are based on PTAA or poly[*N,N'*-bis(4-butylphenyl)-*N,N'*-bis(phenyl)-benzidine] (poly-TPD) as the HTL.^{57,58} In contrast to *n-i-p* structure, a thin HTL (<10 nm) between the perovskite layer and the bottom electrode is sufficient, which considerably lowers the series resistance of the device even without using chemical dopants in the HTL.⁵⁹ On the other hand, fullerene and its derivatives, including C₆₀, phenyl-C₆₁-butyric acid methyl ester (PCBM), and indene-C₆₀ bisadduct (ICBA), are commonly used as the ETL in *p-i-n* PSCs.⁶⁰ Fullerenes have shown favorable energy level alignment with perovskites and high electron mobilities. Moreover, they can effectively passivate trap states on the top of the perovskite layer, eliminating the photocurrent hysteresis of solar cells.⁶¹

The choice of electrodes also has a significant impact on the performance and stability of PSCs.⁴² For device structures as illustrated in Figure 1.3, transparent conductive oxides (TCOs) such as indium tin oxide (ITO) or FTO are the commonly used bottom electrodes for their high transparency and low sheet resistance. Opaque devices typically use conductive metals as the counter (top) electrodes, which also serve as a reflective mirror for better light absorption.⁶² However, metals such as Al and Ag can adversely react with I-species from the perovskite layer, causing fast deterioration of cell performance in an ambient environment. Huang and co-workers have shown that a Cu electrode is more stable on top of the perovskite film and hence improves the long-term stability.⁶³ On the other hand, transparent top contacts have also been developed for semitransparent and multijunction PSCs.⁶⁴ Compared to the

sputtered TCO, alternatives are the solution-processed metal-nanowires and thermally evaporated dielectric-metal-dielectric multilayered electrodes.^{65,66}

1.4 Deposition methods of perovskite films

Controlling the morphology and crystallinity of the perovskite absorber layer is of vital importance for the performance of PSCs. There are some prerequisites for high-quality perovskite films in PV applications. The photo-active layer should be reasonably thick (typically between 400 nm to 1 μm) to harvest most of the incident light. In planar-structured devices, the perovskite film should be flat (low surface roughness) and pinhole-free, which ensure a conformal coating of the charge transport layer and electrode on top and thereby preventing shunting pathways and leakage currents in the PSCs.⁶⁷ Preferably, the perovskite film should have a high crystallinity with large-sized and vertically oriented grains, which facilitate charge transport along the vertical direction by avoiding trap-rich grain boundaries.⁶⁸ However, the formation of crystalline perovskites involves very complex processes that depend on variables such as precursor composition, additive, solvent, temperature, deposition atmosphere, and the substrate.⁶⁹ Given the high boiling points of the commonly used solvent systems, the nucleation of perovskite is often limited, which leads to dendritic morphologies as a result of the preferential growth of perovskite crystals.⁶⁹ Based on classical nucleation and crystallization models, most studies adopt strategies that can promote a high nuclei density in the precursor film, which results in small-grained but dense and full-coverage perovskite layers.⁷⁰

The processing of perovskite film can be divided into one-step and two-step methods, which represent the number of steps involved in depositing the precursors through either a solution or a vapor phase.⁶⁹ For lab-scale research, spin coating is the most used deposition technique for the fast screening of novel perovskite compositions. Altering the ink formulation and coating conditions can drastically change the thinning and smoothing behavior of the precursor films,⁷¹ which in turn dictates the crystallization dynamics of perovskite phases.

All the precursors are deposited simultaneously in the one-step spin coating. For the MAPbI_3 recipe, stoichiometric PbI_2 and MAI are dissolved in a polar aprotic solvent such as DMF, dimethyl sulfoxide (DMSO), or γ -butyrolactone (GBL).⁶⁹ The precursor solution is then dropped onto a rotating substrate, on which surplus ink is ejected by centrifugal force and followed by a top-down solvent evaporation process. Meanwhile, the precursor gradually reaches a supersaturation state that leads to the formation of perovskite phases.⁷² After spin

coating, a thermal annealing process (100–150 °C) is necessary to allow grain coarsening in the MAPbI₃ film.⁶⁷ As mentioned above, despite its simplicity, the largely uncontrolled (and slow) drying process of one-step spin coating often results in poorly covered perovskite films with inferior device performance. Several varieties of one-step spin coating, which include the use of heat (hot casting), anti-solvent washing, inert gas (N₂) quenching, and vacuum-assisted drying, have been developed (Figure 1.4).⁷⁰ All these additional procedures aim for fast solvent removal, which creates a high density of perovskite nuclei (and the like) directly after spin coating.⁶⁹ Alternatively, the use of fast-crystallizing chemical additives such as lead acetate (Pb(CH₃CO₂)₂) or a volatile solvent such as 2-methoxyethanol, can also lead to smooth and uniformly crystallized perovskite films.^{73,74}

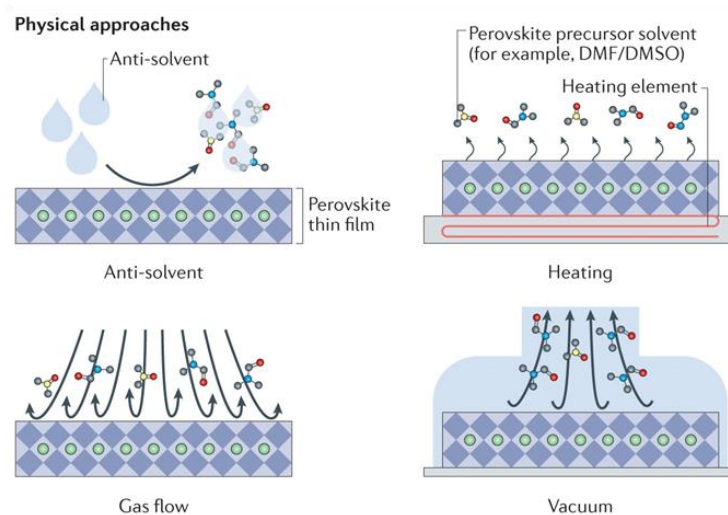


Figure 1.4 Typical approaches for fast nucleation of perovskite phases in a one-step solution process.⁷⁰ Reprinted by permission from Springer Nature.

Compared to a one-step process in which the layer-thinning and crystal formation coincide, two-step spin coating provides much better morphological control for perovskite thin films.⁷⁰ In this method, a metal halide (PbI₂) precursor film is first deposited on the substrate and is converted to the perovskite phase by casting an organic halide (MAI) solution on top. Thermal annealing is usually applied to enlarge the grain sizes. The final morphology of such perovskite film is mainly dependent on the intermediate inorganic template (PbI₂), which is reportedly much easier to form a smooth layer over a large area.⁷⁵ Furthermore, a two-step process has shown a much broader processing window with improved reproducibility, in contrast to the short time window of anti-solvent or inert-gas flow application in a one-step process (typically limited to a few seconds before reaching the supersaturation point).⁷⁶ One big challenge of two-step processing is to fabricate thick perovskite films without unconverted

PbI₂.⁷⁵ A rapid formation of perovskite phase can take place upon dripping an MAI solution onto the PbI₂ precursor, which leads to a two-fold volume expansion as a result of MAI intercalation into the layered PbI₂ structure.⁷⁷ Therefore, the as-formed perovskites at the top surface retard the further reaction of the bottom PbI₂. Research has shown that the solvation state of PbI₂ can drastically change the crystallization dynamics of perovskite films.⁷⁸ Seok and co-workers have reported the use of a complexed PbI₂-DMSO precursor to ensure a fast and yet complete conversion into perovskite.⁷⁷ Recently, by using a similar two-step spin coating method, You et al. have demonstrated over 23% PSCs with an 800 nm-thick perovskite absorber layer.³⁹

However, the spin coating technique is unsuitable for large-scale production and wastes a large amount of material during the process. Scalable deposition methods such as blade coating, slot-die coating, spray coating and inject printing have been utilized for continuous roll-to-roll fabrication of perovskite films.⁷⁹ To date, the performance of perovskite solar modules based on scalable deposition techniques still lags behind the lab-scale PSCs using spin coating. This is mainly attributed to the increasing difficulty of depositing uniform and defect-free perovskite films over a larger area.⁷⁹ Besides, the aforementioned ink formulation and processing conditions that have been exclusively optimized for spin coating cannot be directly applied to other scalable processing methods. A profound understanding of the processing conditions and their impact on perovskite growth is crucial for the technology transfer from lab-scale to large-scale device fabrication.⁷⁹ Recently, *in situ/operando* thin-film characterization techniques such as optical absorption, photoluminescence, optical microscopy, and grazing-incidence wide-angle X-ray scattering (GIWAX) have been used to monitor the dynamic processes during perovskite film deposition.^{80,81} These methods provide new insights correlating the temporal evolution of optical properties, phase transition, and microstructure with coating parameters such as precursor compositions as well as drying processes, which is critical for the performance of the final perovskite devices.

1.5 Characterization of perovskite solar cells

Under light illumination, the perovskite layer absorbs photons with energy higher than its optical bandgap ($E_{\text{photon}} \geq E_g$) and generates unbound electron-hole pairs. Due to the large dielectric constant and long carrier diffusion length of perovskites, free electrons/holes are formed in picoseconds and selectively driven to the electron/hole transporting layer via a built-in electric field.⁸² The charge carriers are then extracted at the corresponding electrodes, creating a photocurrent and photovoltage (Figure 1.5).

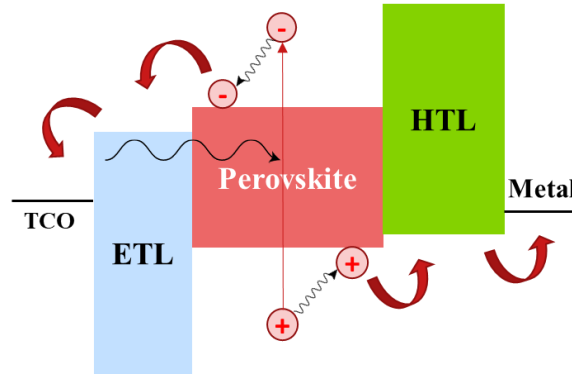


Figure 1.5 Schematic energy diagram and charge transfer processes in a perovskite solar cell.

The characterization of solar cells is done by measuring the current density under a fast sweeping voltage bias applied between the two electrodes. Figure 1.6a and b display the J - V characteristics of a representative PSC under dark (log-linear scale) and illuminated (linear scale) conditions. In the dark, the solar cell should behave like a diode, of which the leakage current (shunt resistance) is obtained at the low-voltage region, the high voltage region can evaluate the series resistance, and the slope in the exponential region determines the charge recombination regime (ideality factor).⁸³ Under light illumination, the output current is the summation of the dark current and the photocurrent. Several critical parameters, including the open-circuit voltage (V_{oc} , V), short-circuit current density (J_{sc} , mA cm^{-2}), fill factor (FF), and maximum output power density (P_{MPP} , mW cm^{-2}) of solar cells can be extracted in the fourth quadrant of the J - V plot. The FF is determined by the equation

$$FF = \frac{P_{MPP}}{J_{sc} \times V_{oc}} = \frac{J_{MPP} \times V_{MPP}}{J_{sc} \times V_{oc}}$$

Where J_{MPP} (mA cm^{-2}) and V_{MPP} (V) represent current density and voltage at the corresponding maximum power point, the FF indicates the charge extraction capacity and is closely related to the resistivity of a solar cell. Furthermore, the power conversion efficiency (PCE) is defined as

$$PCE (\%) = \frac{P_{MPP}}{P_{in}}$$

Where P_{in} (mW cm^{-2}) is the power density of the incident light. To accurately report the cell efficiency, in the spectral region of the test cell (e.g., 300 to 1100 nm for different types of PSCs), the light source should be closely matched with the terrestrial solar spectrum at a global air mass (AM) of 1.5. As such, the number of photons absorbed by the test cell from the light source will be equal to that from standard AM1.5G illumination (one sun condition, defined as 100 mW cm^{-2}).⁸⁴ Besides, to prevent an overestimation of the photocurrent, the device under

illumination needs to be shielded by a non-transparent mask with a well-defined aperture area that is slightly smaller than the active cell area.⁸⁵

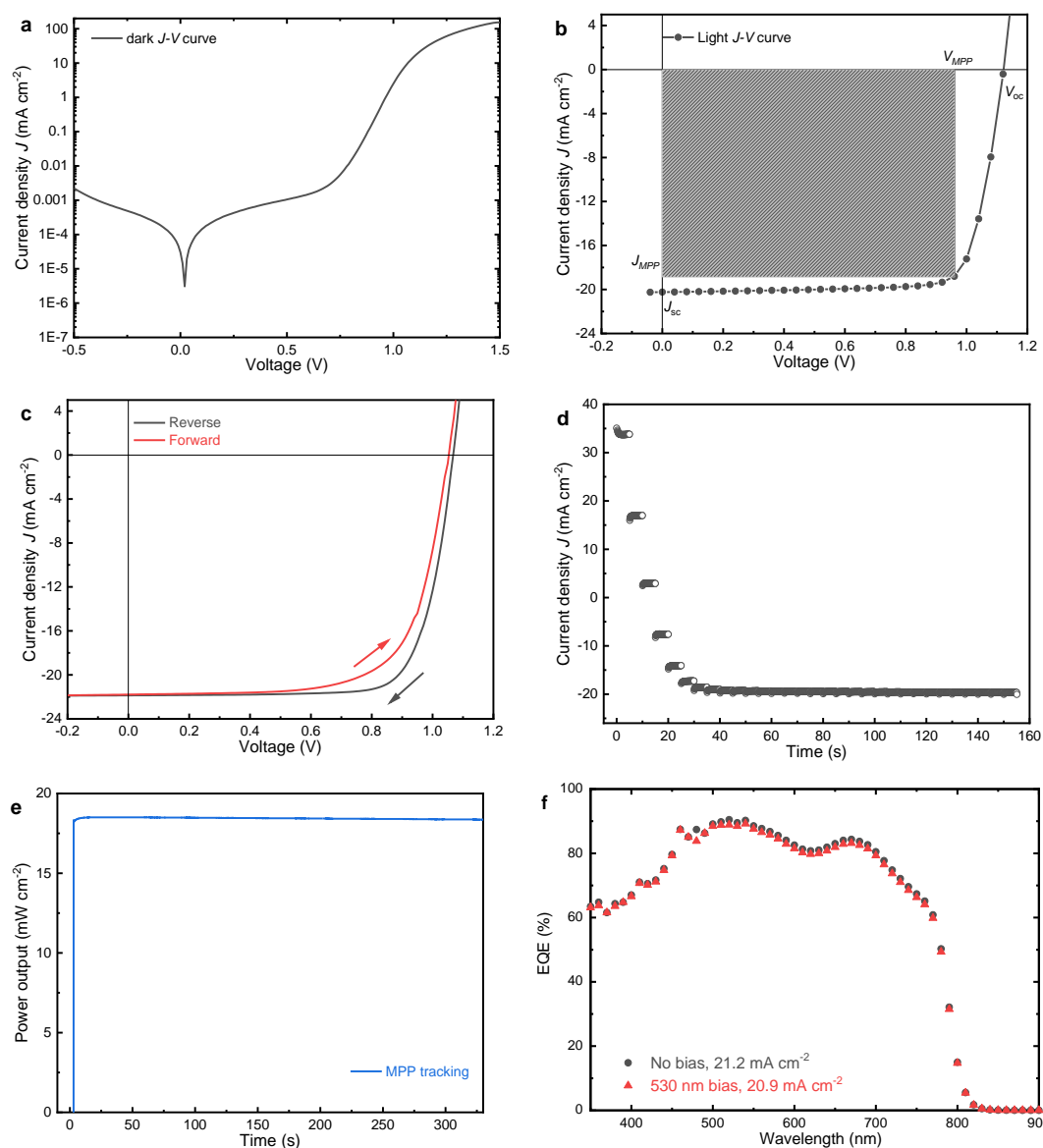


Figure 1.6 Typical J - V curves of PSCs measured in (a) dark and (b) under a solar simulator. (c) J - V curves measured in reverse and forward directions. (d) Stabilized J - V curve, where the voltage was swept from the open-circuit to the short-circuit at every 0.04 V. The wait time at each voltage was 5 sec. (e) The steady-state power output of a PSC operated at V_{MPP} under a solar simulator. (f) EQE spectra of a PSC measured with or without a green LED (530 nm) bias light.

Importantly, a massive inconsistency of J - V curves measured in the reverse scan (from V_{OC} to J_{sc}) and forward scan (from J_{sc} to V_{OC}), namely the hysteresis effect, is often seen in low-performing perovskite solar cells (Figure 1.6c).⁸⁶ This behavior is likely related to the capacitive current induced by trap states and ion migration at the perovskite/transport material interface.⁸⁷ Also, the hysteresis effect is susceptible to the specific measuring protocol (e.g., voltage sweep

rate) and therefore makes it difficult to determine the efficiency of PSCs accurately.⁸⁶ Compared to the common practice of performing J - V measurements only in fast sweeps (~ 0.1 to 1 V s^{-1}), slow sweep measurements during which the current is stabilized at each voltage step can provide much more reliable results (Figure 1.6d). Besides, steady-state power output tracking near the maximum power point should also be presented when evaluating the performance of PSCs (Figure 1.6e).⁸⁶

As discussed, measuring the J - V curves of solar cells at standard illumination conditions is crucial to determine the true PCEs. Since the current density of solar cells should be directly proportional to the solar irradiation, a small discrepancy between the spectrum of a sun simulator and AM1.5G illumination can drastically affect the final J_{sc} .⁸⁸ In comparison, the external quantum efficiency (EQE) spectrum is more accurate at determining the J_{sc} .⁸⁹ The EQE is defined as the ratio of charges collected at the outer circuit to the number of incident photons per wavelength (Figure 1.6f). Therefore, the convolution of $EQE(\lambda)$ with AM1.5G solar power density $I_{AM1.5G}(\lambda)$ yields the J_{sc} :

$$J_{sc} = \int EQE(\lambda) I_{AM1.5G}(\lambda) \frac{q\lambda}{hc} d\lambda$$

Where q is the elementary charge, h is the Plank constant, and c is the speed of light. It should be noted, however, that the EQE spectrum at a single wavelength is acquired by modulated monochromatic light of low intensity. For a solar cell that shows a nonlinear trend between the charge collection efficiency and light intensity, the J_{sc} value determined solely by the normal EQE spectrum could be somewhat overestimated.⁸⁹ To mimic the one sun condition used for the J - V measurement, an additional bias illumination should be provided to the device during EQE measurement.⁵⁴

1.6 Shockley-Queisser limit and multijunction solar cells

The theoretical limit of photovoltaic devices based on detailed balance principles was firstly analyzed by Shockley and Queisser (S-Q) in 1961.⁹⁰ Under solar radiation, the photoactive material with a defined bandgap (E_g) can only absorb high energy photons ($E \geq E_g$) and generates charge carriers. The excess energy above E_g is, however, lost due to the relaxation of carriers towards the conduction band (E_C) and valence band (E_V) of the material (thermalization loss). Meanwhile, photons with energy lower than the material bandgap ($E < E_g$) are not absorbed and hence do not contribute to the photocurrent (transmission loss).⁹¹ Theoretically, a wide bandgap material should exhibit a high V_{oc} but a low J_{sc} due to insufficient absorption of

photons. In contrast, a narrow bandgap material presents a higher J_{sc} but a lower V_{oc} as a result of increased thermalization loss. According to the S-Q calculations, the maximum attainable PCE for single-junction solar cells with a ~ 1.3 eV bandgap is $\sim 33\%$ (Figure 1.1).⁹²

New solar technologies with higher efficiency and lower production costs than c-Si are needed to accelerate the upcoming terawatt-scale PV industry.¹¹ Developing multijunction solar cells with complementary bandgaps is a viable strategy to surpass the S-Q efficiency limit for single-junction devices.¹² In a multijunction cell, the widest bandgap absorber is placed at the front to harvest the highest-energy photons, whereas a subsequent narrower bandgap material absorbs the transmitted lower-energy photons.⁹³ In this way, carrier thermalization loss can be minimized while a broader range of the solar spectrum is harvested by the stacked PV absorbers (Figure 1.7). Theoretically, tandem and triple-junction solar cells can increase the efficiency limit to 46% and 52%, respectively, and up to 65% when combining an infinite number of junctions.⁹⁴

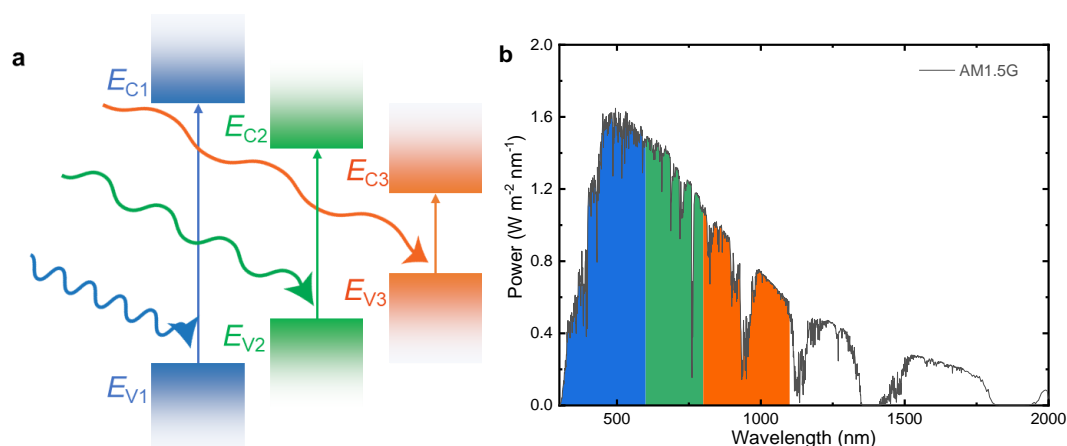


Figure 1.7 (a) Schematic energy diagram of a multijunction solar cell, where the wide bandgap absorber is placed at the front. (b) Standard solar irradiance spectrum (AM 1.5G). The colored areas represent the spectral regions being absorbed by different light-absorbers.

In practice, high-quality III–V semiconductors have achieved high PCEs of 39.2% and 37.9% in monolithic six-junction (6J) and triple-junction solar cells, respectively.^{6,94} However, high-costs and intricate deposition processes are the limiting factors for their large-scale terrestrial applications.⁹⁴ Inexpensive and solution-processable organic semiconductors have also been exploited for multijunction solar cells. Nevertheless, their efficiencies are suboptimal due to the lack of comparably high-performing organic absorbers over a wide range of bandgaps.⁹³ Perovskite semiconductors, which exhibit a widely tunable bandgap via compositional engineering, hold a unique promise for the development of cost-effective

multijunction solar cells.^{92,95} A tandem solar cell comprising a wide bandgap perovskite and a narrow bandgap (1.1 eV) c-Si has reached a certified PCE of 29.1%, already higher than the c-Si single-junction record.⁶ Such a hybrid tandem approach can boost the efficiency of existing c-Si at a relatively low cost and is believed to be the first step in commercializing perovskite-based photovoltaics.⁹⁵ More recently, advances in efficient narrow bandgap Pb-Sn hybrid perovskites (1.2–1.3 eV) have accelerated the development of all-perovskite tandem solar cells.⁹⁶ The solution processability of all components at low-temperature would greatly enhance incentives to explore the large-scale implementation of such devices. Device and optical modeling have suggested that all-perovskite tandem cells with 1.8 eV wide-bandgap and 1.2 eV narrow-bandgap perovskite absorbers can reach a feasible PCE of 33.4%.⁹⁷ Recently, by reducing Sn vacancies and thereby increasing the charge-carrier diffusion length in Pb-Sn perovskite to 3 μm , Tan and co-workers have demonstrated PCEs of 21.1% for 1.22 eV narrow bandgap and 24.8% for 1.77/1.22 eV all-perovskite tandem solar cells.⁹⁸ Furthermore, simulations have predicted that triple-junction solar cells with 2.04/1.58/1.22 eV perovskite absorbers and 1.95/1.44/1.10 eV perovskite/perovskite/silicon materials can reach PCEs as high as 36.6% and 38.8%, respectively.⁹⁷ Lately, proof-of-concepts PCEs of 6.7% and 13%, respectively, have been demonstrated for all-perovskite and perovskite/perovskite/Si triple-junction solar cells.^{99,100} Very recently, Tan et al. demonstrated all-perovskite triple-junction solar cells with efficiency exceeding 20%.¹⁰¹

In a monolithic, series-connected multijunction solar cell, the total voltage is equal to the sum of voltages across each sub-cell at equal currents.¹⁰² The absorber layers with complementary bandgaps are both optically and electrically connected by the interconnecting layers (ICLs), which typically consist of an HTL and an ETL as used in single-junction cells.¹⁰³ In addition to the band alignment with the contacting perovskite layers, the ICLs should have sufficient Ohmic conductance to enable the fast recombination of holes and electrons from the adjacent sub-cells and thereby to prevent resistive losses.¹⁰³ Meanwhile, the ICLs should maintain a low lateral conductivity to avoid shunting paths.¹⁰⁴ To balance the light absorption and current generation of each sub-cell, reflection losses and parasitic absorption of the ICLs should be minimized such that more lower energy photons can reach the narrower bandgap absorbing layers.¹⁰⁵ More importantly, the ICLs should ensure a good barrier property to prevent damage to the underlying layers caused by the processing of subsequent layers.^{99,104} This is especially important for multijunction devices based on perovskite absorbers, for which

polar solvents such as DMF and DMSO can easily re-dissolve any underlying perovskite layers.^{65,99,104}

For monolithic all-perovskite multijunction (tandem) cells, examples of solution-processed ICLs are PEDOT:PSS/ITO nanoparticles and p-doped cross-linked PTAA/n-doped PCBM.^{99,106} In the latter case, PTAA was cross-linked with 1,2-bis[4-(azidomethyl) phenyl]-1,2-diphenylethane (TPE-MN3) by UV irradiation to enhance the solvent barrier property and doped by molybdenum tris[1-(trifluoroacetyl)-2-(trifluoromethyl)ethane-1,2-dithiolene] ($\text{Mo}(\text{tfdCOCF}_3)_3$) to increase the electrical conductivity. In addition, transfer-laminated PEDOT:PSS, chemical vapor deposited fluoride silane-incorporated polyethylenimine ethoxylated hybrid system have enabled the direct spin coating of perovskite solutions (with DMF) on top.^{107,108} Alternatively, all-perovskite tandems can also be fabricated via thermal evaporation, where evaporated p-doped $N^4, N^4, N^{4''}, N^{4''}$ -tetrakis([1,1'-biphenyl]-4-yl)-[1,1':4',1''-terphenyl]-4,4''-diamine (TaTm) and n-doped C_{60} were sandwiched between the evaporated perovskite absorbers.¹⁰⁹ To date, most of the high-efficiency tandem solar cells have been reported by using (DMF) solution-processed perovskite absorbers and sputtered TCO (e.g., ITO) as the recombination layer, which serves as a good physical barrier and has a low-resistivity.¹¹⁰⁻¹¹² However, a thick TCO layer causes reflection loss and parasitic absorption in the near-infrared region, limiting the J_{sc} of the narrow bandgap sub-cell.¹¹² The high conductivity of the TCO layer could also induce shunt pathways between sub-cells.¹⁰⁴ Moreover, the sputtering process can cause damage to the underlying layers, for which a thin metal oxide layer such as SnO_2 prepared by atomic layer deposition (ALD) has been used.^{104,113} It was found that changing the growth conditions can yield a compact and conductive ALD layer, which alone shows an excellent permeation barrier property and allows for fast charge transport without using the sputtered TCO layer.⁶⁵ More recently, Tan et al. demonstrated a 24.2% all-perovskite tandem solar cell low-resistivity ICLs based on $\text{C}_{60}/\text{ALD-SnO}_2/\text{Au}/\text{PEDOT:PSS}$.⁹⁸

1.7 Outline

Recent advances in perovskite solar cells (PSCs) have enabled a record PCE of 25.2%, already approaching the conventional inorganic technologies. Defect passivation at the metal oxide layer/perovskite interface is a common approach to improve device performance. However, the nature of passivation is not fully understood. On the other hand, developing all-perovskite multijunction solar cells is a viable strategy to attain high efficiencies at low cost. To this end, high-quality perovskite materials with complementary optical bandgaps are required. In addition, a rational design of the device structure is needed to mitigate the optical

and electrical losses and to tackle the processing challenges encountered in depositing widely different perovskite layers on top of each other. This thesis aims to gain new insights into the role of interfaces for perovskite photovoltaics and advance the understanding of film formation kinetics on the perovskite device performance. The thesis also encompasses a cell design strategy to achieve efficient all-perovskite multijunction solar cells.

In Chapter 2, different fullerenes are compared to study the passivation effect at the SnO_2 /perovskite interface. X-ray photoelectron spectroscopy depth profiling is used to study the distribution of fullerenes in the ETL. A direct correlation is established between the formation of interfacial chemical bonds and the retention of passivating fullerene (monolayers) at the SnO_2 interface that effectively reduces the number of defects and enhances electron mobility. For a fullerene with a carboxylic acid functional group (PCBA), the chemical binding is the most efficient and results in the best cell performance of 18.8%. For a fullerene with an ester side chain (PCBM), the passivation effect is activated only when thermal annealing was used. This observation is further demonstrated by introducing a solvent-robust PCBM-dimer layer at the interface, where the device performance still shows a large dependence on the thermal annealing treatment.

Developing efficient narrow bandgap Pb–Sn hybrid perovskite solar cells with high Sn-content is crucial for all perovskite-based multijunction devices. However, compared to its Pb-based analogs, the fast-crystallizing Sn-based perovskite imposes a greater processing challenge. In Chapter 3, a sequential (two-step) deposition method is used to fabricate Sn-based perovskites. To understand the growth mechanism of Pb–Sn hybrid perovskites, in situ optical spectroscopy is performed during sequential deposition of Pb–Sn hybrid perovskite films and combined with ex-situ characterization techniques to reveal the temporal evolution of crystallization in Pb–Sn hybrid perovskite films. The study shows that the crystallization to pure-Sn perovskite phase is completed while casting the solution. In contrast, the formation of the pure-Pb based perovskite is considerably suppressed before thermal annealing. It is further demonstrated that despite the different crystallization behavior of Pb and Sn-based perovskite precursors, the beneficial sequential deposition method ensures a homogeneous transformation to the Pb–Sn hybrid perovskite phase. PSCs based on a 1.23 eV perovskite absorber exhibit a PCE of 16.1% with good ambient stability. Together with a 1.57 eV semitransparent cell, a mechanically stacked four-terminal tandem exhibit a PCE of 21.1%.

In a monolithic, series-connected multijunction solar cell, adjacent absorber layers are both electrically and optically connected by the ICLs, which serve as a physical barrier to

prevent processing damages to the underlying layers. In Chapter 4, spatial-ALD (SALD) grown SnO_2 has been studied in all-perovskite tandem solar cells. A compact SALD layer significantly reduces solvent permeation. It also enhances the thermal stability and allows the deposition of PEDOT:PSS and perovskite layers on the top of a bottom perovskite sub-cell. By optimizing the intermediate electrical contact, the ICLs demonstrate efficient charge recombination with low-resistivity losses. Tandem devices combining 1.73 eV and 1.23 eV perovskite sub-cells yield PCEs of above 19%.

Furthermore, in Chapter 5, using the processing methods developed in the previous chapters, 1.73 eV, 1.57 eV, and 1.23 eV perovskite absorbers are integrated with low-resistivity ICLs to form a monolithic, all-perovskite triple-junction solar cell. A promising PCE of 16.8% is achieved with a low potential energy drop of 80 mV in comparison to the summed V_{oc} of all three sub-cells ($V_{oc} = 2.78$ V) and low resistivity loss (FF = 0.81). Simulation data suggests that the performance loss of the current triple configuration is from the overlapped spectral response of the sub-cells, parasitic absorption of ITO and PEDOT:PSS, reflection, and incomplete light absorption in the near-infrared due to a relatively thin 1.23 eV absorber layer.

The most used HTL for narrow bandgap PSCs is PEDOT:PSS, despite its instability with Pb-Sn hybrid perovskite materials. The parasitic absorption of PEDOT:PSS in the near-infrared region also lowers the attainable J_{sc} of the narrow bandgap sub-cell in a multijunction device. In Chapter 6, ultrathin small organic molecule layers are used as the HTLs in narrow-bandgap PSCs. Driven by hydrogen bonds and π - π interactions, such molecules can be self-assembled into planar-stacked molecular structures with high crystallinity. Compared to PEDOT:PSS, the new HTLs display good hole extraction properties and result in comparable V_{oc} and FF in the solar cells. It is also found that an ultrathin HTL leads to a slightly higher J_{sc} by changing the optical interference of the device and reducing reflectance and parasitic absorption of PEDOT:PSS layer.

1.8 References

1. Chu, S., Majumdar, A. Opportunities and challenges for a sustainable energy future. *Nature* **488**, 294-303 (2012).
2. Gielen, D., Boshell, F., Saygin, D., Bazilian, M. D., Wagner, N., Gorini, R. The role of renewable energy in the global energy transformation. *Energy Strategy Rev.* **24**, 38-50 (2019).
3. Chu, S., Cui, Y., Liu, N. The path towards sustainable energy. *Nat. Mater.* **16**, 16-22 (2016).
4. Haegel, N. M. et al. Terawatt-scale photovoltaics: Transform global energy. *Science* **364**, 836-838 (2019).
5. Chapin, D. M., Fuller, C. S., Pearson, G. L. A New Silicon p-n Junction Photocell for Converting Solar Radiation into Electrical Power. *J. Appl. Phys.* **25**, 676-677 (1954).
6. Green, M. A., Dunlop, E. D., Hohl-Ebinger, J., Yoshita, M., Kopidakis, N., Hao, X. Solar cell efficiency tables (version 56). *Prog. Photovolt. Res. Appl.* **28**, 629-638 (2020).
7. Sutherland, B. R. Perovskite-Silicon Tandems Edge Forward. *Joule* **4**, 722-723 (2020).
8. Andre, T. *Renewables 2020 Global Status Report*. Paris: REN21 Secretariat (2020).
9. Kurtz, S., Haegel, N., Sinton, R., Margolis, R. A new era for solar. *Nat. Photonics* **11**, 3-5 (2017).
10. Rühle, S. Tabulated values of the Shockley–Queisser limit for single junction solar cells. *Sol. Energy* **130**, 139-147 (2016).
11. Haegel, N. M. et al. Terawatt-scale photovoltaics: Trajectories and challenges. *Science* **356**, 141-143 (2017).
12. Green, M. A., Bremner, S. P. Energy conversion approaches and materials for high-efficiency photovoltaics. *Nat. Mater.* **16**, 23-34 (2016).
13. Kayes, B. M. et al. 27.6% conversion efficiency, a new record for single-junction solar cells under 1 sun illumination. *2011 37th IEEE Photovoltaic Specialists Conference*, 4-8 (2011).
14. Hagfeldt, A., Boschloo, G., Sun, L., Kloo, L., Pettersson, H. Dye-Sensitized Solar Cells. *Chem. Rev.* **110**, 6595-6663 (2010).
15. Yan, C. et al. Non-fullerene acceptors for organic solar cells. *Nat. Rev. Mater.* **3**, 18003 (2018).
16. Yuan, M., Liu, M., Sargent, E. H. Colloidal quantum dot solids for solution-processed solar cells. *Nat. Energy* **1**, 16016 (2016).
17. Søndergaard, R., Hösel, M., Angmo, D., Larsen-Olsen, T. T., Krebs, F. C. J. M. t. Roll-to-roll fabrication of polymer solar cells. *Mater. Today* **15**, 36-49 (2012).
18. NREL Best Research-Cell Efficiencies. <https://www.nrel.gov/pv/assets/pdfs/best-research-cell-efficiencies.20200128.pdf> (2020).
19. Frost, J. M., Butler, K. T., Brivio, F., Hendon, C. H., Van Schilfgaarde, M., Walsh, A. Atomistic origins of high-performance in hybrid halide perovskite solar cells. *Nano Lett.* **14**, 2584-2590 (2014).
20. Green, M. A., Ho-Baillie, A., Snaith, H. J. The emergence of perovskite solar cells. *Nat. Photonics* **8**, 506-514 (2014).
21. Chen, Q. et al. Under the spotlight: The organic–inorganic hybrid halide perovskite for optoelectronic applications. *Nano Today* **10**, 355-396 (2015).
22. Weber, D. CH₃NH₃PbX₃, a Pb (II)-system with cubic perovskite structure. *Z. Naturforsch.* **33b**, 1443-1445 (1978).
23. Weber, D. CH₃NH₃SnBrxI_{3-x} (x= 0-3), a Sn (II)-system with cubic perovskite structure. *Z. Naturforsch.* **33**, 862-865 (1978).
24. Mitzi, D. B., Feild, C., Harrison, W., Guloy, A. Conducting tin halides with a layered organic-based perovskite structure. *Nature* **369**, 467-469 (1994).
25. Kojima, A., Teshima, K., Shirai, Y., Miyasaka, T. Organometal halide perovskites as visible-light sensitizers for photovoltaic cells. *J. Am. Chem. Soc.* **131**, 6050-6051 (2009).
26. Correa-Baena, J.-P. et al. The rapid evolution of highly efficient perovskite solar cells. *Energy Environ. Sci.* **10**, 710-727 (2017).
27. Saliba, M., Correa-Baena, J. P., Grätzel, M., Hagfeldt, A., Abate, A. Perovskite Solar Cells: From the Atomic Level to Film Quality and Device Performance. *Angew. Chem. Int. Ed.* **57**, 2554-2569 (2018).

28. Hao, F., Stoumpos, C. C., Chang, R. P., Kanatzidis, M. G. Anomalous Band Gap Behavior in Mixed Sn and Pb Perovskites Enables Broadening of Absorption Spectrum in Solar Cells. *J. Am. Chem. Soc.* **136**, 8094-8099 (2014).
29. Lin, Q., Armin, A., Nagiri, R. C. R., Burn, P. L., Meredith, P. Electro-optics of perovskite solar cells. *Nat. Photonics* **9**, 106-112 (2015).
30. Stranks, S. D. et al. Electron-Hole Diffusion Lengths Exceeding 1 Micrometer in an Organometal Trihalide Perovskite Absorber. *Science* **342**, 341 (2013).
31. Tvingstedt, K. et al. Radiative efficiency of lead iodide based perovskite solar cells. *Sci. Rep.* **4**, 6071 (2014).
32. Im, J.-H., Lee, C.-R., Lee, J.-W., Park, S.-W., Park, N.-G. 6.5% efficient perovskite quantum-dot-sensitized solar cell. *Nanoscale* **3**, 4088-4093 (2011).
33. Lee, M. M., Teuscher, J., Miyasaka, T., Murakami, T. N., Snaith, H. J. Efficient hybrid solar cells based on meso-superstructured organometal halide perovskites. *Science* **338**, 643-647 (2012).
34. Seok, S. I., Grätzel, M., Park, N. G. Methodologies toward highly efficient perovskite solar cells. *Small* **14**, 1704177 (2018).
35. Rong, Y. et al. Challenges for commercializing perovskite solar cells. *Science* **361**, 1214 (2018).
36. Kim, H., Lim, K.-G., Lee, T.-W. Planar heterojunction organometal halide perovskite solar cells: roles of interfacial layers. *Energy Environ. Sci.* **9**, 12-30 (2016).
37. Correa-Baena, J.-P. et al. Promises and challenges of perovskite solar cells. *Science* **358**, 739-744 (2017).
38. Liu, M., Johnston, M. B., Snaith, H. J. Efficient planar heterojunction perovskite solar cells by vapour deposition. *Nature* **501**, 395-398 (2013).
39. Jiang, Q. et al. Surface passivation of perovskite film for efficient solar cells. *Nat. Photonics* **13**, 460-466 (2019).
40. Zheng, X. et al. Managing grains and interfaces via ligand anchoring enables 22.3%-efficiency inverted perovskite solar cells. *Nat. Energy* **5**, 131-140 (2020).
41. Jiang, Q., Zhang, X., You, J. SnO₂: A Wonderful Electron Transport Layer for Perovskite Solar Cells. *Small* **14**, 1801154 (2018).
42. Han, T. H., Tan, S., Xue, J., Meng, L., Lee, J. W., Yang, Y. Interface and Defect Engineering for Metal Halide Perovskite Optoelectronic Devices. *Adv. Mater.* **31**, 1803515 (2019).
43. Wang, Y., Yue, Y., Yang, X., Han, L. Toward Long-Term Stable and Highly Efficient Perovskite Solar Cells via Effective Charge Transporting Materials. *Adv. Energy Mater.* **8**, 1800249 (2018).
44. Aydin, E., De Bastiani, M., De Wolf, S. Defect and Contact Passivation for Perovskite Solar Cells. *Adv. Mater.* **31**, e1900428 (2019).
45. Pham, H. D., Yang, T. C. J., Jain, S. M., Wilson, G. J., Sonar, P. Development of Dopant-Free Organic Hole Transporting Materials for Perovskite Solar Cells. *Adv. Energy Mater.* **10**, 1903326 (2020).
46. Arora, N. et al. Perovskite solar cells with CuSCN hole extraction layers yield stabilized efficiencies greater than 20. *Science* **358**, 768-771 (2017).
47. Haque, M. A., Sheikh, A. D., Guan, X., Wu, T. Metal Oxides as Efficient Charge Transporters in Perovskite Solar Cells. *Adv. Energy Mater.* **7**, 1602803 (2017).
48. Correa Baena, J. P. et al. Highly efficient planar perovskite solar cells through band alignment engineering. *Energy Environ. Sci.* **8**, 2928-2934 (2015).
49. Zhang, P. et al. Perovskite Solar Cells with ZnO Electron-Transporting Materials. *Adv. Mater.* **30**, 1703737 (2018).
50. Mingorance, A. et al. Interfacial Engineering of Metal Oxides for Highly Stable Halide Perovskite Solar Cells. *Adv. Mater. Interfaces* **5**, 1800367 (2018).
51. Gatti, T., Menna, E., Meneghetti, M., Maggini, M., Petrozza, A., Lamberti, F. The Renaissance of fullerenes with perovskite solar cells. *Nano Energy* **41**, 84-100 (2017).
52. Zhu, P. et al. Simultaneous Contact and Grain-Boundary Passivation in Planar Perovskite Solar Cells Using SnO₂-KCl Composite Electron Transport Layer. *Adv. Energy Mater.* **10**, 1903083 (2019).

53. Shao, S. et al. Enhancing the Performance of the Half Tin and Half Lead Perovskite Solar Cells by Suppression of the Bulk and Interfacial Charge Recombination. *Adv. Mater.* **30**, 1803703 (2018).
54. Bruijnaers, B. J., Schiepers, E., Weijtens, C. H. L., Meskers, S. C. J., Wienk, M. M., Janssen, R. A. J. The effect of oxygen on the efficiency of planar p-i-n metal halide perovskite solar cells with a PEDOT:PSS hole transport layer. *J. Mater. Chem. A* **6**, 6882-6890 (2018).
55. Du, T. et al. p-Doping of organic hole transport layers in p-i-n perovskite solar cells: correlating open-circuit voltage and photoluminescence quenching. *J. Mater. Chem. A* **7**, 18971-18979 (2019).
56. Prasanna, R. et al. Design of low bandgap tin-lead halide perovskite solar cells to achieve thermal, atmospheric and operational stability. *Nat. Energy* **4**, 939-947 (2019).
57. Zhang, S. et al. Interface Engineering of Solution-Processed Hybrid Organohalide Perovskite Solar Cells. *ACS Appl. Mater. Interfaces* **10**, 21681-21687 (2018).
58. Xu, J. et al. Triple-halide wide-band gap perovskites with suppressed phase segregation for efficient tandems. *Science* **367**, 1097-1104 (2020).
59. Wang, Q., Bi, C., Huang, J. Doped hole transport layer for efficiency enhancement in planar heterojunction organolead trihalide perovskite solar cells. *Nano Energy* **15**, 275-280 (2015).
60. Liang, P.-W., Chueh, C.-C., Williams, S. T., Jen, A. K. Y. Roles of Fullerene-Based Interlayers in Enhancing the Performance of Organometal Perovskite Thin-Film Solar Cells. *Adv. Energy Mater.* **5**, 1402321 (2015).
61. Shao, Y., Xiao, Z., Bi, C., Yuan, Y., Huang, J. Origin and elimination of photocurrent hysteresis by fullerene passivation in CH₃NH₃PbI₃ planar heterojunction solar cells. *Nat. Commun.* **5**, 5784 (2014).
62. Chen, B. et al. Enhanced optical path and electron diffusion length enable high-efficiency perovskite tandems. *Nat. Commun.* **11**, 1257 (2020).
63. Deng, Y., Dong, Q., Bi, C., Yuan, Y., Huang, J. Air-Stable, Efficient Mixed-Cation Perovskite Solar Cells with Cu Electrode by Scalable Fabrication of Active Layer. *Adv. Energy Mater.* **6**, 1600372 (2016).
64. Tai, Q., Yan, F. Emerging Semitransparent Solar Cells: Materials and Device Design. *Adv. Mater.* **29**, 1700192 (2017).
65. Gahlmann, T. et al. Impermeable Charge Transport Layers Enable Aqueous Processing on Top of Perovskite Solar Cells. *Adv. Energy Mater.* **10**, 1903897 (2020).
66. Della Gaspera, E. et al. Ultra-thin high efficiency semitransparent perovskite solar cells. *Nano Energy* **13**, 249-257 (2015).
67. Eperon, G. E., Burlakov, V. M., Docampo, P., Goriely, A., Snaith, H. J. Morphological control for high performance, solution-processed planar heterojunction perovskite solar cells. *Adv. Funct. Mater.* **24**, 151-157 (2014).
68. Nie, W. et al. High-efficiency solution-processed perovskite solar cells with millimeter-scale grains. *Science* **347**, 522-525 (2015).
69. Dunlap-Shohl, W. A., Zhou, Y., Padture, N. P., Mitzi, D. B. Synthetic Approaches for Halide Perovskite Thin Films. *Chem. Rev.* **119**, 3193-3295 (2019).
70. Li, Z. et al. Scalable fabrication of perovskite solar cells. *Nat. Rev. Mater.* **3**, 18017 (2018).
71. van Franeker, J. J., Turbiez, M., Li, W., Wienk, M. M., Janssen, R. A. J. A real-time study of the benefits of co-solvents in polymer solar cell processing. *Nat. Commun.* **6**, 6229 (2015).
72. Wang, J. et al. Understanding the Film Formation Kinetics of Sequential Deposited Narrow-Bandgap Pb-Sn Hybrid Perovskite Films. *Adv. Energy Mater.* **10**, 2000566 (2020).
73. Hendriks, K. H., van Franeker, J. J., Bruijnaers, B. J., Anta, J. A., Wienk, M. M., Janssen, R. A. J. 2-Methoxyethanol as a new solvent for processing methylammonium lead halide perovskite solar cells. *J. Mater. Chem. A* **5**, 2346-2354 (2017).
74. Zhang, W. et al. Ultrasoft organic-inorganic perovskite thin-film formation and crystallization for efficient planar heterojunction solar cells. *Nat. Commun.* **6**, 1-10 (2015).
75. Chen, H. Two-Step Sequential Deposition of Organometal Halide Perovskite for Photovoltaic Application. *Adv. Funct. Mater.* **27**, 1605654 (2017).

76. Conings, B. et al. A Universal Deposition Protocol for Planar Heterojunction Solar Cells with High Efficiency Based on Hybrid Lead Halide Perovskite Families. *Adv. Mater.* **28**, 10701-10709 (2016).
77. Yang, W. S. et al. High-performance photovoltaic perovskite layers fabricated through intramolecular exchange. *Science* **348**, 1234-1237 (2015).
78. Barrit, D. et al. Impact of the Solvation State of Lead Iodide on Its Two-Step Conversion to MAPbI₃: An In Situ Investigation. *Adv. Funct. Mater.* **29**, 1807544 (2019).
79. Liu, C., Cheng, Y. B., Ge, Z. Understanding of perovskite crystal growth and film formation in scalable deposition processes. *Chem. Soc. Rev.* **49**, 1653-1687 (2020).
80. Babbe, F., Sutter-Fella, C. M. Optical Absorption-Based In Situ Characterization of Halide Perovskites. *Adv. Energy Mater.* **10**, 1903587 (2020).
81. Mundt, L. E., Schelhas, L. T. Structural Evolution During Perovskite Crystal Formation and Degradation: In Situ and Operando X-Ray Diffraction Studies. *Adv. Energy Mater.* **10**, 1903074 (2019).
82. Sandberg, O. J. et al. On the Question of the Need for a Built-In Potential in Perovskite Solar Cells. *Adv. Mater. Interfaces* **7**, 2000041 (2020).
83. Tress, W. et al. Interpretation and evolution of open-circuit voltage, recombination, ideality factor and subgap defect states during reversible light-soaking and irreversible degradation of perovskite solar cells. *Energy Environ. Sci.* **11**, 151-165 (2018).
84. Snaith, H. J. The perils of solar cell efficiency measurements. *Nat. Photonics* **6**, 337-340 (2012).
85. Snaith, H. J. How should you measure your excitonic solar cells? *Energy Environ. Sci.* **5**, 6513-6520 (2012).
86. Snaith, H. J. et al. Anomalous hysteresis in perovskite solar cells. *J. Phys. Chem. Lett.* **5**, 1511-1515 (2014).
87. Wang, Y. et al. Reliable Measurement of Perovskite Solar Cells. *Adv. Mater.* **31**, 1803231 (2019).
88. Shrotriya, V., Li, G., Yao, Y., Moriarty, T., Emery, K., Yang, Y. Accurate Measurement and Characterization of Organic Solar Cells. *Adv. Funct. Mater.* **16**, 2016-2023 (2006).
89. Zimmermann, E., Ehrenreich, P., Pfadler, T., Dorman, J. A., Weickert, J., Schmidt-Mende, L. Erroneous efficiency reports harm organic solar cell research. *Nat. Photonics* **8**, 669-672 (2014).
90. Shockley, W., Queisser, H. J. Detailed Balance Limit of Efficiency of p-n Junction Solar Cells. *J. Appl. Phys.* **32**, 510-519 (1961).
91. Guillemoles, J.-F., Kirchartz, T., Cahen, D., Rau, U. Guide for the perplexed to the Shockley–Queisser model for solar cells. *Nat. Photonics* **13**, 501-505 (2019).
92. Eperon, G. E., Hörantner, M. T., Snaith, H. J. Metal halide perovskite tandem and multiple-junction photovoltaics. *Nat. Rev. Chem.* **1**, 0095 (2017).
93. Di Carlo Rasi, D., Janssen, R. A. J. Advances in Solution-Processed Multijunction Organic Solar Cells. *Adv. Mater.* **31**, 1806499 (2019).
94. Geisz, J. F. et al. Six-junction III–V solar cells with 47.1% conversion efficiency under 143 Suns concentration. *Nat. Energy* **5**, 326-335 (2020).
95. Leijtens, T., Bush, K. A., Prasanna, R., McGehee, M. D. Opportunities and challenges for tandem solar cells using metal halide perovskite semiconductors. *Nat. Energy* **3**, 828-838 (2018).
96. Wang, C., Song, Z., Li, C., Zhao, D., Yan, Y. Low-Bandgap Mixed Tin-Lead Perovskites and Their Applications in All-Perovskite Tandem Solar Cells. *Adv. Funct. Mater.* **29**, 1808801 (2019).
97. Hörantner, M. T. et al. The Potential of Multijunction Perovskite Solar Cells. *ACS Energy Lett.* **2**, 2506-2513 (2017).
98. Lin, R. et al. Monolithic all-perovskite tandem solar cells with 24.8% efficiency exploiting comproportionation to suppress Sn(II) oxidation in precursor ink. *Nat. Energy* **4**, 864-873 (2019).
99. McMeekin, D. P. et al. Solution-Processed All-Perovskite Multi-Junction Solar Cells. *Joule* **3**, 387-401 (2019).
100. Werner, J. et al. Perovskite/Perovskite/Silicon Monolithic Triple-Junction Solar Cells with a Fully Textured Design. *ACS Energy Lett.* **3**, 2052-2058 (2018).

101. Xiao, K. et al. Solution-Processed Monolithic All-Perovskite Triple-Junction Solar Cells with Efficiency Exceeding 20%. *ACS Energy Lett.*, 10.1021/acsenergylett.0c01184, 2819-2826 (2020).
102. Timmreck, R. et al. Characterization of tandem organic solar cells. *Nat. Photonics* **9**, 478-479 (2015).
103. Di Carlo Rasi, D. et al. A Universal Route to Fabricate n-i-p Multi-Junction Polymer Solar Cells via Solution Processing. *Solar RRL* **2**, 1800018 (2018).
104. Palmstrom, A. F. et al. Enabling Flexible All-Perovskite Tandem Solar Cells. *Joule* **3**, 2193-2204 (2019).
105. Zhao, D. et al. Efficient two-terminal all-perovskite tandem solar cells enabled by high-quality low-bandgap absorber layers. *Nat. Energy* **3**, 1093-1100 (2018).
106. Chang, C.-Y., Tsai, B.-C., Hsiao, Y.-C., Lin, M.-Z., Meng, H.-F. Solution-processed conductive interconnecting layer for highly-efficient and long-term stable monolithic perovskite tandem solar cells. *Nano Energy* **55**, 354-367 (2019).
107. Jiang, F. et al. A two-terminal perovskite/perovskite tandem solar cell. *J. Mater. Chem. A* **4**, 1208-1213 (2016).
108. Li, C. et al. Thermionic Emission-Based Interconnecting Layer Featuring Solvent Resistance for Monolithic Tandem Solar Cells with Solution-Processed Perovskites. *Adv. Energy Mater.* **8**, 1801954 (2018).
109. Forgács, D. et al. Efficient Monolithic Perovskite/Perovskite Tandem Solar Cells. *Adv. Energy Mater.* **7**, 1602121 (2017).
110. Yang, Z. et al. Enhancing electron diffusion length in narrow-bandgap perovskites for efficient monolithic perovskite tandem solar cells. *Nat. Commun.* **10**, 4498 (2019).
111. Tong, J. H. et al. Carrier lifetimes of $> 1 \mu\text{s}$ in Sn-Pb perovskites enable efficient all-perovskite tandem solar cells. *Science* **364**, 475-479 (2019).
112. Zhao, D. et al. Low-bandgap mixed tin-lead iodide perovskite absorbers with long carrier lifetimes for all-perovskite tandem solar cells. *Nat. Energy* **3**, 1093-1100 (2017).
113. Eperon, G. E. et al. Perovskite-perovskite tandem photovoltaics with optimized band gaps. *Science* **354**, 861-865 (2016).

Chapter 2

Insights into fullerene passivation of SnO₂ electron transport layers in perovskite solar cells*

Abstract

Interfaces between the photo-active and charge transport layers are crucial for the performance of perovskite solar cells (PSCs). Surface passivation of SnO₂ as an electron transport layer (ETL) by fullerene derivatives is known to improve the performance of n-i-p devices. Nevertheless, organic passivation layers are susceptible to removal during perovskite deposition. Understanding the nature of the passivation is essential for further optimization of SnO₂ ETLs. X-ray photoelectron spectroscopy (XPS) depth profiling is a convenient tool to monitor the concentration of fullerene passivation layers at a SnO₂ interface. Through a comparative study using [6,6]-phenyl-C₆₁-butyric acid methyl ester (PCBM) and [6,6]-phenyl-C₆₁-butyric acid (PCBA) passivation layers, a direct correlation is established between the formation of interfacial chemical bonds and the retention of passivating fullerene molecules at the SnO₂ interface that effectively reduce the number of defects and enhance the electron mobility. Devices with only a PCBA-monolayer passivated SnO₂ ETL exhibit significantly improved performance and reproducibility, achieving an efficiency of 18.8%. Investigating thick and solvent-resistant C₆₀ and PCBM-dimer layers demonstrate that the charge transport in the ETL is only improved by chemisorption of the fullerene at the SnO₂ surface.

*This chapter is published as: Wang J., Datta K., Weijtens C.H.L., Wienk M.M., Janssen R.A.J. *Adv. Funct. Mater.*, **2019**, 29, 1905883.

2.1. Introduction

Organic-inorganic hybrid perovskite solar cells (PSCs) have attracted unprecedented interests from the photovoltaic (PV) research community in recent years. Robust strategies have been developed for small-area devices with various perovskite compositions and device architectures, resulting in power conversion efficiencies (PCEs) well above 20%.¹⁻⁸ Compared to other PV technologies, perovskites present distinct advantages by combining high PCEs, with cost-effectiveness and solution processability, providing the incentive to explore large-area implementation.⁹⁻¹² In state-of-the-art *n-i-p* PSC architectures, mesoporous TiO₂ is commonly used as the electron transport layer (ETL). Mesoporous TiO₂, however, requires a high temperature (≥ 450 °C) process, which limits its potential for up-scalable processing on flexible substrates.^{9,12,13} Numerous early studies¹⁴⁻¹⁷ have pinpointed the excellent characteristics of lead halide perovskites, i.e., a high absorption coefficient, long carrier diffusion length, and bi-polar carrier transport, suggesting that high PCEs can also be achieved in planar PSCs, eliminating the mesoporous TiO₂ layer and the need for high-temperature processing.

In the planar *n-i-p* PSC architecture, *n*-type semiconducting metal oxides with tailored compositions and structures have been extensively explored as the ETLs.^{18,19} Tin oxide (SnO₂) is considered as a superior candidate for high-performing PSCs.²⁰⁻²⁵ Compared to other metal oxides, it has been shown to provide better energy level alignment with the perovskite absorber, higher electron mobility, enhanced UV-stability, and visible light transparency.^{21,23,25,26} Recently, several low-temperature processing techniques such as the sol-gel process,²¹ atomic layer deposition,²⁵⁻²⁷ and chemical bath deposition²⁸ have been utilized for high-quality planar SnO₂ ETLs. Moreover, by using a commercialized SnO₂ colloidal dispersion, the best PCE of SnO₂-based PSCs (23.32%) is now comparable to that of mesoporous-TiO₂ cells.²⁹ It is noteworthy, however, that metal oxides are prone to contain imperfections. Depending on the fabrication method, the number of defects (e.g., oxygen vacancies) of SnO₂ can vary dramatically, affecting the device performance and stability.^{22,30} Specifically, defects at the SnO₂/perovskite interface can induce ionic charge accumulation^{31,32} and non-radiative interfacial recombination,³³ both contributing to the hysteresis effect and performance loss in the devices.³⁴ Surface passivation of SnO₂ can considerably suppress the formation of interfacial defects.^{20,33} By introducing an organic modification layer between the perovskite and SnO₂ layers, PSCs exhibit reduced interfacial loss, less pronounced hysteresis, and thereby better PV performance.^{30,33,35-39}

There are some prerequisites for efficient surface passivation of SnO₂.^{19,40} First is the activation of the SnO₂ surface.⁴⁰ By UV-ozone treatment, organic binders and adventitious contaminants of SnO₂ can be easily removed while the number of surface-bound hydroxyl groups is increased, providing more anchoring sites for the passivation layer.^{22,41,42} Second, a judicious selection of organic surface modifier is required. Fullerene derivatives, as well as other carboxylate self-assembled monolayers (SAMs), are among the most studied owing to the ease of forming covalent bonds between the carboxylate moiety and SnO₂ surface, and the broad availability of electron-accepting groups which facilitate charge transport at the SnO₂/perovskite interface.^{19,33,35-39,43-46} Third, the deposition condition of organic modifiers could also affect their binding strength towards the substrate.¹⁹ While no special treatment is required for carboxylic acid-based SAMs,^{35,47-49} a thermal treatment is commonly used when employing passivation by [6,6]-phenyl-C₆₁-butyric acid methyl ester (PCBM)^{37,38,48} to enhance binding to the SnO₂ surface. However, it is remarkable that most organic modifiers are not solvent-resistant and can be easily removed upon the spin coating of perovskite solutions.⁵⁰⁻⁵⁶ Despite improving the PCE,^{35,39,47,56,57} very few studies were able to pinpoint the whereabouts of the passivation layer.^{47,56-58} Therefore, the direct correlation between the presence of interfacial modifiers and the PSC performance remains obscure. On the other hand, tremendous research efforts have been made to improve the robustness of the organic modification layer, for instance, by introducing thermal evaporated C₆₀^{37,48,59} or by developing cross-linkable fullerene derivatives,^{53-55,60,61} after which a bi-layered ETL is formed. In this case, however, the impact of a chemical interaction between the SnO₂ and the passivation layer is often neglected.

Herein, three representative fullerenes, C₆₀, PCBM, and [6,6]-phenyl-C₆₁-butyric acid (PCBA) (Figure 2.1), were used to passivate a SnO₂ ETL in planar *n-i-p* PSCs. Through X-ray photoelectron spectroscopy (XPS) depth profiling, the precise distribution of fullerenes in the ETL is revealed. It is found that a PCBA-monolayer easily binds to the SnO₂ interface, whereas a PCBM-monolayer can only be created and preserved when employing a thermal annealing treatment prior to depositing the perovskite. It is demonstrated that fullerenes with the ability to react with surface hydroxyl groups effectively passivate defects at the SnO₂ interface and improve the performance and reproducibility of the PSCs. After optimization, the best-performing device with a PCE of 18.8% is achieved by using PCBA-monolayer passivated SnO₂. Although thermally evaporated C₆₀ is mostly retained after the solvent treatment, the deteriorated PV performance indicates that no efficient passivation is developed at the SnO₂ interface. By exposing an as-deposited PCBM layer to UV light, a less-soluble dimeric state of

PCBM is obtained,⁶²⁻⁶⁴ which enabled us to study the role of fullerene passivation in a bilayered SnO₂/fullerene ETL configuration. It is found that even when a PCBM-dimer layer entirely covers the SnO₂ surface, the charge transport in the ETL remains inefficient unless thermal annealing is applied after depositing the PCBM. Our results highlight that chemisorption (PCBA) rather than physisorption (C₆₀ and PCBM) to SnO₂ is the most influential factor in enhancing the interfacial charge transport process.



Figure 2.1 Chemical structure of C₆₀, [60]PCBM, and [60]PCBA.

2.2 Device performance of planar *n-i-p* perovskite solar cells

Planar *n-i-p* PSCs were fabricated based on a device structure of indium tin oxide (ITO)/SnO₂/perovskite/Spiro-OMeTAD/MoO₃/Au, in which the SnO₂ ETL was spin coated from a colloidal dispersion and passivated by different fullerene layers. A double-cation perovskite FA_{0.66}MA_{0.34}PbI_{2.85}Br_{0.15} (FA is formamidinium, MA is methylammonium) was deposited on the ETL *via* a two-step solution process reported by Qiu and co-workers.^{55,65} To optimize the processing condition for the ETL, a SnO₂ layer (~20 nm) was spin coated from a ~2.8 wt% colloidal aqueous solution,²³ thermally annealed in air at 150 °C, and treated by UV-ozone before depositing PCBM from chlorobenzene (10 mg mL⁻¹) and subsequent annealing at 100 °C for 20 min. The UV-ozone treatment increases the open-circuit voltage (V_{oc}) from 0.97 to 1.04 V (Figure 2.2a). XPS spectra confirm that together with the removal of carbon contaminant or organic binders of the SnO₂ layer,⁴² a more hydroxylated SnO₂ surface is obtained after UV-ozone treatment, which promotes the passivation of SnO₂ by PCBM (Figure 2.2b-d).⁶⁶ Different from a previous study,²³ it is found that the V_{oc} of PSCs can be further improved when increasing the thickness of the SnO₂ layer from ~20 to ~110 nm because of better coverage and reduced shunting pathways (Figure 2.3 and Table 2.1).⁶⁷ Surprisingly, the fill factor (FF) is not influenced when increasing the SnO₂ layer thickness, probably due to its

high electron mobility. As a result, the optimum PSC performance can be achieved by using 10 min UV-ozone treated ~110 nm SnO₂ layers as ETL.

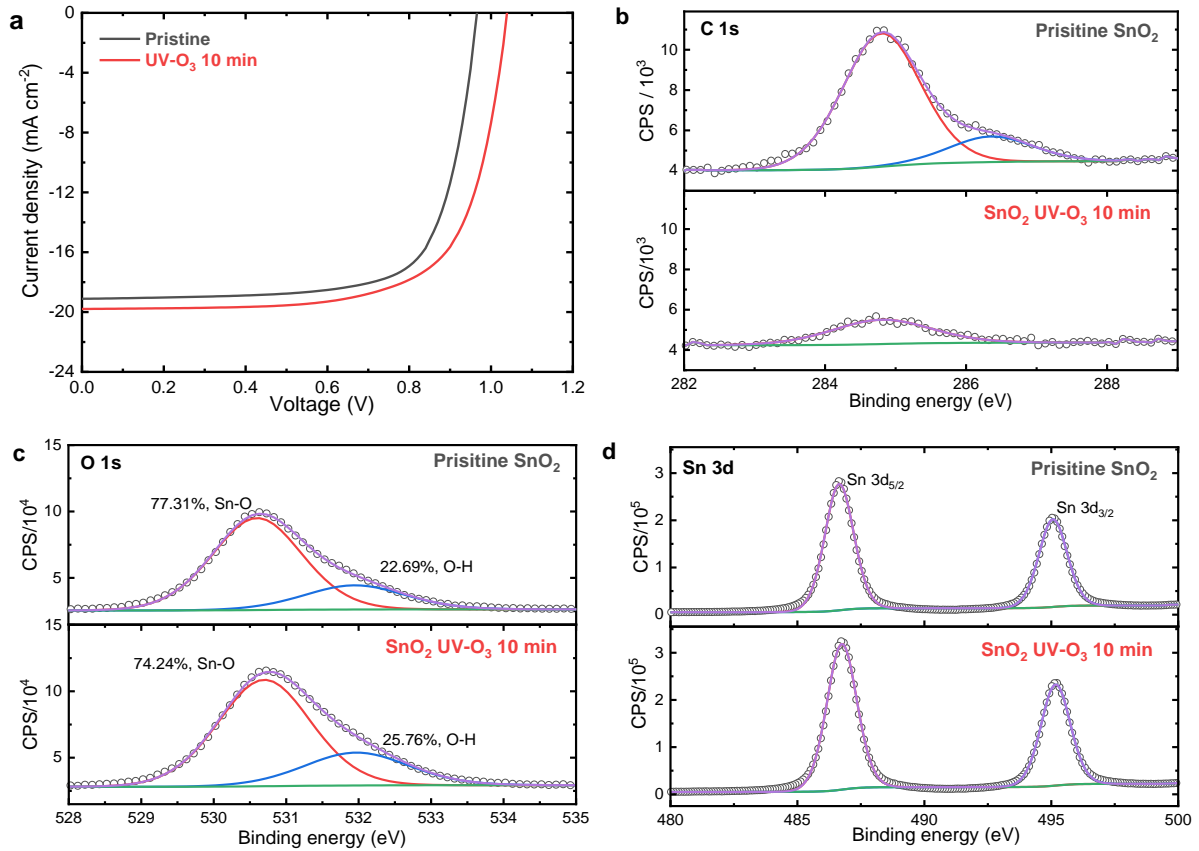


Figure 2.2 (a) Current density–voltage (J – V) curves of ITO/SnO₂/FA_{0.66}MA_{0.34}PbI_{2.85}Br_{0.15}/Spiro-OMeTAD/MoO₃/Au solar cells with UV-ozone treatment on the SnO₂ ETL. XPS high-resolution scan spectra of the (b) C 1s, (c) O 1s, and (d) Sn 3d core-levels of SnO₂ layer before and after UV-ozone treatment.

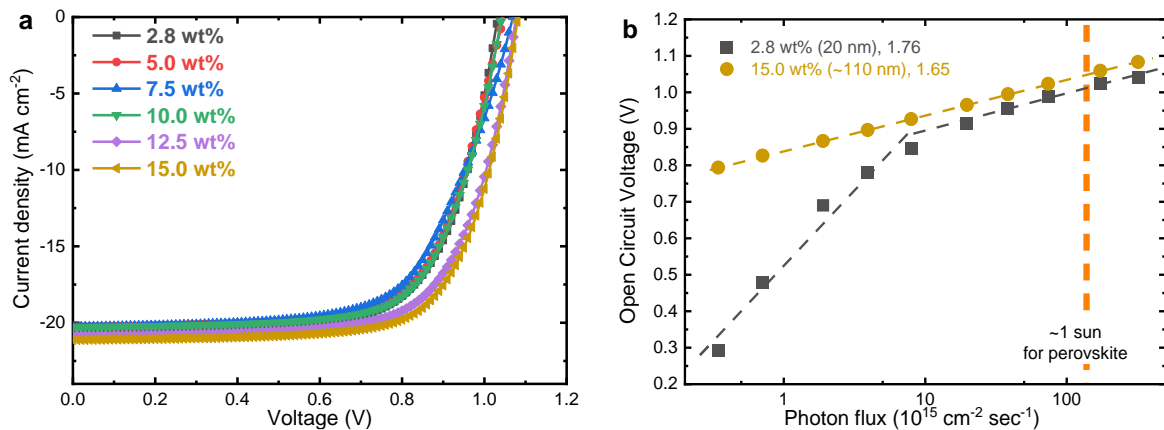


Figure 2.3 (a) J – V curves and (b) light-intensity dependent (730 nm LED) open-circuit voltage of ITO/SnO₂/PCBM/FA_{0.66}MA_{0.34}PbI_{2.85}Br_{0.15}/Spiro-OMeTAD/MoO₃/Au devices in which the weight percentage of SnO₂ in the aqueous dispersion was varied.

Table 2.1 Photovoltaic parameters of *n-i-p* devices using different water-diluted SnO₂ ETL, measured under simulated AM 1.5G illumination (100 mW cm⁻²).

SnO ₂ diluted in H ₂ O	J_{sc} (mA cm ⁻²)	V_{oc} (V)	FF	PCE (%)
2.8 wt%, 20 nm	20.6	1.03	0.69	14.6
5.0 wt%, 31 nm	20.3	1.05	0.68	14.4
7.5 wt%	20.3	1.07	0.65	14.1
10.0 wt%, 65 nm	20.3	1.04	0.69	14.6
12.5 wt%	20.9	1.08	0.69	15.6
15.0 wt%, 112 nm	21.1	1.08	0.71	16.2

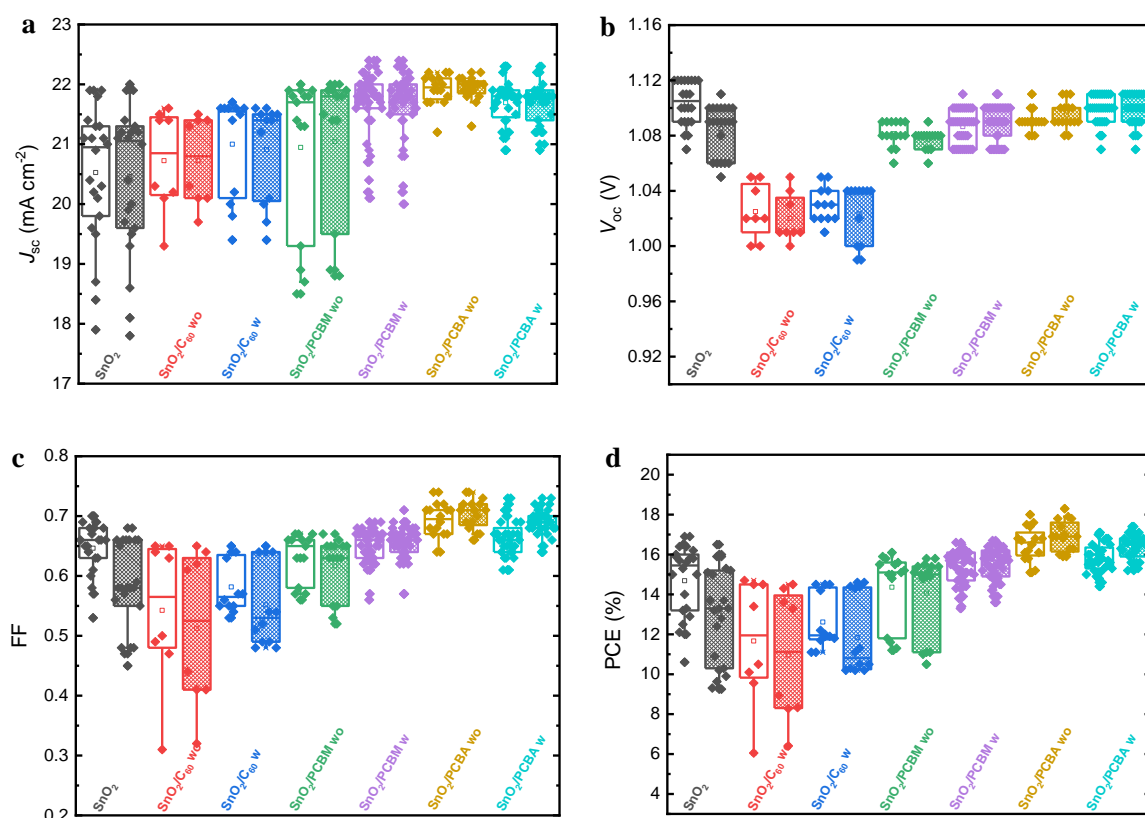


Figure 2.4 A statistical distribution of (a) J_{sc} , (b) V_{oc} , (c) FF, and (d) PCE of the ITO/SnO₂/fullerene/FA_{0.66}MA_{0.34}PbI_{2.85}Br_{0.15}/Spiro-OMeTAD/MoO₃/Au PSCs using different fullerene passivation layers, either with (w) or without (wo) thermal annealing and measured in a reverse scan (left) and forward scan (right).

To study the effect of fullerene passivation on the device performance, C₆₀, PCBM, and PCBA were introduced at the SnO₂/perovskite interface, either with or without a thermal annealing treatment at 100 °C for 20 min. Figure 2.4 shows the statistical distribution of

performance characteristics of the devices with different passivation layers. The corresponding averaged PV parameters are summarized in Table 2.2. Figure 2.4 demonstrates that without a passivation layer, the SnO₂ control device exhibits a large inconsistency in performance, showing an average PCE of $14.7 \pm 1.79\%$ in the reverse scan and $13.0 \pm 2.45\%$ in the forward scan. The differences can be ascribed to an uncontrolled number of trap states, which induces localized ionic charges at the SnO₂/perovskite interface and results in the formation of a potential barrier that hampers the charge extraction process.³¹

Table 2.2 Photovoltaic parameters of control and passivation devices with different fullerene layers, measured in reverse (Rev, V_{oc} to J_{sc}) and forward direction (Fwd, J_{sc} to V_{oc}), respectively, under simulated AM 1.5G illumination (100 mW cm^{-2}).

Passivation layer	Scan direction	J_{sc} (mA cm^{-2})	V_{oc} (V)	FF	PCE (%)
SnO ₂ reference	Rev	20.5 ± 1.10	1.10 ± 0.02	0.65 ± 0.04	14.7 ± 1.79
	Fwd	20.5 ± 1.26	1.09 ± 0.02	0.58 ± 0.07	13.0 ± 2.45
C ₆₀ not-annealed	Rev	20.7 ± 0.86	1.03 ± 0.02	0.54 ± 0.12	11.7 ± 3.12
	Fwd	20.7 ± 0.74	1.02 ± 0.01	0.51 ± 0.13	11.0 ± 3.27
C ₆₀ annealed	Rev	21.0 ± 0.87	1.03 ± 0.01	0.58 ± 0.04	12.6 ± 1.38
	Fwd	20.9 ± 0.84	1.02 ± 0.02	0.55 ± 0.07	11.8 ± 1.95
PCBM not-annealed	Rev	21.0 ± 1.34	1.08 ± 0.01	0.63 ± 0.04	14.4 ± 1.84
	Fwd	21.1 ± 1.29	1.08 ± 0.01	0.62 ± 0.05	14.1 ± 1.98
PCBM annealed	Rev	21.7 ± 0.56	1.09 ± 0.01	0.65 ± 0.03	15.3 ± 0.84
	Fwd	21.6 ± 0.54	1.09 ± 0.01	0.66 ± 0.03	15.5 ± 0.86
PCBA not-annealed	Rev	21.9 ± 0.26	1.09 ± 0.01	0.69 ± 0.03	16.5 ± 0.84
	Fwd	21.9 ± 0.21	1.10 ± 0.01	0.70 ± 0.03	16.9 ± 0.78
PCBA annealed	Rev	21.7 ± 0.37	1.10 ± 0.01	0.66 ± 0.03	15.8 ± 0.71
	Fwd	21.7 ± 0.36	1.10 ± 0.01	0.69 ± 0.02	16.4 ± 0.62

To test the effect of interfacial passivation layers, a thermally evaporated C₆₀ layer was first employed. It has previously been reported that ≥ 35 nm-thick C₆₀ layers are needed to retain complete coverage of the substrate after processing the perovskite layer from solution without changing its electron transport properties.⁵⁹ However, it is found that the device with a thermally evaporated C₆₀ layer (35 nm) performed inferior compared to the SnO₂ device. The V_{oc} is reduced from 1.10 ± 0.02 V to 1.03 ± 0.02 V, while the FF drops from 0.65 ± 0.04 to 0.54 ± 0.12 , resulting in a moderate PCE of $11.7 \pm 3.12\%$ (reverse). The low FF is ascribed to high

series resistance, resulting from the thick C₆₀ layer. Thermal annealing of the C₆₀ layer provides only a marginal improvement, delivering an average PCE of $12.6 \pm 1.38\%$ (reverse). To reduce the effect of series resistance, PSCs with thinner C₆₀ interfacial layers were tested, but their performance remained inferior to the SnO₂ device without passivation (Figure 2.5). These results demonstrate that inserting a C₆₀ layer at the SnO₂/perovskite interface affords no effective passivation, but rather restricts the electron extraction and induces non-radiative interfacial recombination, lowering both the FF and V_{oc} .

In the second approach, a ~15 nm PCBM interfacial layer was applied by solution processing from chlorobenzene (10 mg mL^{-1}). The PV characteristics are almost identical to the SnO₂ device without a passivation layer. A similar broad distribution is observed for both the reverse scan ($14.4 \pm 1.84\%$) and the forward scan ($14.1 \pm 1.98\%$). However, an additional thermal treatment of the PCBM layer ($100 \text{ }^\circ\text{C}$, 20 min. under N₂) prior to depositing the perovskite layer results in a significant enhancement in the performance and reproducibility. Compared to the bare SnO₂ device, the annealed PCBM device displays a higher average PCE of 15.3% and a small standard deviation of 0.84% in the reverse scan, due to an increased J_{sc} of $21.7 \pm 0.56 \text{ mA cm}^{-2}$, a comparable V_{oc} of $1.09 \pm 0.01 \text{ V}$, and a FF of 0.65 ± 0.03 . The PCE difference between both scanning directions is negligible, by showing an average PCE of $15.5 \pm 0.86\%$ in the forward scan. Apparently, thermal annealing leads to a passivated ETL interface that remains intact during the perovskite solution processing. Possibly, thermal annealing causes the ester side chains of PCBM to react with the hydroxyl groups of the SnO₂ surface, forming covalent bonds.

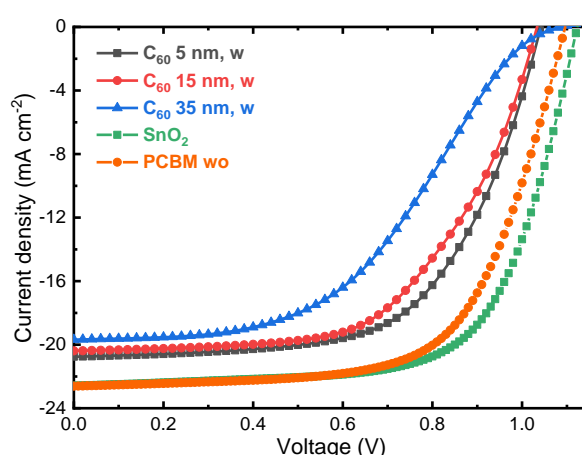


Figure 2.5 J - V curves of the PSCs for different C₆₀ layer thicknesses deposited on the SnO₂ ETL.

Following this idea, a PCBA monolayer⁴⁷ spin coated from a dilute (0.2 mg mL^{-1}) solution in dichlorobenzene exhibits a distinctively improved passivation compared to PCBM

or C₆₀, regardless of the thermal annealing process. Without thermal annealing, PCBA gives the best performance, showing a PCE of $16.5 \pm 0.84\%$ in the reverse scan, with a reduced standard deviation in J_{sc} of $21.9 \pm 0.26 \text{ mA cm}^{-2}$, a V_{oc} of $1.09 \pm 0.01 \text{ V}$, and a significantly improved FF of 0.69 ± 0.03 . Comparable high performance is also obtained in the forward scan, with an average PCE of $16.9 \pm 0.78\%$. This supports the idea that the higher reactivity of the carboxylic acid side chain in PCBA towards the hydroxyl groups of the SnO₂ surface play a role in the improved passivation.

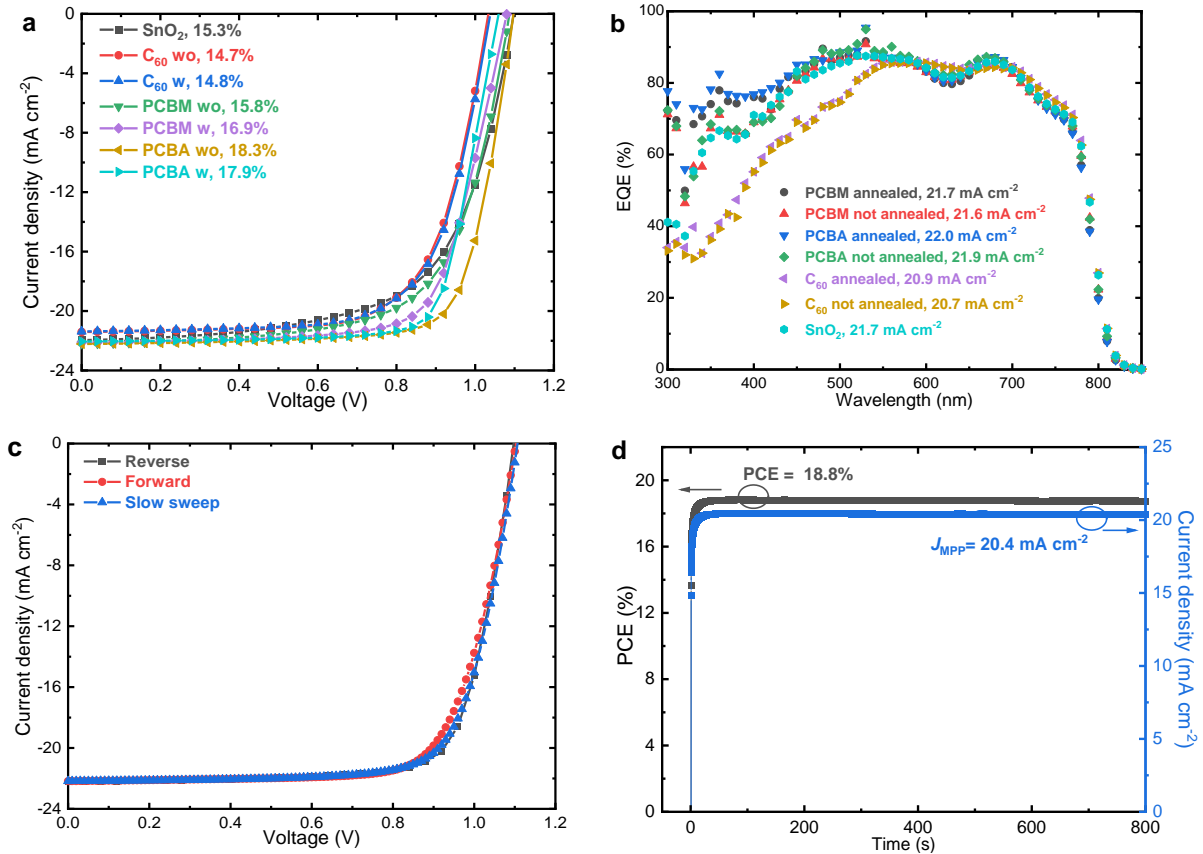


Figure 2.6 (a-b) Stabilized $J-V$ curves and EQE spectra of the best-performing PSCs with different passivation layers, either with (w) or without (wo) thermal annealing. (c) $J-V$ curves of the champion device with SnO₂/PCBA (non-annealed). (d) Steady-state power and photocurrent output tracking over time of the champion device operated at the maximum power point under the simulated AM1.5G illumination condition.

Figure 2.6a-b display the stabilized current density–voltage ($J-V$) curves and external quantum efficiency (EQE) spectra of the champion PSCs for the different passivation conditions. The corresponding parameters are summarized in Table 2.3. Similar to the performance metrics shown in Figure 2.4, the devices based on non-annealed PCBA, annealed PCBA, and annealed PCBM exhibit higher performance, with PCEs of 18.3%, 17.9%, and

16.9%, respectively. The enhanced performance of the PCBA modified devices is mainly a consequence of the improved FF of 0.76, which suggests an improved electron extraction, originating from an efficiently passivated SnO_2 ETL. The EQE measured with bias illumination provides an estimated J_{sc} in close correspondence with the J - V data measured with simulated AM1.5G (100 mW cm^{-2}) illumination. The best-performing PSC device based on PCBA exhibits negligible hysteresis by showing almost identical J - V curves (Figure 2.6c) measured in reverse, forward, and stabilized scans. Figure 2.6d shows the steady-state power and photocurrent output of the best device, measured at its maximum power point ($V_{\text{MPP}} = 0.92 \text{ V}$) for 800 s. In this experiment, the PCBA-modified device exhibits a PCE of 18.8%, which is very close to the values extracted from the J - V curves.

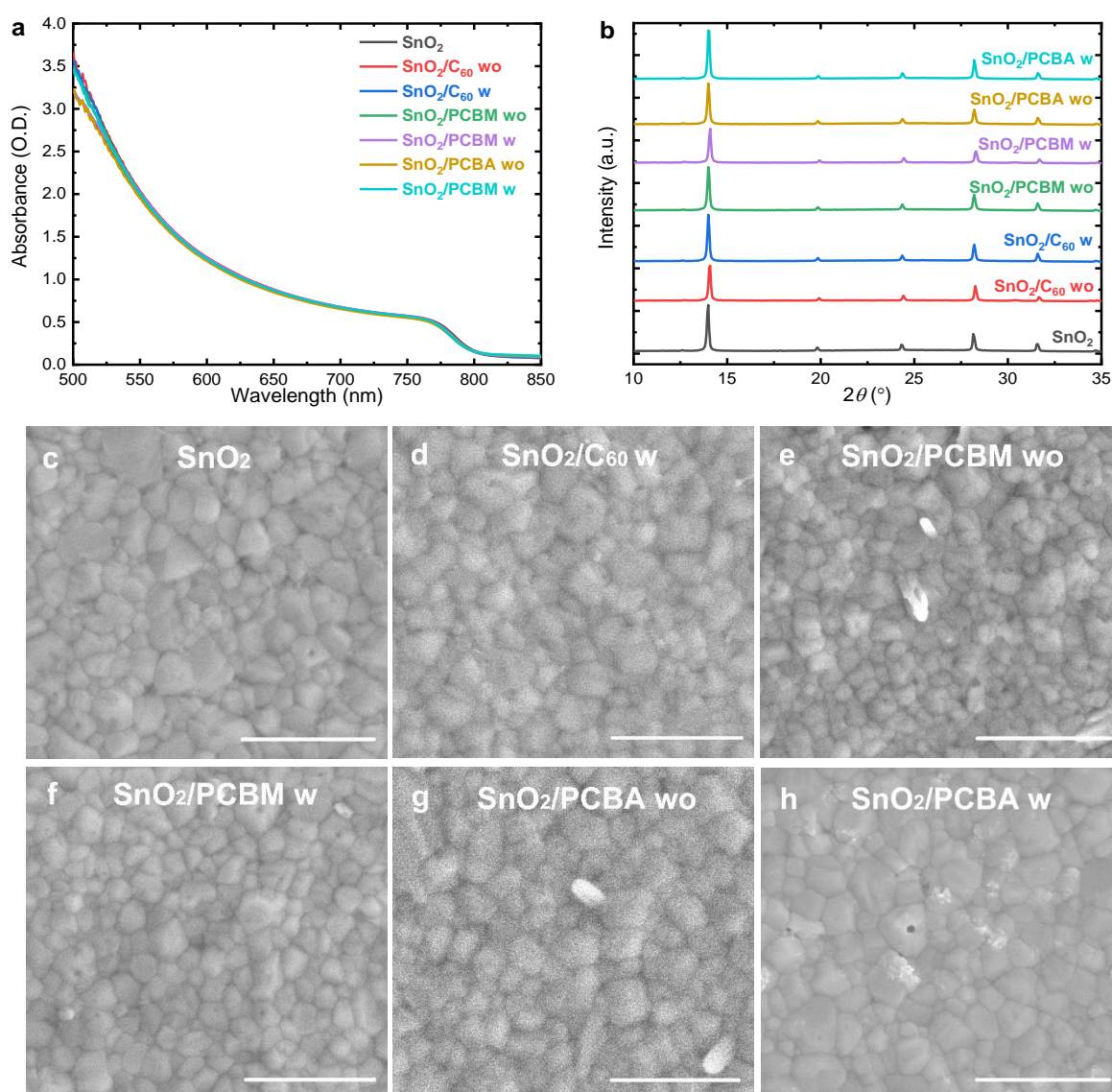


Figure 2.7 (a) UV-vis-NIR spectra and (b) XRD patterns of $\text{FA}_{0.66}\text{MA}_{0.34}\text{PbI}_{2.85}\text{Br}_{0.15}$ perovskite films deposited on different ETLs with (w) or without (wo) thermal annealing. Top-view SEM images of

perovskite films on (c) SnO₂, (d) SnO₂/C₆₀ (annealed), (e) SnO₂/PCBM (not-annealed), (f) SnO₂/PCBM (annealed), (g) SnO₂/PCBA(not-annealed), and (h) SnO₂/PCBA (annealed). Scale bars are 1 μm.

2.3 Morphology and crystallinity of perovskite films

To validate our hypothesis that the device performance is determined by the electron transport properties of the ETL, we investigated the quality of the perovskite films deposited on different fullerene passivated SnO₂ substrates. All the perovskite films display similar UV–vis–NIR absorption spectra, with a characteristic onset at around 800 nm (Figure 2.7a). Also, the X-ray diffraction (XRD) patterns of the as-prepared perovskite films are virtually identical (Figure 2.7b). No significant shift in the diffraction peak positions or intensities is observed, indicating that the crystallinity of perovskites is largely independent of the underlying fullerene layers. The primary diffraction peaks at 14° and 28° are assigned to the (110) and (220) lattice planes of the perovskite structure, respectively, and no significant trace of PbI₂ and non-perovskite phase can be identified. Figure 2.7c-h display the top-view scanning electron microscope (SEM) images of the corresponding perovskite films deposited on different ETLs. All the layers exhibit a compact and pinhole-free surface morphology, with an average grain size of ~300 nm. We attribute the independence of the perovskite morphology and crystallinity on different substrates to the two-step solution process utilized for depositing the perovskite layer, in which the crystallization dynamics are affected by the inorganic PbI₂ framework rather than the ETL substrate.^{33,68} Accordingly, we rule out the impact of perovskite bulk properties on the variation trend of device performance.

Table 2.3 Photovoltaic parameters of the champion PSCs with different fullerene layers.

Passivation layer	J_{sc} (mA cm ⁻²)	V_{oc} (V)	FF	PCE ^a (%)	J_{sc}^b (mA cm ⁻²)	PCE ^c (%)
SnO ₂ reference	22.0	1.10	0.64	15.4	21.7	15.3
C ₆₀ not-annealed	21.4	1.03	0.69	15.3	20.7	14.7
C ₆₀ annealed	21.4	1.04	0.69	15.3	20.9	14.8
PCBM not-annealed	22.2	1.09	0.67	16.1	21.6	15.8
PCBM annealed	22.1	1.08	0.72	17.1	21.7	16.9
PCBA not-annealed	22.2	1.10	0.76	18.6	21.9	18.3
PCBA annealed	22.1	1.06	0.77	18.0	22.0	17.9

^a The data were extracted from stabilized J – V curves under simulated AM 1.5G illumination (100 mW cm⁻²). ^b Calculated by integrating the EQE spectrum with the AM1.5G spectrum. ^c Corrected PCE obtained by calculating the J_{sc} integrated from EQE spectrum and V_{oc} and FF from the stabilized J – V measurement.

2.4 Fullerene profile at the interface

To gain insight into the distribution of the fullerene in the passivation layers, XPS depth profiling was performed. The depth profiles of pristine SnO₂ layers show no significant amounts of carbon (<1 at%) after UV-ozone cleaning (Figure 2.8a). Also, the carbon concentration remains negligible after rinsing with *N,N*-dimethylformamide (DMF). Hence, by monitoring the carbon signal of fullerene passivated SnO₂ layers, we can determine the fullerene concentration profile. Figure 2.8b-c show the XPS depth profiles of SnO₂ substrates with annealed and not-annealed PCBM layers after rinsing with DMF. In both cases, the tin concentration increases abruptly from the surface ($t = 0$ s), suggesting that DMF has removed most of the capping PCBM layer. Meanwhile, the carbon concentration of the annealed PCBM substrate is remarkably higher (29 at%) than that of the non-annealed PCBM substrate (11 at%). From the attenuated Sn 3*d* signal (Figure 2.8f),⁴⁹ the thickness of the annealed and not-annealed PCBM layers at the SnO₂ interface is estimated to be 1.3 nm and 0.2 nm, respectively. This implies that without thermal annealing, the interfacial PCBM layer is almost entirely removed by DMF, and no passivation can be developed at the SnO₂ interface; while with annealing, a PCBM-monolayer passivated SnO₂ interface is formed, which remains intact during the solution processing. Interestingly, both SnO₂/PCBM substrates exhibit a plateau of carbon signal (>7 at%) during the sputtering process, suggesting that the PCBM infiltrates into the porous SnO₂ layer and that DMF does not remove such penetrated PCBM. These SnO₂ layers have been shown to have pore sizes on the order of 10 nm.⁴² On the other hand, for the annealed and non-annealed PCBA-modified SnO₂ substrates, after DMF rinsing, the carbon concentrations at the surface ($t = 0$ s) are 43 and 40 at% (Figure 2.8d-e), much higher than their PCBM counterpart. From Figure 2.8f, the thicknesses of the interfacial PCBA layers are estimated to be 1.9 nm (annealed) and 1.6 nm (non-annealed), respectively, indicating that a PCBA-monolayer with better coverage is obtained at the SnO₂ interface. It is also found that when compared to the non-passivated SnO₂, the shift in the binding energies of Sn 3*d* core-level for both the PCBA modified SnO₂ (>0.14 eV) is higher than that for the annealed- and non-annealed-PCBM modified SnO₂ (0.10 eV and 0.03 eV), respectively. Here, the positive shift of the Sn 3*d* peaks is attributed to the decreased electron density near the Sn atoms, which could be induced by the bonding between the SnO₂ surface and the fullerenes.^{39,69} The result confirms the higher reactivity of the carboxylic acid functional group of PCBA than the methyl ester side of PCBM towards the hydroxyl (–OH) enriched SnO₂ surface in forming stable monolayers. The depth profiles (Figure 2.8d-e) also show that PCBA penetrates less deep into

the SnO₂ layer than PCBM, which is attributed to the use of a diluted PCBA solution (0.2 mg mL⁻¹) compared to the PCBM solution (10 mg mL⁻¹). The fact that PCBA penetrates less deep into the SnO₂ layer as compared to PCBM, while at the same time the PCBA concentration at the SnO₂ surface is higher, confirms that the carbon signals for the PCBM samples are unlikely due to ion knock-on effects. Together with the PV performance derived from the PCBA and PCBM modified ETLs, it is concluded that only the fullerenes located at the SnO₂/perovskite interface are essential for the charge transport processes.

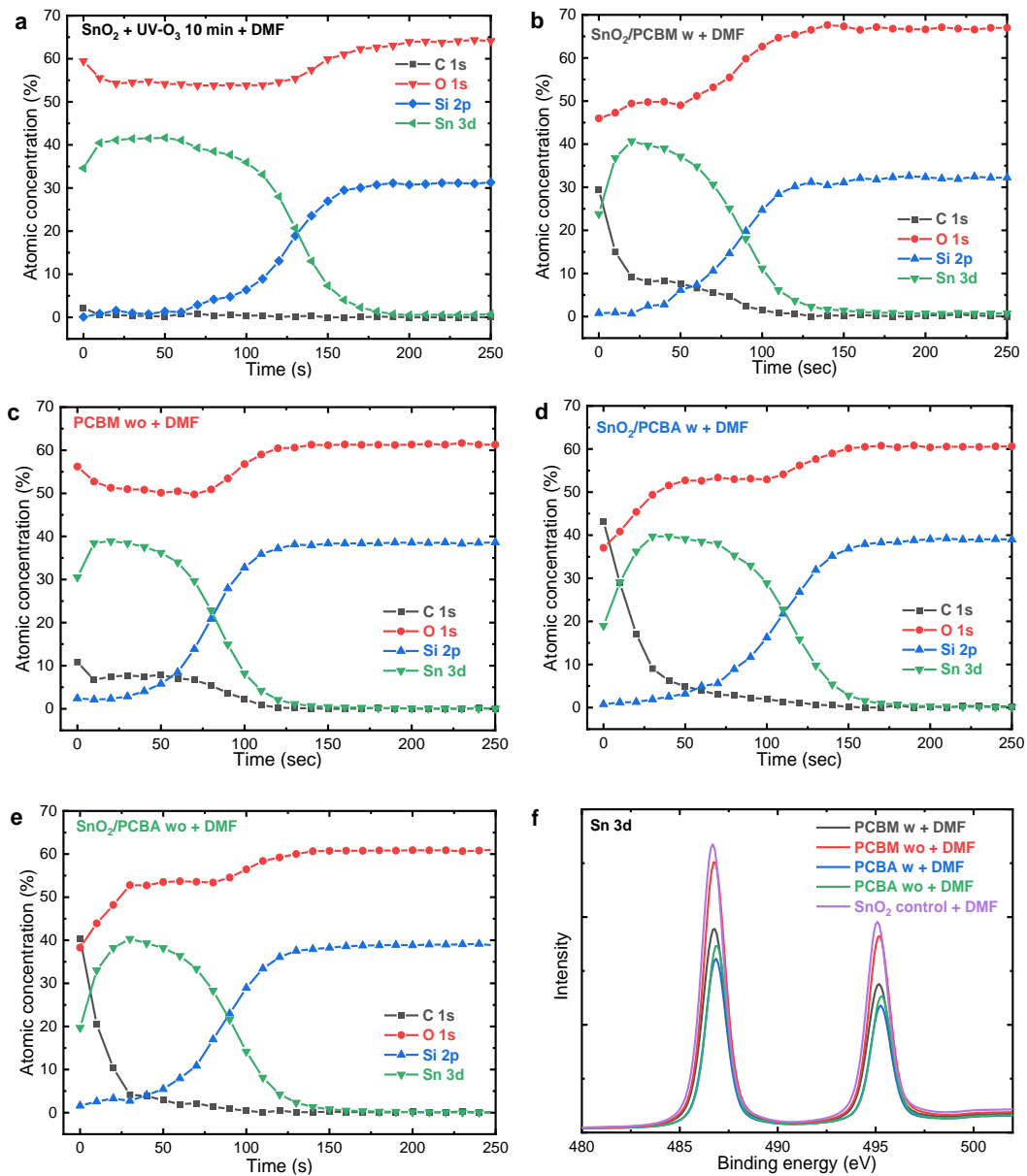


Figure 2.8 XPS depth profiles of (a) a pristine SnO₂ film treated by 10 minutes of UV-ozone, (b) SnO₂/PCBM (annealed), (c) SnO₂/PCBM (non-annealed), (d) SnO₂/PCBA (annealed) and (e) SnO₂/PCBA (non-annealed) ETLs deposited on glass substrates. The layers were rinsed by DMF shortly

before the XPS experiments. (f) XPS high-resolution scan spectra of the Sn 3d core-level for different ETL substrate surface. The initial SnO₂ layer thickness was ~20 nm for all depth profiles.

XPS depth profiles for the C₆₀-modified SnO₂ substrates after DMF rinsing (Figure 2.9) show that the carbon concentration only starts to decrease after a long-sputtering process when the as-deposited C₆₀ layer is above 15 nm. This indicates that the thermally evaporated C₆₀ layer is resilient against DMF solvent treatment. However, for the 5 nm thick C₆₀ layer, the carbon concentration at the surface ($t = 0$ s) is reduced to 18 at%, only slightly higher than that of the non-annealed PCBM substrate (11 at%). Notably, compared to the device with non-annealed PCBM, the 5 nm thick C₆₀ modified device exhibits decreased PV performance (Figure 2.5).

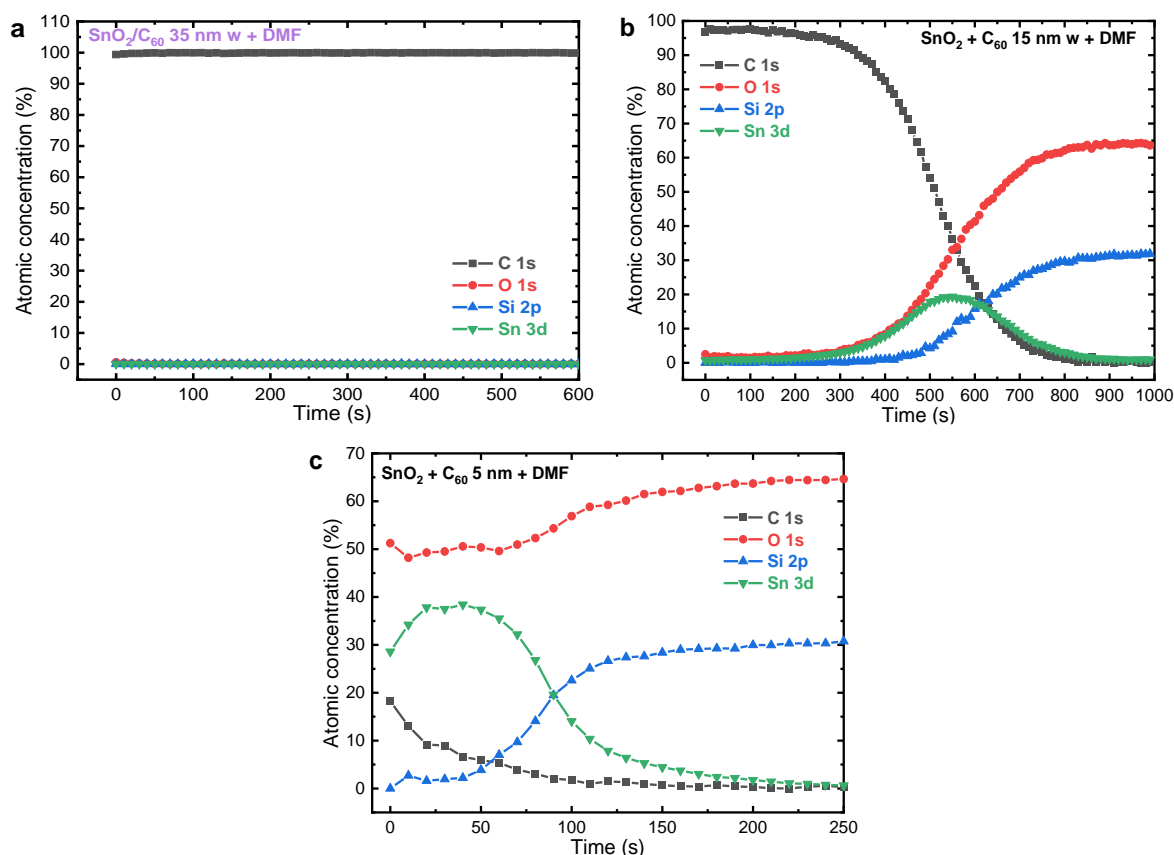


Figure 2.9 XPS depth profiles of (a) SnO₂/C₆₀ 35 nm (annealed), (b) SnO₂/C₆₀ 15 nm (annealed) and (c) SnO₂/C₆₀ 5 nm (annealed) ETL deposited on glass substrate, respectively. All the measurements were conducted shortly after rinsing in DMF. The initial SnO₂ layer thickness was ~20 nm for all depth profiles.

To verify the observations from the XPS analysis, UV–vis–NIR absorption spectra were performed on different fullerene modified SnO₂ substrates before and after DMF rinsing (Figure 2.10). As expected, the SnO₂/C₆₀ (15 nm) substrate only displays a slight decrease in absorbance due to the high resilience of the C₆₀ film against DMF treatment. In contrast, a significant

reduction in the absorbance is observed for both the SnO₂/PCBM substrates with and without annealing, since DMF washes away most of the capping PCBM layer. However, it is found that the absorbance of the annealed PCBM is still higher than that of the non-annealed PCBM, which confirms that more PCBM is retained on the substrate when thermally annealed. For PCBA-modified SnO₂ substrates, the absorbance before DMF rinsing is already low due to the dilute (0.2 mg mL⁻¹) PCBA solution used. After DMF rinsing, both the annealed and not-annealed PCBA substrates show a negligible reduction in absorbance, confirming that DMF rinsing removes very little PCBA. Among the DMF-washed PCBM and PCBA passivation layers, the annealed PCBM layer exhibits the highest absorbance. This is attributed to the PCBM infiltrated into the SnO₂ layer that cannot be removed by DMF, as is evidenced by the XPS depth profiles (Figure 2.8b-c).

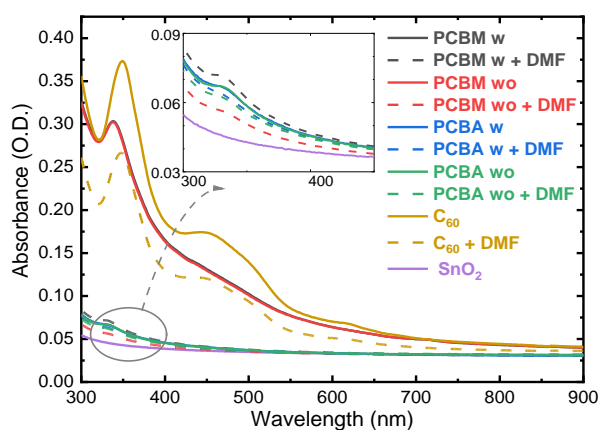


Figure 2.10 UV-vis-NIR absorption spectra of different fullerene-passivated SnO₂ ETLs deposited on quartz substrates, measured before and after DMF rinsing.

To explore the impact of PCBM (annealed) and PCBA monolayers on the charge transport of the SnO₂ ETL, their energy band structures were characterized by ultraviolet photoelectron spectroscopy (UPS). Figure 2.11a depicts that the secondary electron edge of the SnO₂ layer shifts to lower binding energies after PCBM and PCBA passivation. This corresponds to a significant increase in the work function from 3.58 eV for the pristine SnO₂, to 3.80 eV and 4.00 eV for the PCBM- and PCBA-passivated SnO₂, respectively. From the onset of the valence band spectrum, the ionization potential of the SnO₂, SnO₂/PCBM, and SnO₂/PCBA films are calculated to be 7.60 eV, 6.11 eV, and 6.28 eV, respectively. Figure 2.11b illustrates a schematic energy level diagram for different ETLs, assuming a fixed Fermi level for all the measurements.²⁴ Consistent with the shift in Sn 3*d* binding energies (Figure 2.8f), the increase in the work function of PCBM- and PCBA-passivated SnO₂ ETLs can be

attributed to the formation of surface dipoles, which induce an electric field that accelerates the charge collection at the SnO₂ interface and reduces the recombination losses.^{33,70}

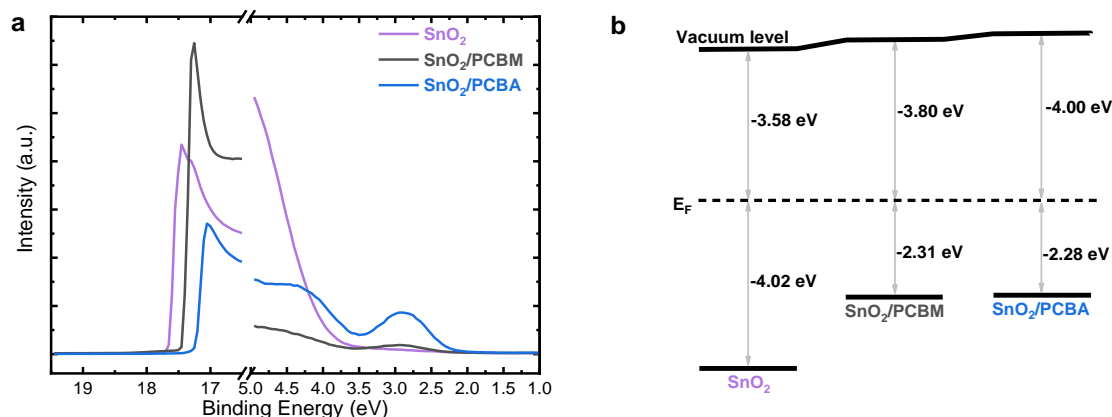


Figure 2.11 (a) UPS measurements of SnO₂, SnO₂/PCBM, and SnO₂/PCBA, respectively. All samples were rinsed by DMF before the measurement. (b) Energy diagram of different ETL substrates, assuming a fixed Fermi-level.

2.5 PCBM-dimer layers

Based on the XPS analysis, one might expect that introduction of a better-covered PCBM layer at the SnO₂ interface would improve the device performance. Alternatively, an interfacial chemical reaction between the PCBM and SnO₂ could be of vital importance for improving the charge extraction. To gain further understanding of the role of the PCBM interlayer, we introduced a solvent-resistant PCBM layer on the SnO₂. Following the methods reported by Edman and co-workers,⁶²⁻⁶⁴ we exposed an as-prepared PCBM layer to UV light for some time before DMF or perovskite solution casting. UV light creates a robust and less-soluble dimeric state of PCBM, yet with retained electronic properties. According to the XPS depth profiles, when using 10 mg mL⁻¹ PCBM and UV light (Figure 2.12a-b), both DMF rinsed SnO₂/PCBM-dimer layers (w/o thermal annealing) exhibit much higher carbon concentrations at the surface (>70 at%) than the SnO₂/PCBM reference (Figure 2.8b-c) due to a thicker PCBM layer on the SnO₂. This observation is well supported by the UV-vis-NIR measurement (Figure 2.12f) and the thickness of the capping PCBM layer (12 nm), measured by surface profilometry. Using a higher (20 mg mL⁻¹) PCBM concentration in combination with UV illumination, the depth profiles of both SnO₂/PCBM-dimer layers (w/o thermal annealing, Fig 2.12c, d) are similar to that of the SnO₂/C₆₀ (35 nm) layer (Figure 2.9a) and show a constant carbon concentration of 100 at% during entire the sputtering process. Independent of w/o thermal annealing, the PCBM thickness was 23 nm. This indicates the successful fabrication of a DMF-resilient SnO₂/PCBM bi-layered ETL in which the thickness and the

chemical interaction of the capping PCBM layer can be tuned by changing the PCBM solution concentration and the thermal annealing treatment. Notably, Figure 2.12a-b do not show a clear peak for the Sn, and also the onset of the Si signal is much less clear than in Figure 2.8 for PCBM layers that were treated without UV light. We think that this is because after UV illumination, the rate of removal of the thin (12 nm) PCBM is drastically reduced, and the Sn and Si signals result from regions below the top PCBM layer. This explanation is consistent with Figure 2.12c-d, where the thicker (23 nm) UV-treated PCBM layer is not removed and prevents observing Sn and Si below.

Figure 2.13 shows the $J-V$ curves of the PSC devices prepared with different concentrations of PCBM (5 to 20 mg mL⁻¹). Without exposure to UV light, all devices deliver virtually identical PCEs of 16.0% with negligible hysteresis when the PCBM layer is thermally annealed (Figure 2.13a). For low PCBM concentrations (≤ 10 mg mL⁻¹), only the PCBM chemically bonded to the SnO₂ is preserved at the interface. For the highest PCBM concentration (20 mg mL⁻¹), however, DMF rinsing does not wash away the entire PCBM layer but leaves a ~ 13 nm film as determined by profilometry and confirmed by XPS depth profiling (Figure 2.12e). The results suggest that the passivation capacity of PCBM at the SnO₂ interface is mostly independent of the concentrations of the PCBM solution and that, next to a surface-bound monolayer, a thin (~ 13 nm) residual PCBM layer offers no additional improvement.

In contrast, when using UV illumination to create PCBM-dimers at the SnO₂ surface, a strong dependence of the PCE on the PCBM concentration is found, both with and without thermal annealing (Figure 2.13b-c). At low PCBM concentrations (≤ 10 mg mL⁻¹), thermally annealed PCBM-dimer layers provide high PCEs of $\sim 16.4\%$, comparable to devices without UV-exposure, indicating that a thin PCBM-dimer layer gives good passivation. Strikingly, the devices with not-annealed PCBM-dimer layer exhibit much inferior performance (PCE $\sim 14\%$), despite the good coverage of the fullerene on the SnO₂ substrate (Figure 2.12b). We conclude that the thermally induced chemical interaction between the PCBM and SnO₂ is the most influential factor in enhancing the interfacial charge transport process.

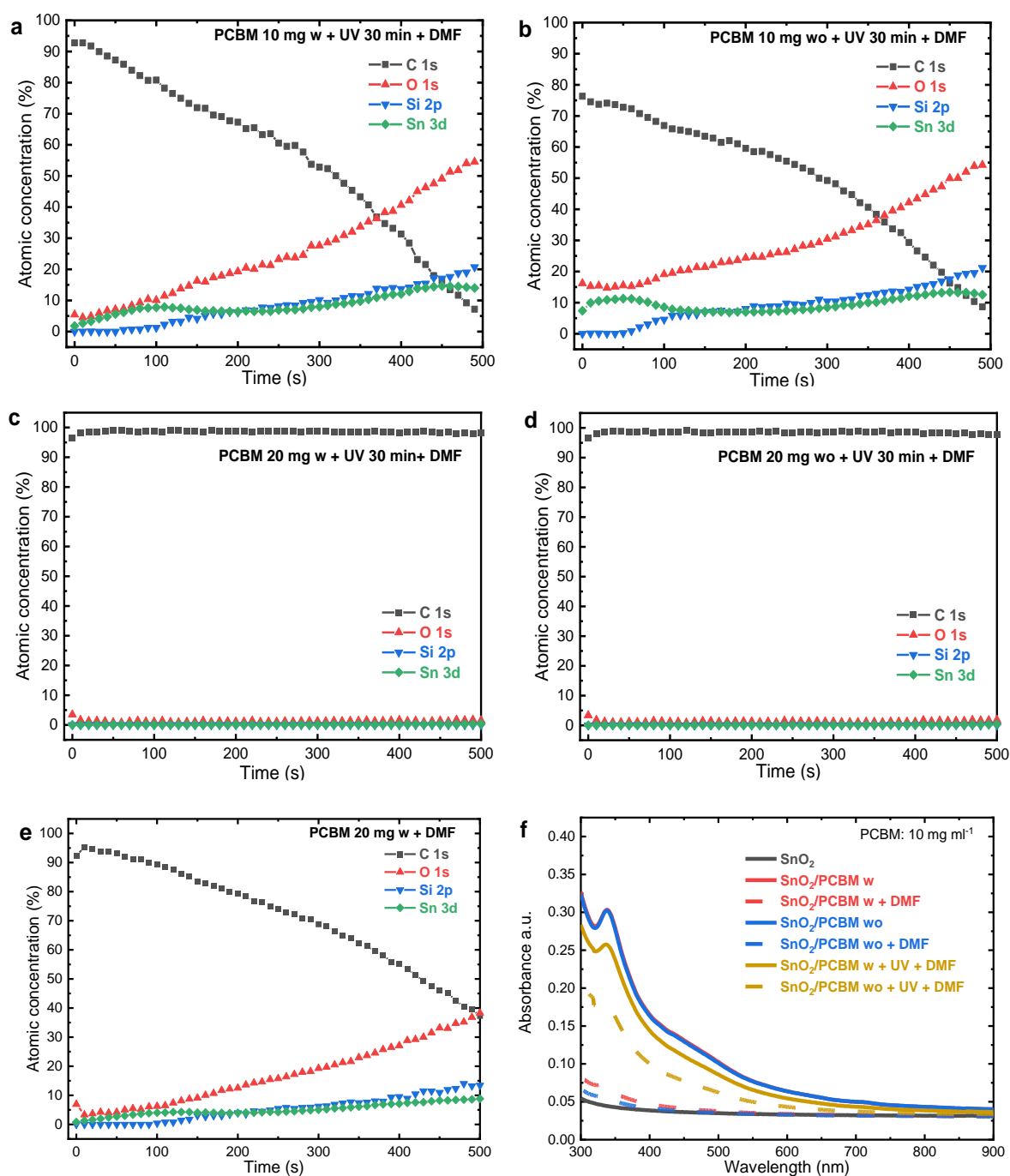


Figure 2.12 XPS depth profiles of the glass/ SnO_2 substrates passivated by 10 mg mL^{-1} PCBM (a-b) with (w) or without (wo) thermal annealing and 20 mg mL^{-1} PCBM (c-e) w/wo thermal annealing. UV-light illumination was applied to the samples a-d. All the samples were washed by DMF. (f) UV-vis-NIR absorption spectra of SnO_2/PCBM layers (from 10 mg mL^{-1} chlorobenzene solution) on quartz substrates treated w/wo thermal annealing and w/wo UV-light illumination, measured before and after DMF rinsing. The initial SnO_2 layer thickness was $\sim 20 \text{ nm}$ for all depth profiles.

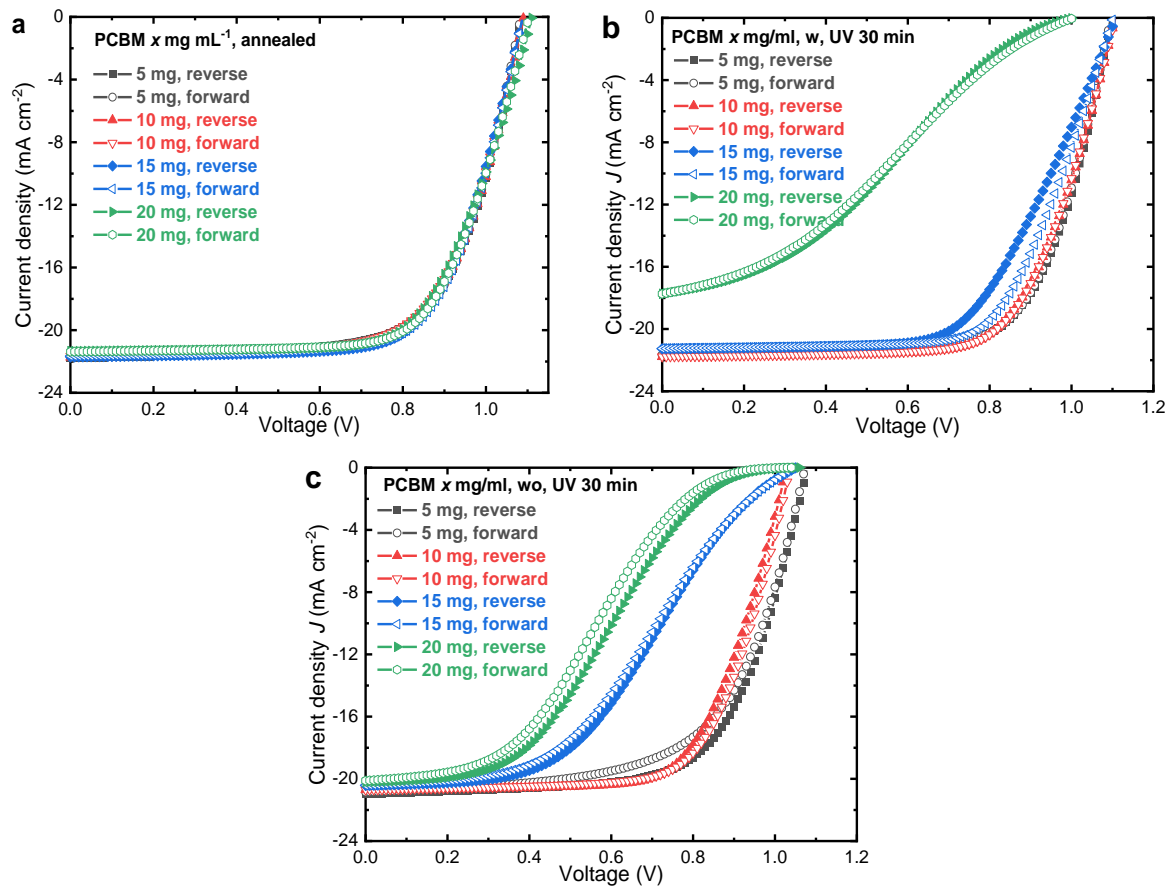


Figure 2.13 J - V curves of PSCs based on SnO₂/PCBM (5 to 20 mg mL^{-1}) ETLs. (a) For cells where the PCBM layers were thermally annealed (100 °C, 20 min). For cells with (b) and without (c) thermal annealing, and with UV-light illumination on the PCBM layers before the perovskite deposition.

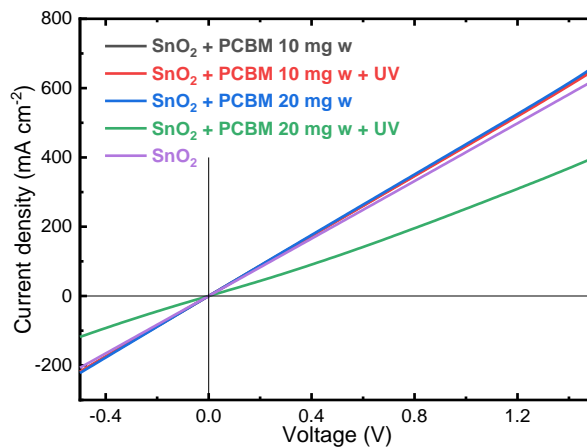


Figure 2.14 J - V curves of the ETL-only devices based on the structure of ITO/SnO₂/PCBM/LiF/Al.

As the concentration of PCBM solution increases to 20 mg mL^{-1} , for both cells made with or without thermal annealing, the corresponding J - V curves show strong s-shapes with reduced V_{oc} , J_{sc} , and FF, yielding PCEs lower than 10% (Figure 2.13b, c). Again, the effect of perovskite bulk films on the device performance is negligible since they present virtually

identical XRD patterns and SEM images on different PCBM-dimer layers. In conductivity measurements for different ETLs (Figure 2.14), it is found that compared to other thin PCBM layers, the conductivity extracted from the J - V curve is reduced when applying a slightly thicker (20 mg mL^{-1}) PCBM-dimer layer on the SnO_2 substrate. This increased resistivity of the PCBM-dimer layer limits the charge transport and induce non-radiative recombination at the SnO_2 /perovskite interface, resulting in reduced device performance. Collectively, our observations imply that the fabrication of a robust SnO_2 /fullerene ETL does not necessarily improve the interfacial charge transport and that the introduction of a fullerene monolayer with the controlled chemical interaction with the SnO_2 ETL is sufficient to boost the PSC device performance.

2.6 Conclusions

We have performed a comprehensive study correlating the chemical interactions at the SnO_2 /fullerene interface with the PSC device performance. XPS depth profiling is a useful tool to monitor the precise location of thin-film fullerene residues in the SnO_2 ETL. In the case of depositing PCBM from $\leq 10 \text{ mg mL}^{-1}$ solutions, thermal annealing is essential to create a surface-bound PCBM monolayer that is resilient to depositing a perovskite layer on top. The surface-bound PCBM monolayer significantly improves the device performance and reproducibility. Although PCBM partly infiltrates into the porous SnO_2 layer, only the fullerenes located at the SnO_2 /perovskite interface are essential for electron extraction. The passivation capacity of PCBM is not affected by the concentration of the solution from which it is deposited because DMF removes PCBM that is not bound to the surface in subsequent processing. While thermally evaporated C_{60} shows high resilience against DMF, the performance of the corresponding PSC is inferior to the thermally annealed PCBM devices. This is attributed to the absence of a chemical bond between C_{60} and the SnO_2 surface. In accordance, the carboxylic acid-based PCBA derivative exhibits much higher passivation efficiency. A PCBA-monolayer with excellent coverage and DMF-resilience can be formed from dilute (0.2 mg mL^{-1}) solutions without any thermal treatment. After optimization, the best-performing device using a PCBA-modified SnO_2 ETL exhibits a PCE of 18.8%.

Interfaces are of significant importance for the PSCs based on metal oxide layers. Depending on the fabrication method, the passivation of metal oxide is often found critical for high-performing devices. This study explored the essence of the passivation layer between the photo-active and charge transport layers. The new insights into the interface passivation of the

metal oxide-based charge transport layer offer a strategy for future development toward high-efficiency PSCs.

2.7 Experimental section

Materials and solution preparation: All materials and reagents were purchased from commercial sources unless stated otherwise. For the electron transport layer (ETL), the SnO₂ precursor solution was prepared by diluting the commercial 15 wt% SnO₂ aqueous colloidal dispersion (Alfa Aesar) with deionized water to the desired concentrations (2.8, 5.0, 7.5, 10.0, 12.5 wt%). [6,6]-phenyl-C₆₁-butyric acid methyl ester (PCBM) (Solenne BV, 99%) was dissolved in chlorobenzene (CB) (Sigma-Aldrich, anhydrous 99.8%) at concentrations of 5, 10, 15 and 20 mg mL⁻¹ and stirred overnight at 60 °C. [6,6]-phenyl-C₆₁-butyric acid (PCBA) was dissolved in 1,2-dichlorobenzene (oDCB, Sigma-Aldrich, anhydrous 99%) at 0.1 ~ 0.2 mg mL⁻¹ and stirred at 60 °C. C₆₀ was purchased from SES Research (99.8%) and used without purification. For the perovskite precursor solutions, PbI₂ (553 mg) (TCI Chemicals, 99.99% trace metal basis) was dissolved in DMF (0.876 mL) (Sigma-Aldrich, anhydrous 99.8%) and dimethyl sulfoxide (DMSO, 0.0864 mL) (Sigma-Aldrich, anhydrous 99.9%) at 60 °C and stirred overnight. Formamidinium iodide (54.0 mg) (FAI, Greatcell Solar), methylammonium iodide (14.3 mg) (MAI, Greatcell Solar) and methylammonium bromide (7.6 mg) (MABr, Greatcell Solar) were dissolved in 1 mL 2-propanol (Sigma-Aldrich, anhydrous 99.5%) at 60 °C and stirred overnight. For the HTL, Spiro-OMeTAD (80 mg) (Lumtec, 99.5%) was dissolved in CB (1 mL) with 4-tert-butylpyridine (28.5 µL) (TBP, Sigma-Aldrich, 99.5%) and bis(trifluoromethylsulfonyl)amine lithium salt (17.5 µL) (Li-TFSI, Sigma-Aldrich, 99.95% trace metal basis) of a stock solution (520 mg mL⁻¹) in acetonitrile (ACN, Sigma-Aldrich, anhydrous 99.8%) at 60 °C. Before the HTL deposition, tris(2-(1H-pyrazol-1-yl)-4-tert-butylpyridine)cobalt(III) tri[bis(trifluoromethane)sulfonimide] (20 µL) (Co(III)-TFSI, Greatcell Solar) of a stock solution (500 mg mL⁻¹) in ACN was added to the Spiro-OMeTAD solution.

Device fabrication: Pre-patterned ITO glass (Naranjo Substrates) was cleaned sequentially by sonication in acetone, scrubbing and sonication in a sodium dodecyl sulfate (Acros, 99%) solution in water, rinsing in deionized water and sonication in 2-propanol. Shortly before the deposition, the substrate was dried and treated with UV-ozone for 30 min. The SnO₂ dispersion was spin coated onto the ITO substrate at 2800 rpm (with a 2000 rpm s⁻¹ acceleration) for 60 s and dried at 150 °C for 30 min in ambient atmosphere. The SnO₂ film was treated with UV-ozone for 10 min. and then quickly transferred into a nitrogen-filled glovebox. For PCBM and PCBA passivation, the fullerene solution was spin coated onto the SnO₂ substrate at 2000 rpm (with a 2000 rpm s⁻¹ acceleration) for 30 s and was annealed/not-annealed at 100 °C for 20 min. Depending on the passivation protocol, PCBM was illuminated with UV-light (Spectroline, E-Series UV lamp, 365 nm) for 30 min. in N₂ atmosphere. C₆₀ was deposited by thermal evaporation under high vacuum (~3 × 10⁻⁷ mbar). The perovskite layer was

fabricated *via* a two-step process, the PbI₂ solution was spin coated at 3000 rpm (with a 2000 rpm s⁻¹ acceleration) for 30 s, and then the FAI/MAI/MABr solution was dynamically cast on the PbI₂ layer at a spin speed of 3000 rpm for 30 s. Afterward, the sample was immediately annealed in the glovebox at 100 °C for 30 min. After cooling, the chemically doped Spiro-OMeTAD solution was dynamically spin coated onto the perovskite layer at 2000 rpm (with a 20000 rpm s⁻¹ acceleration) for 50 s. The sample was then exposed to dry air for 20 min., before being transferred back into the glovebox. Finally, MoO₃ (10 nm) and Au (100 nm) were sequentially evaporated under high vacuum ($\sim 3 \times 10^{-7}$ mbar). The active area (0.09 cm² or 0.16 cm²) was determined by the overlap of the top Au and bottom ITO contacts.

For the electron-only devices, an ITO/SnO₂/fullerene/perovskite/C₆₀/bathocuproine (BCP)/Al device structure was used. The fabrication up until the perovskite layers are described above. The sample was then transferred into the thermal evaporator, where C₆₀ (20 nm), BCP (8 nm), and Al (100 nm) were sequentially evaporated under a high vacuum ($\sim 3 \times 10^{-7}$ mbar).

The ITO/SnO₂/PCBM/LiF/Al ETL-only device was fabricated with LiF (1 nm) and Al (100 nm) deposited *via* thermal evaporation under high vacuum ($\sim 3 \times 10^{-7}$ mbar).

Device characterization: *J–V* characteristics were measured in the glovebox by a Keithley 2400 source meter. For solar cell characterization, a tungsten-halogen lamp filtered by a Schott GG385 UV filter and a Hoya LB120 daylight filter was used to simulate the 100 mW cm⁻² solar light. A black shadow mask with an aperture area of 0.0676 or 0.1296 cm² was used to define the illuminated cell area. During the fast *J–V* scan, the Keithley swept the voltage either from +1.5 to -0.5 V (reverse scan) or from -0.5 to +1.5 V (forward scan) at a scan rate of 0.25 V s⁻¹. For the stabilized *J–V* measurement, the solar cell was first tracked by *V*_{oc} for 5 min under light soaking and followed by a reverse sweep from (*V*_{oc} + 0.04) V to -0.04 V with a step size of 0.04 V, the acquisition time of current density at each voltage step was 5 s. The voltage at the maximum power point determined from the stabilized *J–V* curve, which was then applied to the solar cell during the maximum power output tracking under illumination. EQE measurement was performed in a nitrogen atmosphere. The probe light source was generated by a 50 W tungsten-halogen lamp (Philips focusline), which was modulated with a mechanical chopper (Stanford Research, SR 540) before passing into a monochromator (Oriel, Cornerstone 130). The spectral response of the device was recorded as a voltage from a pre-amplifier (Stanford Research, SR 570) using a lock-in amplifier (Stanford Research, SR 830), and was calibrated by a reference silicon cell. To accurately determine the current density, a green LED (530 nm, Thorlabs M530L3, driven by a DC4104 driver) was used as a light bias to provide the solar cell with approximately one sun illumination intensity during the measurement.

The DC conductivity σ of different SnO₂/PCBM ETLs was determined by fitting the *J–V* curves of ETL-only devices (Figure 2.14) to the equation⁷¹

$$J = \frac{A\sigma V}{L}$$

Film characterization: The surface morphology of perovskite films was analyzed by SEM (FEI Quanta 3D FEG) using a 5 kV electron beam and a secondary electron detector. All the samples were deposited on glass substrates. UV–vis–NIR absorption spectra were measured by PerkinElmer Lambda 900 UV–vis–NIR spectrophotometer at room temperature between 300 and 900 nm. For the absorption measurement, all the perovskite films were deposited on glass substrates; for other samples, they were deposited on quartz substrates. XRD patterns were measured by a Bruker 2D Phaser using Cu K α ($\lambda = 1.5405 \text{ \AA}$) as the X-ray source. The increment step size was 0.05° between 10 to 40° . XPS measurements were performed using a Thermo Scientific K-Alpha with a 180° double focusing hemispherical analyzer and a 128-channel detector. Monochromatic Al K α (1486.6 eV) radiation was used, and the X-ray spot size was $400 \text{ }\mu\text{m}$. For the surface analysis, a survey spectrum was first measured for 15 scans with a pass energy of 200 eV. High-resolution scan (30 times) of each element was conducted with a pass energy of 50 eV. During the sputtering experiment, in order to improve the depth resolution, the sample was removed layer-by-layer by argon ion etching operated at low current and low ion energy (1000 eV). The crater region generated by argon ions is $\sim 2 \times 4 \text{ mm}^2$. For the depth profiles, snapshot mode was used for each element, and the number of frames was $5 \times 1 \text{ s}$.

UPS was carried out in a multi-chamber ESCALAB II system using He-I radiation ($E_{\text{He-I}} = 21.22 \text{ eV}$) and a -6 V bias. The samples were deposited on full ITO substrates and transferred into the vacuum chamber directly from N₂ atmosphere.

2.8 References

1. NREL Best Research-Cell Efficiencies. <https://www.nrel.gov/pv/assets/pdfs/best-research-cell-efficiencies.20200128.pdf> (2020).
2. Saliba, M. et al. How to Make over 20% Efficient Perovskite Solar Cells in Regular (n-i-p) and Inverted (p-i-n) Architectures. *Chem. Mater.* **30**, 4193-4201 (2018).
3. Saliba, M. et al. Cesium-containing triple cation perovskite solar cells: improved stability, reproducibility and high efficiency. *Energy Environ. Sci.* **9**, 1989-1997 (2016).
4. Saliba, M. et al. Incorporation of rubidium cations into perovskite solar cells improves photovoltaic performance. *Science* **354**, 206-209 (2016).
5. Yang, W. S. et al. Iodide management in formamidinium-lead-halide-based perovskite layers for efficient solar cells. *Science* **356**, 1376-1379 (2017).
6. Luo, D. et al. Enhanced photovoltage for inverted planar heterojunction perovskite solar cells. *Science* **360**, 1442-1446 (2018).
7. Jiang, Q. et al. Planar-Structure Perovskite Solar Cells with Efficiency beyond 21%. *Adv. Mater.* **29**, 1703852 (2017).
8. Tan, H. et al. Efficient and stable solution-processed planar perovskite solar cells via contact passivation. *Science* **355**, 722-726 (2017).
9. Galagan, Y. Perovskite Solar Cells: Toward Industrial-Scale Methods. *J. Phys. Chem. Lett.* **9**, 4326-4335 (2018).
10. Wang, J. et al. Highly Efficient Perovskite Solar Cells Using Non-Toxic Industry Compatible Solvent System. *Solar RRL* **1**, 1700091 (2017).
11. Williams, S. T., Rajagopal, A., Chueh, C. C., Jen, A. K. Current Challenges and Prospective Research for Upscaling Hybrid Perovskite Photovoltaics. *J. Phys. Chem. Lett.* **7**, 811-819 (2016).
12. Rong, Y. et al. Challenges for commercializing perovskite solar cells. *Science* **361**, 1214 (2018).
13. Kim, H., Lim, K.-G., Lee, T.-W. Planar heterojunction organometal halide perovskite solar cells: roles of interfacial layers. *Energy Environ. Sci.* **9**, 12-30 (2016).
14. Liu, M., Johnston, M. B., Snaith, H. J. Efficient planar heterojunction perovskite solar cells by vapour deposition. *Nature* **501**, 395-398 (2013).
15. Stranks, S. D. et al. Electron-Hole Diffusion Lengths Exceeding 1 Micrometer in an Organometal Trihalide Perovskite Absorber. *Science* **342**, 341 (2013).
16. Green, M. A., Ho-Baillie, A., Snaith, H. J. The emergence of perovskite solar cells. *Nat. Photonics* **8**, 506-514 (2014).
17. Xing, G. et al. Long-Range Balanced Electron- and Hole-Transport Lengths in Organic-Inorganic $\text{CH}_3\text{NH}_3\text{PbI}_3$. *Science* **342**, 344 (2013).
18. Haque, M. A., Sheikh, A. D., Guan, X., Wu, T. Metal Oxides as Efficient Charge Transporters in Perovskite Solar Cells. *Adv. Energy Mater.* **7**, 1602803 (2017).
19. Mingorance, A. et al. Interfacial Engineering of Metal Oxides for Highly Stable Halide Perovskite Solar Cells. *Adv. Mater. Interfaces* **5**, 1800367 (2018).
20. Xiong, L. et al. Review on the Application of SnO_2 in Perovskite Solar Cells. *Adv. Funct. Mater.* **28**, 1802757 (2018).
21. Ke, W. et al. Low-temperature solution-processed tin oxide as an alternative electron transporting layer for efficient perovskite solar cells. *J. Am. Chem. Soc.* **137**, 6730-6733 (2015).
22. Jiang, Q., Zhang, X., You, J. SnO_2 : A Wonderful Electron Transport Layer for Perovskite Solar Cells. *Small* **14**, 1801154 (2018).
23. Jiang, Q. et al. Enhanced electron extraction using SnO_2 for high-efficiency planar-structure $\text{HC}(\text{NH}_2)_2\text{PbI}_3$ -based perovskite solar cells. *Nat. Energy* **2**, 16177 (2016).
24. Lee, Y. et al. Efficient Planar Perovskite Solar Cells Using Passivated Tin Oxide as an Electron Transport Layer. *Adv. Sci.* **5**, 1800130 (2018).
25. Correa Baena, J. P. et al. Highly efficient planar perovskite solar cells through band alignment engineering. *Energy Environ. Sci.* **8**, 2928-2934 (2015).
26. Ayguler, M. F. et al. Influence of Fermi Level Alignment with Tin Oxide on the Hysteresis of Perovskite Solar Cells. *ACS Appl. Mater. Interfaces* **10**, 11414-11419 (2018).

27. Kuang, Y. et al. Low-Temperature Plasma-Assisted Atomic-Layer-Deposited SnO₂ as an Electron Transport Layer in Planar Perovskite Solar Cells. *ACS Appl. Mater. Interfaces* **10**, 30367-30378 (2018).
28. Anaraki, E. H. et al. Highly efficient and stable planar perovskite solar cells by solution-processed tin oxide. *Energy Environ. Sci.* **9**, 3128-3134 (2016).
29. Jiang, Q. et al. Surface passivation of perovskite film for efficient solar cells. *Nat. Photonics* **13**, 460-466 (2019).
30. Choi, K. et al. Thermally stable, planar hybrid perovskite solar cells with high efficiency. *Energy Environ. Sci.* **11**, 3238-3247 (2018).
31. Weber, S. A. L. et al. How the formation of interfacial charge causes hysteresis in perovskite solar cells. *Energy Environ. Sci.* **11**, 2404-2413 (2018).
32. Hermes, I. M., Hou, Y., Bergmann, V. W., Brabec, C. J., Weber, S. A. L. The Interplay of Contact Layers: How the Electron Transport Layer Influences Interfacial Recombination and Hole Extraction in Perovskite Solar Cells. *J. Phys. Chem. Lett.* **9**, 6249-6256 (2018).
33. Zuo, L. et al. Tailoring the Interfacial Chemical Interaction for High-Efficiency Perovskite Solar Cells. *Nano Lett.* **17**, 269-275 (2017).
34. Stolterfoht, M. et al. Visualization and suppression of interfacial recombination for high-efficiency large-area pin perovskite solar cells. *Nat. Energy* **3**, 847-854 (2018).
35. Liu, K. et al. Fullerene derivative anchored SnO₂ for high-performance perovskite solar cells. *Energy Environ. Sci.* **11**, 3463-3471 (2018).
36. Gatti, T., Menna, E., Meneghetti, M., Maggini, M., Petrozza, A., Lamberti, F. The Renaissance of fullerenes with perovskite solar cells. *Nano Energy* **41**, 84-100 (2017).
37. Ke, W. et al. Cooperative tin oxide fullerene electron selective layers for high-performance planar perovskite solar cells. *J. Mater. Chem. A* **4**, 14276-14283 (2016).
38. Kegelman, L. et al. It Takes Two to Tango—Double-Layer Selective Contacts in Perovskite Solar Cells for Improved Device Performance and Reduced Hysteresis. *ACS Appl. Mater. Interfaces* **9**, 17245-17255 (2017).
39. Yang, D. et al. High efficiency planar-type perovskite solar cells with negligible hysteresis using EDTA-complexed SnO₂. *Nat. Commun.* **9**, 3239 (2018).
40. Pujari, S. P., Scheres, L., Marcelis, A. T., Zuilhof, H. Covalent surface modification of oxide surfaces. *Angew. Chem. Int. Ed.* **53**, 6322-6356 (2014).
41. Wu, W.-Q., Chen, D., Caruso, R. A., Cheng, Y.-B. Recent progress in hybrid perovskite solar cells based on n-type materials. *J. Mater. Chem. A* **5**, 10092-10109 (2017).
42. Tebby, Z. et al. Low-temperature UV processing of nanoporous SnO₂ layers for dye-sensitized solar cells. *ACS Appl. Mater. Interfaces* **3**, 1485-1491 (2011).
43. Wojciechowski, K. et al. Heterojunction modification for highly efficient organic-inorganic perovskite solar cells. *ACS Nano* **8**, 12701-12709 (2014).
44. Wang, C. et al. Low-temperature plasma-enhanced atomic layer deposition of tin oxide electron selective layers for highly efficient planar perovskite solar cells. *J. Mater. Chem. A* **4**, 12080-12087 (2016).
45. Wang, C. et al. Compositional and morphological engineering of mixed cation perovskite films for highly efficient planar and flexible solar cells with reduced hysteresis. *Nano Energy* **35**, 223-232 (2017).
46. Wang, C. et al. Understanding and Eliminating Hysteresis for Highly Efficient Planar Perovskite Solar Cells. *Adv. Energy Mater.* **7**, 1700414 (2017).
47. Dong, Y. et al. Highly Efficient Planar Perovskite Solar Cells Via Interfacial Modification with Fullerene Derivatives. *Small* **12**, 1098-1104 (2016).
48. Wong, K. K. et al. Interface-Dependent Radiative and Nonradiative Recombination in Perovskite Solar Cells. *J. Phys. Chem. C* **122**, 10691-10698 (2018).
49. An, Q. et al. High performance planar perovskite solar cells by ZnO electron transport layer engineering. *Nano Energy* **39**, 400-408 (2017).
50. Zhang, Y. et al. Enhanced performance and light soaking stability of planar perovskite solar cells using an amine-based fullerene interfacial modifier. *J. Mater. Chem. A* **4**, 18509-18515 (2016).

51. Wojciechowski, K. et al. C₆₀ as an Efficient n-Type Compact Layer in Perovskite Solar Cells. *J. Phys. Chem. Lett.* **6**, 2399-2405 (2015).
52. Tao, C. et al. 17.6% stabilized efficiency in low-temperature processed planar perovskite solar cells. *Energy Environ. Sci.* **8**, 2365-2370 (2015).
53. Tao, C. et al. Fully Solution-Processed n-i-p-Like Perovskite Solar Cells with Planar Junction: How the Charge Extracting Layer Determines the Open-Circuit Voltage. *Adv. Mater.* **29**, 1604493 (2017).
54. Watson, B. L., Rolston, N., Bush, K. A., Leijtens, T., McGehee, M. D., Dauskardt, R. H. Cross-Linkable, Solvent-Resistant Fullerene Contacts for Robust and Efficient Perovskite Solar Cells with Increased J_{sc} and V_{oc} . *ACS Appl. Mater. Interfaces* **8**, 25896-25904 (2016).
55. Qiu, W. et al. Highly efficient perovskite solar cells with crosslinked PCBM interlayers. *J. Mater. Chem. A* **5**, 2466-2472 (2017).
56. Liu, X. et al. Exploring Inorganic Binary Alkaline Halide to Passivate Defects in Low-Temperature-Processed Planar-Structure Hybrid Perovskite Solar Cells. *Adv. Energy Mater.* **8**, 1800138 (2018).
57. Bu, T. et al. Universal passivation strategy to slot-die printed SnO₂ for hysteresis-free efficient flexible perovskite solar module. *Nat. Commun.* **9**, 4609 (2018).
58. Tu, B. et al. Novel Molecular Doping Mechanism for n-Doping of SnO₂ via Triphenylphosphine Oxide and Its Effect on Perovskite Solar Cells. *Adv. Mater.* **31**, 1805944 (2019).
59. Yoon, H., Kang, S. M., Lee, J.-K., Choi, M. Hysteresis-free low-temperature-processed planar perovskite solar cells with 19.1% efficiency. *Energy Environ. Sci.* **9**, 2262-2266 (2016).
60. Wojciechowski, K. et al. Cross-Linkable Fullerene Derivatives for Solution-Processed n-i-p Perovskite Solar Cells. *ACS Energy Lett.* **1**, 648-653 (2016).
61. Song, S. et al. Surface modified fullerene electron transport layers for stable and reproducible flexible perovskite solar cells. *Nano Energy* **49**, 324-332 (2018).
62. Wang, J., Larsen, C., Wågberg, T., Edman, L. Direct UV Patterning of Electronically Active Fullerene Films. *Adv. Funct. Mater.* **21**, 3723-3728 (2011).
63. Enevold, J., Larsen, C., Zakrisson, J., Andersson, M., Edman, L. Realizing Large-Area Arrays of Semiconducting Fullerene Nanostructures with Direct Laser Interference Patterning. *Nano Lett.* **18**, 540-545 (2018).
64. Dzwilewski, A., Wågberg, T., Edman, L. Photo-Induced and Resist-Free Fullerenes Imprint Patterning of Fullerene Materials for Use in Functional Electronics. *J. Am. Chem. Soc.* **131**, 4006-4011 (2009).
65. Qiu, W. et al. An Interdiffusion Method for Highly Performing Cesium/Formamidinium Double Cation Perovskites. *Adv. Funct. Mater.* **27**, 1700920 (2017).
66. Pachoumi, O., Bakulin, A. A., Sadhanala, A., Siringhaus, H., Friend, R. H., Vaynzof, Y. Improved Performance of ZnO/Polymer Hybrid Photovoltaic Devices by Combining Metal Oxide Doping and Interfacial Modification. *J. Phys. Chem. C* **118**, 18945-18950 (2014).
67. Hendriks, K. H., van Franeker, J. J., Bruijnaers, B. J., Anta, J. A., Wienk, M. M., Janssen, R. A. J. 2-Methoxyethanol as a new solvent for processing methylammonium lead halide perovskite solar cells. *J. Mater. Chem. A* **5**, 2346-2354 (2017).
68. Yang, W. S. et al. High-performance photovoltaic perovskite layers fabricated through intramolecular exchange. *Science* **348**, 1234-1237 (2015).
69. Tian, J. et al. Dual Interfacial Design for Efficient CsPbI₂Br Perovskite Solar Cells with Improved Photostability. *Adv. Mater.* **31**, 1901152 (2019).
70. Vaynzof, Y., Kabra, D., Zhao, L., Ho, P. K. H., Wee, A. T. S., Friend, R. H. Improved photoinduced charge carriers separation in organic-inorganic hybrid photovoltaic devices. *Appl. Phys. Lett.* **97**, 033309 (2010).
71. Zhao, Y. et al. Thick TiO₂-Based Top Electron Transport Layer on Perovskite for Highly Efficient and Stable Solar Cells. *ACS Energy Lett.* **3**, 2891-2898 (2018).

Chapter 3

Understanding the film formation kinetics of sequential deposited narrow-bandgap Pb–Sn hybrid perovskite films*

Abstract

Developing efficient narrow bandgap Pb–Sn hybrid perovskite solar cells with high Sn-content is crucial for perovskite-based tandem devices. Film properties such as crystallinity, morphology, surface roughness, and homogeneity dictate photovoltaic performance. However, compared to Pb-based analogs, controlling the formation of Sn-containing perovskite films is much more challenging. A deeper understanding of the growth mechanisms in Pb–Sn hybrid perovskites is needed to improve power conversion efficiencies. Here, in-situ optical spectroscopy is performed during sequential deposition of Pb–Sn hybrid perovskite films and combined with ex-situ characterization techniques to reveal the temporal evolution of crystallization in Pb–Sn hybrid perovskite films. Using a two-step deposition method, homogeneous crystallization of mixed Pb–Sn perovskites can be achieved. Solar cells based on the narrow bandgap (1.23 eV) $\text{FA}_{0.66}\text{MA}_{0.34}\text{Pb}_{0.5}\text{Sn}_{0.5}\text{I}_3$ perovskite absorber exhibit the highest efficiency among mixed Pb–Sn perovskites and feature a relatively low dark carrier density compared to Sn-rich devices. By passivating defect sites on the perovskite surface, the device achieves a power conversion efficiency of 16.1%, which is the highest efficiency reported for sequential solution-processed narrow bandgap perovskite solar cells with 50% Sn-content.

*This chapter is published as: Wang J., Datta K., Li J., Verheijen M.A., Zhang D., Wienk M.M., Janssen R.A.J. *Adv. Energy Mater.*, **2020**, 10, 2000566.

3.1 Introduction

Organic-inorganic hybrid perovskites hold great promise as light-absorbers for low-cost and high-efficiency solar cells owing to their exceptional optoelectronic characteristics such as high absorption coefficient, long carrier diffusion length, and large defect tolerance.¹⁻³ Within a decade, the power conversion efficiency (PCE) of single-junction perovskite solar cells (PSCs) has increased from 3.8% to a record of 25.2%, on par with the state-of-the-art inorganic photovoltaic (PV) technologies.⁴ Developing all-perovskite tandem solar cells with complementary bandgaps is considered the next step to surpass the Shockley-Queisser efficiency limit for single-junction devices.⁵⁻⁸ Solution processability of all components at low-temperature would enhance incentives to explore the large-scale implementation of such multi-junction cells.⁹

Previous studies¹⁰⁻¹² of tandem solar cells have suggested that a combination of a wide-bandgap (1.7 to 1.9 eV) front cell and a narrow-bandgap (0.9 to 1.2 eV) rear cell is ideal for high performance. Hybrid perovskites AMX_3 , where A is a monovalent cation (formamidinium (FA^+), methylammonium (MA^+) or Cs^+), M is a divalent metal cation (Pb^{2+} or Sn^{2+}), and X is a halide anion (I^- or Br^-),¹³ have a broadly tunable bandgap *via* compositional engineering.¹⁴ The bandgap of Pb-based perovskites can be continuously tuned from 1.5 to 2.3 eV by substituting I with Br.^{15,16} On the other hand, a nonlinear bandgap behavior¹⁷ is observed when alloying Pb (1.5 eV) and Sn-based (1.3 eV) perovskites, providing a minimum bandgap of ~ 1.2 eV at 50% to 75% Sn-content.¹⁸⁻²¹ Such mixed Pb–Sn perovskites are considered the most promising narrow-bandgap perovskite materials for tandem devices.^{21,22} However, compared to their Pb analogs, Sn-based perovskite precursors have a greater tendency to react and crystallize at room temperature,²³ which makes it difficult to grow compact, smooth, and homogeneous Pb–Sn hybrid perovskite films.^{24,25} It has also been shown that readily oxidation of Sn^{2+} to Sn^{4+} can drastically increase trap density of the perovskite absorber and deteriorate performance of mixed Pb–Sn PSCs.^{8,26} Strategies such as precursor engineering have since been exploited for high-quality Pb–Sn perovskite films.^{12,27} Most recently, by adding guanidinium thiocyanate and metallic Sn powder to the precursor solution, high PCEs of 20.2% and 21.1%, respectively, have been demonstrated in mixed Pb–Sn low bandgap PSCs.^{5,8}

Notably, most high-quality Pb–Sn perovskite films to date are prepared by the antisolvent method.^{12,28} Despite being efficient in producing dense, crystalline perovskite films, the laborious antisolvent dripping procedure presents a potential risk of irreproducibility among different perovskite recipes and is considered to be less compatible with large-scale

processes.^{29,30} In comparison, a sequential deposition method provides better morphological control for Pb-based perovskites since the crystallization originates from an intermediate PbI_2 framework.^{31,32} Furthermore, separate optimizations for each step are possible, which leads to a broader processing window with improved reproducibility.³³ However, only a handful of studies have used this method for Pb–Sn hybrid perovskite films,^{26,34–38} and the highest PCE (16.26%)²⁶ is lower than achieved with the antisolvent method. Moreover, among sequentially-deposited, high-performing Pb–Sn perovskites, most films contain less than 30% Sn, leading to suboptimal bandgaps for tandem applications.^{26,34,35} Understanding the growth mechanism of sequential solution-processed Pb–Sn hybrid perovskite films is critical for further optimizing high-performing Pb–Sn perovskite films with higher Sn-content.

In this study, we explore the compositional space of high-quality $\text{FA}_{0.66}\text{MA}_{0.34}\text{Pb}_{1-x}\text{Sn}_x\text{I}_3$ perovskite films prepared using a simple sequential deposition method. Through in-situ optical absorption spectroscopy during spin coating, we reveal the impact of the Pb/Sn ratio on the film formation kinetics of hybrid perovskite films. Sn-containing precursors are found to accelerate the conversion to the perovskite phase. Combining with ex-situ characterization, the direct formation of large perovskite grains after coating the Sn-based precursor solutions is evidenced. In comparison, only small perovskite nuclei are formed for the Pb-only precursor films. The sequential deposition approach enables the formation of homogeneous Pb–Sn hybrid perovskite phases despite the very different crystallization behavior of the Pb- and Sn-only perovskite precursors. We demonstrate compact and smooth perovskite films with Sn-contents up to 60%. After optimization, the narrow-bandgap (1.23 eV) $\text{FA}_{0.66}\text{MA}_{0.34}\text{Pb}_{0.5}\text{Sn}_{0.5}\text{I}_3$ perovskite provides a current density of 28.0 mA cm^{-2} and a PCE of 16.1% in a planar solar cell.

3.2 Formation kinetics of Pb–Sn perovskite films

Figure 3.1a illustrates the fabrication of $\text{FA}_{0.66}\text{MA}_{0.34}\text{Pb}_{1-x}\text{Sn}_x\text{I}_3$ ($x = 0, 0.25, 0.4, 0.5, 0.6, 0.75, 1$) perovskite films via sequential deposition. First, a solution mixture of $(1-x) \text{PbI}_2$ and $x \text{SnI}_2$ (denoted as $\text{Pb}_{1-x}\text{Sn}_x\text{I}_2$) in *N,N*-dimethylformamide (DMF) and dimethyl sulfoxide (DMSO) is spin coated to obtain the intermediate precursor film. The film is kept at room temperature for some time to evaporate excess solvents. The film is in an amorphous state that remains for hours due to the strong coordination between SnI_2 and DMSO.²³ In a second step, an isopropanol solution of FAI/MAI (66:34 in molar ratio) is spin coated on top, followed by thermal annealing to promote the crystallization of the perovskite film.

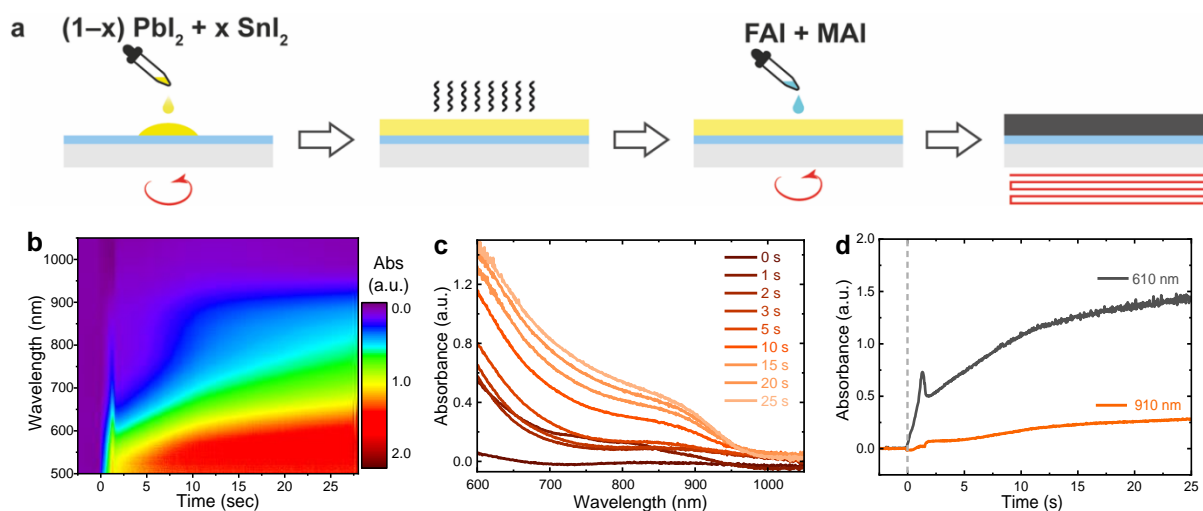


Figure 3.1 (a) Schematic fabrication process of $\text{FA}_{0.66}\text{MA}_{0.34}\text{Pb}_{1-x}\text{Sn}_x\text{I}_3$ perovskite films using a sequential deposition method. (b) Time-resolved absorption intensity maps during spin coating of FAI/MAI solution on the $\text{Pb}_{0.5}\text{Sn}_{0.5}\text{I}_2$ precursor film. (c) Corresponding absorption spectra. (d) Time-evolution of absorbance at 610 and 910 nm during the spin coating process.

To gain insight into the transformation dynamics of the $\text{Pb}_{1-x}\text{Sn}_x\text{I}_2$ precursor, we performed in-situ optical absorption measurements during the spin coating of the FAI/MAI solution. Following a previously described protocol,³⁹ the temporal evolution of the absorption spectrum was recorded by collecting the light that was reflected from rotating substrates with a white reflector at the back. Figure 3.1b exhibits the absorption spectra of a typical $\text{FA}_{0.66}\text{MA}_{0.34}\text{Pb}_{0.5}\text{Sn}_{0.5}\text{I}_3$ ($x = 0.5$) precursor film at different times during spin coating. Directly after dripping the FAI/MAI solution ($t = 0$ s), the absorbance increases abruptly over a broad wavelength region, giving rise to the characteristic narrow-bandgap perovskite spectrum at the earliest stages of the deposition (Figure 3.1c). The absorption intensity then slightly decreases when the material is radially ejected from the substrate during the flow phase ($t < 3$ s).³⁹ Subsequently, during the drying phase ($t < 30$ s), the optical absorption increases owing to the formation of the perovskite phase. This implies that the transition from the amorphous $\text{Pb}_{0.5}\text{Sn}_{0.5}\text{I}_2$ precursor to the crystalline perovskite is initiated by casting the FAI/MAI solution. Also, the simultaneous increase of absorbance in both the visible (610 nm) and near-infrared (910 nm) regions suggests that there is no significant preferential formation of segregated Pb- and Sn-rich perovskite phases (Figure 3.1d).

Understanding the Film Formation Kinetics of Sequential Deposited Narrow-Bandgap Pb–Sn Hybrid Perovskite Films

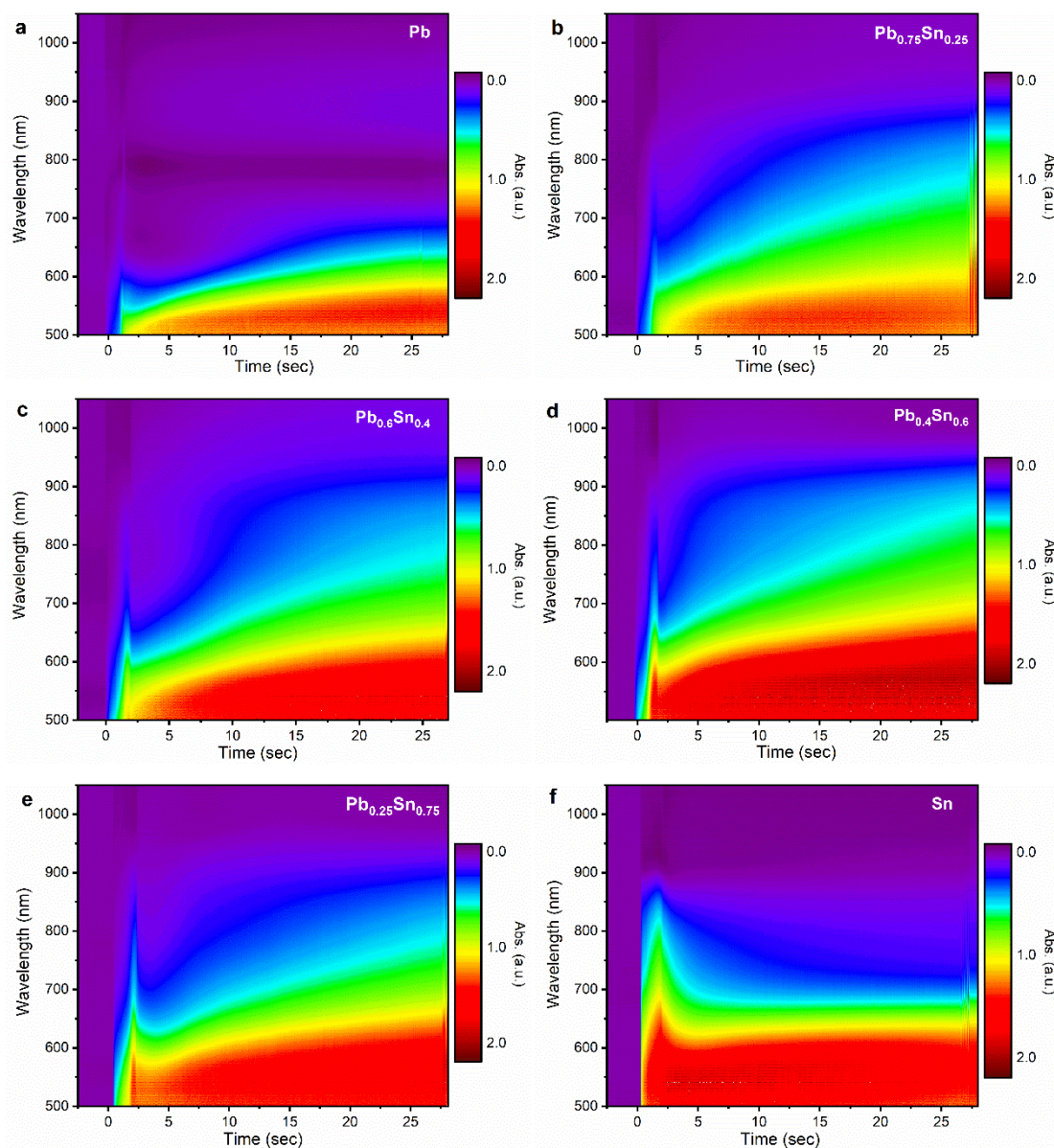


Figure 3.2 2D colored maps showing the time-resolved absorption intensity during spin coating of a FAI/MAI (66:34) solution onto the $\text{Pb}_{1-x}\text{Sn}_x\text{I}_2$ precursor film (from $t = 0$ s), where x is (a) 0, (b) 0.25, (c) 0.4, (d) 0.6, (e) 0.75 and (f) 1.

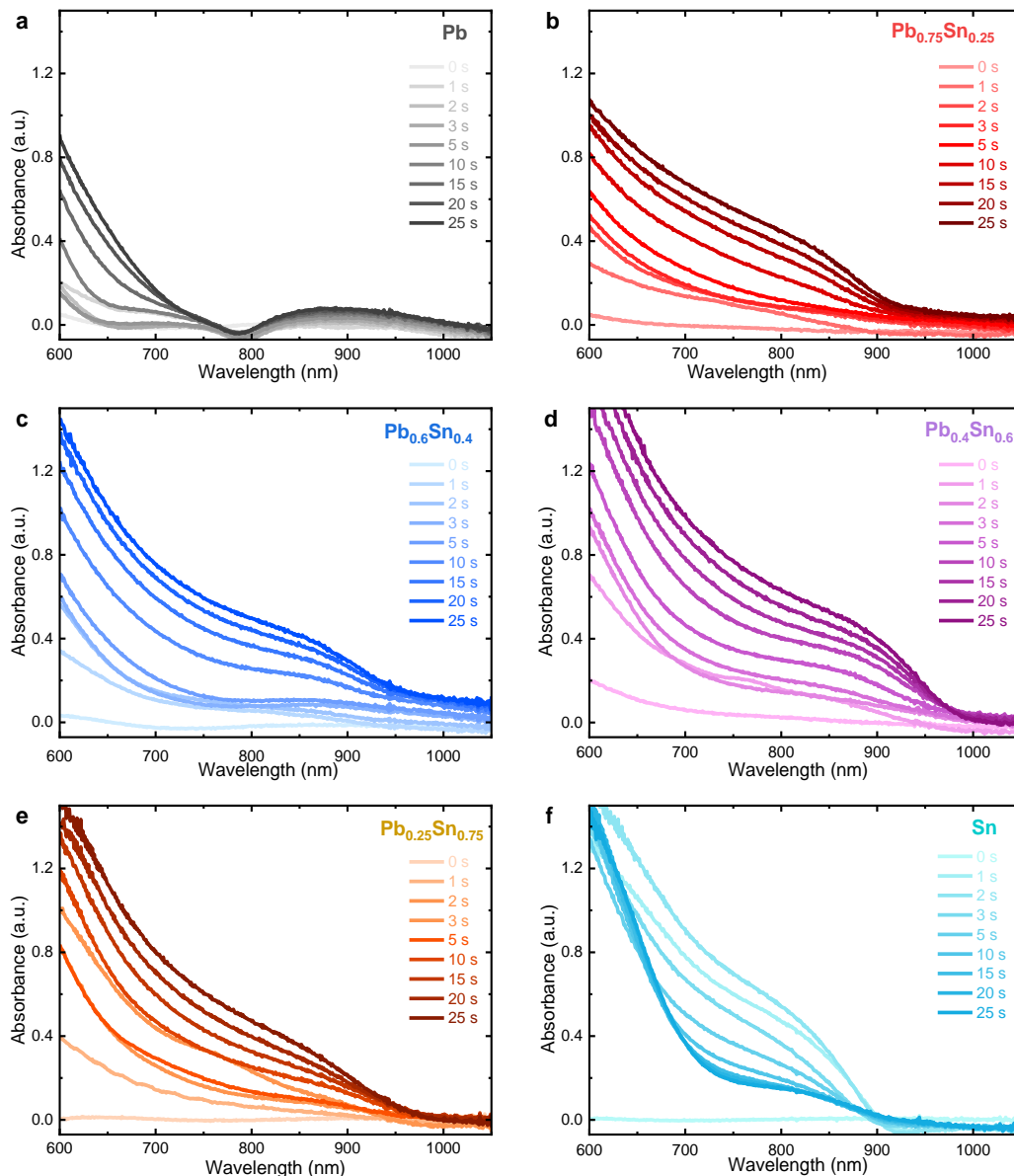


Figure 3.3 The time-resolved absorption spectra during spin coating of a FAI/MAI (66:34) solution onto the $\text{Pb}_{1-x}\text{Sn}_x\text{I}_2$ precursor film (from $t = 0$ s), where x is (a) 0, (b) 0.25, (c) 0.4, (d) 0.6, (e) 0.75 and (f) 1. The apparent absorption between 800 and 1000 nm in panel (a) is due to the interference of light reflected from the top of the film and the glass surface.

When comparing the in-situ absorption spectra of different mixed Pb–Sn compositions (Figure 3.2 and 3.3), we found that the conversion to the perovskite phase is accelerated at higher Sn contents. For the Sn-only precursor film ($x = 1$), a sharp absorption onset at around 900 nm is observed immediately after dripping the FAI/MAI solution. Afterward, the absorbance is initially lowered due to the layer thinning and then remains constant. This implies that the formation of a Sn-only perovskite phase is completed, directly after casting the FAI/MAI solution. On the contrary, the transformation to the perovskite phase is considerably slow for the Pb-only composition ($x = 0$), as evidenced by the weak absorption throughout the

deposition process. Ex-situ scanning electron microscopy (SEM) and X-ray diffraction (XRD) measurements for as-cast (non-annealed) films (Figure 3.4 and 3.5) confirm that only small-sized nanocrystals were formed in the Pb-only precursor film ($x = 0$), which correlates with slow crystal growth of Pb-based nuclei before the thermal annealing. In comparison, the Sn-only precursor film exhibits a much higher crystallinity, accompanied by the formation of micrometer-sized grains on the surface. The results confirm the higher affinity of the organic components FAI/MAI toward SnI_2 , which facilitates crystal growth of Sn-based perovskite at room temperature.

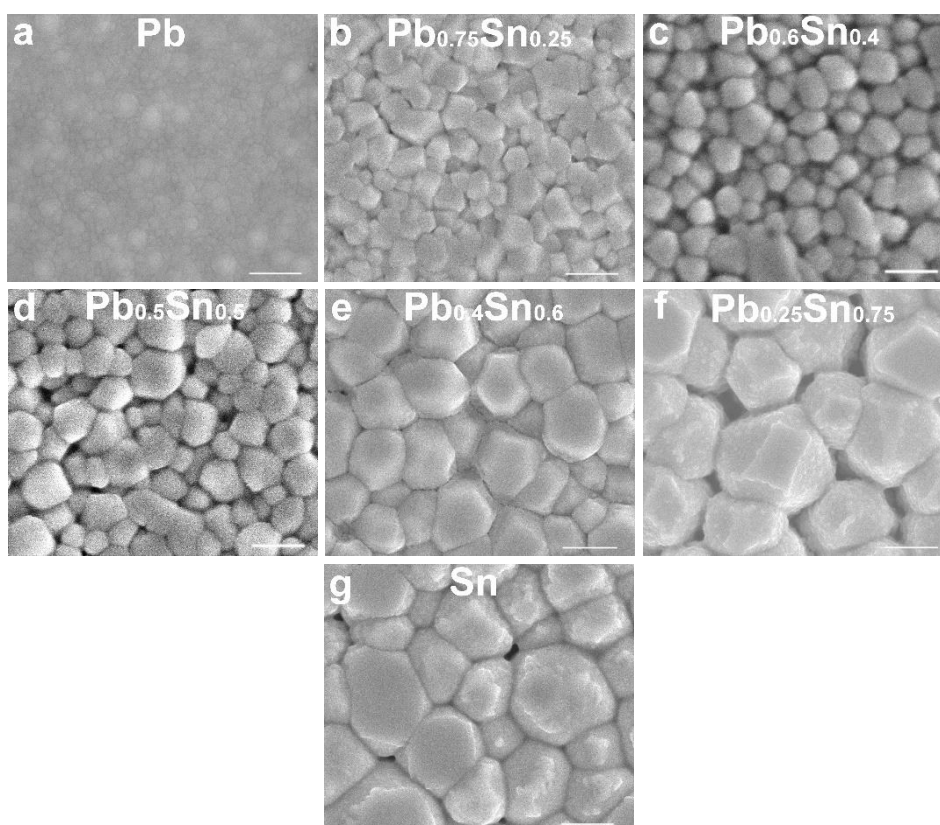


Figure 3.4 Top-view SEM images of non-annealed $\text{FA}_{0.66}\text{MA}_{0.34}\text{Pb}_{1-x}\text{Sn}_x\text{I}_3$ perovskite films (after spin coating), where x is (a) 0, (b) 0.25, (c) 0.4, (d) 0.5, (e) 0.6, (f) 0.75 and (g) 1. The voids are formed in some films due to the instant evaporation of residue solvent under the SEM vacuum analysis chamber. Scale bars in SEM images are 500 nm.

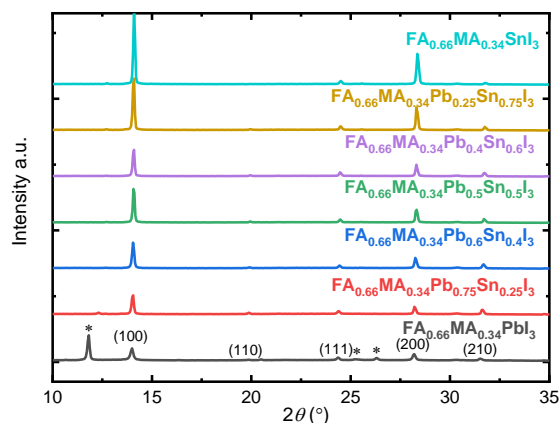


Figure 3.5 XRD patterns of $\text{FA}_{0.66}\text{MA}_{0.34}\text{Pb}_{1-x}\text{Sn}_x\text{I}_3$ ($x = 0, 0.25, 0.4, 0.5, 0.6, 0.75, 1$) precursor films without thermal annealing. Some δ perovskite phases (marked as *) were formed in the pure-Pb ($x = 0$) precursor film, which is attributed to the unstable α perovskite phase without thermal annealing (nanocrystals). The XRD measurements were performed in the ambient condition.

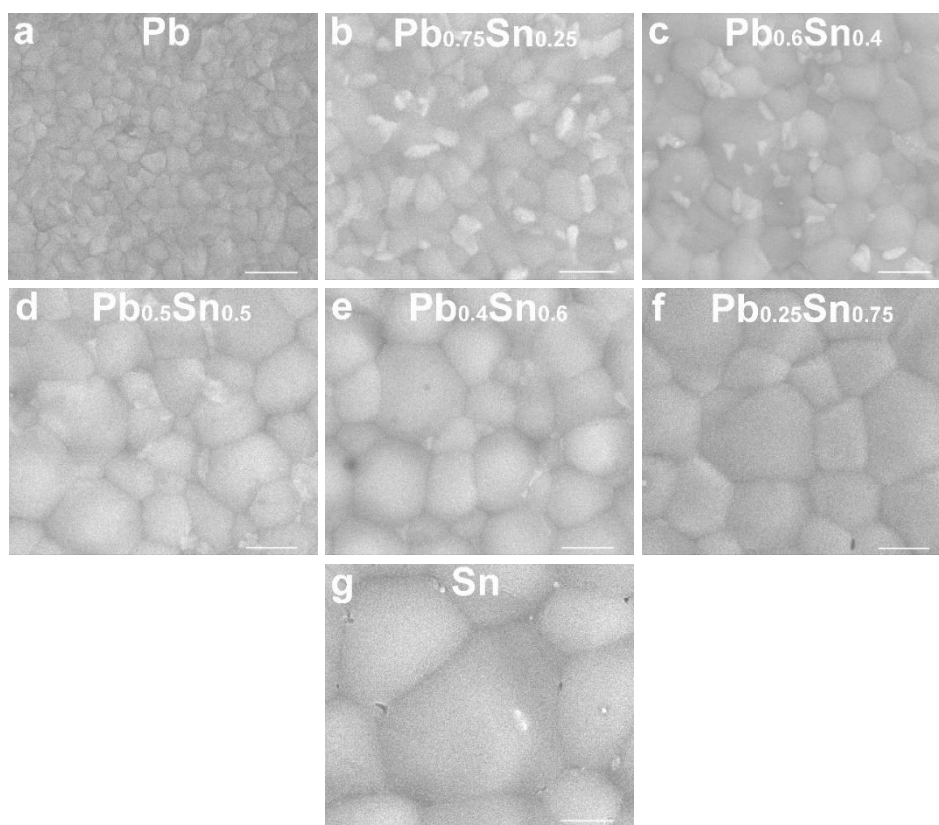


Figure 3.6 Top-view SEM images of annealed $\text{FA}_{0.66}\text{MA}_{0.34}\text{Pb}_{1-x}\text{Sn}_x\text{I}_3$ perovskite films, where x is (a) 0, (b) 0.25, (c) 0.4, (d) 0.5, (e) 0.6, (f) 0.75 and (g) 1. Scale bars are 500 nm. The sheet-like crystals on the perovskite surface visible in panel (b-d) are attributed to SnF_2 .^{40,41}

3.3 Structural properties of Pb–Sn perovskite films

The crystallization behavior of Pb/Sn-based precursors has a significant impact on the quality of the final perovskite films. Figure 3.6 displays top-view SEM images of the annealed perovskite samples with different Pb/Sn ratios. Compared to non-annealed precursor films (Figure 3.4), thermal annealing causes coarsening of the perovskite crystals. It is found that all annealed films display a compact and pinhole-free surface morphology, with the average grain size starting at 240 ± 80 nm for the Pb-only perovskite film ($x = 0$), 530 ± 140 nm for $\text{Pb}_{0.5}\text{Sn}_{0.5}$ ($x = 0.5$) and 1.3 ± 0.3 μm for Sn-only ($x = 1$) perovskite. Meanwhile, atomic force microscope (AFM) (Figure 3.7) shows that the root-mean-square (RMS) surface roughness of the Sn-rich perovskite films ($x > 0.5$) is considerably higher than that of the Pb-rich films ($x \leq 0.5$), in line with their propensity to form large crystallites at room temperature.

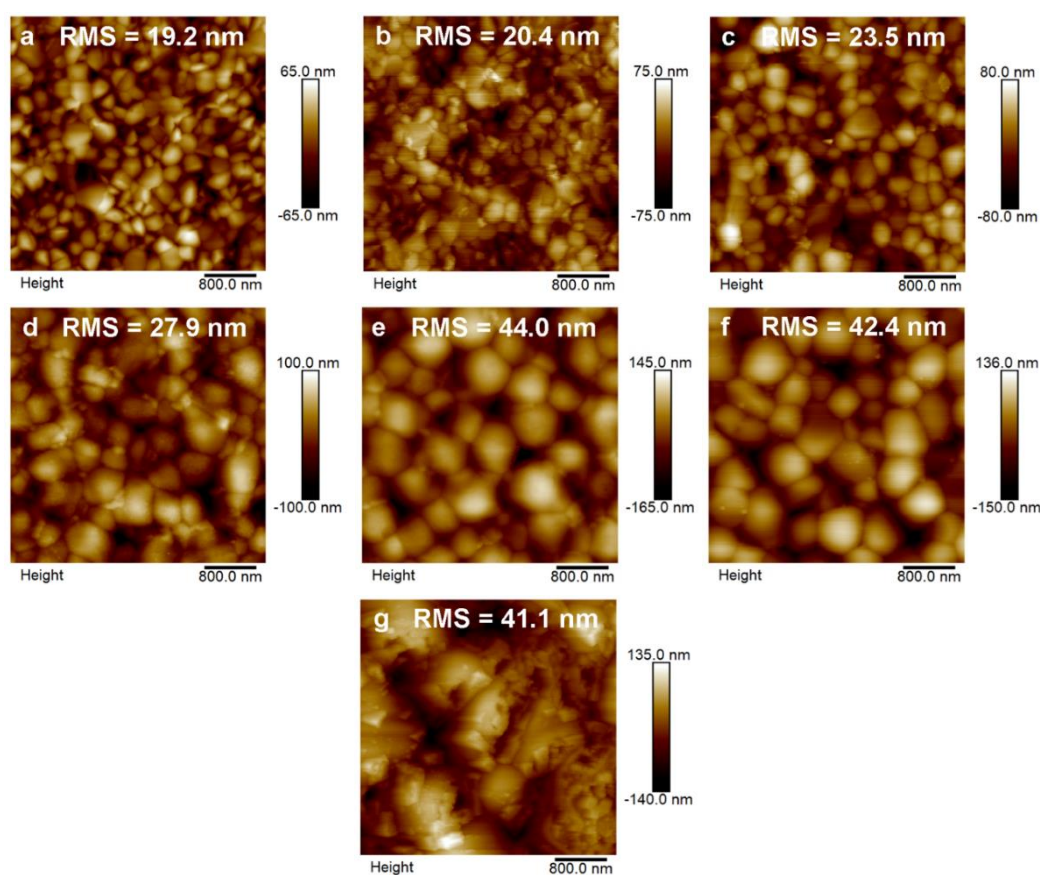


Figure 3.7 AFM height images of annealed $\text{FA}_{0.66}\text{MA}_{0.34}\text{Pb}_{1-x}\text{Sn}_x\text{I}_3$ perovskite films, where x is (a) 0, (b) 0.25, (c) 0.4, (d) 0.5, (e) 0.6, (f) 0.75 and (g) 1. Scale bars are 800 nm.

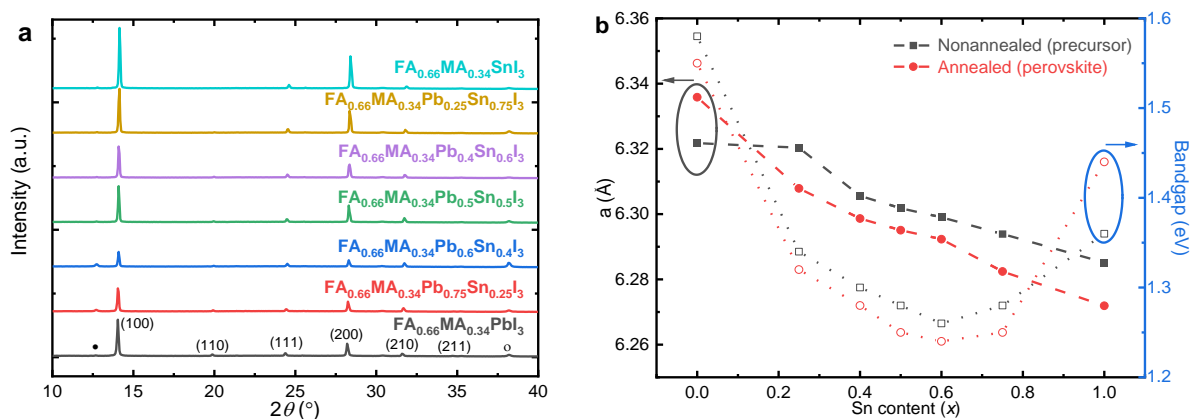


Figure 3.8 (a) XRD patterns of annealed $\text{FA}_{0.66}\text{MA}_{0.34}\text{Pb}_{1-x}\text{Sn}_x\text{I}_3$ ($x = 0$ to 1) perovskite films with different Pb/Sn ratios, which are indexed to the cubic space group $Pm\bar{3}m$. (b) Cubic lattice constant a and optical bandgaps of the non-annealed (black cubes) and annealed (red dots) perovskite films with different Sn contents (x), respectively. The lattice constant of the pure-Pb ($x = 0$) precursor film does not fit in the monotonic decreasing trend. This can be attributed to the formation of the δ perovskite phase, which complexes the XRD patterns and hampers the extraction of a reliable lattice parameter.⁴²

XRD patterns confirm the formation of single-phase Pb–Sn hybrid perovskite crystallites in sequentially deposited $\text{FA}_{0.66}\text{MA}_{0.34}\text{Pb}_{1-x}\text{Sn}_x\text{I}_3$ systems (Figure 3.8a). Following crystallographic data reported by Kanatzidis and co-workers,⁴³ we indexed all Pb–Sn hybrid perovskites to the cubic space group $Pm\bar{3}m$ and determined the corresponding lattice parameters (Figure 3.8b). When replacing Pb^{2+} with smaller Sn^{2+} (x from 0 to 1),⁴⁴ the (100)/(200) diffraction peaks gradually shift toward higher angles, corresponding to a monotonic decrease of the cubic lattice constant from 6.34 to 6.27 Å. Interestingly, a similar trend can also be found in the non-annealed precursor films, of which the lattice constant decreases linearly with the increasing Sn content. Our observation indicates that despite the very different crystallization behavior of the Pb- and Sn-based perovskite precursors, uniform Pb–Sn hybrid perovskite phases can be formed before thermal annealing. This can be attributed to the amorphous intermediate film used in the sequential deposition process. During the FAI/MAI solution dripping, the intermixed $\text{PbI}_2(1-x)$ and $\text{SnI}_2(x)$ phases enable a simultaneous and yet homogeneous transformation to the Pb–Sn hybrid perovskite crystallites. In optical absorption spectra, the characteristic bandgap bowing¹⁷ is seen for both non-annealed and annealed Pb–Sn perovskite (Figure 3.8b). This result also indicates that homogeneous crystallization has occurred. The narrowest bandgap of ~ 1.23 eV is obtained between 50% and 75% Sn contents, whereas the pure Pb- and Sn-compounds show bandgaps of 1.55 and 1.44 eV, respectively.

Understanding the Film Formation Kinetics of Sequential Deposited Narrow-Bandgap Pb–Sn Hybrid Perovskite Films

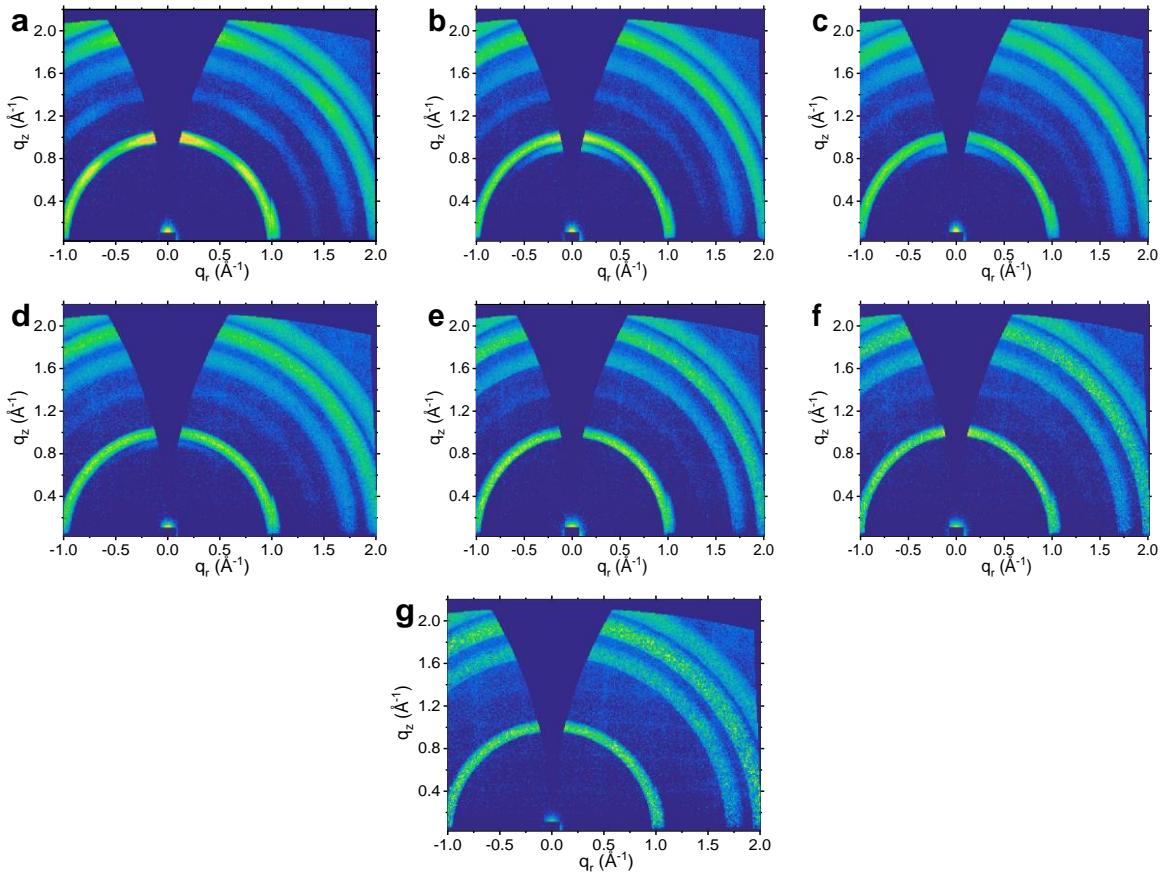


Figure 3.9 2D GIWAX patterns from annealed $\text{FA}_{0.66}\text{MA}_{0.34}\text{Pb}_{1-x}\text{Sn}_x\text{I}_3$ perovskite films, where x is (a) 0, (b) 0.25, (c) 0.4, (d) 0.5, (e) 0.6, (f) 0.75, and (g) 1.

It has been reported that the perovskite crystal orientation depends on the microstructure of the as-deposited precursor film.^{44,45} Figure 3.9 shows the grazing-incidence wide-angle X-ray scattering (GIWAXS) patterns of different Pb–Sn hybrid perovskite films. All Sn-containing perovskite films ($x \geq 0.25$) exhibit isotropic diffraction rings for the various lattice spacings, suggesting no preferred orientation of the Pb–Sn hybrid perovskite crystals.⁴⁶ This is attributed to the predominant growth of randomly oriented crystals in the precursor film (Figure 3.4), which suppresses re-orientation during thermal annealing. In Figure 3.9b-d, the scattering feature at $q = 0.91 \text{ \AA}^{-1}$ ($2\theta = 12.7^\circ$) corresponds to the PbI_2 phase, which originates from degradation during sample transfer in ambient air to the X-ray system. In comparison, a varying reflection intensity and more distinct Bragg spots along the diffraction ring of the (100) plane ($q = 1 \text{ \AA}^{-1}$) are observed for the Pb-only perovskite film ($x = 0$), indicating a slightly higher degree of texture (Figure 3.9a).⁴⁷ It is anticipated that during the thermal annealing, the pure Pb-based nuclei have more freedom to grow along the preferred directions.

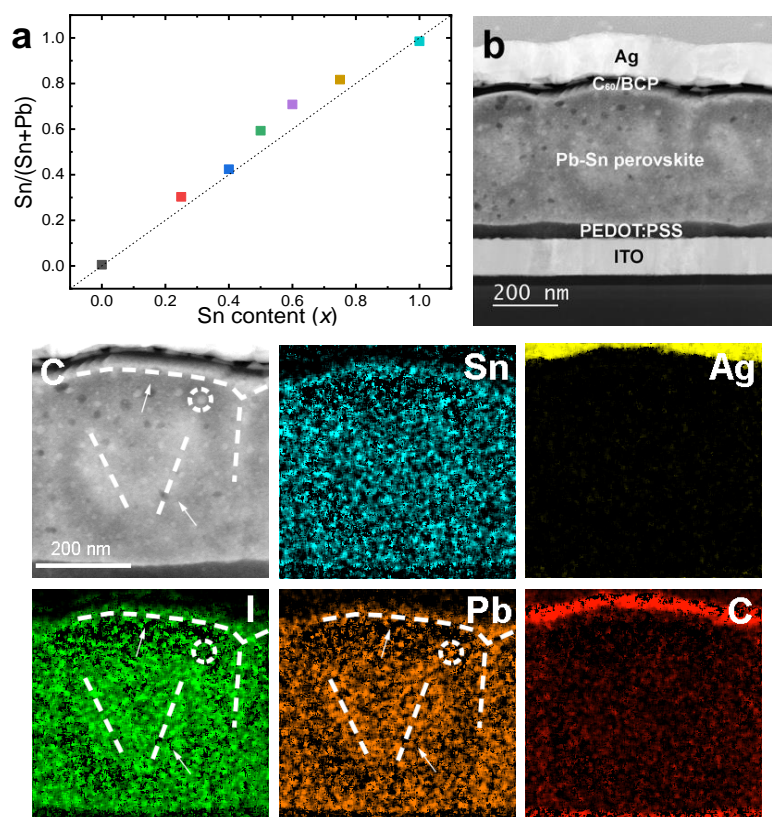


Figure 3.10 (a) The atomic ratio $\text{Sn}/(\text{Sn} + \text{Pb})$ measured by XPS versus the nominal composition used in the precursor solutions. The atomic ratio varies from 0 to 1. (b) HAADF cross-sectional STEM image. (c) Corresponding EDS elemental maps of a PSC based on the ITO/PEDOT:PSS/ $\text{FA}_{0.66}\text{MA}_{0.34}\text{Pb}_{0.5}\text{Sn}_{0.5}\text{I}_3/\text{C}_{60}/\text{BCP}/\text{Ag}$ structure. To reduce the background X-ray artifacts, quantitative EDS mapping was performed by binning 5×5 pixels for each pixel to be quantified (see details in the Experimental Section, Supporting Information). Circles and dashed lines are drawn in the TEM image, and Pb/I elemental maps highlight the formation of PbI_2 -rich domains due to sample degradation.

Improving the homogeneity of the perovskite film is of critical importance to the electrical properties such as defect density and carrier lifetime.^{24,48} To investigate the phase distribution of Pb–Sn hybrid perovskite films using a sequential deposition method, we carried out a detailed microstructure analysis. First, surface X-ray photoelectron spectroscopy (XPS) reveals that the Sn/Pb atomic ratio matches the composition used in precursor solutions. A monotonic increase in the Sn atomic concentration can be found as x increases (Figure 3.10). It is noted that even when the XPS samples were prepared and transferred in a N_2 atmosphere, a small trace of oxygen (O 1s) can be found in all Pb–Sn hybrid perovskite films (Figure 3.11). Deconvolution of the Sn 3d peaks suggests that the formation of Sn^{4+} species is largely uncontrolled (5–10 at%) among different Pb/Sn ratios, which confirms the ease of oxidation of Sn^{2+} in the Sn-containing perovskite films.⁸

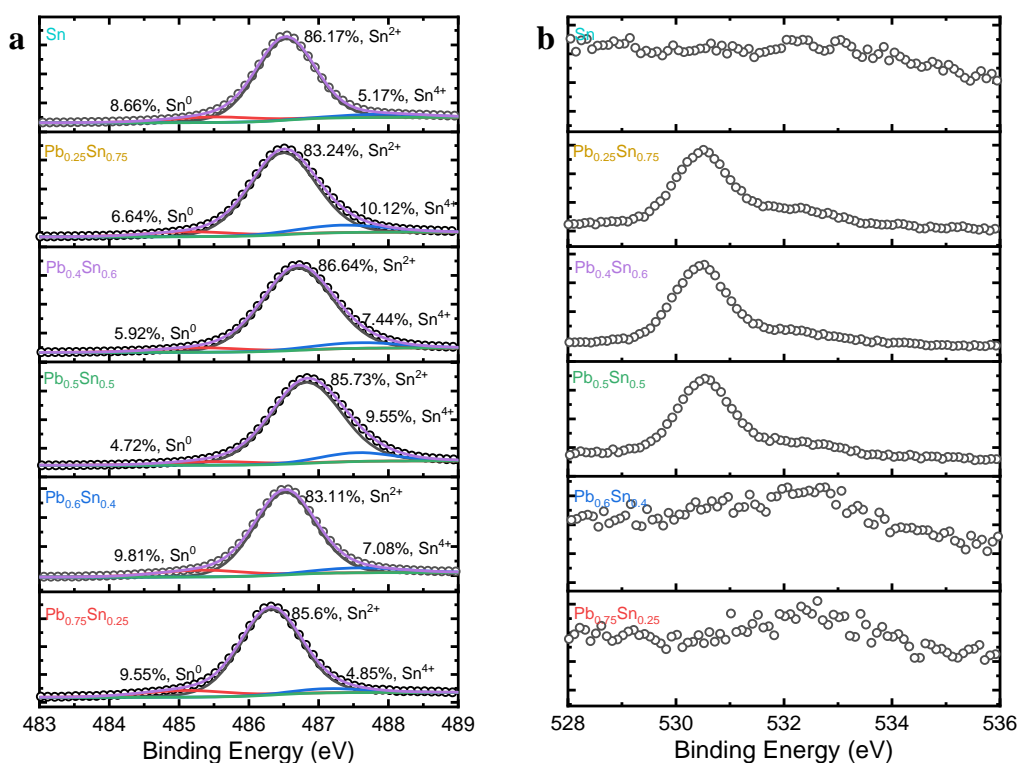


Figure 3.11 XPS spectra of the (a) Sn 3d and (b) O 1s core-levels of the annealed FA_{0.66}MA_{0.34}Pb_{1-x}Sn_xI₃ ($x = 0.25, 0.4, 0.5, 0.6, 0.75, 1$) perovskite films. The sample preparation and transfer were done in an inert atmosphere.

Furthermore, cross-sectional scanning transmission electron microscopy (STEM) and energy-dispersive X-ray spectroscopy (EDS) analysis were performed on a PSC based on FA_{0.66}MA_{0.34}Pb_{0.5}Sn_{0.5}I₃ absorber (the device performance will be discussed later). The high-angle annular dark-field (HAADF) STEM image (Figure 3.10b) shows well-defined interfaces between different layers over the cross-section region, and the perovskite film exhibits large grains that span the entire thickness of the active layer (~400 nm). The conformal and homogeneous hole- and electron-transport layers of poly(3,4-ethylenedioxythiophene):polystyrene sulfonate (PEDOT:PSS) and C₆₀/bathocuproine (BCP) prevent the perovskite film from making direct contact to the indium tin oxide (ITO) and Ag electrodes, respectively. In line with the TEM image, EDS elemental mappings acquired in the same region also confirm the integrity of the device stack. The Ag signal is confined to the top electrode region. The intense C signal located at both perovskite interfaces corresponds to the C₆₀/BCP (top) and PEDOT:PSS (bottom) layers, respectively. The relatively homogeneous distribution of Sn, Pb, I, and C suggests the high quality of the Pb–Sn perovskite film prepared by the sequential deposition method. It is noted that the formation of small PbI₂-rich domains

(displayed as brighter regions highlighted along with circles and defined lines in Figure 3.10c) is mainly due to sample degradation induced by prolonged air exposure.⁴⁹

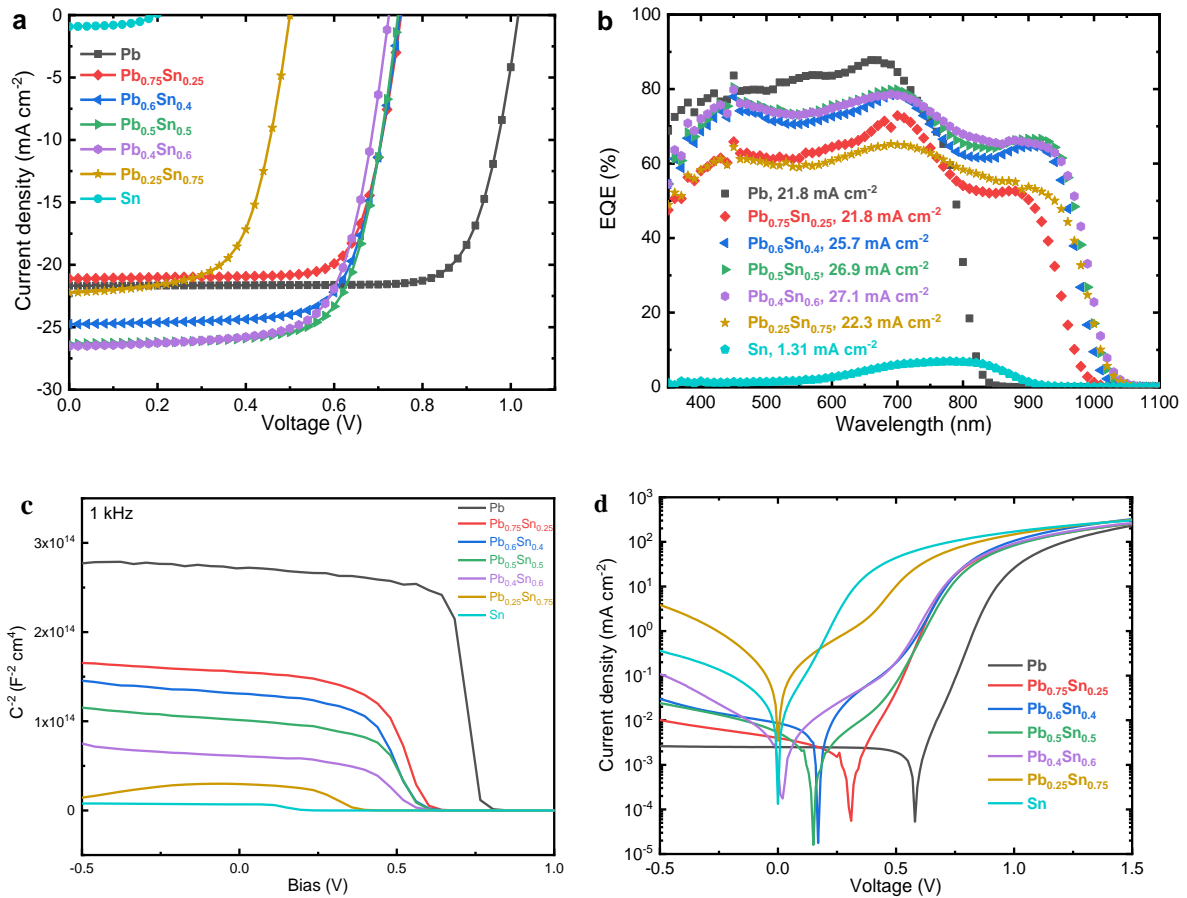


Figure 3.12 (a) Stabilized $J-V$ curves of the best-performing PSCs based on ITO/PTAA or PEDOT:PSS/FA_{0.66}MA_{0.34}Pb_{1-x}Sn_xI₃/C₆₀/BCP/Ag device structure, where $x = 0, 0.25, 0.4, 0.5, 0.6, 0.75$, and 1. (b) Corresponding EQE spectra. The inset lists the current densities obtained by integrating the EQE with the AM1.5G spectrum. (c) Mott-Schottky plots ($C^{-2}-V$) and (d) dark $J-V$ curves of the corresponding PSCs.

Table 3.1 Photovoltaic parameters of devices based on different FA_{0.66}MA_{0.34}Pb_{1-x}Sn_xI₃ perovskite components, measured under simulated AM 1.5G illumination (100 mW cm⁻²).

Sn content (x)	J_{sc}^a (mA cm ⁻²)	V_{oc}^a (V)	FF ^a	PCE ^a (%)	J_{sc}^b (mA cm ⁻²)	PCE ^c (%)
0	21.7	1.02	0.79	17.4	21.8	17.6
0.25	21.1	0.75	0.75	12.0	21.8	12.2
0.4	24.8	0.75	0.72	13.3	25.7	13.9
0.5	26.3	0.74	0.71	14.0	26.9	14.1
0.6	26.5	0.72	0.70	13.4	27.1	13.7
0.75	22.2	0.5	0.63	7.1	22.3	7.0
1	0.9	0.19	0.52	0.1	1.31	0.1

^a The data was extracted from the stabilized J – V scans under simulated AM 1.5G illumination (100 mW cm^{-2}). ^b Calculated by integrating the EQE spectrum with the AM1.5G spectrum. ^c Corrected PCE obtained by using the J_{sc} obtained from the EQE spectrum.

3.4 Performance of Pb–Sn perovskite solar cells

To evaluate the PV performance of sequential processed Pb–Sn hybrid perovskites, we fabricated planar p – i – n PSCs using an ITO/hole transport layer (HTL)/FA_{0.66}MA_{0.34}Pb_{1– x} Sn _{x} I₃/C₆₀/BCP/Ag device structure. For the Pb-only device, poly[bis(4-phenyl)(2,4,6-trimethylphenyl)amine (PTAA) was used as the HTL, whereas PEDOT:PSS was used for Sn-containing solar cells ($x \geq 0.25$). Figure 3.12a displays the stabilized current density–voltage (J – V) curves of PSCs with different Sn-content, and the corresponding photovoltaic parameters are summarized in Table 3.1. The external quantum efficiency (EQE) spectra were measured with ≈ 1 sun equivalent bias illumination to provide more accurate data for the short-circuit current density (J_{sc}) and PCE (Figure 3.12b). It is found that the pure Pb-based ($x = 0$) device exhibits a PCE of 17.6%, with a J_{sc} of 21.8 mA cm^{-2} , an open-circuit voltage (V_{oc}) of 1.02 V, and a fill factor (FF) of 0.79. As the Sn-content reaches 50% ($x = 0.5$), the J_{sc} gradually increases to 26.9 mA cm^{-2} , whereas V_{oc} and FF drop to 0.74 V and 0.71, respectively, resulting in the highest PCE (of 14.1%) among the Pb–Sn hybrid PSCs. The changes in J_{sc} and V_{oc} can be attributed to the narrowed bandgap after incorporation of Sn, as seen in the EQE onset that redshifts from 840 nm ($x = 0$) to 1040 nm ($x = 0.5$). The decrease in FF can result from the uncontrolled p-doping induced by Sn²⁺ oxidation to Sn⁴⁺ (Figure 3.11), which significantly reduces the charge carrier diffusion length of Sn-based perovskite films.^{8,48} While the PSC with 60% Sn still shows a PCE of 13.7%, the performance quickly deteriorates upon further increasing Sn-content ($x \geq 0.75$). It is expected that the rough Sn-rich perovskite films (Figure 3.7) introduce shunting pathways and thereby more recombination losses in the solar cells.

To estimate the background carrier density of Pb–Sn hybrid PSCs, we performed capacitance-voltage (C – V) measurements under dark conditions.^{50,51} According to Mott-Schottky plots (Figure 3.12c), pure Pb-based ($x = 0$) PSC exhibits a carrier density of $1.91 \times 10^{15} \text{ cm}^{-3}$, which slightly increases to $3.95 \times 10^{15} \text{ cm}^{-3}$ for 50% Sn-based PSC ($x = 0.5$), and quickly ramps up to $1.06 \times 10^{16} \text{ cm}^{-3}$ for pure Sn-based PSC ($x = 1$). The high background carrier density of Sn-rich PSCs is consistent with the high leakage current density extracted from dark J – V curves (Figure 3.12d). Based on the discussion above, it is concluded that the increased dark carrier density can be mainly attributed to shunts in Sn-rich PSCs, which deteriorates device performance.

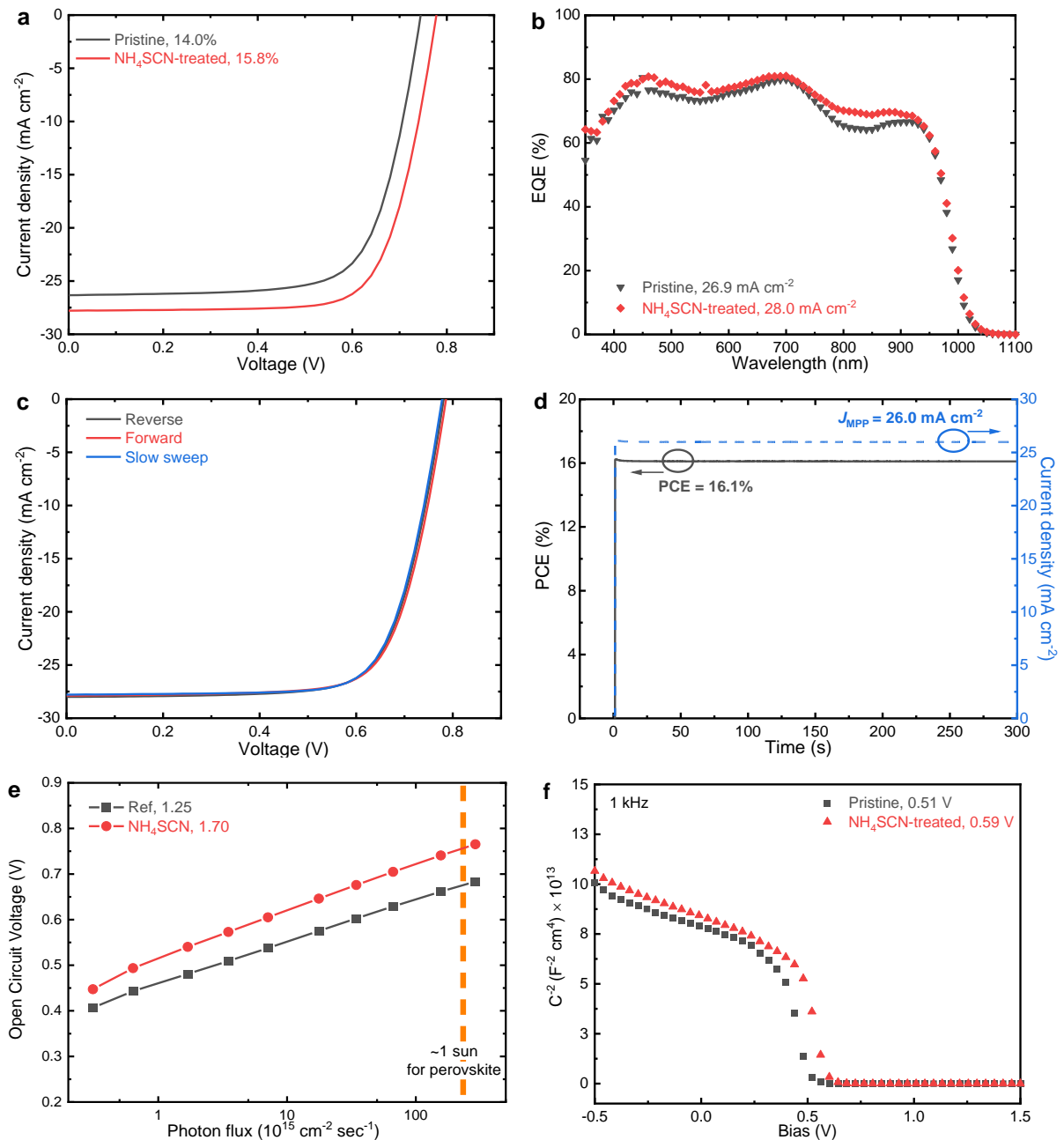


Figure 3.13 (a) Stabilized J - V curves, (b) EQE spectra with current densities obtained by integrating with the AM1.5G spectrum, (c) J - V curves for the device with NH_4SCN post-treatment. (d) Steady-state power/photocurrent output tracking for the device with NH_4SCN post-treatment. (e) Mott-Schottky plots (C^{-2} - V), and (f) light-intensity dependent V_{oc} of PSCs based on $\text{FA}_{0.66}\text{MA}_{0.34}\text{Pb}_{0.5}\text{Sn}_{0.5}\text{I}_3$ without (pristine) and with NH_4SCN (1 mg mL^{-1}) post-treatment.

To further improve the performance of $\text{Pb}_{0.5}\text{Sn}_{0.5}$ -based PSCs, a post-deposition treatment was introduced by spin coating an isopropanol-based ammonium thiocyanate (NH_4SCN) solution onto the perovskite film. Through optimization of processing conditions, the best performance is obtained when using a 1 mg mL^{-1} of NH_4SCN solution without additional thermal annealing. Compared to the pristine $\text{Pb}_{0.5}\text{Sn}_{0.5}$ -based PSCs, solar cells with

NH₄SCN treatment exhibits a much higher PCE of 15.9%, with a J_{sc} of 28.0 mA cm⁻², a V_{oc} of 0.78 V, and an FF of 0.73 (Figure 3.13a-b, Table 3.2). Meanwhile, almost identical J – V curves were measured in reverse, forward, and stabilized scans, indicating negligible hysteresis (Figure 3.13c). NH₄SCN-treated PSC shows a stabilized PCE of 16.1% after 300 s of steady-state power output tracking (measured at the maximum power point $V_{MPP} = 0.62$ V, Figure 3.13d), which is the highest PCE reported for sequentially solution-processed narrow bandgap PSCs with 50% Sn content. Device statistics (Figure 3.14) suggest that the PCE enhancement is mainly due to an increase in V_{oc} from 0.70 ± 0.02 V for the control device to 0.76 ± 0.02 V for the NH₄SCN-treated device. From the light-intensity dependent V_{oc} measurements (Figure 3.13e), it is found that the NH₄SCH-treated device exhibits consistently higher V_{oc} at various illumination intensities. The Mott-Schottky analysis shows an increase in built-in voltage from 0.51 to 0.59 V when the perovskite layer was treated by NH₄SCN solution (Figure 3.13f), which correlates to a more efficient charge transfer process at the perovskite/ETL interface.^{52,53}

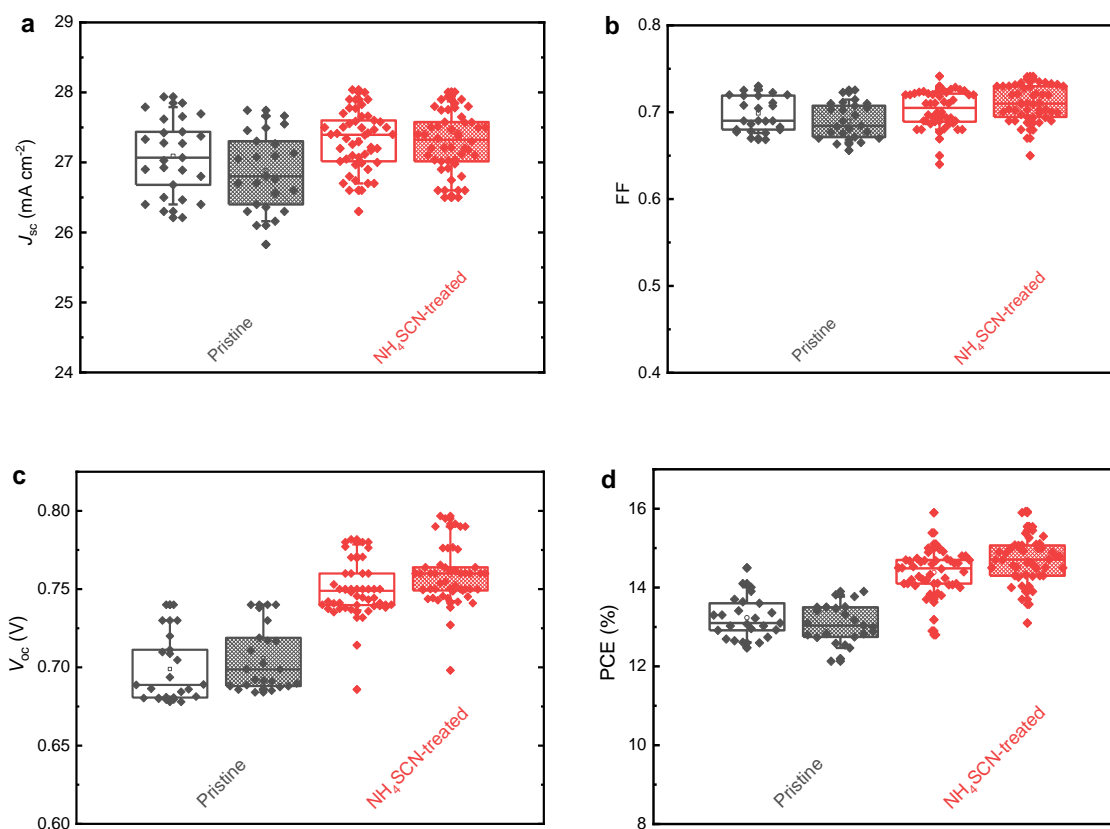


Figure 3.14 The statistical distribution of (a) J_{sc} and (b) FF, (c) V_{oc} , and (d) PCE for the PSCs without (Pristine) and with NH₄SCN treatment (1 mg mL⁻¹). The J – V measurements were done in the fast sweep, both in reverse (left) and forward (right) directions.

Table 3.2 Photovoltaic parameters of the devices with and without NH_4SCN post-treatment on the $\text{FA}_{0.66}\text{MA}_{0.34}\text{Pb}_{0.5}\text{Sn}_{0.5}\text{I}_3$ perovskite film, measured under simulated AM 1.5G illumination (100 mW cm^{-2}).

	J_{sc}^a (mA cm^{-2})	V_{oc}^a (V)	FF^a	PCE^a (%)	J_{sc}^b (mA cm^{-2})	PCE^c (%)
Without NH_4SCN	26.3	0.74	0.71	14.0	26.9	14.1
With NH_4SCN	27.8	0.78	0.73	15.8	28.0	15.9

^a The data was extracted from the stabilized J - V scans under simulated AM 1.5G illumination (100 mW cm^{-2}). ^b Calculated by integrating the EQE spectrum with the AM1.5G spectrum. ^c Corrected PCE obtained by using the J_{sc} obtained from the EQE spectrum.

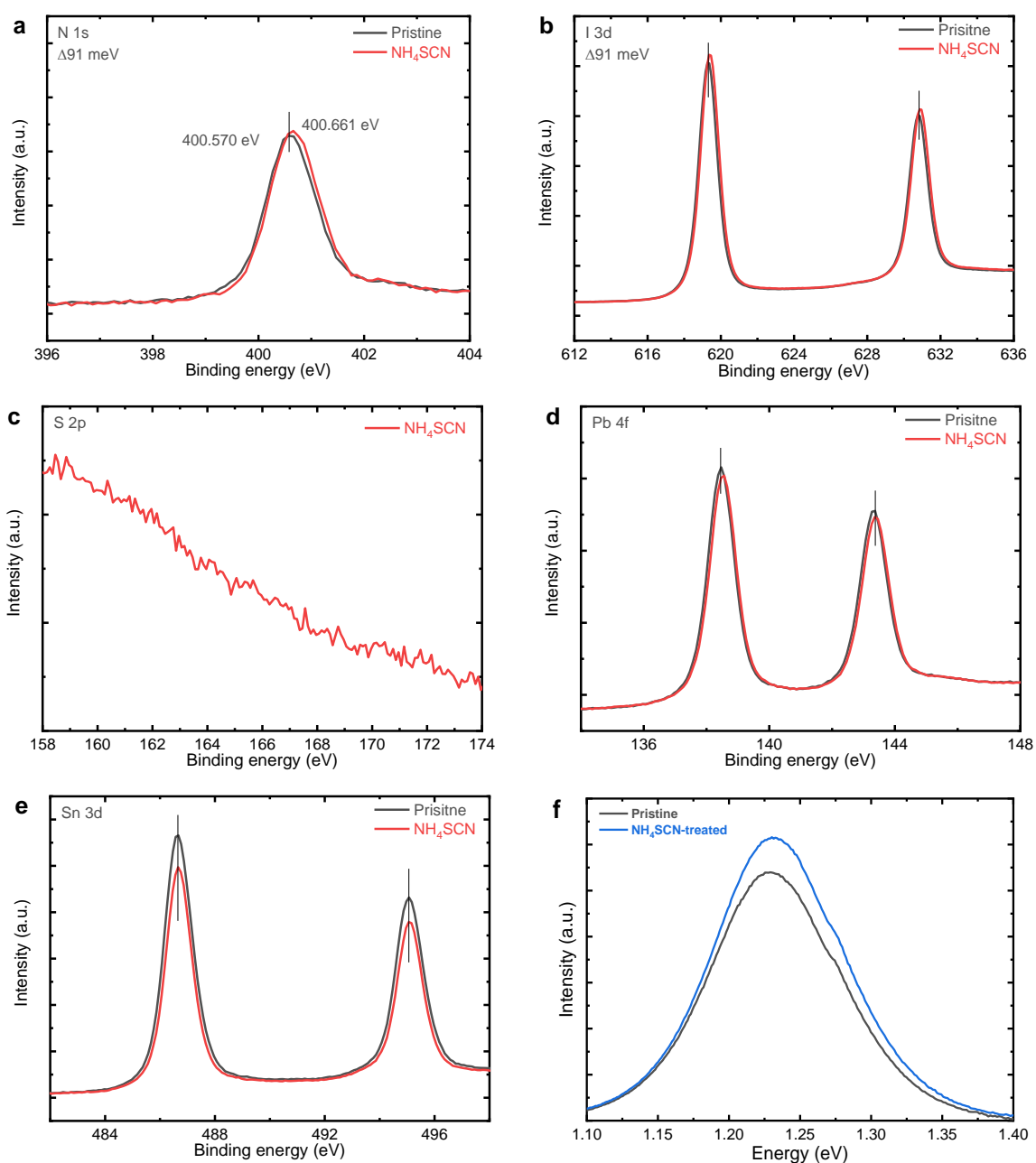


Figure 3.15 XPS spectra of the (a) N 1s, (b) I 3d, (c) S 2p, (d) Pb 4f, and (e) Sn 3d core-levels of the pristine and NH_4SCN -treated perovskite films. All the XPS spectra were calibrated using 284.8 eV of

C 1s. (f) Steady-state PL spectra of pristine and NH₄SCN-treated perovskite films deposited on a glass substrate.

It is noted that the improved device performance is not caused by changes in morphology and crystallinity, as both films display similar surface morphology and XRD patterns. To study the effect of NH₄SCN treatment on the surface composition of Pb_{0.5}Sn_{0.5}-based perovskite films, we performed XPS measurements. Compared to pristine perovskite films, the NH₄SCN-treated perovskite exhibits negligible changes in the spectral shape, and no signal from the S 2p peak can be detected (Figure 3.15). This can be attributed to the use of a dilute NH₄SCN solution and the volatile nature of NH₄SCN. On the other hand, it is noted that the peak intensities of both I 3d and N 1s core levels are slightly increased, together with a shift of 91 meV towards higher peak binding energies. The small, the positive shift in I 3d and N 1s binding energies can possibly indicate hydrogen bond formation between NH₄⁺ and [PbI₆]⁴⁻/[SnI₆]⁴⁻ moieties.^{54,55} The NH₄SCN treatment also results in an increase of the I/(Pb + Sn) atomic ratio from 1.97:1 for the pristine perovskite to 2.30:1 for the NH₄SCN-treated perovskite films. Besides, the NH₄SCN-treated perovskite film exhibits higher photoluminescence (PL) intensity than the pristine perovskite (Figure 3.15f), indicating a reduced non-radiative recombination process. Although the exact reason why NH₄SCN treatment improves the performance is not entirely clear, it is expected that the number of defect sites at the perovskite surface is reduced after NH₄SCN treatment, reducing non-radiative recombination losses at the surface and thereby providing a higher V_{oc} in the Pb–Sn hybrid PSCs.

We proceeded to monitor the shelf life of a laminated narrow bandgap PSC under ambient conditions (25 °C, 20-30 RH%). As shown in Figure 3.16a, the device exhibited an almost negligible decrease in the PCE (~14.9%) over the tracking period, suggesting good stability of such narrow bandgap perovskite materials when air ingression is significantly reduced. We then fabricated a 4-terminal all-perovskite tandem solar cell by mechanically stacking a narrow bandgap back cell (1.23 eV) with a semitransparent front cell based on a 1.57 eV FA_{0.66}MA_{0.34}PbI_{2.85}Br_{0.15} perovskite (Figure 3.16b-c). Here, the front cell utilizes a device structure of glass/ITO/PTAA/Perovskite/PCBM/Al-doped ZnO/ITO, where MgF₂ was deposited both on the glass side and the top ITO side to minimize the optical loss in the back cell. The semitransparent front cell shows a PCE of 16.0%, with a J_{sc} of 19.8 mA cm⁻², V_{oc} of 1.02 V, and FF of 0.79. Meanwhile, the filtered narrow bandgap cell exhibits a PCE of 5.1%, with a J_{sc} of 9.3 mA cm⁻², V_{oc} of 0.72 V, and FF of 0.76 (Table 3.3). Compared to the stand-alone narrow bandgap cell, the EQE of the filtered cell shows a small decrease between 800

and 1000 nm, confirming high transparency of the front cell in the near-infrared. As a result, a high PCE of 21.1% in the 4-terminal tandem cell is achieved.

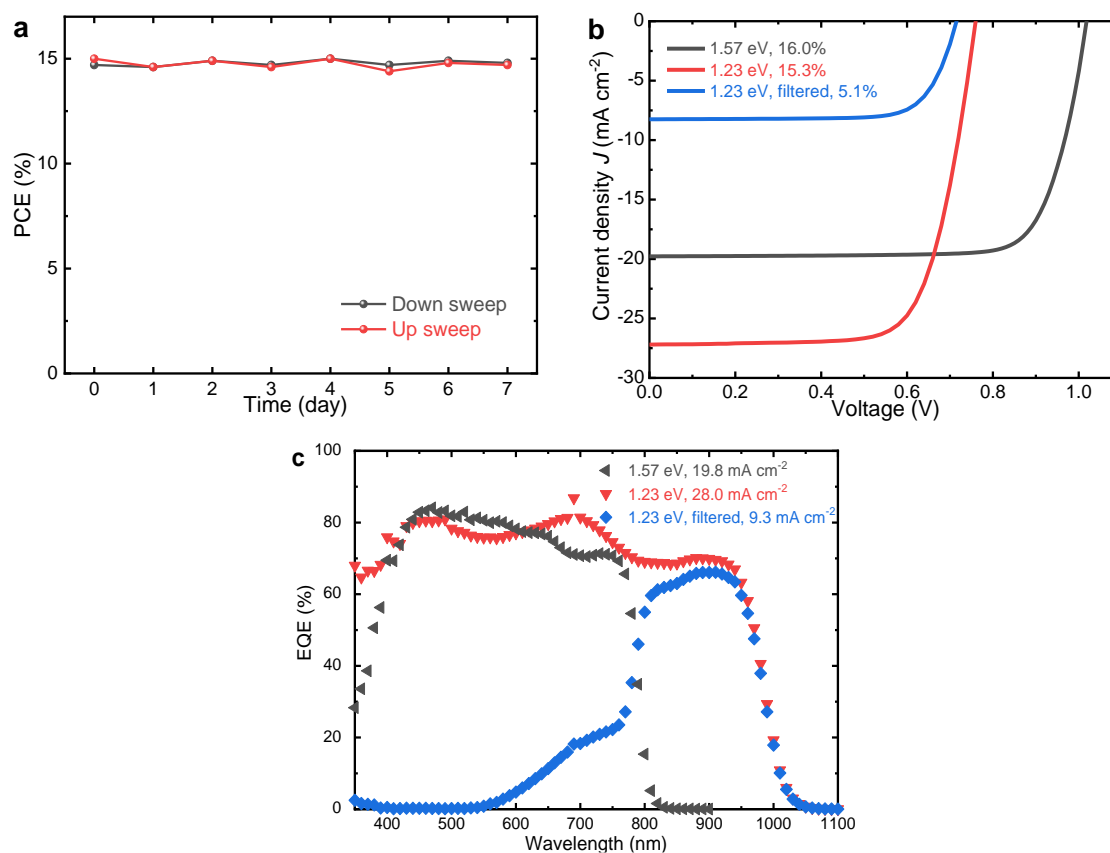


Figure 3.16 (a) PCE of a laminated narrow bandgap solar cell based on a glass/ITO/PEDOT:PSS/FA_{0.66}MA_{0.34}Pb_{0.5}Sn_{0.5}I₃/C₆₀/BCP/Cu device structure. The device was stored under ambient conditions (25 °C, 20-30 RH%). (b) J - V curves, and (c) the corresponding EQE spectra of a semitransparent front cell with 1.53 eV bandgap perovskite, a 1.23 eV bandgap perovskite stand-alone cell, and a 1.23 eV bandgap perovskite cell measured by using the 1.53 eV cell as an optical filter.

Table 3.3. Photovoltaic parameters of a 1.57 eV front cell, a 1.23 eV back cell before and after filtering by the front cell. The J - V curves were measured under simulated AM 1.5G illumination (100 mW cm⁻²).

	J_{sc}^a (mA cm ⁻²)	V_{oc}^a (V)	FF ^a	PCE ^a (%)	J_{sc}^b (mA cm ⁻²)	PCE ^c (%)
1.58 eV	19.8	1.02	0.79	16.0	19.8	16.0
1.23 eV	27.2	0.76	0.72	14.9	28.0	15.3
1.23 eV filtered	8.3	0.72	0.76	4.5	9.3	5.1

^a The data was extracted from the stabilized J - V scans under simulated AM 1.5G illumination (100 mW cm⁻²). ^b Calculated by integrating the EQE spectrum with the AM1.5G spectrum. ^c Corrected PCE obtained by using the J_{sc} obtained from the EQE spectrum.

3.5 Conclusions

In summary, we have investigated the film formation and performance of Pb–Sn hybrid perovskites ($\text{FA}_{0.66}\text{MA}_{0.34}\text{Pb}_{1-x}\text{Sn}_x\text{I}_3$, $0 \leq x \leq 1$) deposited via a simple sequential deposition method. In-situ absorption measurements, combined with ex-situ characterizations, reveal the dynamic transformation of different Pb–Sn precursors and the impact on perovskite films. While the crystallization to pure-Sn perovskite phase is completed during casting the solution, the formation of the pure-Pb based perovskite is considerably slow without thermal annealing. It is shown that despite the different crystallization behavior of Pb- and Sn-based perovskite precursors, the use of an amorphous $\text{PbI}_2/\text{SnI}_2$ precursor film in the sequential deposition ensures a uniform transformation to the Pb–Sn hybrid perovskite phase. Owing to the high affinity between the SnI_2 and organic halides, the crystal growth at room temperature is accelerated with increasing Sn contents, in line with the enlarged grain sizes from ~ 200 nm to over $1 \mu\text{m}$ for the pure-Pb and pure-Sn based perovskites, respectively. However, the fast crystal growth of the Sn-rich perovskite films ($x > 0.6$) also results in a higher surface roughness, which introduces large shunts and is hence detrimental to the device performance. Meanwhile, we demonstrate smooth and homogeneous narrow bandgap (1.23 eV) perovskite films with 50% Sn content. Additional treatment with NH_4SCN is found to efficiently passivate defect sites on the perovskite surface, which reduces non-radiative recombination and improves V_{oc} . The best performing device based on a 460 nm thick $\text{FA}_{0.66}\text{MA}_{0.34}\text{Pb}_{0.5}\text{Sn}_{0.5}\text{I}_3$ exhibits a PCE of 16.1%, with good stability under the ambient condition. Using this narrow bandgap cell, a 21.1% 4-terminal all-perovskite tandem solar cell is demonstrated.

Controlling the morphology of perovskite films is of critical importance for large-scale fabrication. Compared to its pure-Pb counterpart, the fast-crystallizing Sn-based perovskite imposes a greater processing challenge, for which the sequential deposition route with a broad processing window can be beneficial. This study provides new insights into the film formation kinetics of the Pb–Sn hybrid perovskite films and highlights the potential of exploring high-efficiency narrow bandgap Pb–Sn PSCs using the sequential deposition method.

3.6 Experimental Section

Materials and solution preparation: Unless stated otherwise, all the materials were purchased from commercial sources and used without purification. For the hole transport layer (HTL), PEDOT:PSS aqueous dispersion (PVP Al 4083) was purchased from Heraeus Clevis and filtered by a PVDF syringe filter ($0.45 \mu\text{m}$) before use. PTAA was dissolved in toluene at a concentration of 3 mg mL^{-1} and stirred overnight at $60 \text{ }^\circ\text{C}$. For the sequential solution-processed Pb-Sn hybrid perovskite

precursor solutions, a 1.2 mmol PbI_2 (Sigma-Aldrich, beads, 99.999% trace metal basis) and SnI_2 (Sigma-Aldrich, beads, 99.99% trace metals basis) mixture was dissolved in *N,N*-dimethylformamide (DMF, 0.876 mL) (Sigma-Aldrich, anhydrous 99.8%) and dimethyl sulfoxide (DMSO, 0.0864 mL) (Sigma-Aldrich, anhydrous 99.9%). In the solution mixture, the molar fraction of SnI_2 (x) was varied between 0, 0.25, 0.4, 0.5, 0.6, 0.75, and 1, and 10 mol% SnF_2 (Sigma-Aldrich, 99%) with respect to SnI_2 was added. The precursor solutions were stirred at 60 °C for 1 hour and filtered by a polytetrafluoroethylene (PTFE) syringe filter (0.22 μm) before use. Formamidinium iodide (53.48 mg) (FAI, Greatcell Solar) and methylammonium iodide (25.6 mg) (MAI, Greatcell Solar) mixture was dissolved in 1 mL of 2-propanol (Sigma-Aldrich, anhydrous 99.5%) at 60 °C. For the perovskite surface passivation, ammonium thiocyanate (NH_4SCN) (Sigma-Aldrich, ACS reagent, $\geq 97.5\%$) was dissolved in 2-propanol at a concentration of 1 mg mL^{-1} at room temperature. For the electron transport layers (ETLs), both C_{60} (SES Research, 99.95%) and bathocuproine (BCP) (Lumtec, 99%) were used as received.

Solar cell fabrication: Patterned glass/ITO (Naranjo Substrates) were cleaned by sonication in acetone, sodium dodecyl sulfate (Acros, 99%) soapy water, deionized water, and 2-propanol, each step for 15 min. The ITO substrate was then treated under UV-ozone for 30 min before use. For the Sn-containing solar cells ($x \geq 0.25$), PEDOT:PSS solution was spin coated on the ITO substrate at 3000 rpm for 60 s and dried at 140 °C for 15 min in the ambient atmosphere. For the Pb-only ($x = 0$) device, PTAA was spin coated at 5700 rpm for 30 s and annealed at 100 °C for 10 min in the N_2 glovebox. In the same glovebox, the perovskite film was deposited on the HTL using a sequential solution process, first the $(1-x)\text{PbI}_2 : x\text{SnI}_2$ mixture was spin coated at 3000 rpm (with a 2000 rpm s^{-1} acceleration) for 30 s, and dried at room temperature for 30 min. Afterward, the FAI/MAI solution was dynamically spin coated on the $(1-x)\text{PbI}_2 : x\text{SnI}_2$ film at 3000 rpm for 60 s. The substrate was then annealed at 100 °C for 30 min before cooling down. For the $\text{FA}_{0.66}\text{MA}_{0.34}\text{Pb}_{0.5}\text{Sn}_{0.5}\text{I}_3$ perovskite film with additional surface treatment, the NH_4SCN solution was dynamically spin coated on top at 5000 rpm for 30 s. Finally, the device was completed by evaporating C_{60} (20 nm), BCP (8 nm), and Ag (100 nm) layers under a high vacuum ($\sim 3 \times 10^{-7}$ mbar). For the ambient stability test a Cu (100 nm) electrode was used instead of Ag. The active area of the solar cell was determined by the overlap of the Ag and ITO contacts (0.09 or 0.16 cm^2).

For the 1.57 eV $\text{FA}_{0.66}\text{MA}_{0.34}\text{PbI}_{2.85}\text{Br}_{0.15}$ semitransparent front cell, both the bottom and the top ITO were deposited at room temperature by RF magnetron sputtering. The deposition was performed under a power of 56 W and a pressure of 2 mTorr (Ar with 0.6 mPa partial pressure of O_2). After UV-ozone cleaning for 30 min., PTAA was spin coated at 5700 rpm for 30 s and annealed at 100 °C for 10 min. in the N_2 glovebox. The $\text{FA}_{0.66}\text{MA}_{0.34}\text{PbI}_{2.85}\text{Br}_{0.15}$ was prepared by a sequential deposition protocol, where a PbI_2 (1.24 mol L^{-1} in 10.1:1 volume ratio of DMF and DMSO) was spin coated at 3000 rpm (with a 2000 rpm s^{-1} acceleration) for 30 s, followed by the spin coating of FAI/MAI/MABr (54.0 mg/14.3 mg/7.6 mg in 1 mL 2-propanol) solution at 3300 rpm for 30 s. The substrate was immediately

annealed at 100 °C for 30 min. Afterward, a PCBM (Solenne BV, 99%, 20 mg mL⁻¹ in 1:1 volume ratio of CB and CF) solution was spin coated at 1000 rpm (with a 20000 rpm s⁻¹ acceleration) for 60 s, and annealed at 100 °C for 30 min. Before the top ITO layer deposition, Al:ZnO nanoparticles (Avantama, 2.5 wt% in mixture of alcohols) were spin coated on top twice at 2000 rpm for 60 s, and dried at 75 °C for 5 min. Finally, MgF₂ layers were thermally evaporated on the glass and ITO surfaces to enhance the NIR transmission.

Solar cell characterization: The current density–voltage (J – V) characteristics were measured in the N₂ glovebox at room temperature. A tungsten-halogen lamp combined with a Schott GG385 UV filter and a Hoya LB120 daylight filter was used to simulate the 100 mW cm⁻² solar light. To better define the illuminated area, a black shadow mask with an aperture slightly smaller than the cell area (0.0676 or 0.1296 cm²) was used. In the fast and reverse (forward) J – V sweep, the Keithley 2400 source meter swept the voltage from +1.5 V (–0.5 V) to –0.5 V (1.5 V) at a scan rate of 0.25 V s⁻¹. For the stability test, the laminated narrow bandgap perovskite solar cell was kept in the dark under ambient conditions (25 °C, 20-30 RH%), and fast J – V measurements were performed in the N₂ glovebox. During the stabilized J – V scan, the solar cell was operated at V_{oc} for 5 min under light soaking, followed by a reverse voltage sweep from ($V_{oc} + 0.04$) V to –0.04 V with a step size of 0.02 V. At each voltage step, the current density was recorded for 5 s. From the stabilized J – V curve, the voltage at the maximum power point was extracted, which was then applied to the solar cell during the steady-state power output tracking. For EQE measurement, a modulated monochromatic probe-light (Philips focusline tungsten-halogen lamp, 50 W; monochromator from Oriel, Cornerstone 130) was used to illuminate the solar cell, which was fixed behind a circular aperture with 1 mm radius and sealed in a nitrogen-filled box with a quartz window. The spectral response was amplified from a pre-amplifier (Stanford Research, SR 570) and measured by a lock-in amplifier (Stanford Research, SR 830). Afterward, the result was converted to the EQE using a reference silicon cell. To mimic the one sun illumination condition used in the J – V measurements, the solar cell was illuminated under a high-power LED (530 nm or 940 nm, Thorlabs, driven by a DC4104 driver) during the EQE measurement.

The light intensity-dependent measurement was performed by using the same EQE setup, where a 730 nm LED was driven between 1-1000 mA, and the V_{oc} at different light intensity was measured with a Keithley 2400 source meter.

The capacitance–voltage (C – V) measurements were performed on solar cells using an electrochemical station (Solartron SI1260 impedance/gain-phase analyzer). The measurements were performed in the N₂ atmosphere under a dark condition. For the Mott-Schottky analysis, the capacitance was measured by sweeping the (DC) voltage from –0.5 V to 1.2 V with a step of 40 mV. The frequency was kept at 1 kHz with an AC perturbation voltage of 10 mV. The background carrier density N is calculated from the equation $C^{-2} = 2 \left(\frac{V_{bi} - V}{q\epsilon_r\epsilon_0 N} \right)$; where C is the capacitance, V_{bi} is the built-in potential, V is the applied bias, ϵ_r is the relative dielectric constant of the perovskite absorber, q is the elemental

charge, and ϵ_0 is the vacuum permittivity. The ϵ_r can be determined from the dark C - f measurement at a DC voltage of 0 V and AC perturbation voltage of 10 mV. In the 10 kHz to 100 kHz frequency range, assuming that the PSC is a geometric capacitor and the geometric capacitance $C_g = \frac{\epsilon_r \epsilon_0 A}{d}$, where A is the cell area, and d is the perovskite layer thickness, respectively.

Film characterization: XRD measurements were performed on a Bruker 2D phaser using Cu $K\alpha$ ($\lambda = 1.5405 \text{ \AA}$) radiation. The increment step size was 0.05° , and the measurements were performed between 10 - 40° . Grazing incidence wide angle X-ray scattering (GIWAXS) experiments were carried out on a GANESHA 300 XL+ system from JJ X-ray equipped with a Pilatus 300K detector (pixel size $172 \mu\text{m} \times 172 \mu\text{m}$). The X-ray source was a Genix 3D Microfocus sealed tube X-ray Cu-source with integrated monochromator and the wavelength used was $\lambda = 1.5408 \text{ \AA}$. SEM images were obtained by a FEI Quanta 3D FEG microscope, using a 5 kV electron beam and a secondary electron detector. To avoid degradation, all the non-annealed perovskite precursor films were stored in the N_2 -filled tube before quickly transferred to the measuring setup for analysis. AFM measurements were performed using a Veeco MultiMode microscope with Nanosensor PPP-NCHR-50 tips.

A Thermo Scientific K-Alpha was used to measure the surface XPS with a 180° double-focusing hemispherical analyzer and a 128-channel detector. Monochromatic Al $K\alpha$ (1486.6 eV) radiation was used with a spot size of $400 \mu\text{m}$. The measurements were performed under a dark condition, with a base pressure below 8×10^{-8} mbar. A survey spectrum (15 scans) was first measured with a pass energy of 200 eV, followed by a high-resolution scan (30 scans) of each element with a pass energy of 50 eV. To avoid oxidation, the samples were transferred directly from a N_2 glovebox to the XPS analysis chamber via an air-tight XPS sample holder.

A ~ 100 nm thick cross-section lamella was prepared by a focused ion beam (FIB) lift-out technique and transferred onto a molybdenum grid. Cross-sectional TEM imaging was performed by a probe-corrected JEOL ARM 200F microscope (200 kV), equipped with a 100 mm^2 silicon drift detector for EDS elemental mapping. Note that elemental maps based on raw counts (which includes both the peak and background intensity in the energy window) might not represent the real distribution of atoms in the region of interest. Elements with a high atomic number give large background X-ray counts (X-ray continuum), which can contribute to other elemental maps. In order to reduce such background artifacts, a quantification of the EDS mappings by binning 5×5 pixels for each pixel to be quantified without reducing spatial resolution.

Ex-situ UV-vis-NIR absorption spectra were measured by PerkinElmer Lambda 900 UV-vis-NIR spectrophotometer between 400 and 1100 nm. To avoid sample degradation, all the samples were stored in an air-tight box, with two glass windows fixed on both sides of the substrate.

In-situ UV-vis-NIR absorption measurements were performed using a previously reported method.³⁹ White paint was applied on the backside of the glass substrate, whereas the $(1-x)\text{PbI}_2: x\text{SnI}_2$ precursor film was deposited on the other side and dried in the N_2 glovebox. The substrate was then

Understanding the Film Formation Kinetics of Sequential Deposited Narrow-Bandgap Pb–Sn Hybrid Perovskite Films

placed on the spin coater, where it was illuminated by a focused light from the halogen lamp. A fiber optical cable was placed at an off-specular angle, which collected the light that was scattered by the white paint and transmitted through the whole layer stack. The optical fiber was connected to a spectrometer, which analyzed the raw photon counts before and after the perovskite layer formation (during the FAI-MAI dripping), and generated an absorption spectrum following the equation

$$A(\lambda) = -\log_{10}\left(\frac{I_m(\lambda) - I_{m,dark}(\lambda)}{I_{m,blank}(\lambda) - I_{m,dark}(\lambda)}\right)$$

Here I_m represents the wavelength-dependent counts; the dark and blank refer to a dark reference and blank reference on the same substrate before the spin coating was started, respectively. By monitoring the absorption spectrum in situ during the spin coating process ($t = 0$ s when the FAI-MAI was dripped onto the rotating substrate), the time-evolution of absorbance for the Pb-Sn hybrid perovskites can be obtained.

3.7 References

1. Dong, Q. et al. Electron-hole diffusion lengths $> 175 \mu\text{m}$ in solution-grown $\text{CH}_3\text{NH}_3\text{PbI}_3$ single crystals. *Science* **347**, 967-970 (2015).
2. Green, M. A., Ho-Baillie, A., Snaith, H. J. The emergence of perovskite solar cells. *Nat. Photonics* **8**, 506-514 (2014).
3. Correa-Baena, J.-P. et al. The rapid evolution of highly efficient perovskite solar cells. *Energy Environ. Sci.* **10**, 710-727 (2017).
4. NREL Best Research-Cell Efficiencies. <https://www.nrel.gov/pv/assets/pdfs/best-research-cell-efficiencies.20200128.pdf> (2020).
5. Tong, J. H. et al. Carrier lifetimes of $> 1 \mu\text{s}$ in Sn-Pb perovskites enable efficient all-perovskite tandem solar cells. *Science* **364**, 475-479 (2019).
6. Eperon, G. E. et al. Perovskite-perovskite tandem photovoltaics with optimized band gaps. *Science* **354**, 861-865 (2016).
7. Leijtens, T. et al. Tin-lead halide perovskites with improved thermal and air stability for efficient all-perovskite tandem solar cells. *Sustain. Energy Fuels* **2**, 2450-2459 (2018).
8. Lin, R. et al. Monolithic all-perovskite tandem solar cells with 24.8% efficiency exploiting comproportionation to suppress Sn(II) oxidation in precursor ink. *Nat. Energy* **4**, 864-873 (2019).
9. Chang, C.-Y., Tsai, B.-C., Hsiao, Y.-C., Lin, M.-Z., Meng, H.-F. Solution-processed conductive interconnecting layer for highly-efficient and long-term stable monolithic perovskite tandem solar cells. *Nano Energy* **55**, 354-367 (2019).
10. Rajagopal, A. et al. Highly Efficient Perovskite-Perovskite Tandem Solar Cells Reaching 80% of the Theoretical Limit in Photovoltage. *Adv. Mater.* **29**, 1702140 (2017).
11. Leijtens, T., Bush, K. A., Prasanna, R., McGehee, M. D. Opportunities and challenges for tandem solar cells using metal halide perovskite semiconductors. *Nat. Energy* **3**, 828-838 (2018).
12. Wang, C., Song, Z., Li, C., Zhao, D., Yan, Y. Low-Bandgap Mixed Tin-Lead Perovskites and Their Applications in All-Perovskite Tandem Solar Cells. *Adv. Funct. Mater.* **29**, 1808801 (2019).
13. Seok, S. I., Grätzel, M., Park, N. G. Methodologies toward Highly Efficient Perovskite Solar Cells. *Small* **14**, 1704177 (2018).
14. Saliba, M., Correa-Baena, J. P., Grätzel, M., Hagfeldt, A., Abate, A. Perovskite Solar Cells: From the Atomic Level to Film Quality and Device Performance. *Angew. Chem. Int. Ed.* **57**, 2554-2569 (2018).
15. McMeekin, D. P. et al. A mixed-cation lead mixed-halide perovskite absorber for tandem solar cells. *Science* **351**, 151-155 (2016).
16. Noh, J. H., Im, S. H., Heo, J. H., Mandal, T. N., Seok, S. I. Chemical management for colorful, efficient, and stable inorganic-organic hybrid nanostructured solar cells. *Nano Lett.* **13**, 1764-1769 (2013).
17. Goyal, A., McKechnie, S., Pashov, D., Tumas, W., van Schilfgaarde, M., Stevanović, V. Origin of Pronounced Nonlinear Band Gap Behavior in Lead-Tin Hybrid Perovskite Alloys. *Chem. Mater.* **30**, 3920-3928 (2018).
18. Parrott, E. S., Green, T., Milot, R. L., Johnston, M. B., Snaith, H. J., Herz, L. M. Interplay of Structural and Optoelectronic Properties in Formamidinium Mixed Tin-Lead Triiodide Perovskites. *Adv. Funct. Mater.* **28**, 1802803 (2018).
19. Hao, F., Stoumpos, C. C., Chang, R. P., Kanatzidis, M. G. Anomalous Band Gap Behavior in Mixed Sn and Pb Perovskites Enables Broadening of Absorption Spectrum in Solar Cells. *J. Am. Chem. Soc.* **136**, 8094-8099 (2014).
20. Yang, Z. et al. Stable Low-Bandgap Pb-Sn Binary Perovskites for Tandem Solar Cells. *Adv. Mater.* **28**, 8990-8997 (2016).
21. Eperon, G. E., Hörantner, M. T., Snaith, H. J. Metal halide perovskite tandem and multiple-junction photovoltaics. *Nat. Rev. Chem.* **1**, 0095 (2017).
22. Prasanna, R. et al. Band Gap Tuning via Lattice Contraction and Octahedral Tilting in Perovskite Materials for Photovoltaics. *J. Am. Chem. Soc.* **139**, 11117-11124 (2017).

23. Zhu, H. L. et al. Achieving High-Quality Sn–Pb Perovskite Films on Complementary Metal-Oxide-Semiconductor-Compatible Metal/Silicon Substrates for Efficient Imaging Array. *ACS Nano* **13**, 11800-11808 (2019).
24. Zhu, H. L., Xiao, J., Mao, J., Zhang, H., Zhao, Y., Choy, W. C. H. Controllable Crystallization of $\text{CH}_3\text{NH}_3\text{Sn}_{0.25}\text{Pb}_{0.75}\text{I}_3$ Perovskites for Hysteresis-Free Solar Cells with Efficiency Reaching 15.2%. *Adv. Funct. Mater.* **27**, 1605469 (2017).
25. Jiang, T. et al. Power Conversion Efficiency Enhancement of Low-Bandgap Mixed Pb–Sn Perovskite Solar Cells by Improved Interfacial Charge Transfer. *ACS Energy Lett.* **4**, 1784-1790 (2019).
26. Lian, X. et al. Highly Efficient Sn/Pb Binary Perovskite Solar Cell via Precursor Engineering: A Two-Step Fabrication Process. *Adv. Funct. Mater.* **29**, 1807024 (2019).
27. Zhu, H. L., Choy, W. C. H. Crystallization, Properties, and Challenges of Low-Bandgap Sn-Pb Binary Perovskites. *Sol. RRL* **2**, 1800146 (2018).
28. Ke, W., Stoumpos, C. C., Kanatzidis, M. G. "Unleaded" Perovskites: Status Quo and Future Prospects of Tin-Based Perovskite Solar Cells. *Adv. Mater.* **31**, 1803230 (2019).
29. Babayigit, A., D'Haen, J., Boyen, H.-G., Conings, B. Gas Quenching for Perovskite Thin Film Deposition. *Joule* **2**, 1205-1209 (2018).
30. Li, Z. et al. Scalable fabrication of perovskite solar cells. *Nat. Rev. Mater.* **3**, 18017 (2018).
31. Wang, J., Datta, K., Weijtens, C. H. L., Wienk, M. M., Janssen, R. A. J. Insights into Fullerene Passivation of SnO_2 Electron Transport Layers in Perovskite Solar Cells. *Adv. Funct. Mater.* **29**, 1905883 (2019).
32. Barrit, D. et al. Impact of the Solvation State of Lead Iodide on Its Two-Step Conversion to MAPbI_3 : An In Situ Investigation. *Adv. Funct. Mater.* **29**, 1807544 (2019).
33. Bing, J. et al. The Impact of a Dynamic Two-Step Solution Process on Film Formation of $\text{Cs}_{0.15}(\text{MA}_{0.7}\text{FA}_{0.3})_{0.85}\text{PbI}_3$ Perovskite and Solar Cell Performance. *Small* **15**, 1804858 (2019).
34. Liu, C., Li, W., Li, H., Zhang, C., Fan, J., Mai, Y. C_{60} additive-assisted crystallization in $\text{CH}_3\text{NH}_3\text{Pb}_{0.75}\text{Sn}_{0.25}\text{I}_3$ perovskite solar cells with high stability and efficiency. *Nanoscale* **9**, 13967-13975 (2017).
35. Wang, Y., Fu, W., Yan, J., Chen, J., Yang, W., Chen, H. Low-bandgap mixed tin–lead iodide perovskite with large grains for high performance solar cells. *J. Mater. Chem. A* **6**, 13090-13095 (2018).
36. Li, Y. et al. 50% Sn-Based Planar Perovskite Solar Cell with Power Conversion Efficiency up to 13.6%. *Adv. Energy Mater.* **6**, 1601353 (2016).
37. Liu, C., Fan, J., Li, H., Zhang, C., Mai, Y. Highly Efficient Perovskite Solar Cells with Substantial Reduction of Lead Content. *Sci. Rep.* **6**, 35705 (2016).
38. Zhu, L. et al. Solvent-molecule-mediated manipulation of crystalline grains for efficient planar binary lead and tin triiodide perovskite solar cells. *Nanoscale* **8**, 7621-7630 (2016).
39. van Franeker, J. J., Turbiez, M., Li, W., Wienk, M. M., Janssen, R. A. J. A real-time study of the benefits of co-solvents in polymer solar cell processing. *Nat. Commun.* **6**, 6229 (2015).
40. Zong, Y., Zhou, Z., Chen, M., Padture, N. P., Zhou, Y. Lewis-Adduct Mediated Grain-Boundary Functionalization for Efficient Ideal-Bandgap Perovskite Solar Cells with Superior Stability. *Adv. Energy Mater.* **8**, 1800997 (2018).
41. Tosado, G. A., Lin, Y.-Y., Zheng, E., Yu, Q. Impact of Cesium in the Phase and Device Stability of Triple Cation Pb–Sn Double Halide Perovskite Films and Solar Cells. *J. Mater. Chem. A* **6**, 17426-17436 (2018).
42. Ball, J. M. et al. Dual-Source Coevaporation of Low-Bandgap $\text{FA}_{1-x}\text{Cs}_x\text{Sn}_{1-y}\text{Pb}_y\text{I}_3$ Perovskites for Photovoltaics. *ACS Energy Lett.* **4**, 2748-2756 (2019).
43. Ke, W. et al. Ethylenediammonium-Based "Hollow" Pb/Sn Perovskites with Ideal Band Gap Yield Solar Cells with Higher Efficiency and Stability. *J. Am. Chem. Soc.* **141**, 8627-8637 (2019).
44. Zhao, B. et al. High Open-Circuit Voltages in Tin-Rich Low-Bandgap Perovskite-Based Planar Heterojunction Photovoltaics. *Adv. Mater.* **29**, 1604744 (2017).
45. Dang, H. X. et al. Multi-cation Synergy Suppresses Phase Segregation in Mixed-Halide Perovskites. *Joule* **3**, 1746-1764 (2019).

46. Hu, J. et al. Synthetic control over orientational degeneracy of spacer cations enhances solar cell efficiency in two-dimensional perovskites. *Nat. Commun.* **10**, 1276 (2019).
47. Meng, K. et al. In Situ Observation of Crystallization Dynamics and Grain Orientation in Sequential Deposition of Metal Halide Perovskites. *Adv. Funct. Mater.* **29**, 1902319 (2019).
48. Bowman, A. R. et al. Microsecond Carrier Lifetimes, Controlled p-Doping, and Enhanced Air Stability in Low-Bandgap Metal Halide Perovskites. *ACS Energy Lett.* **4**, 2301-2307 (2019).
49. Jeangros, Q. et al. In Situ TEM Analysis of Organic–Inorganic Metal-Halide Perovskite Solar Cells under Electrical Bias. *Nano Lett.* **16**, 7013-7018 (2016).
50. Shao, S. et al. Highly Reproducible Sn-Based Hybrid Perovskite Solar Cells with 9% Efficiency. *Adv. Energy Mater.* **8**, 1702019 (2018).
51. Roose, B., Friend, R. H. Extrinsic Electron Concentration in SnO₂ Electron Extracting Contact in Lead Halide Perovskite Solar Cells. *Adv. Mater. Interfaces* **6**, 1801788 (2019).
52. Xu, X. et al. Ascorbic acid as an effective antioxidant additive to enhance the efficiency and stability of Pb/Sn-based binary perovskite solar cells. *Nano Energy* **34**, 392-398 (2017).
53. Lee, J.-H. et al. Introducing paired electric dipole layers for efficient and reproducible perovskite solar cells. *Energy Environ. Sci.* **11**, 1742-1751 (2018).
54. Dai, X. et al. Scalable Fabrication of Efficient Perovskite Solar Modules on Flexible Glass Substrates. *Adv. Energy Mater.* **10**, 1903108 (2019).
55. Ruggeri, E. et al. Controlling the Growth Kinetics and Optoelectronic Properties of 2D/3D Lead-Tin Perovskite Heterojunctions. *Adv. Mater.* **31**, 1905247 (2019).

Chapter 4

Interconnecting layers for all-perovskite tandem solar cells*

Abstract

Perovskite semiconductors hold a unique promise in developing multijunction solar cells with high efficiency and low cost. Besides design constraints to reduce optical and electrical losses, the interconnecting layers (ICLs) of multijunction devices endure compatibility issues in depositing different perovskite layers on top of each other. In this study, we develop robust and low-resistivity ICLs based on a SnO₂ layer prepared by spatial atomic layer deposition. Through optimization of the interconnecting contacts, power conversion efficiencies (PCEs) of above 19% have been achieved for monolithic all-perovskite tandem solar cells with limited loss of potential energy and fill factor.

* This chapter is partially reproduced from: Wang, J., Zardetto, V., Datta, K., Zhang, D., Wienk, M.M., Janssen, R.A.J., *Nat. Commun.*, 2020, 11, 5254.

4.1 Introduction

Over the last decade, hybrid perovskites have been under the spotlight of the photovoltaic (PV) research community for their excellent optoelectronic characteristics, cost-effectiveness as well as solution processability.¹⁻³ The record power conversion efficiency (PCE) of single-junction perovskite solar cells (PSCs) has now increased to 25.2%, approaching the state-of-the-art inorganic PV cells of 29.1% and the Shockley-Queisser (S-Q) efficiency limit of around 33%.⁴⁻⁷ Further increase of efficiency of PSCs alongside high-throughput and low-cost manufacturing processes provides enormous potential for commercializing perovskite PV technologies.⁸

Fundamentally, the PCE of single-junction solar cells is limited by the thermalization loss of photons with energy higher than the bandgap and the transmission loss of photons with energy lower than the bandgap.^{8,9} By strategically stacking two or more light-absorbing layers with complementary bandgaps, monolithic multijunction solar cells can effectively mitigate these losses and raise the theoretical efficiency limit to 68%.^{10,11} In practice, III–V crystalline semiconductors have demonstrated high PCEs of 39.2% and 37.9% in a six- and triple-junction solar cells, respectively. However, their intricate and costly deposition processes prohibit large-scale applications.^{4,12,13} Alternative technologies such as inexpensive organic semiconductors have also been exploited for multijunction solar cells.⁹ Nevertheless, given the lack of comparably high-performing organic absorber layers over a wide range of bandgaps, suboptimal PCEs of 17.4% for tandem,¹⁴ 11.6% for a triple cell,¹⁵ and 7.6% for a quadruple-junction cell¹⁶ have been reported in such multijunction approach. Perovskite semiconductors, by virtue of their cost-effectiveness and widely tunable bandgaps,¹⁷ hold a unique promise for the development of all-perovskite multijunction solar cells. The bandgap of Pb-based perovskites can be continuously tuned from 1.5 eV to 2.3 eV by substituting I with Br,^{18,19} and bandgaps as narrow as 1.2 eV are obtained when mixing Pb- with Sn-based compounds.^{20,21} Device and optical modeling^{10,22,23} have suggested that a monolithic tandem cell with 1.8 eV wide-bandgap and 1.2 eV narrow-bandgap perovskite materials can reach a feasible PCE of 33.4%. Moreover, the monolithic all-perovskite triple-junction solar cell comprising 2.0 eV, 1.5 eV, and 1.2 eV absorbers leads to an even higher PCE of 36.6%.²² To date, tremendous research efforts have been made for all-perovskite tandem devices,²³⁻³⁰ with PCEs up to 24.8% achieved by Tan and co-workers.³¹ In comparison, all-perovskite triple-junction solar cells remain largely unexplored. A proof-of-concept 6.7% triple cell was first demonstrated by Snaith and co-

workers.³² Very recently, Tan et al. demonstrated all-perovskite triple-junction solar cells with efficiency exceeding 20%.³³

It is not trivial to fabricate monolithic all-perovskite multijunction solar cells, bearing in mind the optical and electrical losses inherent to the complex cell design and the processing and compatibility issues encountered in depositing widely different materials on top of each other.⁸ Between series-connected sub-cells, the interconnecting layers (ICLs) should serve as a physical barrier to protect the underlying layer from solvents used for the subsequent layers.²⁶ Also, reflective losses and parasitic absorption of the ICLs need to be minimized such that more low-energy photons can reach the next narrower-bandgap absorbing layers.¹⁰ Besides, the ICLs should possess a large sheet resistance while retaining sufficient mobility such that selected holes and electrons from the adjacent perovskite layers can recombine efficiently.^{26,27} For all-perovskite multijunction cells, examples of solution-processed ICLs are p-doped cross-linked poly[bis(4-phenyl)(2,4,6-trimethylphenyl)amine (PTAA)/n-doped phenyl-C₆₁-butyric acid methyl ester (PCBM)³⁴ and poly(3,4-ethylene dioxythiophene):polystyrene sulfonate (PEDOT:PSS)/indium tin oxide (ITO) nanoparticles.³² Alternatively, dry-transfer PEDOT:PSS,³⁵ chemical vapor deposited fluoride silane-incorporated polyethylenimine ethoxylated hybrid system,³⁶ and thermally evaporated *N*⁴,*N*⁴,*N*^{4''},*N*^{4''}-tetrakis([1,1'-biphenyl]-4-yl)-[1,1':4',1''-terphenyl]-4,4''-diamine (TaTm)³⁷ have been reported. In comparison, using sputtered ITO and indium zinc oxide (IZO) as the recombination layers has enabled higher efficiency in tandem devices,²⁵⁻²⁸ albeit the increased lateral shunt pathways and optical losses in the near-infrared region.²⁷ Moreover, a thin metal oxide layer such as SnO₂ and Al-doped ZnO (AZO) prepared by atomic layer deposition (ALD) was necessary to prevent sputter damage.^{24-26,28} It has been previously demonstrated that tuning the growth conditions can yield compact and conductive ALD layers, which alone prevent solvent damage and allow for fast charge transport after depositing a thin TCO layer.^{26,38,39} Tan et al. utilized TCO-free ICLs based on C₆₀/ALD-SnO₂/Au/PEDOT:PSS for all-perovskite tandem solar cells.³¹ More recently, Huang et al. demonstrated that ambipolar carrier transport could be achieved in the ALD SnO_{2-x} by changing the O:Sn ratio, thus preventing the use of a less-stable PEDOT:PSS layer.³⁰ Nevertheless, the conventional ALD technique requires a vacuum process and is limited by a low deposition rate. Atmospheric pressure spatial ALD (SALD) can be done at a higher deposition rate and therefore has a high-throughput.⁴⁰⁻⁴² Furthermore, to maximize the performance of multijunction solar cells, stringent bandgap and thickness optimizations are needed to balance light absorption and match current density among sub-cells.^{10,12}

In this chapter, we introduce a SALD-grown SnO_2 layer as the interconnecting contact for monolithic all-perovskite tandem solar cells. The SnO_2 layer is successful in protecting the underlying perovskite film from solvent damage and thermal stressing during a multijunction fabrication process while retaining excellent electronic properties for electron transport. A high potential and low-resistivity ICLs combination of $\text{C}_{60}/\text{SALD-SnO}_2/(\text{Au})/\text{PEDOT:PSS}$ is optimized. PCEs of above 19% are achieved in tandem solar cells comprising 1.73 eV and 1.23 eV perovskite absorber layers.

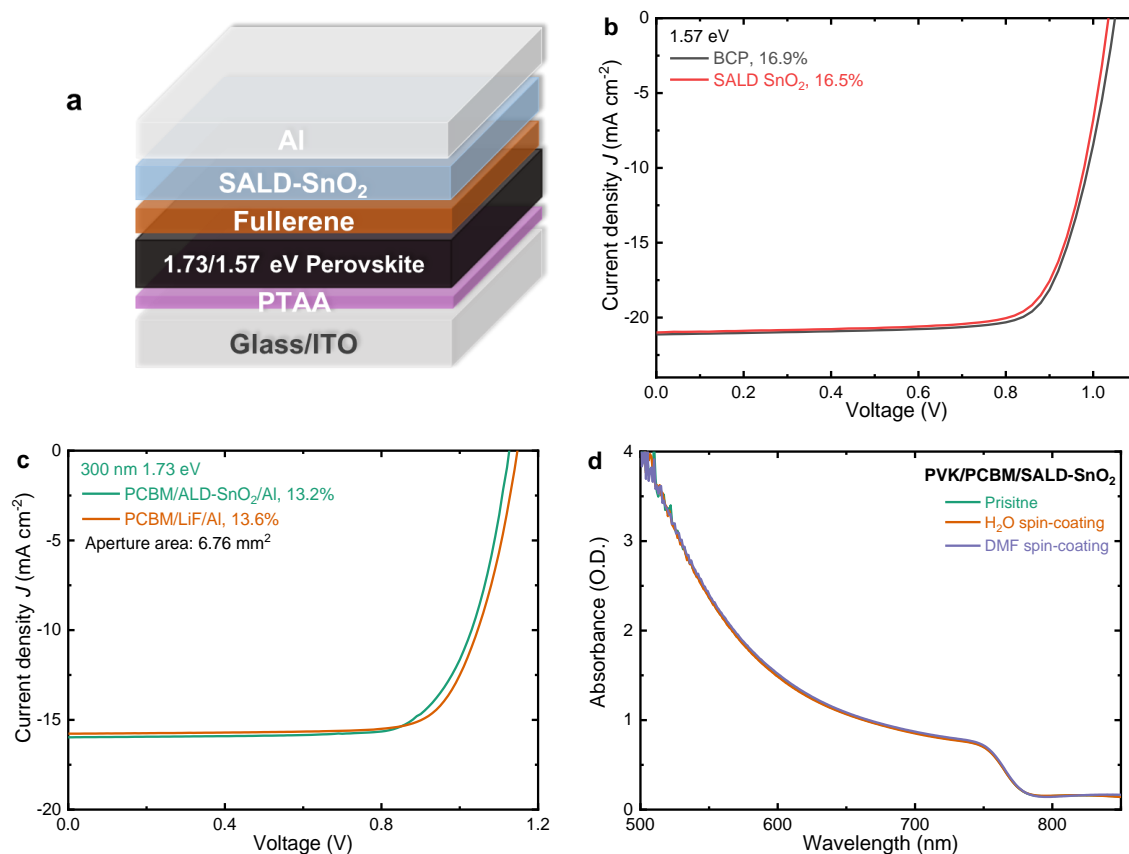


Figure 4.1 (a) Device structure of *p-i-n* solar cells based on 1.73 eV and 1.57 eV perovskite absorber layers. Current density–voltage (J – V) characteristics of (b) 300 nm-thick 1.73 eV cell and (c) 450 nm-thick 1.57 eV cell with/without SALD- SnO_2 layer inserted between the fullerene layer and the Al contact. (d) UV–vis–NIR absorption spectra of perovskite/PCBM/SALD- SnO_2 films after rising with H_2O or DMF.

4.2 SALD- SnO_2 for all-perovskite tandem solar cells

Here, spatial-ALD (SALD) grown SnO_2 was introduced as both an electron transport layer (ETL) and a solvent-barrier layer in the ICLs. We first fabricated single-junction perovskite devices (1.73/1.57 eV, see more discussions in Chapter 5) using a *p-i-n* structure (Figure 4.1a). As can be seen, comparable PCEs are obtained when inserting SALD- SnO_2

between the fullerene and Al electrode (Figure 4.1b-c), suggesting that the SALD-SnO₂ layer is suitable for electron transport. Due to its excellent barrier property,³⁸ the SALD-SnO₂ deposited on a fullerene layer can significantly reduce the permeation of H₂O and *N,N*-dimethylformamide (DMF) and prevent damage to the bottom perovskite film caused by a solution processing. The UV-vis-NIR spectra confirm that the SALD-SnO₂ covered perovskite film remains intact after rinsing with solvents that are used for the hole transport layer (H₂O) and subsequent perovskite layer (DMF), respectively (Figure 4.1d).

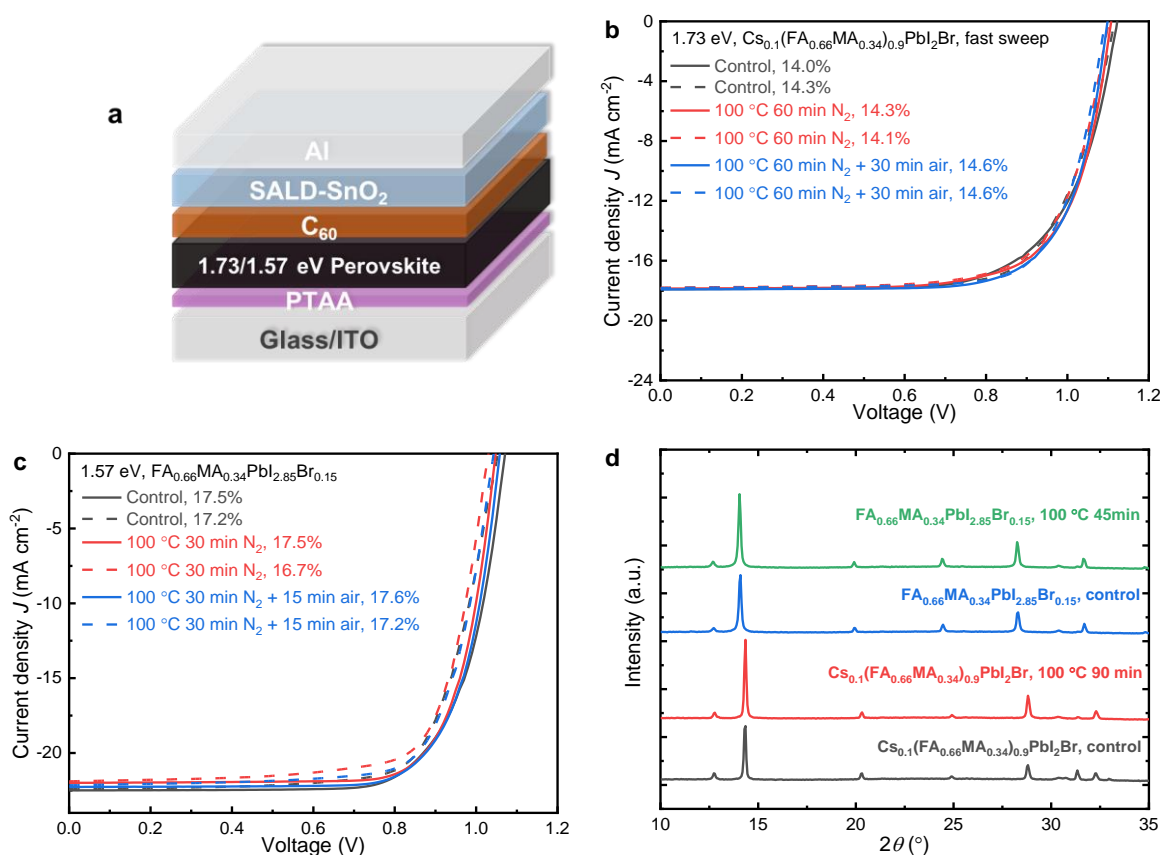


Figure 4.2 (a) Device structure of 1.73/1.57 eV-PSCs for the thermal stressing test. (b-c) The corresponding J - V characteristics of devices annealed in air and/or N₂ atmosphere before finished by depositing Al on top. The measurements were done in fast J - V sweeps in reverse (solid) and forward (dashed) directions. (d) XRD patterns of 1.73/1.57 eV PSCs with and without thermal stressing at 100 °C.

On the other hand, a compact SALD-SnO₂ improves the thermal stability of underlying perovskite layers by suppressing the outgassing of volatile decomposition products⁴³ during a multijunction fabrication process. To study the impact of thermal stressing on the performance of perovskite layers, we fabricated single-junction PSCs based on a device structure of ITO/PTAA/perovskite/C₆₀/SALD-SnO₂/Al (Figure 4.2a). After depositing the SALD-SnO₂, the samples were subjected to the same annealing procedures used for PEDOT:PSS (in the air) and

perovskite layers (in the N₂) during a multijunction cell fabrication (will be discussed later). For the 1.73 eV cell (Cs_{0.1}(FA_{0.66}MA_{0.34})_{0.9}PbI₂Br) (FA is formamidinium, MA is methylammonium), the substrates were annealed at 100 °C either for 60 min in N₂ or 15 min in air + 30 min in the N₂ + 15 min in air + 30 min in N₂; For the 1.57 eV cell (FA_{0.66}MA_{0.34}PbI_{2.85}Br_{0.15}), the substrates were annealed at 100 °C either for 30 min in N₂ or 15 min in air + 30 min in N₂. The devices were then finalized by evaporating Al contact on top. From the current density–voltage (*J–V*) characteristics, all the thermally treated 1.73 eV- and 1.57 eV-PSCs exhibited almost identical PV performance compared to their reference cells prepared in the same batch (Figure 4.2b-c). Furthermore, X-ray diffraction (XRD) measurements suggest that no distinct degradation (formation of PbI₂) was found after thermal stressing (Figure 4.2d). The result suggests that the followed (annealing) processes of multiple layers should not affect the performance of the bottom MA-containing perovskites.

4.3 Optimization for all-perovskite tandem solar cells

To enable the current matching condition in tandem solar cells as outlined above, we prepared semi-transparent PSCs with reduced thicknesses of 1.73 eV perovskite absorbers (Figure 4.3a). As expected, the EQE-integrated *J*_{sc} shows a decrease from 14.7 mA cm⁻² for a ~400 nm-thick perovskite film, to 13.6 and 8.9 mA cm⁻² for 300 and 100 nm-thick absorber layers, respectively (Figure 4.3c). Here, the drop in EQE mainly occurs in the wavelength range of 500 to 720 nm due to reduced light absorption. In comparison, the changes in *V*_{oc} and FF are relatively small for different layer thicknesses, which results from similar film quality, as evidenced by scanning electron microscopy (SEM) and XRD measurements (Figure 4.3d-h).

We proceeded to construct all-perovskite tandem solar cells using a 300 nm 1.73 eV wide bandgap front cell and a 450 nm 1.23 eV narrow bandgap back cell. In a preliminary test, a combination of PCBM (80 nm)/SALD-SnO₂/PEDOT:PSS (45 nm) layers was used as the ICL. The optimized thickness of SLAD-SnO₂ is 45 nm (Figure 4.4). The corresponding *J–V* curves show a PCE of 15.7% under reverse scan, with a *J*_{sc} of 13.2 mA cm⁻², a *V*_{oc} of 1.84 V, and a FF of 0.64. Here, the relatively low FF is caused by an s-kink near the open-circuit voltage, which suggests the formation of electronic barriers in the ICLs.^{27,38}

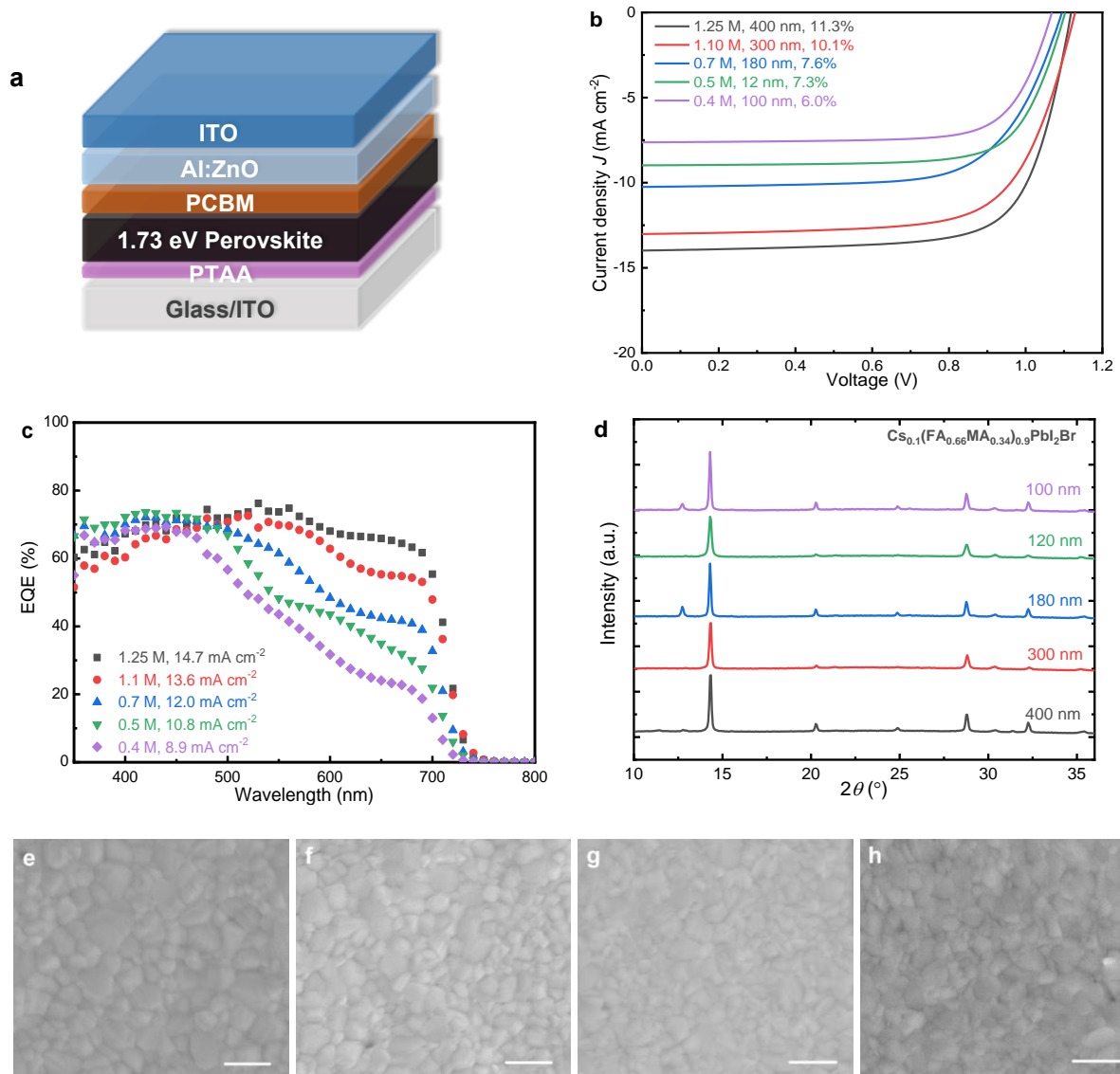


Figure 4.3 (a) Device structure of a semi-transparent 1.73 eV PSC. J - V characteristics (b) and EQE spectra (c) of the 1.73 eV PSCs with different perovskite layer thickness. (d) XRD patterns of 1.73 eV perovskite films. Top-view SEM images of perovskite films with (e) 400 nm, (f) 180 nm, (g) 120 nm, and (h) 100 nm layer thickness.

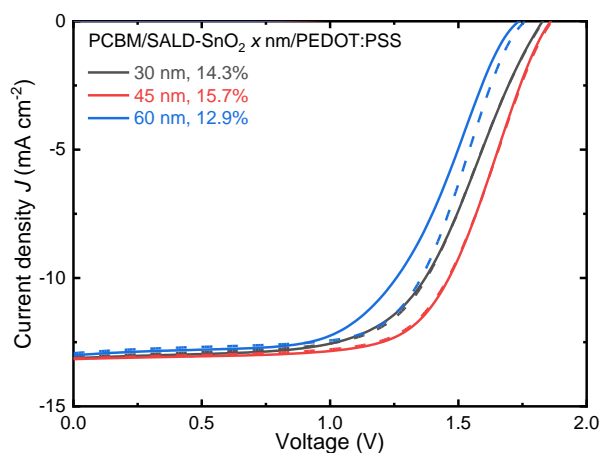


Figure 4.4 J - V characteristics of tandem cells with PCBM/SALD-SnO₂/PEDOT:PSS as the ICL, measured in reverse (solid line) and forward (dashed line) scans.

We then replaced the solution-processed PCBM (80 nm) layer with a thermally evaporated C₆₀ layer (20 nm), which shows comparable PCEs in single-junction p - i - n PSCs (Figure 4.5a). Huang et al. have recently demonstrated that additional thermal annealing processes for tandems drive iodine ions of the perovskite layer into the C₆₀ layer, which becomes heavily n-doped and forms an ohmic contact with the ALD-SnO_x.³⁰ Besides, a thin and yet compact C₆₀ layer has higher electron mobility than PCBM,⁴⁴ which can reduce charge accumulation in the ICLs. Compared to the tandem cell with PCBM, the device based on C₆₀/SALD-SnO₂/PEDOT:PSS produces a much higher FF of 0.77, an improved V_{oc} of 1.91 V, a J_{sc} of 13.1 mA cm⁻², achieving a PCE of 19.3% under reverse scan (Figure 4.5b and Table 4.1). In this case, the J_{sc} is slightly reduced due to a current-limiting 1.23 eV back sub-cell (13.1 mA cm⁻²), caused by the change in optical interference after replacing the PCBM by C₆₀ (Figure 4.5c-e). On the other hand, it has been reported that a low carrier density ALD-SnO₂ layer may form a non-ohmic contact at the interface.³⁸ In comparison, we do not observe a severe s-kink in the J - V curve, suggesting that our ICLs are more conductive and thus provide decent FF also without an additional layer.³⁸ Nevertheless, we found that the device performance can be further improved after inserting a thin Au layer (~1 nm) at the ALD-SnO₂/PEDOT:PSS interface, similar to a previous study.³¹ As shown in Figure 4.5b, the tandem device comprising C₆₀/SALD-SnO₂/Au/PEDOT:PSS as ICL exhibits an improved PCE of 19.7% under reverse scan, thanks to a higher FF of 0.82, together with a J_{sc} of 12.7 mA cm⁻², and a V_{oc} of 1.91 V. Nevertheless, the extra Au layer (~1 nm) reduces transmission in the near-infrared, which further reduces the J_{sc} in the 1.23 eV back sub-cell (Figure 4.5f and Figure 4.6).

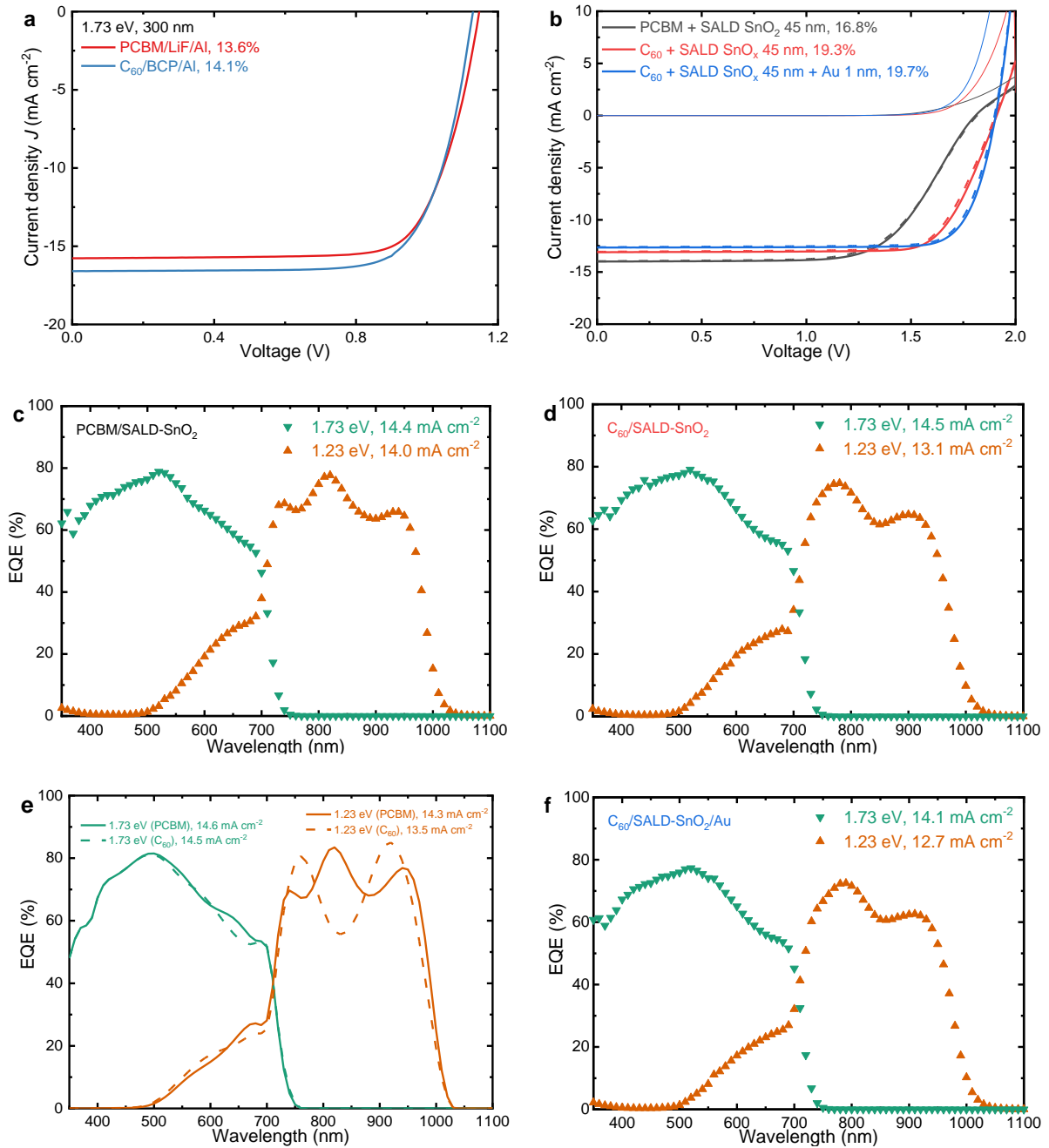


Figure 4.5 J - V characteristics of (a) 1.73 eV wide bandgap using PCBM or C₆₀ as the ETL, and (b) tandem cells with different ICLs. EQE spectra of tandem devices with (c) PCBM/SALD-SnO₂/PEDOT:PSS, (d) C₆₀/SALD-SnO₂/PEDOT:PSS, and (f) C₆₀/SALD-SnO₂/Au/PEDOT:PSS as the ICLs. The J_{sc} was obtained by integrating with the AM1.5G spectrum. (e) Simulated EQE of tandems based on 1.73 eV and 1.23 eV absorber layers. The solid lines and dashed lines represent the EQE spectra of 1.73 eV and 1.23 eV sub-cells using PCBM and C₆₀ in the interconnecting layers, respectively.

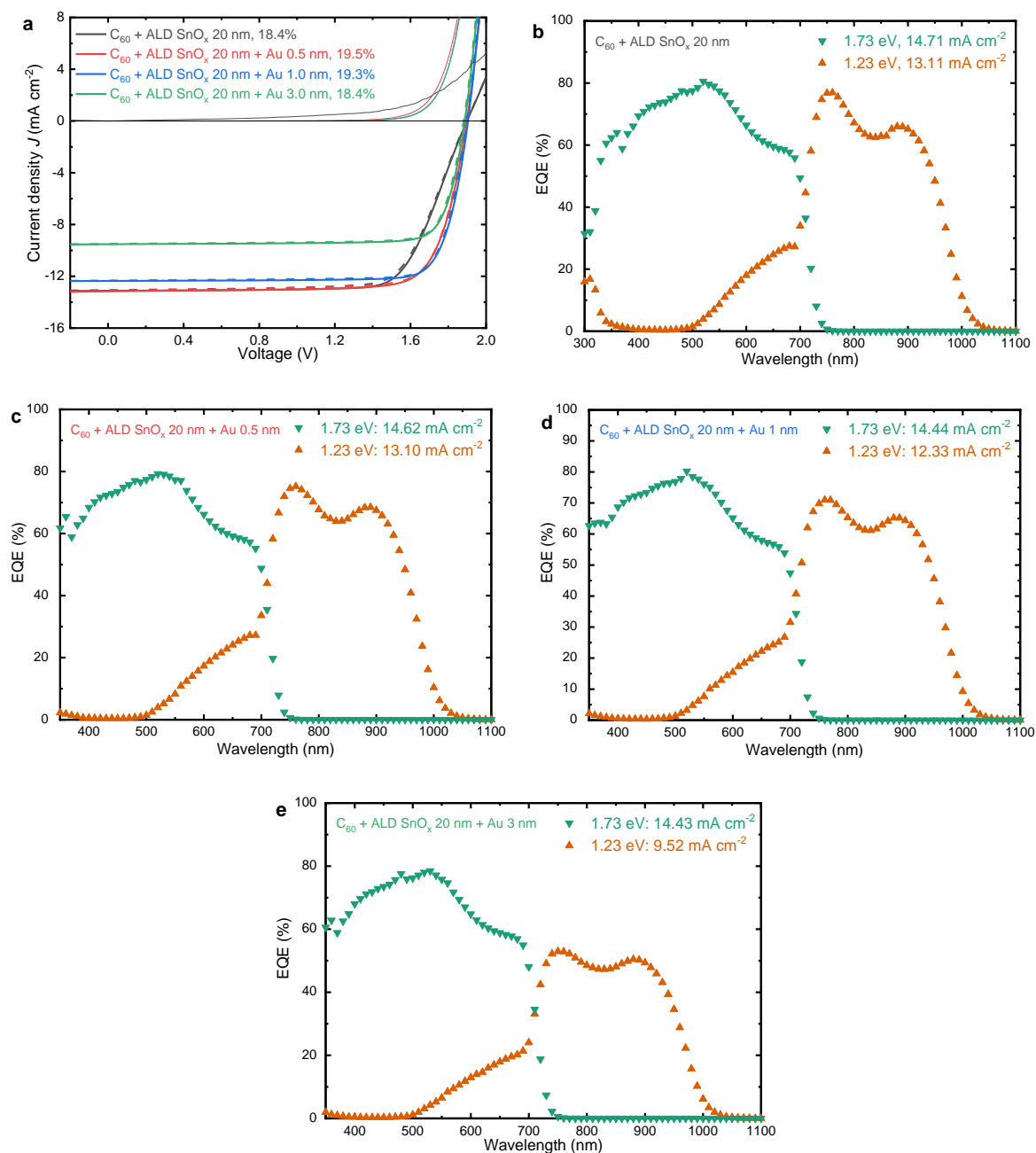


Figure 4.6 J - V characteristics of (a) tandem devices using C_{60} /SALD-SnO₂ (20 nm)/PEDOT:PSS as the ICLs, where a thin Au layer varied from 0–3 nm was inserted between the SnO₂ and PEDOT:PSS layers. The corresponding EQE spectra of tandem devices with (b) 0 nm, (c) 0.5 nm, (d) 1 nm, and (e) 3 nm Au layers, respectively. The J_{sc} was obtained by integrating with the AM1.5G spectrum.

Table 4.1 Photovoltaic parameters of tandem devices with different interconnecting layers, measured under simulated AM 1.5G illumination (100 mW cm^{-2}).

Tandem cells	Scan direction	J_{sc} (mA cm^{-2})	V_{oc} (V)	FF	PCE (%)
PCBM/SnO ₂ /PEDOT:PSS	Rev	14.0	1.81	0.66	16.8
	Fwd	14.0	1.82	0.65	16.5
C ₆₀ /SnO ₂ /PEDOT:PSS	Rev	13.1	1.91	0.77	19.3
	Fwd	13.1	1.90	0.77	19.0
C ₆₀ /SnO ₂ /Au/PEDOT:PSS	Rev	12.7	1.91	0.82	19.7
	Fwd	12.6	1.90	0.81	19.4

^a The aperture area was 6.76 mm^2 .

4.4 Photovoltaic performance of all-perovskite tandem solar cells

Figure 4.7a-b display the device configuration and cross-sectional SEM of the optimized tandem solar cell. In the stabilized J - V measurement, the tandem shows a PCE of 19.2% (6.76 mm^2 aperture area), with negligible hysteresis between reverse and forward scans (Figure 4.7c-d and Table 4.2). A stabilized PCE of 19.5% after 300 s of steady-state power output tracking further confirms the device performance (Figure 4.7e). The device produces a stabilized V_{oc} of 1.89 V, which is very close to the summed V_{oc} value of the 1.73 eV front sub-cell (1.13 V) and 1.23 eV back sub-cell (0.78 V). This low potential energy loss, together with a high FF of 0.81, implies the fast recombination of charges from adjacent sub-cells in the ICLs.²⁷ As discussed, our tandem cell performance is limited by the low J_{sc} . Compared to a J_{sc} of 28.0 mA cm^{-2} obtained for 1.23 eV single-junction PSC, the summed EQE spectrum of both sub-cells is generally lower in the near-infrared range and shows a current density of 26.8 mA cm^{-2} (Figure 4.8). Here, the loss in J_{sc} is mainly attributed to parasitic absorption from the ICL (PEDOT:PSS) and ITO substrate, reflectance, optical interference, and insufficient 1.23 eV absorber layer thickness for light absorption.

Table 4.2 Photovoltaic parameters of the single-junction and tandem PSCs. The aperture area is 6.76 mm^2 .

Devices	J_{sc} (mA cm^{-2})	V_{oc} (V)	FF	PCE ^a (%)	J_{sc}^b (mA cm^{-2})	PCE ^c (%)
1.73 eV (300 nm)	16.0	1.13	0.73	13.2	15.5	12.7
1.23 eV	27.8	0.78	0.73	15.8	28.0	15.9
Tandem	12.6	1.89	0.81	19.2		

^a The data was extracted from stabilized J - V curves under simulated AM 1.5G illumination (100 mW cm^{-2}). ^b Calculated by integrating the EQE spectrum with the AM1.5G spectrum. ^c Corrected PCE

obtained by calculating the J_{sc} integrated from EQE spectrum and V_{oc} and FF from the stabilized $J-V$ measurement.

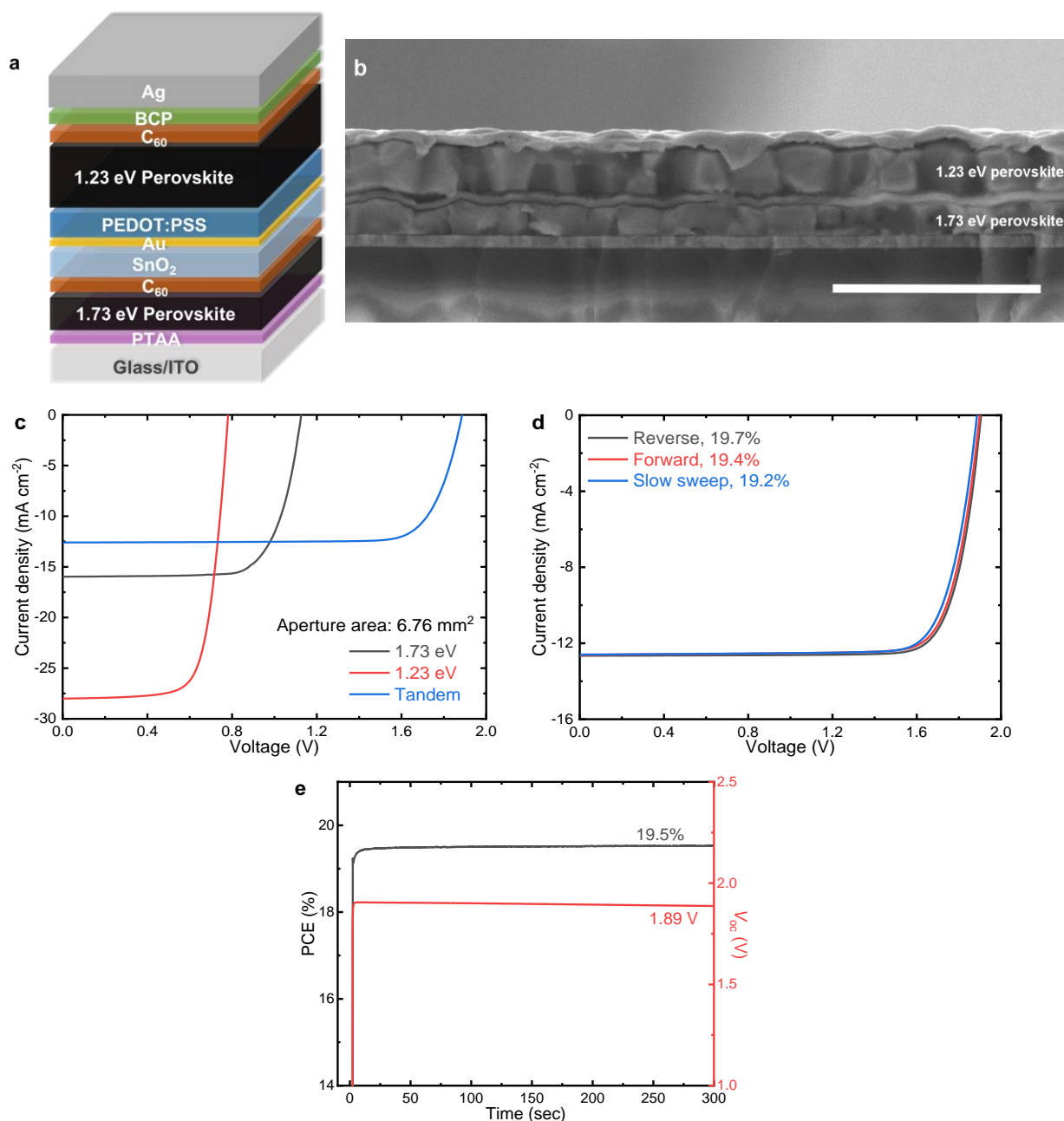


Figure 4.7 Device configuration and performance of optimized monolithic all-perovskite tandem solar cells. (a) Device structure. (b) Corresponding cross-sectional SEM image of the tandem device. The scale bar is 2 μm . (c) Stabilized $J-V$ curves of the best-performing tandem cell and the corresponding 1.73 eV and 1.23 eV single-junction PSCs prepared in the same batch (6.76 mm²). (d) Reverse, forward, and stabilized $J-V$ scans. (e) PCE and V_{oc} tracking of the best-performing tandem solar cell.

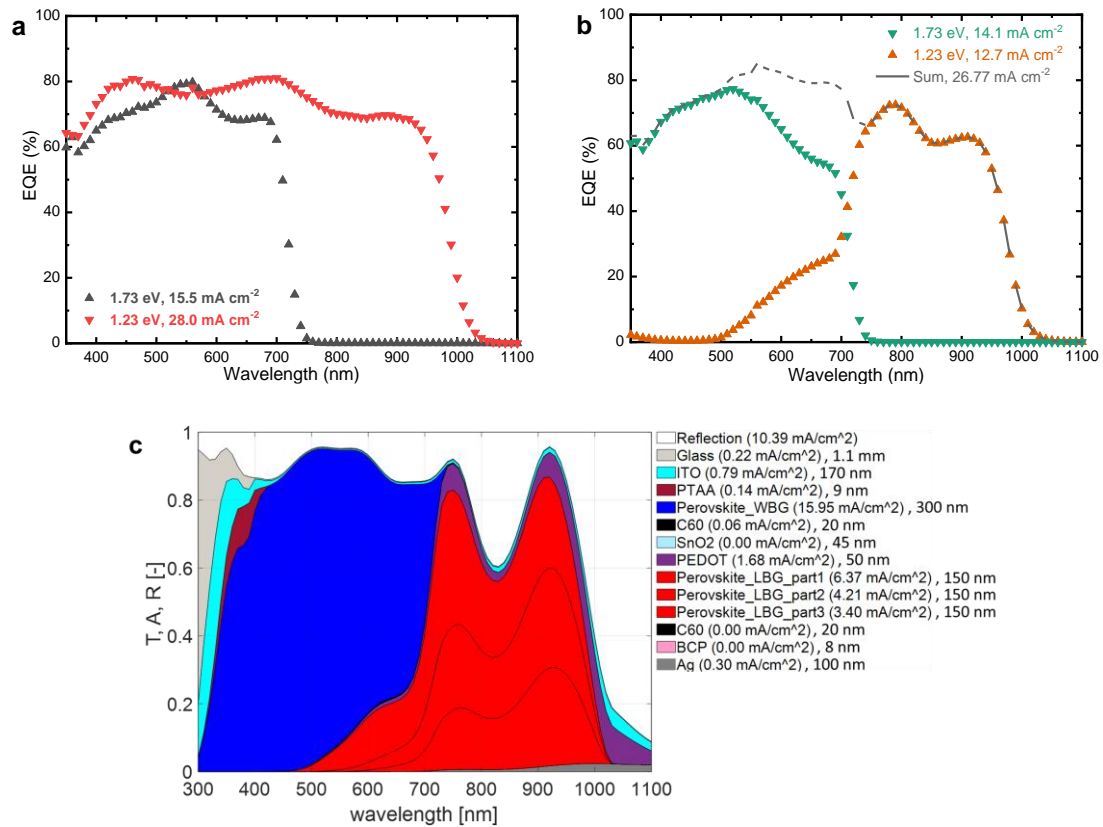


Figure 4.8 EQE of (a) single-junction PSCs with 1.73 eV and 1.23 eV absorber layers and (b) 1.73 eV and 1.23 eV sub-cells of a monolithic tandem device using C₆₀/SALD-SnO₂/Au/PEDOT:PSS as ICL as shown in Figure 4.7. The black dotted line represents the summed EQE of both sub-cells. (c) Analysis of optical losses in monolithic all-perovskite tandem solar cells. The ellipsometry measurement data of 1.23 eV perovskite absorber layer was modeled with three graded layers with slightly different refractive indices.

4.5 Conclusions

In summary, the SALD-grown SnO₂ layer has shown excellent barrier properties, which prevents the degradation of underlying perovskite absorber layers during a multijunction fabrication process. The low-resistivity of SALD-SnO₂ also ensures a good electron-transport property. Ohmic contacts are created when combining C₆₀/SALD-SnO₂/(Au)/PEDOT:PSS ICLs with adjacent perovskite absorber layers. Through optimization, monolithic all-perovskite tandem solar cells with 1.73 eV and 1.23 eV have been demonstrated with very low potential energy drop and resistivity loss, achieving PCEs of above 19%.

4.6 Experimental section

Preparation of perovskite precursor solutions: All materials were purchased from commercial sources and used as received unless stated otherwise. For 1.73 eV Cs_{0.1}(FA_{0.66}MA_{0.34})_{0.9}PbI₂Br, CsI

(Sigma-Aldrich, 99.999%) (34.8 mg) and PbI_2 (Sigma-Aldrich, 99.999%) (553 mg) were dissolved in DMF (876 μL) (99.8%) and dimethyl sulfoxide (DMSO) (99.9%) (86.4 μL) to make a 1.25 M iodide (CsI-PbI_2) solution. The small portion of DMSO was added to form a 1:1 molar ratio of PbI_2 :DMSO. Formamidinium bromide (FABr, Greatcell Solar) (34.9 mg) and methylammonium bromide (MABr, Greatcell Solar) (16.0 mg) were dissolved in isopropanol (99.5%) (1 mL) to make a 0.422 M bromide (FABr-MABr) solution. Thinner $\text{Cs}_{0.1}(\text{FA}_{0.66}\text{MA}_{0.34})_{0.9}\text{PbI}_2\text{Br}$ films were prepared by reducing the precursor concentrations. For a 300 nm-thick layer, 1.1 M CsI-PbI_2 and 0.297 M FABr-MABr solutions were used. For a 100 nm-thick layer, 0.4 M CsI-PbI_2 and 0.095 M FABr-MABr solutions were prepared. For the 1.57 eV $\text{FA}_{0.66}\text{MA}_{0.34}\text{PbI}_{2.85}\text{Br}_{0.15}$ precursor solutions, PbI_2 (553 mg) was dissolved in DMF (876 μL) and DMSO (86.4 μL). Formamidinium iodide (FAI, Greatcell Solar) (54.0 mg), methylammonium iodide (MAI, Greatcell Solar) (14.3 mg), and MABr (7.6 mg) were dissolved in isopropanol (1 mL) to give a 0.471 M halide (FAI-MAI-MABr) solution. All the solutions above were kept at 60 °C overnight. For the 1.23 eV $\text{FA}_{0.66}\text{MA}_{0.34}\text{Pb}_{0.5}\text{Sn}_{0.5}\text{I}_3$ precursor solutions, a mixture of PbI_2 (276.5 mg) and SnI_2 (Sigma-Aldrich, 99.99%) (223.4 mg) was dissolved in DMF (876 μL) and DMSO (86.4 μL), and 10 mol% SnF_2 (Sigma-Aldrich, 99%) was added with respect to SnI_2 . The solution was stirred at 60 °C for 1 hour and filtered by a polytetrafluoroethylene (PTFE) syringe filter (0.22 μm). A mixture of FAI (53.5 mg) and MAI (25.6 mg) was dissolved in of isopropanol (1 mL) and stirred at 60 °C for 1 hour. We note that all materials except PEDOT:PSS and PTAA (stored in ambient) were received and stored in a dry N_2 glovebox. While it was crucial to weigh Sn-containing compounds in a dry N_2 glovebox, other compounds showed little influence on the device performance when weighed either in the N_2 or in an ambient atmosphere. All the solvent bottles were received and stored in an N_2 glovebox for wet chemical processing (spin coating). All the solutions were prepared and stirred in the same glovebox and were cooled before use.

Device fabrication: Pre-patterned ITO glass substrates (Naranjo, 17 Ω/sq) were cleaned by sonication in acetone, sodium dodecyl sulfate (Acros, 99%), soapy water, deionized water, and isopropanol (15 min). Before spin coating, the ITO substrates were further treated under UV-ozone for 30 min. For both the 1.73 eV wide bandgap and 1.57 eV mid bandgap PSCs, 3 mg mL^{-1} of PTAA in toluene (TCI, 99.5%) was spin coated onto the ITO substrate at 5700 rpm for 30 s and annealed at 100 °C for 10 min in the N_2 glovebox. After cooling down, the Pb-containing precursor solution was spin coated at 3000 rpm (with a 2000 rpm s^{-1} acceleration) for 30 s, followed by the dynamic spin coating of FA/MA-based precursor solution at a speed of 3000 rpm for 30 s. The substrate was immediately annealed at 100 °C for 30 min. For the devices using PCBM as the electron transport layer (ETL), a solution (1 mL) of PCBM (Solenne BV, 99%) (20 mg mL^{-1}) in a mixture of chlorobenzene (CB, 99.8%) and chloroform (CF, 99%) (1:1 volume ratio) was spin coated at 1000 rpm for 60 s, followed by thermal annealing at 100 °C for 30 min. Finally, 1 nm LiF (0.2 \AA s^{-1}) and 100 nm Al (2 \AA s^{-1}) were thermally evaporated to complete the device fabrication. For devices with C_{60} (SES Research, 99.95%) as the ETL, 20 nm C_{60}

(0.5 \AA s^{-1}), 8 nm bathocuproine (BCP) (Lumtec, 99%) (0.5 \AA s^{-1}) and 100 nm Al (2 \AA s^{-1}) were thermally evaporated in a sequence. A similar approach was used for 1.23 eV narrow bandgap PSCs. PEDOT:PSS (Heraeus Clevis, PCP Al 4083) was filtered by a polyvinylidene fluoride (PVDF) filter (0.45 \mu m), spin coated on the cleaned ITO substrate at 3000 rpm for 60 s and annealed at $140 \text{ }^\circ\text{C}$ for 15 min in ambient condition. In the N_2 glovebox, the $\text{PbI}_2/\text{SnI}_2$ precursor solution was spin coated at 3000 rpm (with a 2000 rpm acceleration) for 30 s. After drying the wet precursor film at room temperature for 30 min, FAI/MAI precursor solution was dynamically spin coated on top at 3000 rpm for 60 s, followed by thermal annealing at $100 \text{ }^\circ\text{C}$ for 30 min. Afterward, NH_4SCN (Sigma-Aldrich, 97.5%) (1 mg mL^{-1}) dissolved in isopropanol was spin coated on top at 5000 rpm for 30 s. Finally, 20 nm C_{60} (0.5 \AA s^{-1}), 8 nm BCP (0.5 \AA s^{-1}) and 100 nm Ag (2 \AA s^{-1}) were sequentially evaporated on top. The cell area was determined by the overlap of the top and bottom ITO electrodes (0.09 or 0.16 cm^2). For tandem devices, the same procedure was used to fabricate different perovskite sub-cells. Between 1.73/1.23 eV sub-cells, after evaporation of 20 nm C_{60} , the samples were transferred in the air to a homemade spatial ALD reactor,⁴⁵ using tetrakis(dimethylamino)tin(IV) as the tin source and H_2O as co-reactant to deposit a 45 nm SnO_2 layer. The substrates were then transferred back to the thermal evaporator for the deposition of a 1 nm Au layer. For Au evaporation, a shadow mask with an aperture slightly larger than the cell area was applied. The samples were then exposed in air to spin coat PEDOT:PSS at a speed of 3000 rpm for 60 s, and annealed at $100 \text{ }^\circ\text{C}$ for 15 min.

Device characterization: The J - V and EQE characteristics were performed in the N_2 glovebox at room temperature. A tungsten-halogen lamp combined with a UV-filter (Schott GG385) and a daylight filter (Hoya LB120) was used to simulate the solar spectrum, the light intensity was calibrated by Si photodiode to be $\sim 100 \text{ mW cm}^{-2}$. A black shadow mask with an aperture slightly smaller than the cell area was used (0.0676 or 0.1296 cm^2). For the fast J - V measurements, a Keithley 2400 source meter was used to sweep the voltage from $+1.5 \text{ V}$ (-0.5 V) to -0.5 V ($+1.5 \text{ V}$) at a scan rate of 0.25 V s^{-1} in reverse (forward) scan. For the stabilized J - V tests, the solar cell was first monitored at V_{oc} for 5 min, followed by a reverse voltage sweep from $(V_{oc} + 0.02) \text{ V}$ to -0.02 V at a step size of 0.02 V . During the voltage sweep, the source meter measures the current density for 5 s at each voltage point. From the stabilized J - V curves, the voltage at the maximum power point was extracted and was applied to the cell during steady-state power output tracking. In the EQE measurements, a modulated (Oriel, Cornerstone 130) tungsten-halogen lamp (Philips focusline, 50 W) was used as the light source. The signal of solar cells was amplified by a current preamplifier (Stanford Research, SR 570) and measured by a lock-in amplifier (Stanford Research, SR 830). The spectral response was then transformed into EQE using a calibrated silicon reference cell. For single-junction PSCs, to mimic the one-sun condition for the J - V measurements, additional LED bias light (530 nm for 1.73/1.57 eV, 940 nm for 1.23 eV, Thorlabs) was used to generate a photocurrent close to J_{sc} in the cell during the EQE measurement. We note that for our single-junction PSCs, the difference between non-biased and light-biased EQE spectra is negligible.

For tandem solar cells, a 530 nm bias light was used to measure the EQE response of 1.23 eV back sub-cell, whereas a 940 nm bias light was used for the EQE of 1.73 eV front sub-cell. In a triple-junction solar cell, the 530 nm bias light was used for the 1.23 eV back sub-cell, the 730 nm bias light was used for the 1.73 eV front sub-cell, and a combination of 530 + 940 nm bias light was used to measure the 1.57 eV middle sub-cell. We also studied the effect of voltage bias by applying the sum of the V_{oc} of the optically biased sub-cells on our triple-junction solar cells during the EQE measurements and found that the difference between voltage biased and non-voltage biased EQE spectra is insignificant.

Film characterization: SEM images were recorded by an FEI Quanta 3D FEG microscope, using a 5-kV electron beam and a secondary electron detector. XRD patterns were obtained by a Bruker 2D phaser (Cu $K\alpha$ radiation, $\lambda = 1.5405 \text{ \AA}$). UV–vis–NIR absorption measurements were performed by PerkinElmer Lambda 900 UV–vis–NIR spectrophotometer. Steady-state photoluminescence spectra were measured by Edinburgh Instruments FLSP920 double-monochromator luminescence spectrometer, with a near-infrared photomultiplier (Hamamatsu).

Simulations: Optical modeling was carried out with the GenPro4 program.⁴⁶ To ensure the reliability of any conclusions drawn from optical modeling, component materials of the semi-transparent PSCs were prepared individually on glass and characterized with a J.A. Woollam ellipsometer to acquire optical constants. Furthermore, measured reflectance (R) and transmission (T) of each material were compared to those simulated with its optical constants for validation.

4.7 References

1. Dong, Q. et al. Electron-hole diffusion lengths $> 175 \mu\text{m}$ in solution-grown $\text{CH}_3\text{NH}_3\text{PbI}_3$ single crystals. *Science* **347**, 967-970 (2015).
2. Park, N.-G., Zhu, K. Scalable fabrication and coating methods for perovskite solar cells and solar modules. *Nat. Rev. Mater.* **5**, 333-350 (2020).
3. Stranks, S. D. et al. Electron-Hole Diffusion Lengths Exceeding 1 Micrometer in an Organometal Trihalide Perovskite Absorber. *Science* **342**, 341 (2013).
4. NREL Best Research-Cell Efficiencies. <https://www.nrel.gov/pv/assets/pdfs/best-research-cell-efficiencies.20200128.pdf> (2020).
5. Guillemoles, J.-F., Kirchartz, T., Cahen, D., Rau, U. Guide for the perplexed to the Shockley–Queisser model for solar cells. *Nat. Photonics* **13**, 501-505 (2019).
6. Shockley, W., Queisser, H. J. Detailed Balance Limit of Efficiency of p-n Junction Solar Cells. *J. Appl. Phys.* **32**, 510-519 (1961).
7. Saliba, M. et al. How to Make over 20% Efficient Perovskite Solar Cells in Regular (n–i–p) and Inverted (p–i–n) Architectures. *Chem. Mater.* **30**, 4193-4201 (2018).
8. Leijtens, T., Bush, K. A., Prasanna, R., McGehee, M. D. Opportunities and challenges for tandem solar cells using metal halide perovskite semiconductors. *Nat. Energy* **3**, 828-838 (2018).
9. Di Carlo Rasi, D., Janssen, R. A. J. Advances in Solution-Processed Multijunction Organic Solar Cells. *Adv. Mater.* **31**, 1806499 (2019).
10. Eperon, G. E., Hörantner, M. T., Snaith, H. J. Metal halide perovskite tandem and multiple-junction photovoltaics. *Nat. Rev. Chem.* **1**, 0095 (2017).
11. De Vos, A. Detailed balance limit of the efficiency of tandem solar cells. *J. Phys. D. Appl. Phys.* **13**, 839-846 (1980).
12. Werner, J. et al. Perovskite/Perovskite/Silicon Monolithic Triple-Junction Solar Cells with a Fully Textured Design. *ACS Energy Lett.* **3**, 2052-2058 (2018).
13. Geisz, J. F. et al. Six-junction III–V solar cells with 47.1% conversion efficiency under 143 Suns concentration. *Nat. Energy* **5**, 326-335 (2020).
14. Meng, L. et al. Organic and solution-processed tandem solar cells with 17.3% efficiency. *Science* **361**, 1094-1098 (2018).
15. Chen, C. C. et al. An efficient triple-junction polymer solar cell having a power conversion efficiency exceeding 11%. *Adv. Mater.* **26**, 5670-5677 (2014).
16. Di Carlo Rasi, D., Hendriks, K. H., Wienk, M. M., Janssen, R. A. J. Quadruple Junction Polymer Solar Cells with Four Complementary Absorber Layers. *Adv. Mater.* **30**, 1803836 (2018).
17. Saliba, M., Correa-Baena, J. P., Grätzel, M., Hagfeldt, A., Abate, A. Perovskite Solar Cells: From the Atomic Level to Film Quality and Device Performance. *Angew. Chem. Int. Ed.* **57**, 2554-2569 (2018).
18. McMeekin, D. P. et al. A mixed-cation lead mixed-halide perovskite absorber for tandem solar cells. *Science* **351**, 151-155 (2016).
19. Xu, J. et al. Triple-halide wide-band gap perovskites with suppressed phase segregation for efficient tandems. *Science* **367**, 1097-1104 (2020).
20. Hao, F., Stoumpos, C. C., Chang, R. P., Kanatzidis, M. G. Anomalous Band Gap Behavior in Mixed Sn and Pb Perovskites Enables Broadening of Absorption Spectrum in Solar Cells. *J. Am. Chem. Soc.* **136**, 8094-8099 (2014).
21. Gu, S., Lin, R., Han, Q., Gao, Y., Tan, H., Zhu, J. Tin and Mixed Lead-Tin Halide Perovskite Solar Cells: Progress and their Application in Tandem Solar Cells. *Adv. Mater.* **32**, 1907392 (2020).
22. Hörantner, M. T. et al. The Potential of Multijunction Perovskite Solar Cells. *ACS Energy Lett.* **2**, 2506-2513 (2017).
23. Rajagopal, A. et al. Highly Efficient Perovskite-Perovskite Tandem Solar Cells Reaching 80% of the Theoretical Limit in Photovoltage. *Adv. Mater.* **29**, 1702140 (2017).
24. Eperon, G. E. et al. Perovskite-perovskite tandem photovoltaics with optimized band gaps. *Science* **354**, 861-865 (2016).
25. Tong, J. H. et al. Carrier lifetimes of $> 1 \mu\text{s}$ in Sn-Pb perovskites enable efficient all-perovskite tandem solar cells. *Science* **364**, 475-479 (2019).

26. Palmstrom, A. F. et al. Enabling Flexible All-Perovskite Tandem Solar Cells. *Joule* **3**, 2193-2204 (2019).
27. Zhao, D. et al. Efficient two-terminal all-perovskite tandem solar cells enabled by high-quality low-bandgap absorber layers. *Nat. Energy* **3**, 1093-1100 (2018).
28. Yang, Z. et al. Enhancing electron diffusion length in narrow-bandgap perovskites for efficient monolithic perovskite tandem solar cells. *Nat. Commun.* **10**, 4498 (2019).
29. Leijtens, T. et al. Tin–lead halide perovskites with improved thermal and air stability for efficient all-perovskite tandem solar cells. *Sustain. Energy Fuels* **2**, 2450-2459 (2018).
30. Yu, Z. et al. Simplified interconnection structure based on C_{60}/SnO_{2-x} for all-perovskite tandem solar cells. *Nat. Energy*, 10.1038/s41560-020-0657-y, (2020).
31. Lin, R. et al. Monolithic all-perovskite tandem solar cells with 24.8% efficiency exploiting comproportionation to suppress Sn(II) oxidation in precursor ink. *Nat. Energy* **4**, 864-873 (2019).
32. McMeekin, D. P. et al. Solution-Processed All-Perovskite Multi-Junction Solar Cells. *Joule* **3**, 387-401 (2019).
33. Xiao, K. et al. Solution-Processed Monolithic All-Perovskite Triple-Junction Solar Cells with Efficiency Exceeding 20%. *ACS Energy Lett.*, 10.1021/acsenerylett.0c01184, 2819-2826 (2020).
34. Chang, C.-Y., Tsai, B.-C., Hsiao, Y.-C., Lin, M.-Z., Meng, H.-F. Solution-processed conductive interconnecting layer for highly-efficient and long-term stable monolithic perovskite tandem solar cells. *Nano Energy* **55**, 354-367 (2019).
35. Jiang, F. et al. A two-terminal perovskite/perovskite tandem solar cell. *J. Mater. Chem. A* **4**, 1208-1213 (2016).
36. Li, C. et al. Thermionic Emission-Based Interconnecting Layer Featuring Solvent Resistance for Monolithic Tandem Solar Cells with Solution-Processed Perovskites. *Adv. Energy Mater.* **8**, 1801954 (2018).
37. Ávila, J. et al. High voltage vacuum-deposited $CH_3NH_3PbI_3$ – $CH_3NH_3PbI_3$ tandem solar cells. *Energy Environ. Sci.* **11**, 3292-3297 (2018).
38. Gahlmann, T. et al. Impermeable Charge Transport Layers Enable Aqueous Processing on Top of Perovskite Solar Cells. *Adv. Energy Mater.* **10**, 1903897 (2020).
39. Raiford, J. A. et al. Enhanced Nucleation of Atomic Layer Deposited Contacts Improves Operational Stability of Perovskite Solar Cells in Air. *Adv. Energy Mater.* **9**, 1902353 (2019).
40. Hoffmann, L. et al. Spatial Atmospheric Pressure Atomic Layer Deposition of Tin Oxide as an Impermeable Electron Extraction Layer for Perovskite Solar Cells with Enhanced Thermal Stability. *ACS Appl. Mater. Interfaces* **10**, 6006-6013 (2018).
41. Najafi, M. et al. Highly Efficient and Stable Semi-Transparent p-i-n Planar Perovskite Solar Cells by Atmospheric Pressure Spatial Atomic Layer Deposited ZnO. *Solar RRL* **2**, 1800147 (2018).
42. Zardetto, V. et al. Towards Large Area Stable Perovskite Solar Cells and Modules. *IEEE 46th Photovoltaic Specialists Conference (PVSC)*, 10.1109/pvsc40753.2019.8981217, 0838-0840 (2019).
43. Shi, L. et al. Gas chromatography–mass spectrometry analyses of encapsulated stable perovskite solar cells. *Science* **368**, eaba2412 (2020).
44. Yoon, H., Kang, S. M., Lee, J.-K., Choi, M. Hysteresis-free low-temperature-processed planar perovskite solar cells with 19.1% efficiency. *Energy Environ. Sci.* **9**, 2262-2266 (2016).
45. Illiberi, A., Roozeboom, F., Poodt, P. Spatial atomic layer deposition of zinc oxide thin films. *ACS Appl. Mater. Interfaces* **4**, 268-272 (2012).
46. Santbergen, R., Meguro, T., Suezaki, T., Koizumi, G., Yamamoto, K., Zeman, M. GenPro4 Optical Model for Solar Cell Simulation and Its Application to Multijunction Solar Cells. *IEEE J. Photovolt.* **7**, 919-926 (2017).

Chapter 5

16.8% monolithic all-perovskite triple-junction solar cells*

Abstract

All-perovskite multijunction solar cells offer an interesting route to further improve the power conversion efficiencies (PCEs) at a low fabrication cost. To maximize the device performance, stringent bandgap and thickness optimizations are needed to balance light absorption and match current density among sub-cells. In addition, integrating several very different perovskite absorber layers in a multijunction cell imposes a great processing challenge. Here, we report a versatile two-step solution process for high-quality 1.73 eV wide-, 1.57 eV mid-, and 1.23 eV narrow-bandgap perovskite films. By using an interconnecting layer structure developed in Chapter 4, efficient and reproducible monolithic all-perovskite triple-junction solar cells comprising 1.73 eV, 1.57 eV, and 1.23 eV perovskite sub-cells are demonstrated. The best-performing triple-junction cell shows a high PCE of 16.8%, with very low potential energy drop and resistivity loss.

* This chapter is partially reproduced from: Wang, J., Zardetto, V., Datta, K., Zhang, D., Wienk, M.M., Janssen, R.A.J., *Nat. Commun.*, 2020, 11, 5254.

5.1 Introduction

As discussed in Chapters 1 and 4, multijunction solar cells have the potential to exceed the detailed balance limit of single-junction devices by collecting a broader range of solar spectrum with minimized energy losses. Theoretically, solar cells with infinite junctions could reach power conversion efficiencies of 68% under one sun condition and up to 85% at the maximum concentration in the detailed balance limit.¹

Perovskites have great potential for developing highly efficient multijunction solar cells, given its widely tunable bandgaps and prominent optoelectronic properties. Also, the solution processability and low material costs make such devices more profitable than expensive III-V technologies. Device and optical modeling¹⁻³ have suggested that a monolithic tandem with 1.8 eV wide-bandgap and 1.2 eV narrow-bandgap perovskite materials can reach a feasible power conversion efficiency (PCE) of 33.4%. In contrast, a monolithic all-perovskite triple-junction solar cell comprising 2.0 eV, 1.5 eV, and 1.2 eV absorbers leads to an even higher PCE of 36.6%.² While tremendous effort has been made for all-perovskite tandem devices,³⁻¹⁰ all-perovskite triple-junction solar cells remain largely unexplored, with a proof-of-concept 6.7% triple cell first demonstrated by Snaith and co-workers.¹¹ Very recently, Tan et al. demonstrated all-perovskite triple-junction solar cells with efficiency exceeding 20%.¹²

Next to the design constraints of interconnecting layers (ICLs) as discussed in Chapter 4, integrating several very different perovskite layers in such a complex multijunction cell could impose significant processing challenges, as they typically require very specific film formation strategies to achieve high efficiencies in single-junction solar cells.¹³ To this end, using a simple and yet effective fabrication method suitable for various perovskite compositions and bandgaps would greatly benefit the development of all-perovskite multijunction solar cells. In this chapter, we present a two-step solution process for high-quality perovskite thin films. With only minor changes in the processing conditions, we fabricate efficient single-junction perovskite solar cells (PSCs) with bandgaps of 1.73 eV, 1.57 eV, and 1.23 eV (also see in Chapter 3). Using the ICLs of C₆₀/SALD-SnO₂/(Au)/PEDOT:PSS, we demonstrate efficient and reproducible all-perovskite triple-junction solar cells combining 1.73 eV, 1.57 eV, and 1.23 eV absorber layers. The best-performing triple-junction device shows a very promising PCE of 16.8%, with a short-circuit current density (J_{sc}) of 7.4 mA cm⁻², an open-circuit voltage (V_{oc}) of 2.78 V, and a fill factor (FF) of 0.81. Furthermore, the constraints of our current cell design are analyzed by device and optical modeling.

5.2 Formation of wide/mid/narrow bandgap perovskite films

We focused on a mixed perovskite composition of $\text{Cs}_z(\text{FA}_{0.66}\text{MA}_{0.34})_{1-z}\text{Pb}_{1-x}\text{Sn}_x\text{I}_{3-y}(1-z)\text{Br}_y$ (FA is formamidinium, MA is methylammonium). By changing the molar ratio of precursor solutions, perovskites based on wide bandgap $\text{Cs}_{0.1}(\text{FA}_{0.66}\text{MA}_{0.34})_{0.9}\text{PbI}_2\text{Br}$, medium (mid) bandgap $\text{FA}_{0.66}\text{MA}_{0.34}\text{PbI}_{2.85}\text{Br}_{0.15}$, and narrow bandgap $\text{FA}_{0.66}\text{MA}_{0.34}\text{Pb}_{0.5}\text{Sn}_{0.5}\text{I}_3$ are obtained. In a two-step deposition route, inorganic salts (CsI , PbI_2 , and SnI_2) dissolved in *N,N*-dimethylformamide (DMF) and dimethyl sulfoxide (DMSO) are first spin coated to obtain an intermediate precursor film, on which organic salts (FAI, FABr, MAI, and MABr) dissolved in isopropanol are spin coated and followed by thermal annealing to accelerate the transition to perovskite crystals (Figure 5.1a). Similar processing conditions were used for all the three perovskite recipes, except for a room temperature drying process of Sn-containing precursor film before the second deposition step.¹⁴ UV-vis-NIR absorption and photoluminescence (PL) spectra indicate bandgaps of 1.73 eV for $\text{Cs}_{0.1}(\text{FA}_{0.66}\text{MA}_{0.34})_{0.9}\text{PbI}_2\text{Br}$, 1.57 eV for $\text{FA}_{0.66}\text{MA}_{0.34}\text{PbI}_{2.85}\text{Br}_{0.15}$, and 1.23 eV for $\text{FA}_{0.66}\text{MA}_{0.34}\text{Pb}_{0.5}\text{Sn}_{0.5}\text{I}_3$ perovskite absorbers, respectively (Figure 5.1b). X-ray diffraction (XRD) patterns confirm the formation of single-phase crystallites among all perovskite films (Figure 5.1c). Compared to 1.57 eV $\text{FA}_{0.66}\text{MA}_{0.34}\text{PbI}_{2.85}\text{Br}_{0.15}$, the shift of the (100) diffraction peak towards higher angles is consistent with a decrease in the cubic lattice constant from 6.324 Å to 6.303 Å for narrow bandgap $\text{FA}_{0.66}\text{MA}_{0.34}\text{Pb}_{0.5}\text{Sn}_{0.5}\text{I}_3$ (Sn incorporation), and to 6.194 Å for wide bandgap $\text{Cs}_{0.1}(\text{FA}_{0.66}\text{MA}_{0.34})_{0.9}\text{PbI}_2\text{Br}$ (Cs and Br incorporation) (Figure 5.1c). It is also found that the (100) peak intensity of the narrow bandgap layer is significantly higher than the other films, in line with the fast-crystallizing property of Sn-based perovskites (Chapter 3). Top-view scanning electron microscopy (SEM) images reveal a compact and pin-hole free surface morphology for all perovskite films, with an average grain size span from ~250 nm for both wide and mid bandgap absorbers, to ~500 nm for narrow bandgap perovskite (Figure 5.1d-f). The film characteristics suggest the controlled formation of high-quality perovskite absorbers with different bandgaps using a two-step solution process.

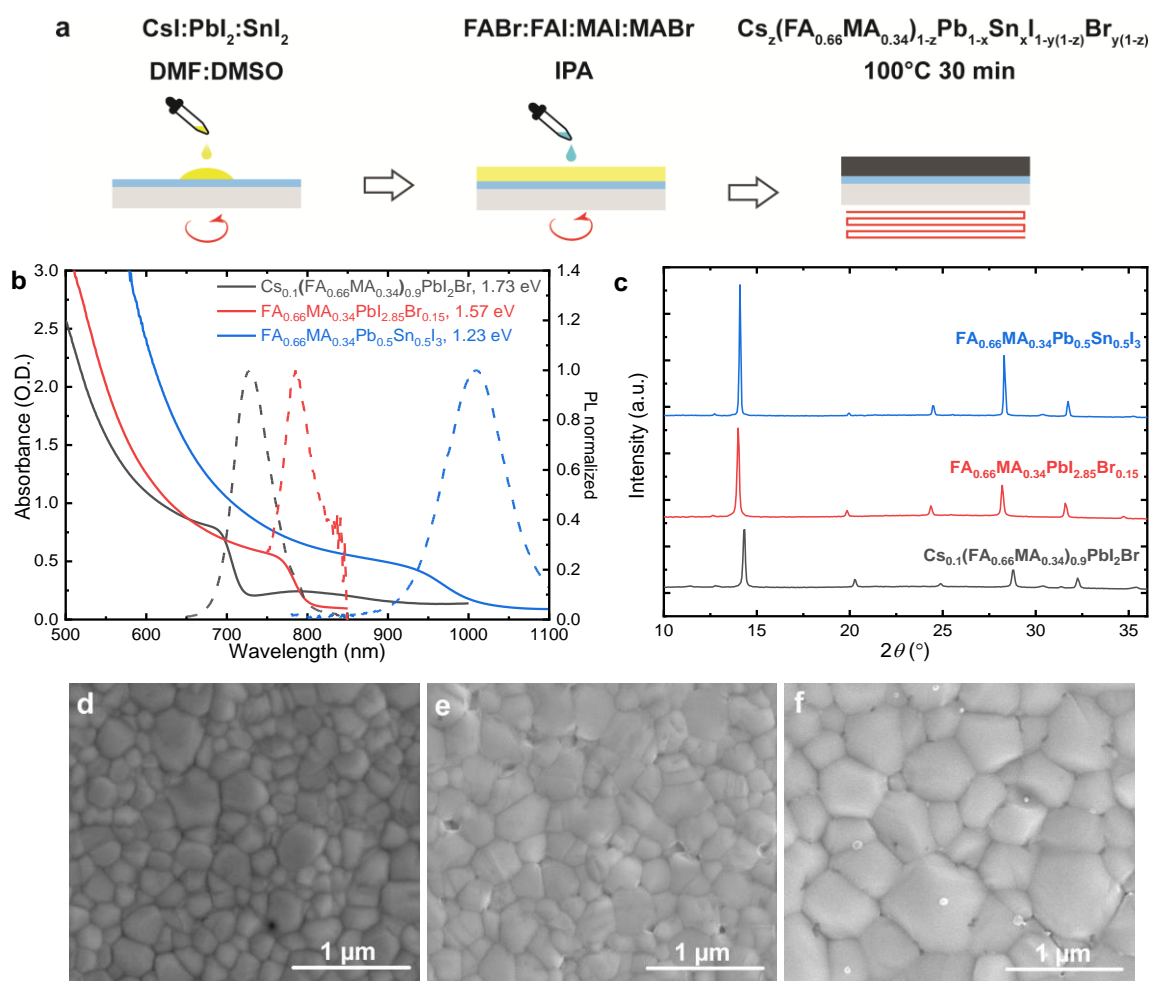


Figure 5.1 (a) Schematic illustration of the two-step solution process for $\text{Cs}_z(\text{FA}_{0.66}\text{MA}_{0.34})_{1-z}\text{Pb}_{1-x}\text{Sn}_x\text{I}_{3-y(1-z)}\text{Br}_{y(1-z)}$ perovskite composition. (b) UV-vis-NIR absorption and steady-state photoluminescence spectra. (c) XRD patterns of perovskite films with different bandgaps. (d-f) Top-view SEM images of 1.73 eV, 1.57 eV, and 1.23 eV perovskite films. Scale bars are 1 μm .

Table 5.1 Photovoltaic parameters of representative single-junction PSCs with different bandgaps.

Bandgap (eV)	J_{sc} (mA cm^{-2})	V_{oc} (V)	FF	PCE ^a (%)	J_{sc}^b (mA cm^{-2})	PCE ^c (%)
1.73	17.0	1.13	0.74	14.2	17.3	14.5
1.57	21.6	1.08	0.80	18.7	21.1	18.3
1.23	27.8	0.78	0.73	15.8	28.0	15.9

^a The data was extracted from stabilized current density–voltage (J – V) curves under simulated AM 1.5G illumination (100 mW cm^{-2}). The aperture area was 6.76 mm^2 . ^b Calculated by integrating the external quantum efficiency (EQE) spectrum with the AM1.5G spectrum. ^c Corrected PCE obtained by calculating the J_{sc} integrated from EQE spectrum and V_{oc} and FF from the stabilized J – V measurement.

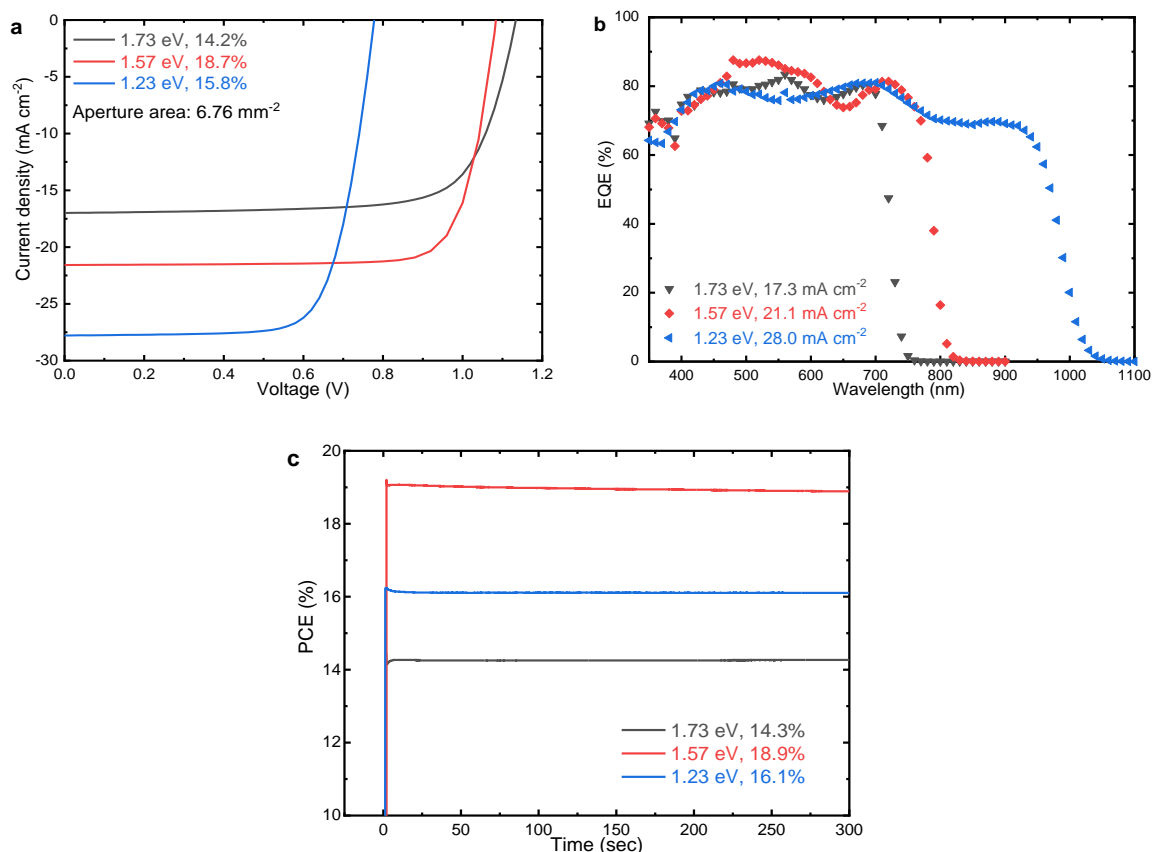


Figure 5.2 (a) Stabilized J - V curves (measured with 6.76 mm^2 aperture area). (b) EQE spectra. (c) Steady-state power output tracking for opaque PSCs with 1.73 eV, 1.57 eV, and 1.23 eV bandgaps.

We fabricated planar p - i - n PSCs to evaluate the photovoltaic (PV) performance of different perovskite absorbers. The wide and mid bandgap PSCs used a device configuration of indium tin oxide (ITO)/poly[bis(4-phenyl)(2,4,6-trimethylphenyl)amine (PTAA)/perovskite/phenyl- C_{61} -butyric acid methyl ester (PCBM)/LiF/Al, whereas a layout of ITO/poly(3,4-ethylene dioxythiophene):polystyrene sulfonate (PEDOT:PSS)/perovskite/ C_{60} /bathocuproine (BCP)/Ag was used for narrow bandgap PSCs. All perovskite layers are 400-450 nm thick. Figure 5.2a-b display the stabilized current density–voltage (J - V) curves and external quantum efficiency (EQE) spectra of representative PSCs with various perovskite bandgaps. The corresponding PV parameters are summarized in Table 5.1. The 1.73 eV wide bandgap PSC shows a PCE of 14.5%, with a J_{sc} of 17.3 mA cm^{-2} , a V_{oc} of 1.13 V, and a FF of 0.74. In comparison, the device based on 1.57 eV mid bandgap exhibits an increased J_{sc} of 21.1 mA cm^{-2} , a decreased V_{oc} of 1.08 V, and a FF of 0.80, resulting in a PCE of 18.3%. The changes in J_{sc} and V_{oc} are attributed to the decreased perovskite bandgap, in line with the redshifted EQE onset from 720 nm to 810 nm. As expected, further decreasing the bandgap to 1.23 eV leads to a higher J_{sc} of 28.0 mA cm^{-2} , a lower V_{oc} of 0.78 V, and a FF of 0.73, yielding a PCE of 15.9%

for the narrow bandgap PSC. The PCEs of $J-V$ measurements are further confirmed by steady-state power output tracking at the maximum power point, where all the devices show a negligible decrease in performance during the tracking period (Fig. 5.2c).

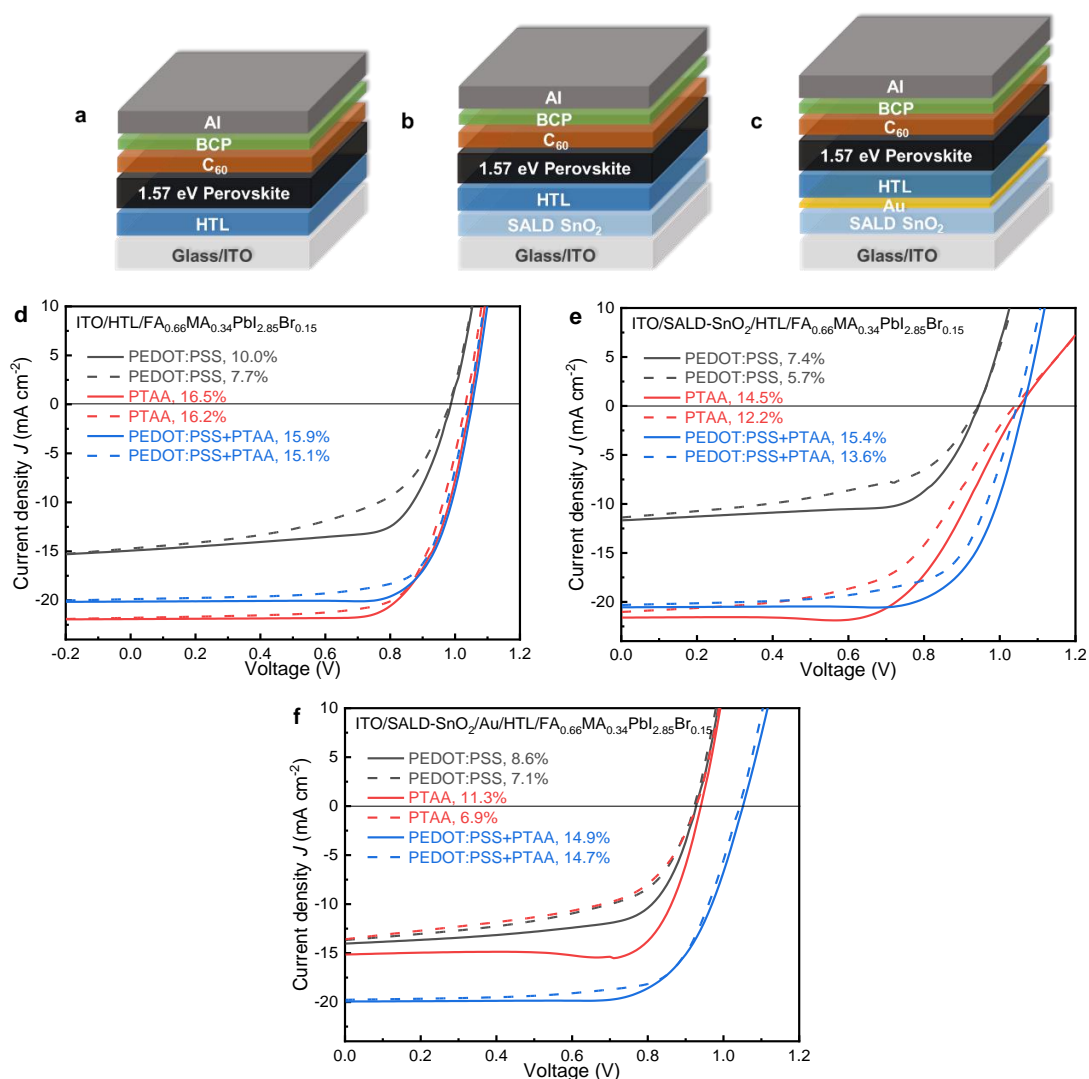


Figure 5.3 Device structure and $J-V$ characteristics of 1.57 eV single-junction solar cells using (a, d) ITO/HTL, (b, e) ITO/SALD-SnO₂/HTL, and (c, f) ITO/SALD-SnO₂/Au/HTL bottom contacts. The HTL is PEDOT:PSS and/or PTAA. The measurements were done in fast $J-V$ sweep in reverse (solid lines) and forward (dashed lines) directions.

5.3 ICLs for all-perovskite triple-junction solar cells

A SnO₂ layer grown by spatial atomic layer deposition (SALD) was introduced in the ICLs for all-perovskite triple-junction solar cells. As is demonstrated in Chapter 4, such a compact layer is fully compatible with the solution processing of multiple perovskite layers on top of each other. While PEDOT:PSS has been reported to be the best performing hole transport layer (HTL) for 1.2 eV perovskite devices, PTAA is more commonly used for the mid-bandgap

(~1.5 eV) perovskite recipes.¹⁵ To study the electrical contact of a SALD-SnO₂/PTAA interconnecting layer, we fabricated 1.57 eV single-junction PSCs based on a structure of ITO/HTL/perovskite/C₆₀/BCP/Al (Figure 5.3 a-c). In configuration A, the HTL consists of PEDOT:PSS and/or PTAA, whereas the HTL was deposited on SALD-SnO₂ in configuration B, and the HTL was deposited on SALD-SnO₂/Au (1 nm) in configuration C. As expected, in configuration A, the device with PTAA layer alone outperforms that with PEDOT:PSS due to much better hole selectivity of PTAA towards the 1.57 eV-perovskite material. When a PEDOT:PSS/PTAA stack is used in the device, only the J_{sc} is slightly reduced as a result of parasitic absorption and reflection loss from PEDOT:PSS. In configuration B and C, again, the SALD-SnO₂/(Au)/PEDOT:PSS layer stack displays lower performance due to the poor hole-selectivity of PEDOT:PSS. However, suboptimal device performance is also seen when using SALD-SnO₂/(Au)/PTAA as the bottom contact. This can be attributed to the low conductivity of our (undoped) PTAA hole transport layer, which forms an electronic barrier at the SALD-SnO₂/(Au)/PTAA interface. In the end, we found that a combination of SALD-SnO₂/(Au)/PEDOT:PSS/PTAA works the best for such 1.57 eV devices.

5.4 Photovoltaic performance of all-perovskite triple-junction solar cells

Furthermore, we integrated our two-step processed 1.73 eV, 1.57 eV, and 1.23 eV perovskite absorbers into monolithic all-perovskite triple-junction solar cells. Similar to tandem cells in Chapter 4, our initial test found that the triple-junction device with PCBM/SALD-SnO₂/PEDOT:PSS ICLs displays an s-kink in the $J-V$ characteristics, which can be removed by replacing PCBM with C₆₀ and inserting a thin Au layer at the SALD-SnO₂/PEDOT:PSS interface (Figure 5.4). As shown in Figure 5.5a and b, the optimized triple-junction cell utilized a device configuration of ITO/PTAA/Cs_{0.1}(FA_{0.66}MA_{0.34})_{0.9}PbI₂Br/C₆₀/SALD-SnO₂/Au/PEDOT:PSS/PTAA/FA_{0.66}MA_{0.34}PbI_{2.85}Br_{0.15}/C₆₀/SALD-SnO₂/Au/PEDOT:PSS/FA_{0.66}MA_{0.34}Pb_{0.5}Sn_{0.5}I₃/C₆₀/BCP/Ag. In such a device stack, the 1.73 eV perovskite absorber was further reduced to ~100 nm to approach a current matching condition (Figure 4.3), and PTAA was deposited on PEDOT:PSS in the 1.57 eV middle sub-cell to achieve better device performance (Figure 5.3). In the stabilized $J-V$ measurement, the best-performing triple device exhibits a PCE of 16.8% (6.76 mm² aperture area), with a J_{sc} of 7.4 mA cm⁻², a V_{oc} of 2.78 V, and a FF of 0.81. The triple cell performance is higher than that of single junction PSCs prepared in the same batch (Figure 5.5c and Table 5.2). The corresponding EQE spectra generate photocurrents of 8.2, 8.9, and 7.6 mA cm⁻² for the 1.73 eV front sub-cell, 1.57 eV middle sub-cell, and 1.23 eV back sub-cell, respectively (Figure 5.5d), indicating that the narrow bandgap

perovskite sub-cell is limiting the J_{sc} of the triple device. Also, the device shows negligible hysteresis between reverse, forward, and stabilized $J-V$ characteristics (Figure 5.6a). The PV performance of the triple-junction cell is further confirmed by a stabilized PCE of 16.9% after 300 s of steady-state power output tracking (Figure 5.6b). Meanwhile, the stabilized V_{oc} (2.78 V) of the triple device is close to the summed V_{oc} value (2.86 V) of the corresponding single-junction PSCs, suggesting the effectiveness of such ICLs in our triple-junction design. Furthermore, a statistical summary of 8 triple cells illustrates a narrow distribution of PCEs, which demonstrates the good reproducibility of our approach to fabricate triple-junction cells (Figure 5.6c).

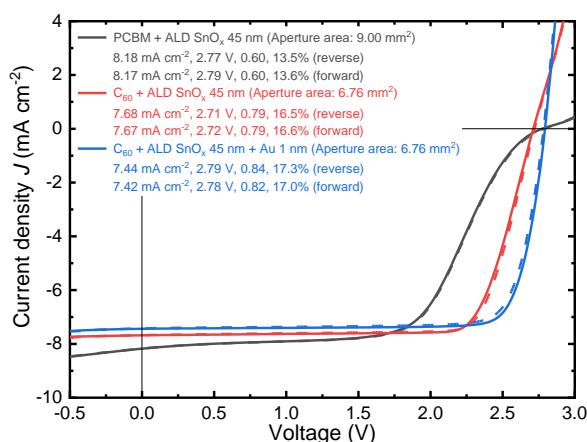


Figure 5.4 $J-V$ characteristics of triple-junction solar cells with PCBM/SALD-SnO₂/PEDOT:PSS, C₆₀/SALD-SnO₂/PEDOT:PSS and C₆₀/SALD-SnO₂/Au/PEDOT:PSS ICLs. The aperture areas are indicated in the legend.

Table 5.2 Photovoltaic parameters of the single-junction and triple-junction PSCs.

Devices	J_{sc} (mA cm ⁻²)	V_{oc} (V)	FF	PCE (%)	J_{sc}^a (mA cm ⁻²)	PCE ^b (%)
1.73 eV (100 nm)	9.9	1.07	0.76	8.1	10.7	8.7
1.57 eV	21.0	1.03	0.76	16.5	20.4	16.0
1.23 eV	26.7	0.76	0.72	14.6	27.0	14.8
Triple	7.4	2.78	0.81	16.8		

^a Calculated by integrating the EQE spectrum with the AM1.5G spectrum. ^c Corrected PCE obtained by calculating the J_{sc} integrated from the EQE spectrum and V_{oc} and FF from the stabilized $J-V$ measurement.

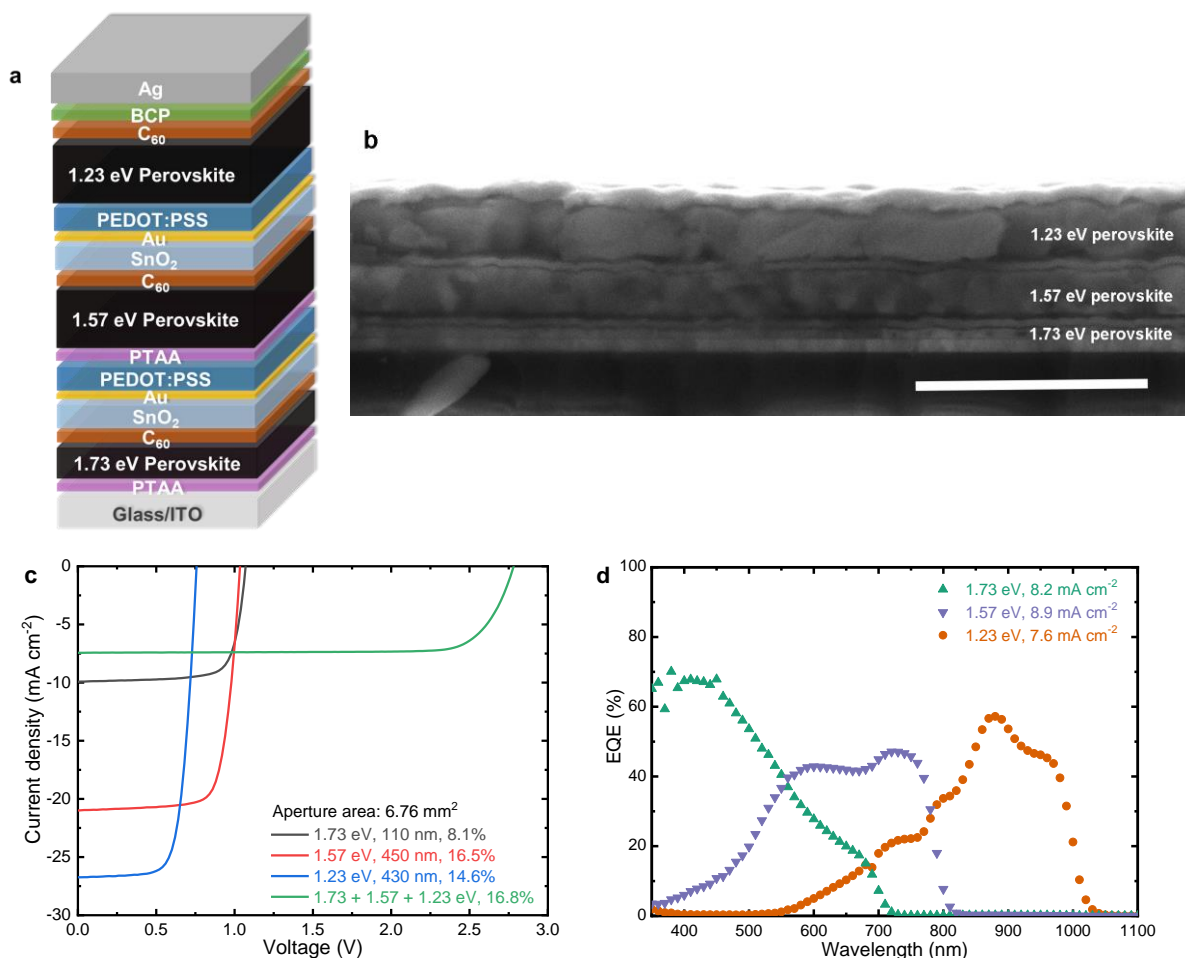


Figure 5.5 Device configuration and performance of optimized monolithic all-perovskite triple-junction solar cells. (a) Device structure and (b) corresponding cross-sectional SEM image of the triple-junction device. The scale bar is 2 μm . (c) Stabilized J - V curves of the best-performing triple-junction cell and the corresponding 1.73 eV, 1.57 eV, and 1.23 eV single-junction PSCs prepared in the same batch (6.76 mm^2). (d) EQE spectra of 1.73 eV, 1.57 eV, and 1.23 eV sub-cells in a triple-junction device with C_{60} /SALD- SnO_2 /Au/PEDOT:PSS ICLs, the J_{sc} was obtained by integrating with the AM 1.5G spectrum.

Under the current design, the PCE of our triple-junction solar cell is limited by the J_{sc} of 1.23 eV back sub-cell. In contrast to the 1.23 eV single-junction cell (27.0 mA cm^{-2}), the summed EQE of all three sub-cells in a triple device (24.7 mA cm^{-2}) suggests a considerable loss in the near-infrared, which accounts for a loss in photocurrent of 2.3 mA cm^{-2} (Figure 5.7a-b). Similar to the tandem analysis, the J_{sc} loss mainly originates from reflection, parasitic absorption of ITO and PEDOT:PSS, optical interference, and also incomplete light absorption in the near-infrared due to a relatively thin 1.23 eV absorber layer (Figure 5.7c). Using light management layers as well as optimizing the layer thicknesses can significantly reduce such optical losses.

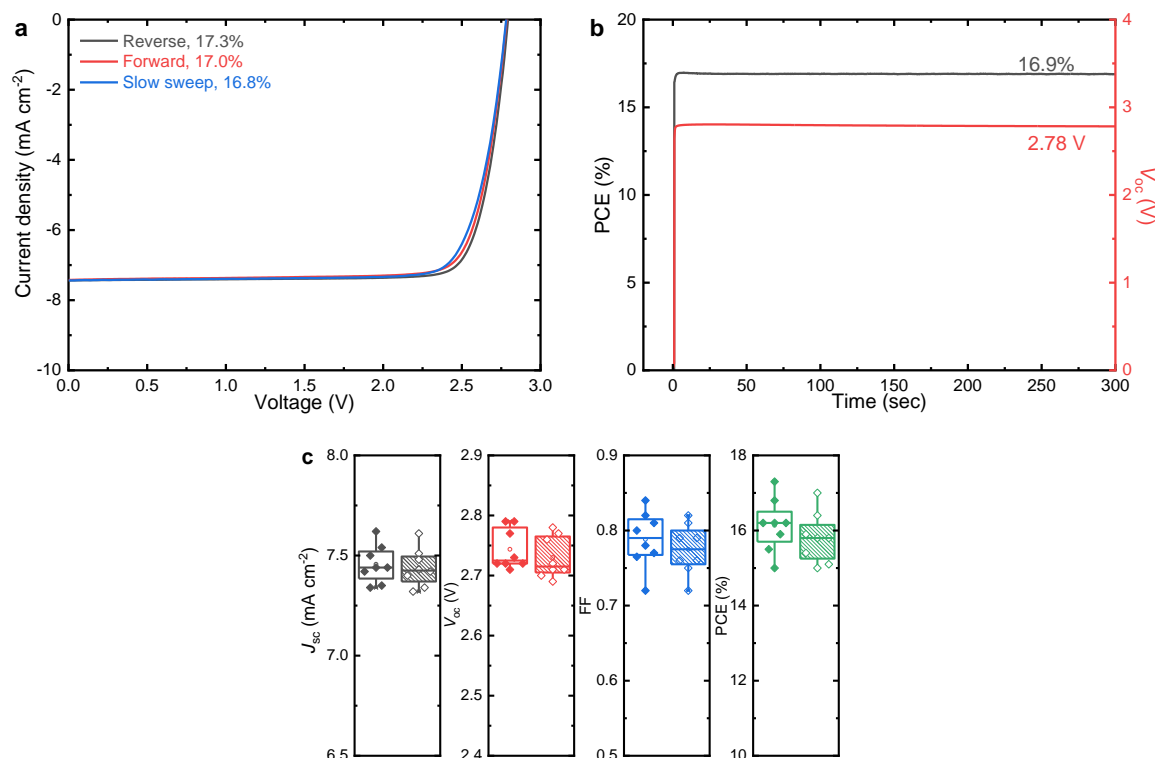


Figure 5.6 (a) Reverse, forward, and stabilized J - V scans and (b) PCE and V_{oc} tracking of the best-performing triple device. (c) Statistical distributions of PV parameters of J_{sc} , V_{oc} , FF, and PCE of triple-junction solar cells, measured under fast J - V sweep in reverse (left) and forward (right) directions.

As previously discussed by Snaith and co-workers,^{1,2} further improving the PCE of all-perovskite triple-junction solar cells would require an efficient ~ 2 eV wide bandgap perovskite, which enables a more balanced light absorption in each absorber layer and provides a much higher V_{oc} in the triple-junction cell. However, such wide bandgap PSCs with low V_{oc} deficit has rarely been reported to date, as our survey of the literature (Figure 5.8) suggests that the V_{oc} deficit ($E_g/q - V_{oc}$) is significantly increased (> 600 mV) for perovskites with bandgaps of above 1.8 eV. Such a high loss-in-potential likely originates from trap-assisted charge recombination in the perovskite bulk and energy misalignment between the perovskite and charge transport layers.¹⁶⁻¹⁸ More importantly, the photo-stability of Br-rich systems is much inferior to that of the I-rich perovskite materials.¹² Nevertheless, recently, Tan and co-workers have reported a 1.99 eV wide bandgap PSC showing a PCE of 10.4%, with a V_{oc} of 1.262 V, J_{sc} of 11.2 mA cm^{-2} , and FF of 73.5%. They further combined such cells in an all-perovskite triple-junction device configuration and achieved an efficiency of over 20%. However, such devices displayed massive performance decay during operation under full AM 1.5G illumination, which was attributed to the poor photo-stability of the Br-rich, wide-bandgap perovskite material.¹²

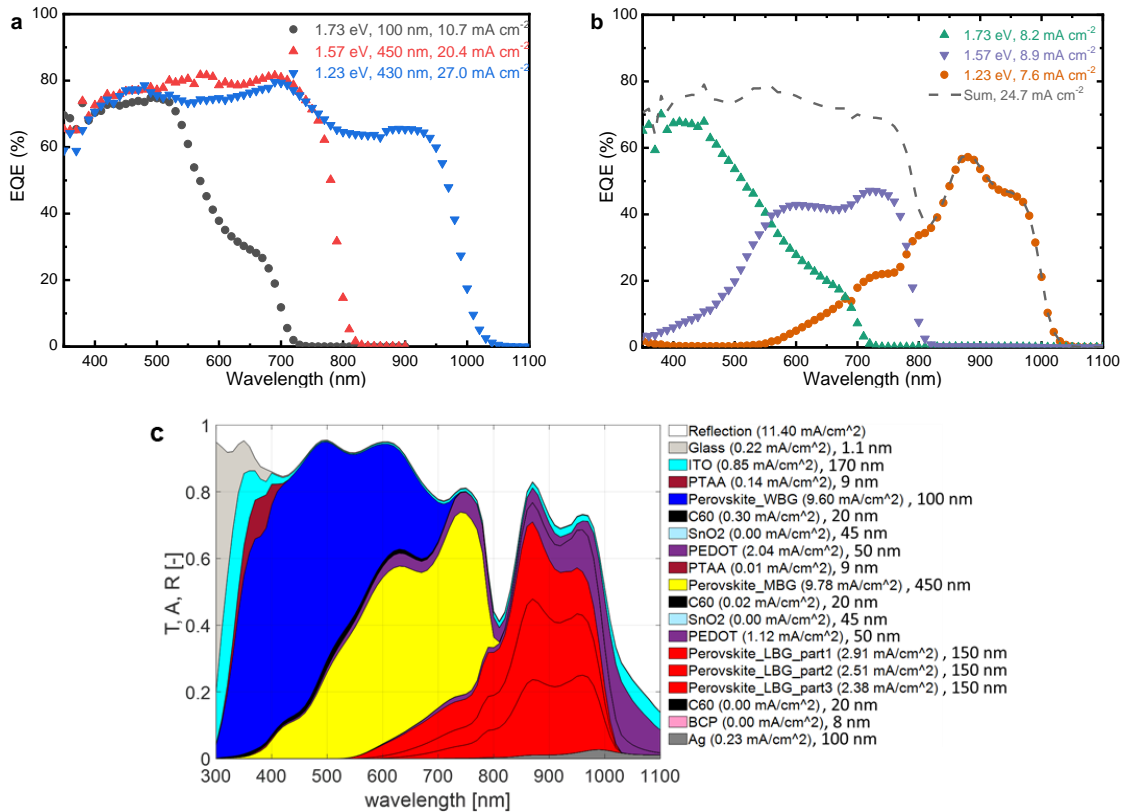


Figure 5.7 EQE of (a) single-junction PSCs with 1.73 eV, 1.57 eV and 1.23 eV absorber layers (Figure 5.5c) and (b) 1.73 eV, 1.57 eV and 1.23 eV sub-cells of a monolithic triple-junction device using C₆₀/SALD-SnO₂/Au/PDOT:PSS ICLs. The dashed line represents the summed EQE of all three sub-cells. (c) Analysis of optical losses in the monolithic all-perovskite triple-junction solar cells.

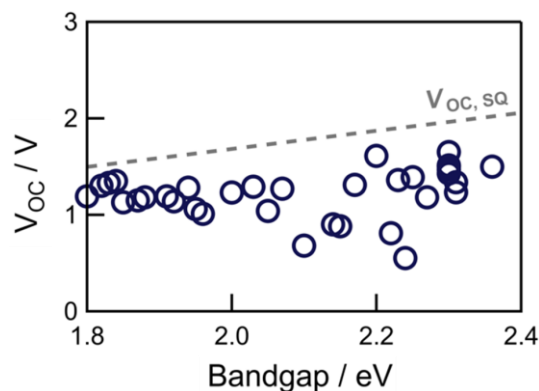


Figure 5.8 Survey of the literature of wide bandgap perovskite solar cells. V_{oc} (V) as a function of perovskite bandgap.

Using a similar two-step method, we fabricated a 2.03 eV wide-bandgap (~380 nm) single-junction cell (Figure 5.9). This cell has a PCE of 5.6%, with a J_{sc} of 8.3 mA cm⁻² (corrected by EQE). Compared to the 1.73 eV perovskite, the 2.03 eV cell is less stable and shows a more pronounced hysteresis effect. The V_{oc} of 1.11 V (after 300 s stabilization) is

comparable to the 1.73 eV sub-cell, but the FF is much lower (0.61), which makes it less desirable in the current triple-junction cell. In a series-connected multijunction solar cell, the voltage is added up from all the sub-cells at equal currents (Chapter 1). Therefore, using a 2.03 eV wide-bandgap perovskite with a large V_{oc} loss and low FF will not necessarily improve the performance of the current triple-junction solar cell.

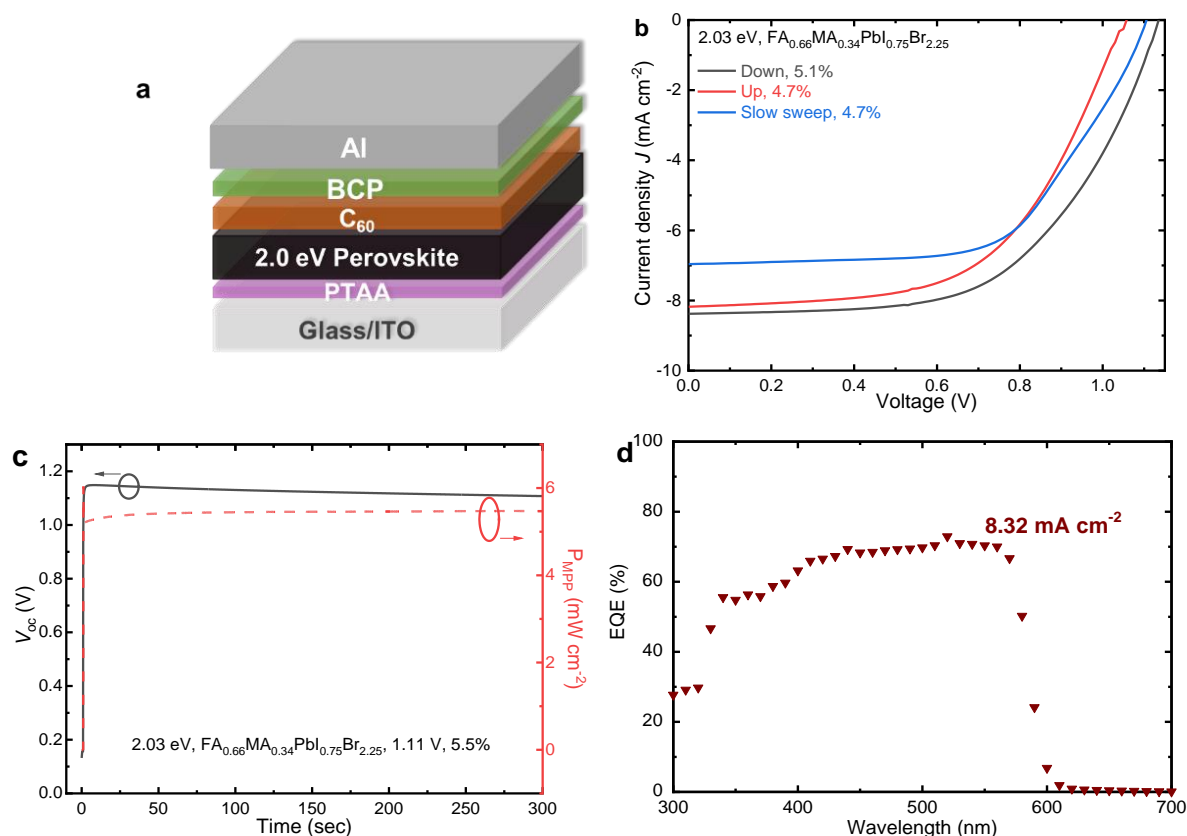


Figure 5.9 (a) *P-i-n* device structure with a 2.03 eV perovskite absorber layer. (b) J - V characteristics of a representative 2.03 eV PSC. The measurements were done in fast J - V sweep in reverse (black) and forward (red) directions, after which a slow sweep J - V (blue) was recorded. (c) V_{oc} and power output at the maximum power point tracking under illumination. (d) EQE spectrum of the corresponding solar cell, measured with a green LED (530 nm) bias illumination.

Furthermore, we performed optical simulations using the same device structure, as displayed in Figure 5.5a. Here, the 1.73 eV sub-cell (110 nm) is changed to a 2.03 eV sub-cell (380 nm). We can see that all the three sub-cells generate a J_{sc} of ~ 8 mA cm $^{-2}$, with the front 2.03 eV cell being slightly current-limited (8.1 mA cm $^{-2}$, Figure 5.10a). To construct the J - V curve of such a triple-junction cell, we scaled the slow-sweep J - V curves of the corresponding single-junction devices (2.03/1.57/1.23 eV, Figure 5.9b and Figure 5.5c) to the J_{sc} of the simulated EQE and added the voltages of the three cells for each current value.¹⁹ As can be seen, the constructed cell displays a J_{sc} of 8.46 mA cm $^{-2}$, a V_{oc} of 2.90 V, a FF of 0.68, and PCE of

16.7% (Figure 5.10b). The V_{oc} can be overestimated, given that the actual sub-cells would be illuminated under a lower light intensity in a triple-junction solar cell. In all, the simulation result suggests that a slightly inferior triple-junction performance (<16.7%) is obtained when using such a 2.03 eV front cell with sub-optimal V_{oc} and FF.

Nevertheless, the results suggest that further developments of wide-bandgap perovskite materials with a small V_{oc} deficit ($E_g/q - V_{oc}$) and adequate photo-stability would greatly benefit the development of highly efficient all-perovskite triple-junction solar cells.

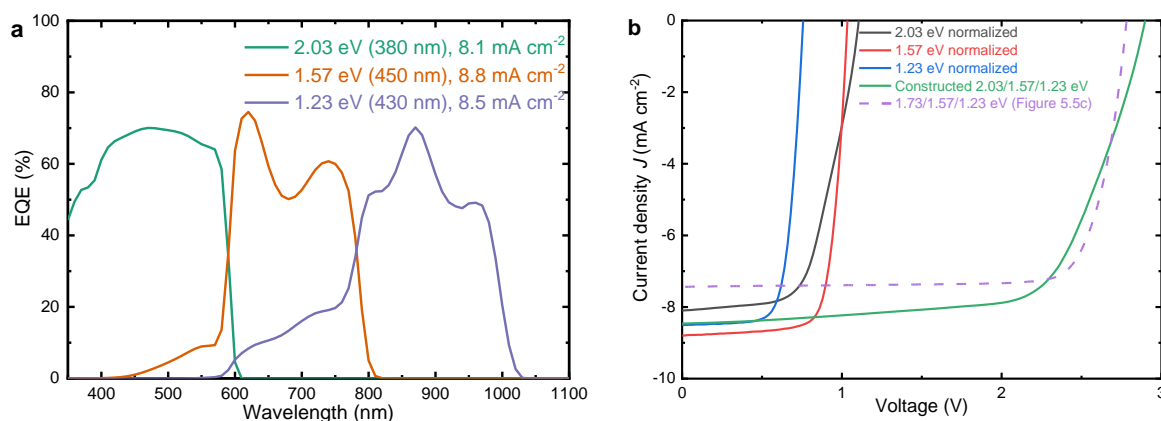


Figure 5.10 (a) Simulated EQE spectra with the device configuration illustrated in Figure 5.5a, where the front 1.73 eV perovskite absorber (110 nm) was replaced by the same 2.03 eV absorber (380 nm). The estimated J_{sc} of each sub-cell is displayed in the legend. (b) Scaled J - V curves (slow sweep data) of the corresponding 2.03/1.57/1.23 eV single-junction reference cells with respect to the simulated J_{sc} for each sub-cell in a triple-device. The constructed J - V curve of the triple cell comprising 2.03/1.57/1.23 eV absorbers was obtained by adding the voltages of the three cells for each current value.

5.5 Conclusions

In summary, we have reported a universal two-step solution process to fabricate PSCs with bandgaps of 1.73 eV, 1.57 eV, and 1.23 eV. Using robust and low-resistivity ICLs based on $C_{60}/\text{SALD-SnO}_2/(\text{Au})/\text{PEDOT:PSS}$ has enabled the fabrication of efficient and reproducible monolithic all-perovskite triple-junction solar cells. A triple device comprising a 1.73 eV, 1.57 eV, and 1.23 eV sub-cells shows a promising PCE of 16.8%, with a very low potential energy drop of only 80 mV in comparison to the summed V_{oc} of all three sub-cells ($V_{oc} = 2.78$ V) and low resistivity loss (FF = 0.81). Further improving the performance of ~2 eV wide bandgap perovskite will be essential for the future development of high-efficiency all-perovskite triple-junction solar cells.

5.6 Experimental section

See Chapter 4.

5.7 References

1. Eperon, G. E., Hörantner, M. T., Snaith, H. J. Metal halide perovskite tandem and multiple-junction photovoltaics. *Nat. Rev. Chem.* **1**, 0095 (2017).
2. Hörantner, M. T. et al. The Potential of Multijunction Perovskite Solar Cells. *ACS Energy Lett.* **2**, 2506-2513 (2017).
3. Rajagopal, A. et al. Highly Efficient Perovskite-Perovskite Tandem Solar Cells Reaching 80% of the Theoretical Limit in Photovoltage. *Adv. Mater.* **29**, 1702140 (2017).
4. Eperon, G. E. et al. Perovskite-perovskite tandem photovoltaics with optimized band gaps. *Science* **354**, 861-865 (2016).
5. Tong, J. H. et al. Carrier lifetimes of $> 1 \mu\text{s}$ in Sn-Pb perovskites enable efficient all-perovskite tandem solar cells. *Science* **364**, 475-479 (2019).
6. Palmstrom, A. F. et al. Enabling Flexible All-Perovskite Tandem Solar Cells. *Joule* **3**, 2193-2204 (2019).
7. Zhao, D. et al. Efficient two-terminal all-perovskite tandem solar cells enabled by high-quality low-bandgap absorber layers. *Nat. Energy* **3**, 1093-1100 (2018).
8. Yang, Z. et al. Enhancing electron diffusion length in narrow-bandgap perovskites for efficient monolithic perovskite tandem solar cells. *Nat. Commun.* **10**, 4498 (2019).
9. Leijtens, T. et al. Tin-lead halide perovskites with improved thermal and air stability for efficient all-perovskite tandem solar cells. *Sustain. Energy Fuels* **2**, 2450-2459 (2018).
10. Yu, Z. et al. Simplified interconnection structure based on $\text{C}_{60}/\text{SnO}_{2-x}$ for all-perovskite tandem solar cells. *Nat. Energy*, 10.1038/s41560-020-0657-y, (2020).
11. McMeekin, D. P. et al. Solution-Processed All-Perovskite Multi-Junction Solar Cells. *Joule* **3**, 387-401 (2019).
12. Xiao, K. et al. Solution-Processed Monolithic All-Perovskite Triple-Junction Solar Cells with Efficiency Exceeding 20%. *ACS Energy Lett.*, 10.1021/acseenergylett.0c01184, 2819-2826 (2020).
13. Conings, B. et al. A Universal Deposition Protocol for Planar Heterojunction Solar Cells with High Efficiency Based on Hybrid Lead Halide Perovskite Families. *Adv. Mater.* **28**, 10701-10709 (2016).
14. Wang, J. et al. Understanding the Film Formation Kinetics of Sequential Deposited Narrow-Bandgap Pb-Sn Hybrid Perovskite Films. *Adv. Energy Mater.* **10**, 2000566 (2020).
15. Pham, H. D., Yang, T. C. J., Jain, S. M., Wilson, G. J., Sonar, P. Development of Dopant-Free Organic Hole Transporting Materials for Perovskite Solar Cells. *Adv. Energy Mater.* **10**, 1903326 (2020).
16. Yang, T. C.-J., Fiala, P., Jeangros, Q., Ballif, C. High-Bandgap Perovskite Materials for Multijunction Solar Cells. *Joule* **2**, 1421-1436 (2018).
17. Mahesh, S. et al. Revealing the origin of voltage loss in mixed-halide perovskite solar cells. *Energy Environ. Sci.* **13**, 258-267 (2020).
18. Noel, N. K. et al. Highly Crystalline Methylammonium Lead Tribromide Perovskite Films for Efficient Photovoltaic Devices. *ACS Energy Lett.* **3**, 1233-1240 (2018).
19. Di Carlo Rasi, D., Hendriks, K. H., Wienk, M. M., Janssen, R. A. J. Accurate Characterization of Triple-Junction Polymer Solar Cells. *Adv. Energy Mater.* **7**, 1701664 (2017).

Chapter 6

Ultrathin hole transport layers for efficient narrow-bandgap perovskite solar cells

Abstract

Lead–tin (Pb–Sn) hybrid perovskite materials present ideal bandgaps (1.2–1.4 eV) for efficient single-junction and tandem solar cells. Poly(3,4-ethylenedioxythiophene):polystyrene sulfonate (PEDOT:PSS) has been the most used hole transport layer (HTL) for narrow-bandgap perovskite solar cells (PSCs), despite its poor stability with Pb–Sn hybrid perovskite materials. In this chapter, we present the use of two novel small molecules, 1,6-pyrenedi-7-azaindole (PyDAI), and 1,6-pyrenediindole (PyDI), as the HTL for narrow-bandgap p-i-n PSCs. Film characterizations reveal that the ultrathin HTL has a negligible impact on the quality of the perovskite film. Meanwhile, PyDAI is more robust against the solution-processed perovskite film due to the hydrogen-bond-directed self-assembly. Transient photocurrent measurements and light-intensity dependent device characteristics indicate that both HTLs possess similar hole extraction properties as PEDOT:PSS. As a result, similar open-circuit voltage and fill factor can be obtained in the PSCs. In addition to the improved device stability, the elimination of PEDOT:PSS in the solar cell also changes optical interference and reduces parasitic absorption of HTL in the near-infrared region, resulting in an improved short-circuit current density.

6.1 Introduction

Metal halide perovskites (AMX_3) have emerged as promising light-absorbing materials for high-efficiency and low-cost photovoltaic (PV) devices. A record power conversion efficiency (PCE) of 25.2% has now been achieved in Pb-based perovskite solar cells (PSCs) with an optical bandgap of ~ 1.5 eV.¹ Recent development on Sn-based PSCs provides a pathway towards higher device performance.² The (partial) substitution of Pb by Sn narrows the bandgap to 1.2–1.4 eV, which is ideal for single-junction devices according to Shockley-Queisser (S-Q) models.³ Such a narrow bandgap is also suitable for developing all-perovskite tandem solar cells.⁴ In addition, reducing the weight percentage of toxic Pb is crucial for the large-scale deployment of perovskite solar modules.⁵

To date, the efficiency of Pb–Sn hybrid perovskite devices (20–21%) is much lower than of their Pb counterparts.^{6–8} Compared to pure Pb perovskites, it is more challenging to grow thick and uniform Sn-based perovskite films due to its fast-crystallizing nature at room temperature.^{9,10} The ease of oxidation of Sn-containing compounds also raises concerns about long-term device stability.¹¹ Moreover, the choice of hole transport layers (HTLs) with a suitable energy band alignment with Pb–Sn perovskite is limited by its smaller ionization potential.^{12,13} Poly(3,4-ethylenedioxythiophene):polystyrene sulfonate (PEDOT:PSS) is the most frequently used HTL for highly efficient Pb–Sn hybrid PSCs.¹³ However, the poor thermal stability of PEDOT:PSS and Pb–Sn perovskite interface leads to a charge extraction barrier upon aging.¹² The PEDOT:PSS layer also causes parasitic absorption in the near-infrared region, which reduces the photocurrent of the narrow-bandgap sub-cell in a tandem device.^{14,15}

Previously, a non-doped, fused azapolyheteroaromatic small molecule, anthradi-7-azaindole (ADAI), was used to replace PEDOT:PSS as the HTL in conventional $CH_3NH_3PbI_3$ solar cells.¹⁶ The hydrogen-bond-directed self-assembled material effectively improved the morphology of the perovskite layer and reduced non-radiative recombination in the perovskite bulk. As a result, higher PCEs of 15.9% were obtained when using ADAI compared to 12.4% for PEDOT:PSS in $CH_3NH_3PbI_3$ devices. In this chapter, two pyrene-based, ultrathin small molecule layers, 1,6-pyrenedi-7-azaindole (PyDAI) and 1,6-pyrenediindole (PyDI) (Figure 6.1) are studied as the HTLs for Pb–Sn hybrid PSCs. Compared to PEDOT:PSS, the new HTLs exhibit comparable charge extraction properties and result in similar open-circuit voltage (V_{oc}) and fill factor (FF) in the solar cells. Besides improved device stability, the use of ultrathin

HTLs also increases the short-circuit current density (J_{sc}) due to the changes of optical interference and reduced parasitic absorption of PEDOT:PSS in the narrow-bandgap devices.

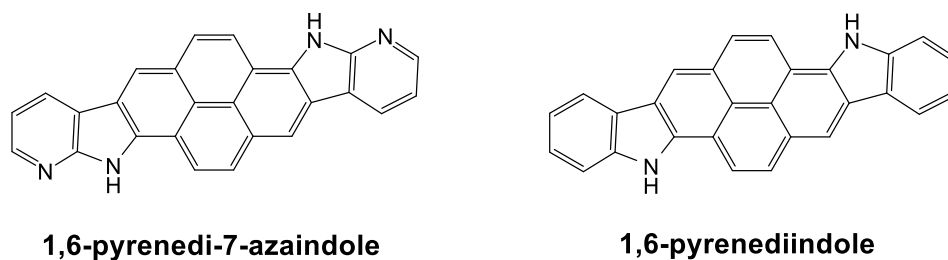


Figure 6.1 Chemical structure of PyDAI and PyDI.

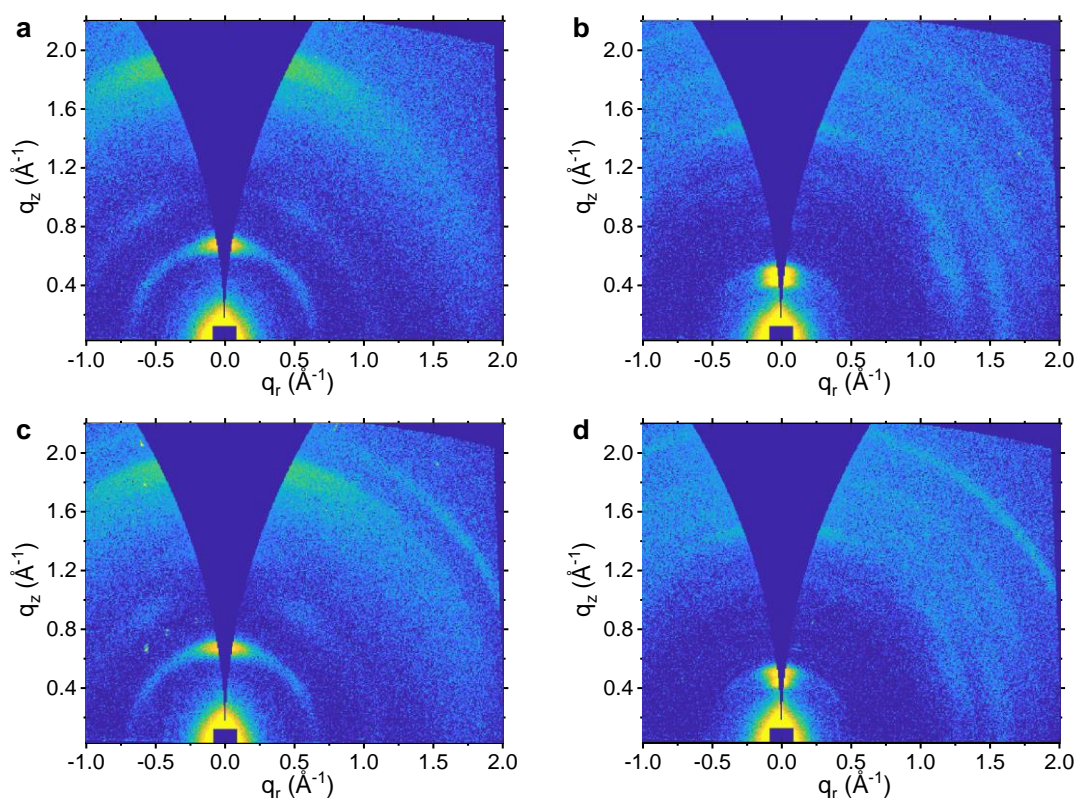


Figure 6.2 2D GIWAX patterns of (a, c) PyDAI and (b, d) PyDI thin films. (a, b) As deposited films. (c, d) Films after thermal annealing at 100 °C for 10 min.

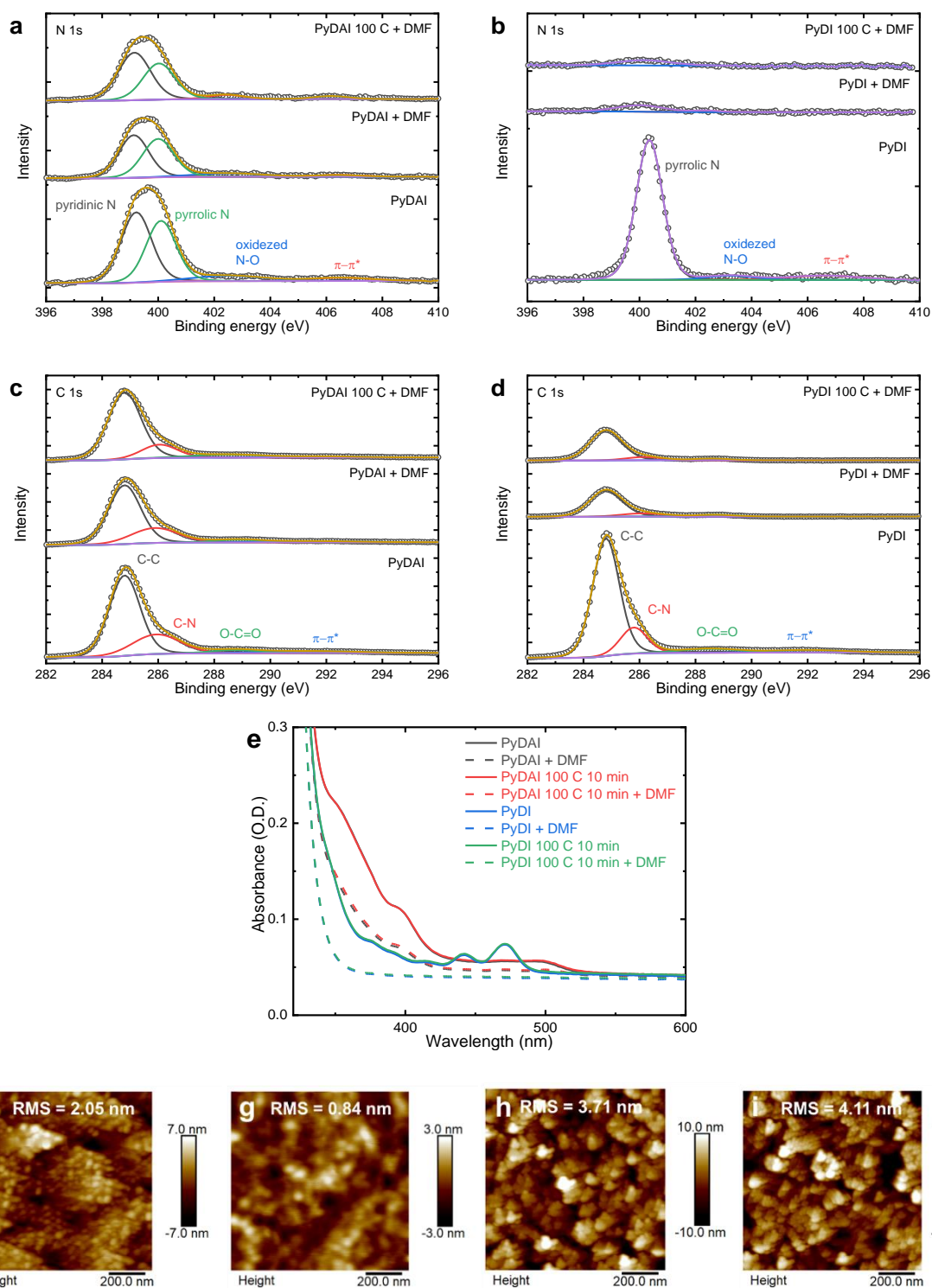


Figure 6.3 XPS high-resolution scan spectra of the (a, b) N 1s and (c, d) C 1s core levels for (a, c) PyDAI and (b, d) PyDI thin films before and after DMF washing. (e) UV-vis-NIR absorption spectra of PyDAI and PyDI thin films on glass substrates before and after DMF treatment. AFM height image of (f) ITO, (g) ITO/PEDOT:PSS, (h) ITO/PyDAI + DMF, and (i) ITO/PyDI + DMF substrates. Scale bars are 200 nm.

6.2 Small molecule organic thin films

Small organic molecules PyDAI and PyDI were synthesized following a previously reported procedure with high yield (see in Experimental section).¹⁶ Both molecules are centrosymmetric and can self-assemble into π -stacked molecular structures.¹⁶ Conformal organic thin films were thermally evaporated onto indium tin oxide (ITO)/glass substrates. Grazing-incidence wide-angle X-ray scattering (GIWAX) measurements reveal that PyDAI has slightly higher crystallinity than PyDI (Figure 6.2a-b). This can be attributed to its ability to form four hydrogen bonds via the nitrogen atoms of the pyridine rings and the NH- of the pyrrole rings, leading to π - π stacked molecular ribbons.¹⁶ Additional thermal annealing on the organic thin-films only provides a minimal improvement in the crystallinity (Figure 6.2c-d). Surface X-ray photoelectron spectroscopy (XPS) spectra of the N 1s core level confirm the presence of two different nitrogen atoms in the as-deposited PyDAI, where the peaks at 399 eV and 400 eV can be assigned to the pyridinic and pyrrolic C-N bonds, respectively (Figure 6.3a).¹⁷ For the as-deposited PyDI, only the pyrrolic C-N bond at 400 eV was found (Figure 6.3b). Both substrates were then washed by *N,N*-dimethylformamide (DMF) to mimic the solution process used for narrow-bandgap perovskite films. It is found that both the C 1s and N 1s signals of PyDI thin films are significantly reduced, suggesting that DMF has removed most of the PyDI layer (Figure 6.3b and d). In comparison, more PyDAI layer (~3 nm) was retained on the substrate after DMF washing, which can be attributed to the formation of hydrogen bonds during the self-assembly (Figure 6.3a and c). It is also found that thermal annealing provides no significant improvements in the DMF-resilience of such materials, where similar C 1s and N 1s intensities are observed for the annealed and non-annealed films. This observation is also verified in the UV-vis-NIR absorption spectra (Figure 6.3e), where a substantial decrease in the absorbance is seen for the DMF-rinsed PyDI layer. In contrast, the more robust PyDAI substrate shows less reduction in the absorbance upon DMF washing. Atomic force microscope (AFM) images (Figure 6.3f-i) indicate that both the DMF-washed PyDAI and PyDI films have a surface morphology that resembles the topology of the ITO substrate. Their root-mean-square (RMS) surface roughness (R_q ~4 nm) is slightly higher than the ITO substrate (R_q ~2 nm). The hole mobilities determined from field-effect transistors (FETs) are $1.0 \times 10^{-4} \text{ cm}^2 \text{ V}^{-1} \text{ s}^{-1}$ for PyDAI and $3.5 \times 10^{-3} \text{ cm}^2 \text{ V}^{-1} \text{ s}^{-1}$ for PyDI, respectively.

6.3 Device performance based on small molecule HTL

We evaluated the performance of ultrathin PyDAI and PyDI HTLs in planar *p-i-n* PSCs based on an ITO/HTL/perovskite/ C_{60} /BCP/Ag device structure. Both PyDAI and PyDI HTLs were deposited on top of the ITO substrate via thermal evaporation (~10 nm, after optimization) and compared with solution-processed PEDOT:PSS (~50 nm). The perovskite absorber $FA_{0.66}MA_{0.34}Pb_{0.5}Sn_{0.5}I_3$ (FA = formamidinium and MA = methylammonium) was then prepared by a two-step solution process and had a bandgap of 1.23 eV, as demonstrated in Chapter 3. Additionally, 130 nm LiF was thermally evaporated on the glass side of the substrate to reduce optical losses in the solar cells.¹³ Figure 6.4a shows the stabilized current density–voltage (J – V) curves of the highest-performing PSCs with PEDOT:PSS, PyDAI, and PyDI as HTLs. The external quantum efficiency (EQE) spectra and device parameters are displayed in Figure 6.4b and Table 6.1, respectively. It is found that the control device with PEDOT:PSS exhibits a PCE of 15.1%, with a short-circuit current density (J_{sc}) of 27.6 mA cm⁻² (corrected by EQE), an open-circuit voltage (V_{oc}) of 0.77 V, and a fill factor (FF) of 0.71. For PSCs with PyDAI and PyDI, comparable V_{oc} and FF are obtained while the J_{sc} was improved by 1.5 mA cm⁻². The EQE spectra suggest that the change in J_{sc} is mainly attributed to an increase of spectral response between the 300–400 nm, 500–700 nm, and 850–950 nm regions (will be discussed later). As a result, both devices exhibit slightly higher PCEs of 16.1%. The PCEs from J – V characteristics are also confirmed by steady-state power output tracking (Figure 6.4c), in which the devices with PyDAI and PyDI are performing slightly better than that with PEDOT:PSS. Notably, the dark J – V curves suggest that the device based on PyDAI has a lower leakage current density than the PyDI (Figure 6.4d), attributed to the better coverage of PyDAI on the ITO substrate after solution processing.

Table 6.1 Photovoltaic parameters of representative narrow-bandgap PSCs with PEDOT:PSS, PyDAI, or PyDI HTL.

HTL	J_{sc} (mA cm ⁻²)	V_{oc} (V)	FF	PCE (%)	$J_{sc, EQE}$ (mA cm ⁻²)	PCE ^a (%)
PEDOT:PSS	28.1	0.77	0.71	15.3	27.6	15.1
PyDAI	29.0	0.77	0.72	16.0	29.1	16.1
PyDI	28.8	0.78	0.71	16.0	29.1	16.1

^a Corrected PCE obtained by calculating the J_{sc} integrated from the EQE spectrum and V_{oc} and FF from the stabilized J – V measurement.

Ultrathin hole transport layers for efficient narrow-bandgap perovskite solar cells

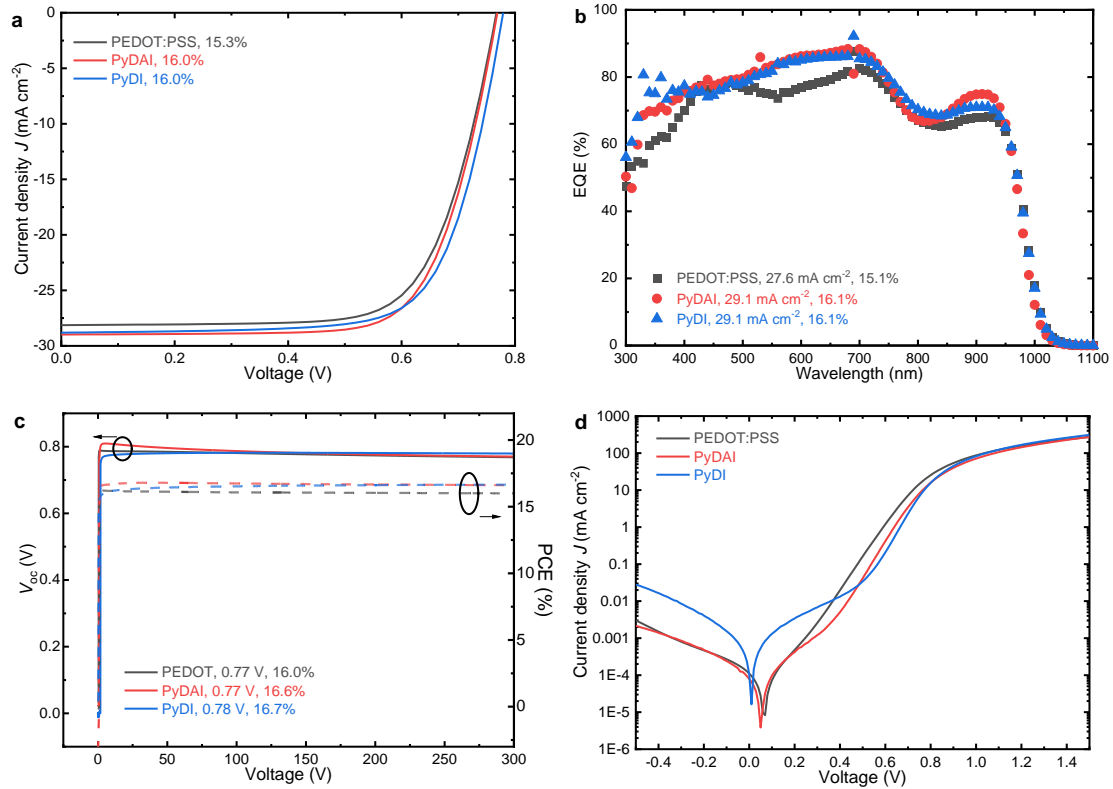


Figure 6.4 (a) Stabilized $J-V$ curves, (b) EQE spectra measured under 940 nm bias light, (c) V_{oc} and PCE tracking, and (d) dark $J-V$ curves of devices based on PEDOT:PSS, PyDAI, and PyDI HTLs.

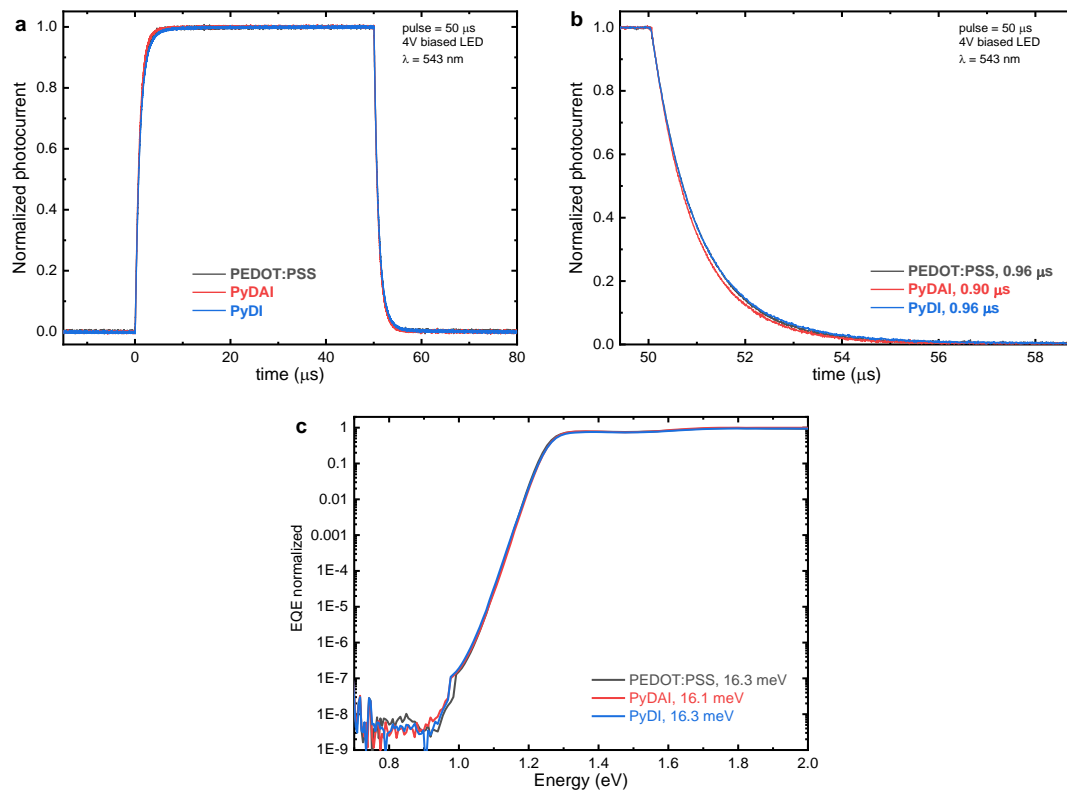


Figure 6.5 (a, b) Short-circuit photocurrent response measured under 50 μ s square-pulse illumination, and (c) sub-bandgap EQE spectra for the PSCs based on PEDOT:PSS, PyDAI, and PyDI HTLs.

To study the charge transport property of different HTLs, we performed transient photocurrent measurements by applying a 50 μs square pulse of monochromatic excitation (543 nm LED) to the device (0 V, dark condition) while monitoring its temporal photocurrent response. As can be seen in Figure 6.5a, all three devices exhibit a fast rise and stabilization of the photocurrent within a few microseconds after turning on the illumination, suggesting a rapid trap filling process in the solar cells.¹⁸ After turning off the illumination (Figure 6.5b), a comparably fast decay process is observed, and the charge transit time is found to be 0.90 μs for PyDAI, and 0.96 μs for both PEDOT:PSS and PyDI. Accordingly, the vertical charge carrier transit mobility¹⁹ is determined to be 2.9, 2.6, and $2.7 \times 10^{-3} \text{ cm}^2 \text{ V}^{-1} \text{ s}^{-1}$ for PyDAI, PEDOT:PSS, and PyDI, respectively. The results indicate that PEDOT:PSS and both small molecule HTLs possess a similar hole-transport property.

To estimate the degree of electronic disorder of the perovskite films, we determined the Urbach energy by fitting the tail of the EQE spectra in the sub-bandgap region (Figure 6.5c). The Urbach energies are around 16.1–16.3 meV for all three devices, suggesting a similar semiconductor quality of $\text{FA}_{0.66}\text{MA}_{0.34}\text{Pb}_{0.5}\text{Sn}_{0.5}\text{I}_3$ films when deposited on PEDOT:PSS, PyDAI, and PyDI.²⁰ We further rule out the impact of different HTLs on the formation of narrow-bandgap perovskite films. Figure 6.6a-c display the top-view scanning electron microscope (SEM) images of $\text{FA}_{0.66}\text{MA}_{0.34}\text{Pb}_{0.5}\text{Sn}_{0.5}\text{I}_3$ deposited on PEDOT:PSS, PyDAI, and PyDI. In all three cases, the perovskite films exhibit a compact and pinhole-free surface morphology, with grain sizes of around 500 nm. Meanwhile, similar UV-vis-NIR absorption spectra are seen for these films, with a characteristic narrow-bandgap onset at around 1000 nm (Figure 6.6d). Furthermore, X-ray diffraction (XRD) patterns (Figure 6.6e) indicate that in each case the perovskite films adopted the same cubic structure (see in Chapter 3), despite the sample on PyDAI shows slightly lower peak intensities. From the light-intensity dependent V_{oc} measurements (Figure 6.6f), a similar ideality factor (determined from the slope of the V_{oc} versus the logarithm of the light intensity over kT/q , where k is Boltzmann constant and q is the elementary charge) and V_{oc} at various illumination intensities were found, which suggests that the devices with different HTLs adopt the same recombination regime.²¹ In addition, the linear relationship ($J_{\text{sc}} \propto I^\alpha$, where $\alpha \approx 1$) between the light intensity and J_{sc} (Figure 6.6g) demonstrates that there are no significant energy barriers or space charges to limit the charge extraction process in such devices.¹⁸

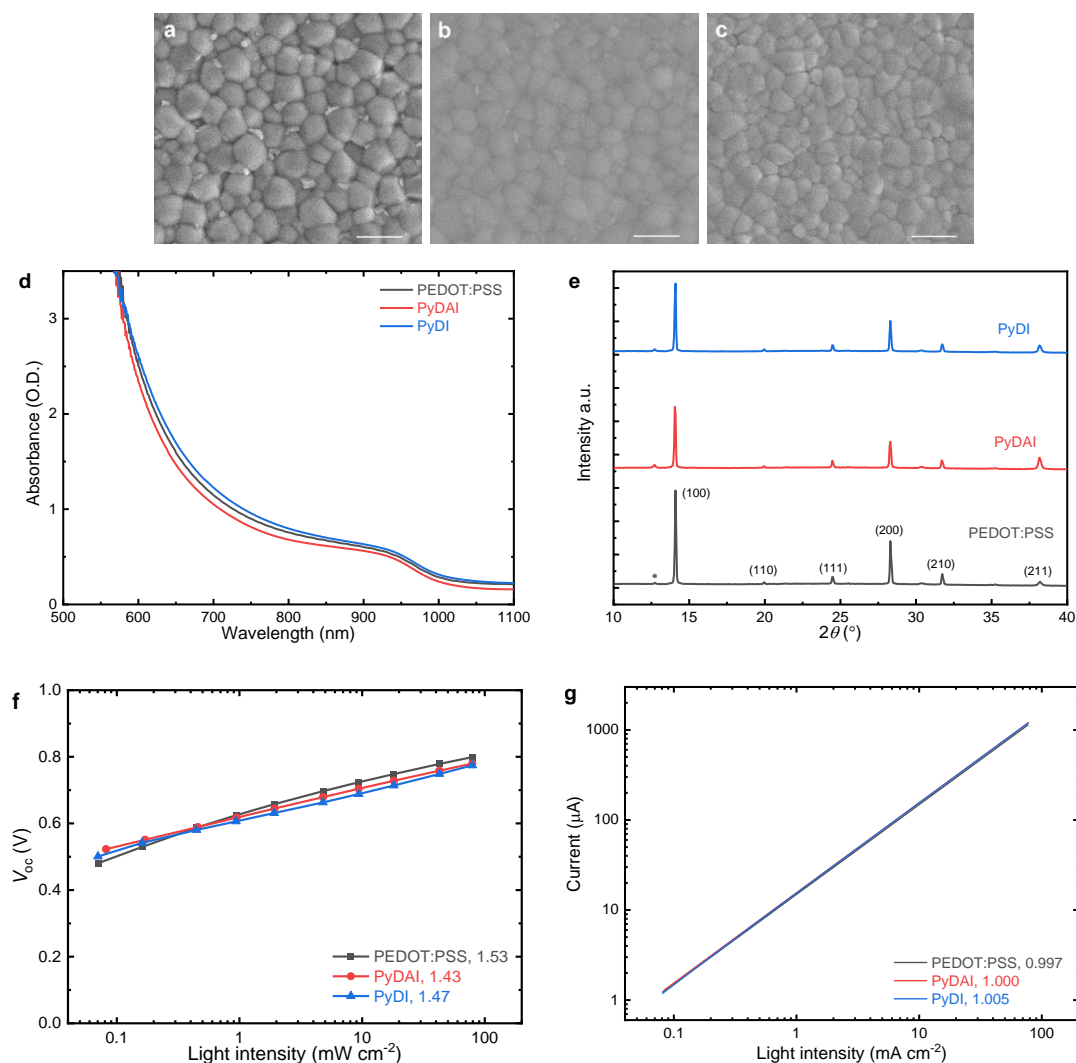


Figure 6.6 Top-view SEM images of $\text{FA}_{0.66}\text{MA}_{0.34}\text{Pb}_{0.5}\text{Sn}_{0.5}\text{I}_3$ films deposited on (a) PEDOT:PSS, (b) PyDAI, and (c) PyDI. Scale bars are 1 μm . UV-vis-NIR absorption spectra (d) and XRD patterns (e) of $\text{FA}_{0.66}\text{MA}_{0.34}\text{Pb}_{0.5}\text{Sn}_{0.5}\text{I}_3$ deposited on different HTLs. The light-intensity dependent V_{oc} (f) and J_{sc} (g) of PSCs with different HTLs. A 730 nm LED was used as the light source.

Figure 6.7a-d show box plots of the statistical distribution of performance characteristics of PSCs with PEDOT:PSS, PyDAI, and PyDI. While the control device with PEDOT:PSS exhibits an average PCE of 14.6% and a small standard deviation of 1.32%, PSCs with PyDI have a much broader spread in the performance ($10.0 \pm 5.49\%$) due to the poor stability of the HTL against perovskite precursor solutions (Figure 6.3). In comparison, the device with PyDAI displays reduced deviation in the PCEs ($13.8 \pm 2.05\%$). It is found that additional thermal annealing (100 $^{\circ}\text{C}$ 10 min) on PyDAI and PyDI further improves the reproducibility, albeit a slightly reduced performance among the best performing devices (Figure 6.7d). Furthermore, as shown in Figure 6.7e, when the devices were stored in a dry N_2

atmosphere at room temperature, the PyDAI-based device exhibits no degradation during the tracking period, suggesting improved device stability compared to that of PEDOT:PSS.

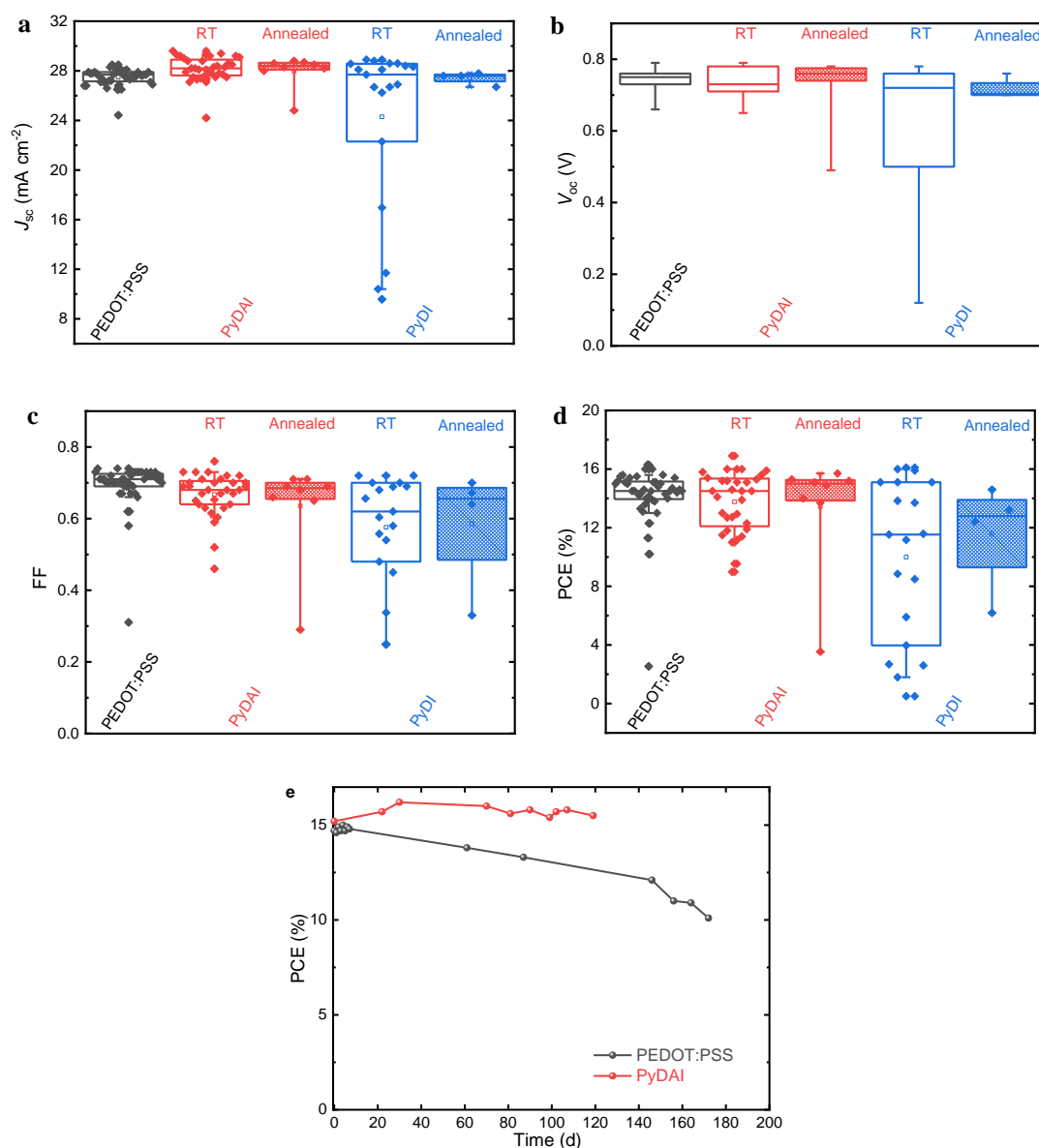


Figure 6.7 Box plots of the statistical distribution of (a) J_{sc} , (b) V_{oc} , (c) FF, and (d) PCE of the PSCs using PEDOT:PSS, PyDAI, or PyDI as the HTL. (e) PCE of unencapsulated PSCs based on PEDOT:PSS and PyDAI upon storage in the N₂ atmosphere at room temperature.

6.4 Ultrathin HTLs for narrow-bandgap PSCs

To understand the J_{sc} enhancement of narrow-bandgap PSCs when using PyDAI and PyDI, we fabricated devices with more commonly used HTLs, including poly[bis(4-phenyl)(2,4,6-trimethylphenyl)amine] (PTAA), poly[*N,N'*-bis(4-butylphenyl)-*N,N'*-bis(phenyl)-benzidine] (poly-TPD), and thin PEDOT:PSS. Here, ~1–2 nm thick PTAA and poly-TPD films were deposited from dilute solutions (1 mg mL⁻¹) at high spinning speeds.

Such a thin PTAA layer is necessary to reduce the series resistance of Pb/Sn-based devices.¹³ The thickness of the PEDOT:PSS layer can be reduced by adding water dropwise onto the spinning PEDOT:PSS substrate, which results in a PEDOT:PSS layer of ~5 nm.^{22,23} Figure 6.8a shows the stabilized $J-V$ curves of PSCs using different HTLs, and the corresponding device performance is summarized in Table 6.2. It is found that all the devices exhibit a comparable V_{oc} between 0.77 and 0.80 V and FF between 0.70 and 0.72. In addition, ideality factors between 1.43 and 1.61 are seen for these devices (Figure 6.8b). Our ultraviolet photoelectron spectroscopy (UPS) measurements for the HTLs on ITO substrates show that the work function of PTAA, PyDAI, and PyDI are 4.37, 4.43, and 4.57 eV, respectively. Correspondingly, their highest occupied molecular orbital (HOMO) levels are 5.00, 4.88, and 5.07 eV, respectively. For PEDOT:PSS, the work function and HOMO level are 4.48 and 4.83 eV, respectively, after DMF washing.²⁴ It is known that an increased energy level offset between the charge transport layers and the perovskite can drastically increase the rate of interface recombination and hence limiting the maximum attainable V_{oc} .²⁵ Contrast to previous studies, the fact that all the cells with different HTLs show a similar V_{oc} suggests that our narrow-bandgap device is currently limited by defect-induced non-radiative recombination in the perovskite bulk or at the interfaces.

The EQE spectra (Figure 6.8c) suggest that an increase of the J_{sc} of up to 2.1 mA cm^{-2} is obtained after replacing the thick PEDOT:PSS layer (~50 nm) with ultrathin HTLs in the narrow-bandgap devices. Similar to the devices using PyDAI and PyDI, the change in the J_{sc} is mainly attributed to the improvement in the spectral regions of 300–450 nm, 500–700 nm, and 850–950 nm. This implies that the J_{sc} enhancement using different HTLs is most likely due to an optical effect. We performed an optical simulation of narrow-bandgap devices based on pristine and water-rinsed PEDOT:PSS HTLs. A good correlation was found when comparing the fractional difference of the EQE spectra between the simulation and measured data (Figure 6.9a). When changing the PEDOT:PSS thickness from 50 to 5 nm, the shape (hills and valleys) of the EQE spectrum is blue-shifted (Figure 6.9b). Between 300–450 nm, the increase in the EQE should be attributed to the blue shift of the reflection peak of a thin PEDOT:PSS film.²³ The change in the 500–700 nm region is mainly due to the blue shift of (both constructive and destructive) optical interference. In the meantime, a decreased parasitic absorption of thin PEDOT:PSS also plays a role. Similarly, at around 900 nm, both constructive interference and reduced parasitic absorption contribute to the increased EQE. Potentially, the use of such ultrathin HTLs for the narrow-bandgap cell is beneficial for the high J_{sc} of single-

junction and multijunction solar cells by reducing the parasitic absorption of PEDOT:PSS layer and without compromising the V_{oc} and FF.

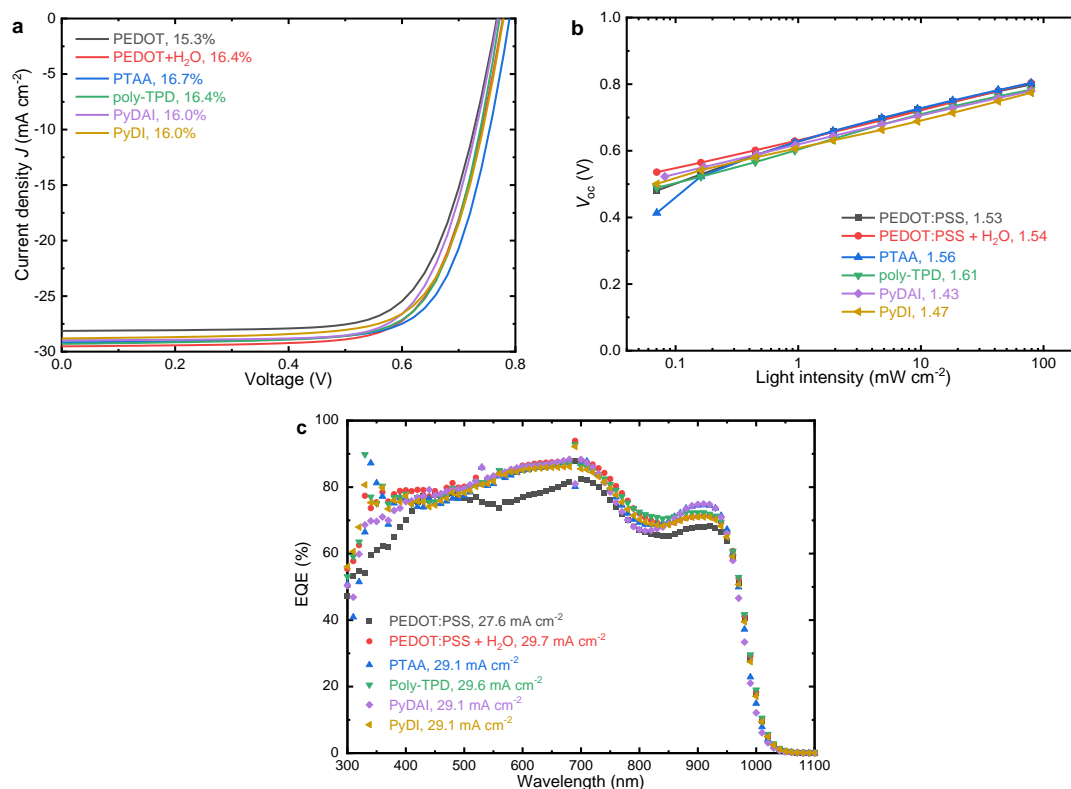


Figure 6.8 (a) Stabilized J - V curves, (b) light-intensity dependent V_{oc} , and (c) the EQE spectra of narrow-bandgap PSCs using different HTLs.

Table 6.2 Photovoltaic parameters of representative narrow-bandgap PSCs with different HTLs.

HTL	J_{sc} (mA cm^{-2})	V_{oc} (V)	FF	PCE (%)	$J_{sc, EQE}$ (mA cm^{-2})	PCE ^a (%)
PEDOT:PSS (50 nm)	28.1	0.77	0.71	15.3	27.6	15.1
PEDOT:PSS (5 nm)	29.5	0.78	0.71	16.4	29.7	16.4
PTAA	28.8	0.80	0.70	16.0	29.1	16.3
Poly-TPD	29.3	0.77	0.72	16.4	29.6	16.4
PyDAI	29.0	0.77	0.72	16.0	29.1	16.1
PyDI	28.8	0.78	0.71	16.0	29.1	16.1

^a Corrected PCE obtained by calculating the J_{sc} integrated from the EQE spectrum and V_{oc} and FF from the stabilized J - V measurement.

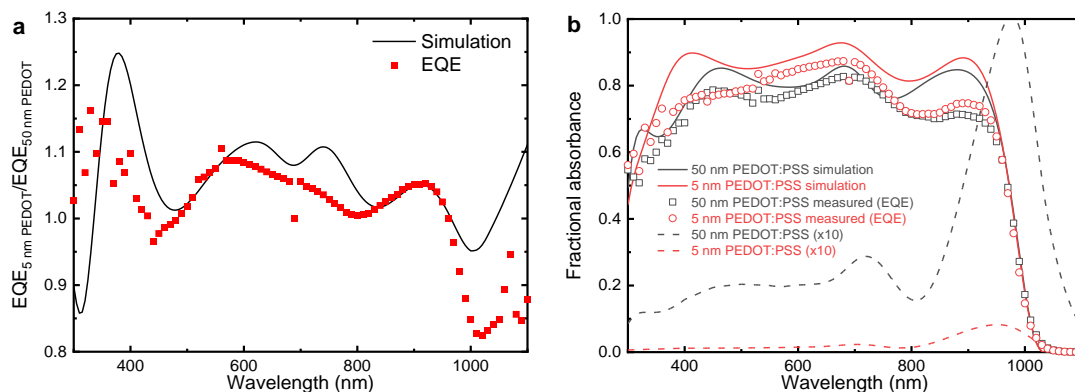


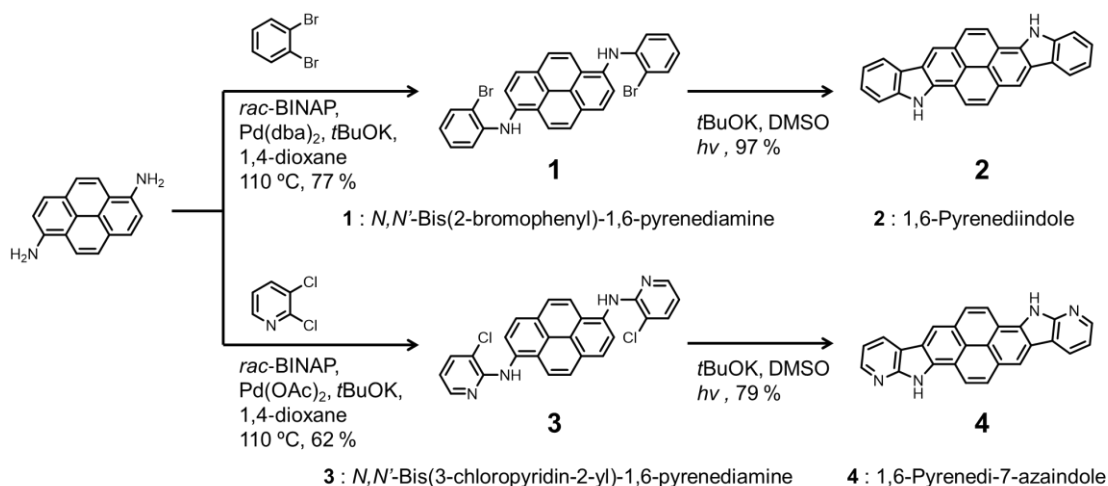
Figure 6.9 (a) The ratio between the EQE of the PSCs using 5 nm and 50 nm PEDOT:PSS layers. The solid line is obtained from the simulated data, and the red dotted plot is from the measured data. (b) The measured EQE (open circles) and simulated fractional absorbance of perovskite films (solid lines) in the devices based on 5 nm and 50 nm PEDOT:PSS. The absorbance of PEDOT:PSS layer (dashed line, x10 multiplied for comparison).

6.5 Conclusions

In summary, we have reported two π -conjugated small molecules, PyDAI and PyDI, for use as HTLs in narrow-bandgap PSCs. It is found that such HTLs have an insignificant impact on the quality of the $\text{FA}_{0.66}\text{MA}_{0.34}\text{Pb}_{0.5}\text{Sn}_{0.5}\text{I}_3$ film deposited on top. Compared to PyDI, PyDAI is more crystalline and robust against solution-processed perovskite films by hydrogen-bond-directed self-assembly. As a result, the devices with PyDAI show much-improved reproducibility. Compared to PEDOT:PSS, both PyDAI and PyDI exhibit similar hole transport properties in narrow-bandgap solar cells, resulting in a comparable V_{oc} and FF. In both cases, the use of ultrathin HTLs further enhances the J_{sc} by changing the optical interference and reducing parasitic absorption from a thick PEDOT:PSS layer. Furthermore, the elimination of PEDOT:PSS HTL also significantly improves the shelf life of narrow-bandgap solar cells.

6.6 Experimental section

Synthesis of small organic molecules: The synthetic procedure started with a palladium-catalyzed Buchwald–Hartwig cross-coupling reaction between 1,6-diaminopyrene and the corresponding dihaloderivative, *o*-dibromobenzene and 2,3-dichloropyridine, to afford the *N*-arylated intermediates **1** and **3**, respectively. Subsequently, a double regiospecific intramolecular photoinduced cyclization, performed under basic conditions, enabled the successful isolation of the final fused polyheteroaromatic derivatives **2** (PyDI) and **4** (PyDAI). The final purification of the materials was performed by gradient sublimation under high vacuum conditions ($<10^{-6}$ mbar).



Scheme 1 Synthetic routes of PyDI and PyDAI molecules.

Solar cell fabrication: Patterned glass/ITO substrates (Naranjo) were cleaned by washing with acetone, sodium dodecyl sulfate (Acros, 99%) soapy water, deionized water, and 2-propanol. Before use, the substrates were dried by flow N_2 and treated with UV-ozone for 30 min. For the control device, acidic PEDOT:PSS (Heraeus Clevis, PVP Al 4083) solution was spin coated at 3000 rpm for 60 s and annealed at 140 °C for 15 min in the ambient condition. For water-rinsed PEDOT:PSS device, 200 μL H_2O was dynamically cast onto the raw PEDOT:PSS at 5000 rpm for 30 s and again annealed at 140 °C for 15 min in the ambient condition. The PTAA (1.0 mg mL^{-1}) and poly-TPD (1.0 mg mL^{-1}) HTLs were spin coated from chlorobenzene at 5700 rpm for 30 s and annealed at 100 °C for 10 min in the N_2 glovebox. For the small molecule HTLs, cleaned ITO substrates were transferred into a thermal evaporator, where 10 nm of HTLs were evaporated under a high vacuum ($\sim 3 \times 10^{-7}$ mbar). The narrow-bandgap perovskite films were prepared by a two-step solution process, where 1.25 M $\text{PbI}_2:\text{SnI}_2$ (1:1) in DMF:DMSO (10.1:1) was spin coated at 3000 rpm (2000 rpm s^{-1} acceleration) for 30 s and dried at room temperature for 10 min. Afterward, a 0.47 M FAI:MAI (0.66:0.34) in 2-propanol was spin coated dynamically at 3000 rpm for 60 s and annealed at 100 °C for 30 min in the N_2 glovebox. After cooling down, 1 mg mL^{-1} NH_4SCN in 2-propanol was spin coated on top of the perovskite film at 5000 rpm for 30 min. The devices were then finished by evaporating 20 nm C_{60} , 8 nm BCP, and 100 nm Ag layers under a high vacuum ($\sim 3 \times 10^{-7}$ mbar). The active area of the solar cell was determined by the overlap of the Ag and ITO contacts (0.09 or 0.16 cm^2).

Device characterization: J - V characteristics were performed in the N_2 glovebox by a Keithley 2400 source meter. A solar simulator was powered by a tungsten-halogen lamp, which is filtered by a Schott GG385 UV filter and a hoya LB120 daylight filter to simulate the 100 mW cm^{-2} light. A black shadow mask with an aperture area of 0.0676 or 0.1296 cm^2 was used. For the stabilized J - V scans, the device was first stabilized at V_{oc} for 5 min, before sweeping the bias from $V_{\text{oc}} + 0.02$ V to -0.02 V with a step size of 0.02 V. The acquisition time for each bias step is 5 s. During the steady-state power output

tracking, the voltage obtained from the maximum power point was then applied to the solar cell when measuring the output photocurrent and hence the maximum power density. EQE spectra were measured in an N₂ atmosphere. Similar to previous chapters, additional infrared LED (940 nm, driven by a DC 4104 driver) was used as a light bias to provide the device with one sun illumination light intensity during the EQE measurement. The light intensity-dependent J_{sc} and V_{oc} were measured by a Keithley 2400 source meter, under the illumination of a 730 nm LED driven between 1–1000 mA. For the transient photocurrent measurements, the device was connected to a current amplifier and an oscilloscope. A 543 nm LED with 50 μ s square pulse in width was used to illuminate the device at the short-circuit.

Film characterization: The morphology of HTL thin films were measured by Dimension 3100 AFM with tapping mode. SEM (FEI Quanta 3D FEG) was used to analyze the surface morphology of perovskite films using 5 kV electron beam and a secondary electron detector. UV–vis–NIR absorption spectra were carried out by PerkinElmer Lambda 900 spectrophotometer at room temperature. All the perovskite samples were sealed in an air-tight holder with glass windows. XRD patterns were recorded by a Bruker 2D phaser using Cu K α (1.5405 Å) as the X-ray source. A step size of 0.05° was used. GIWAX was measured by a GANESHA 300 XL+ system from JIX-ray (Cu K α , 1.5408 Å) equipped with a Pilatus 300 K detector. The surface XPS was measured by a Thermo Scientific K-Alpha with 180° double-focusing hemispherical analyzer and a 128-channel detector. Monochromatic Al K α (1486.6 eV) radiation was used with a spot size of 400 μ m.

6.7 References

- Green, M. A., Dunlop, E. D., Hohl-Ebinger, J., Yoshita, M., Kopidakis, N., Hao, X. Solar cell efficiency tables (version 56). *Prog. Photovolt. Res. Appl.* **28**, 629-638 (2020).
- Nasti, G., Abate, A. Tin Halide Perovskite (ASnX₃) Solar Cells: A Comprehensive Guide toward the Highest Power Conversion Efficiency. *Adv. Energy Mater.* **10**, 1902467 (2020).
- Rühle, S. Tabulated values of the Shockley–Queisser limit for single junction solar cells. *Sol. Energy* **130**, 139-147 (2016).
- Gu, S., Lin, R., Han, Q., Gao, Y., Tan, H., Zhu, J. Tin and Mixed Lead-Tin Halide Perovskite Solar Cells: Progress and their Application in Tandem Solar Cells. *Adv. Mater.* **32**, 1907392 (2020).
- Moody, N. et al. Assessing the Regulatory Requirements of Lead-Based Perovskite Photovoltaics. *Joule* **4**, 970-974 (2020).
- Lin, R. et al. Monolithic all-perovskite tandem solar cells with 24.8% efficiency exploiting comproportionation to suppress Sn(II) oxidation in precursor ink. *Nat. Energy* **4**, 864-873 (2019).
- Yang, Z. et al. Enhancing electron diffusion length in narrow-bandgap perovskites for efficient monolithic perovskite tandem solar cells. *Nat. Commun.* **10**, 4498 (2019).
- Tong, J. H. et al. Carrier lifetimes of > 1 μs in Sn-Pb perovskites enable efficient all-perovskite tandem solar cells. *Science* **364**, 475-479 (2019).
- Wang, J. et al. Understanding the Film Formation Kinetics of Sequential Deposited Narrow-Bandgap Pb–Sn Hybrid Perovskite Films. *Adv. Energy Mater.* **10**, 2000566 (2020).
- Zhu, H. L. et al. Achieving High-Quality Sn–Pb Perovskite Films on Complementary Metal-Oxide-Semiconductor-Compatible Metal/Silicon Substrates for Efficient Imaging Array. *ACS Nano* **13**, 11800-11808 (2019).
- Saidaminov, M. I. et al. Conventional Solvent Oxidizes Sn(II) in Perovskite Inks. *ACS Energy Lett.* **5**, 1153-1155 (2020).
- Prasanna, R. et al. Design of low bandgap tin–lead halide perovskite solar cells to achieve thermal, atmospheric and operational stability. *Nat. Energy* **4**, 939-947 (2019).
- Werner, J. et al. Improving Low-Bandgap Tin–Lead Perovskite Solar Cells via Contact Engineering and Gas Quench Processing. *ACS Energy Lett.* **5**, 1215-1223 (2020).
- Yu, Z. et al. Simplified interconnection structure based on C₆₀/SnO_{2-x} for all-perovskite tandem solar cells. *Nat. Energy*, 10.1038/s41560-020-0657-y (2020).
- Zhao, D. et al. Efficient two-terminal all-perovskite tandem solar cells enabled by high-quality low-bandgap absorber layers. *Nat. Energy* **3**, 1093-1100 (2018).
- Mas-Montoya, M., Gomez, P., Curiel, D., da Silva, I., Wang, J., Janssen, R. A. J. A Self-Assembled Small-Molecule-Based Hole-Transporting Material for Inverted Perovskite Solar Cells. *Chem. Eur. J.* **26**, 10276-10282 (2020).
- Shi, Q., Zhu, C., Engelhard, M. H., Du, D., Lin, Y. Highly uniform distribution of Pt nanoparticles on N-doped hollow carbon spheres with enhanced durability for oxygen reduction reaction. *RSC Adv.* **7**, 6303-6308 (2017).
- Li, Z., McNeill, C. R. Transient photocurrent measurements of PCDTBT:PC₇₀BM and PCPDTBT:PC₇₀BM Solar Cells: Evidence for charge trapping in efficient polymer/fullerene blends. *J. Appl. Phys.* **109**, 074513 (2011).
- Shao, Y., Xiao, Z., Bi, C., Yuan, Y., Huang, J. Origin and elimination of photocurrent hysteresis by fullerene passivation in CH₃NH₃PbI₃ planar heterojunction solar cells. *Nat. Commun.* **5**, 5784 (2014).
- Al-Ashouri, A. et al. Conformal monolayer contacts with lossless interfaces for perovskite single junction and monolithic tandem solar cells. *Energy Environ. Sci.* **12**, 3356-3369 (2019).
- Tress, W. et al. Interpretation and evolution of open-circuit voltage, recombination, ideality factor and subgap defect states during reversible light-soaking and irreversible degradation of perovskite solar cells. *Energy Environ. Sci.* **11**, 151-165 (2018).
- Lu, J. et al. Ultrathin PEDOT:PSS Enables Colorful and Efficient Perovskite Light-Emitting Diodes. *Adv. Sci.* **7**, 2000689 (2020).

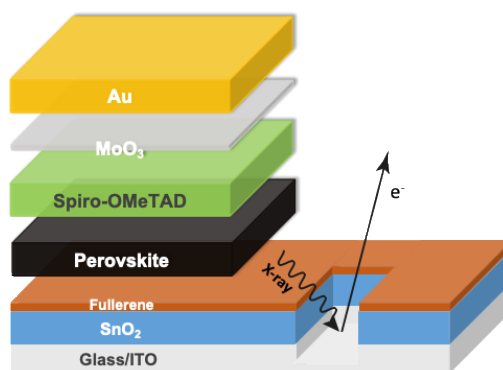
23. Hu, L. et al. PEDOT:PSS monolayers to enhance the hole extraction and stability of perovskite solar cells. *J. Mater. Chem. A* **6**, 16583-16589 (2018).
24. Bruijnaers, B. J., Schiepers, E., Weijtens, C. H. L., Meskers, S. C. J., Wienk, M. M., Janssen, R. A. J. The effect of oxygen on the efficiency of planar p-i-n metal halide perovskite solar cells with a PEDOT:PSS hole transport layer. *J. Mater. Chem. A* **6**, 6882-6890 (2018).
25. Stolterfoht, M. et al. The impact of energy alignment and interfacial recombination on the internal and external open-circuit voltage of perovskite solar cells. *Energy Environ. Sci.* **12**, 2778-2788 (2019).

Summary

Interfacial, Compositional and Morphological Engineering for Single- and Multi-junction Perovskite Solar Cells

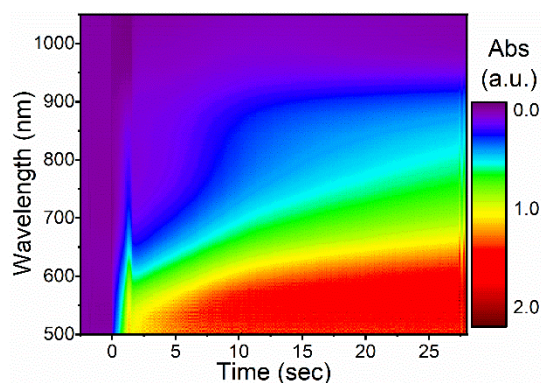
The direct solar-to-electricity conversion enabled by photovoltaic (PV) cells plays a central role in the future energy supply. Benefiting from the development of crystalline silicon (c-Si), solar PV has now become the fastest-growing renewable energy technology. Other than c-Si, new generation solar cells with high cost-effectiveness are needed to accelerate the upcoming terawatt-scale photovoltaic industry. To date, low-cost, lightweight, and highly efficient perovskite solar cells (PSCs) are the most promising candidates. The photo-active perovskite materials have shown excellent optoelectronic properties such as strong optical absorption, long charge diffusion length, and large defect tolerance. Within a decade, PSCs have already achieved a record power conversion efficiency (PCE) of 25.2%, on par with the state-of-the-art inorganic PV technologies.

For the PSCs based on metal-oxide charge transport layers, defect passivation at the metal oxide layer/perovskite interface is often found critical for high performance. Fullerene and its derivatives are the most commonly used modification layers to passivate the tin oxide (SnO_2) electron transport layer (ETL). However, the role of such passivation layers is yet not fully understood as they are susceptible to removal during perovskite deposition. In Chapter 2, solar cell characteristics and XPS depth profiles are presented to link the device performance to the distribution of fullerene passivation layers at the ETL interface. It is found that for a fullerene with an ester side chain, thermal annealing is crucial to create a surface-bound monolayer that can effectively reduce the number of defects and enhance the electron mobility. In comparison, the fullerene with a carboxylic acid side chain can easily bind to the SnO_2 surface without any thermal treatment, thus providing a better device efficiency. Further investigations of solvent-resistant fullerene layers demonstrate that the interfacial charge transport of the SnO_2 ETL can be improved only when chemisorbed fullerene monolayers are introduced.



Summary

Metal halide perovskites have a widely tunable bandgap, which expands from over 3.1 eV when using Cl as the sole anion to 1.2 eV by mixing Pb with Sn (50–75%) as the divalent cation. Compared to pure-Pb perovskites, Sn-containing perovskites have shown a far less controlled film formation process, which is crucial for their PV performance. In Chapter 3, in-situ optical absorption spectroscopy is performed to gain insights into the impact of precursor composition on perovskite growth. It is evidenced that the Sn-containing precursor can accelerate the conversion to the perovskite phase. In contrast, the crystallization of the pure-Pb compound is largely hindered before thermal annealing. Notably, the use of a two-step solution process enables homogeneous crystallization of mixed Pb–Sn perovskite phases. Ex-situ film characterizations further reveal the correlation between morphology and device performance. For Sn-rich PSCs, the performance is deteriorated due to large shunts induced by high surface roughness. Meanwhile, smooth and uniform perovskite films with 50% Sn content is obtained, which shows a desired narrow bandgap of 1.23 eV. By passivating defect sites on the perovskite surface, the PSC exhibits a PCE of 16.1% with good ambient stability. A mechanically stacked 1.57/1.23 eV four-terminal tandem displays a PCE of 21.1%.

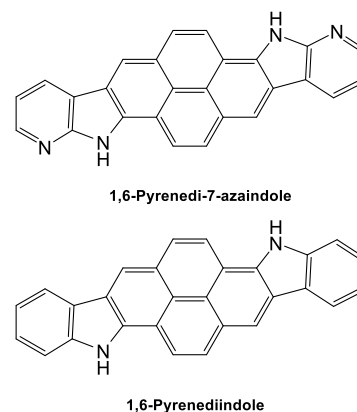


The record PCE of PSCs is now approaching the theoretical efficiency limit of 33% in single-junction solar cells. Perovskite-based multijunction solar cells have the potential to surpass the efficiency limit, given their widely tunable bandgaps and prominent optoelectronic properties. Developing monolithic all-perovskite multijunction solar cells is, however, not a trivial task. Next to the challenges of processing several different perovskite absorbers on top of each other, strict electrical and optical design are to be considered to maximize light absorption and balance the current density of each photo-active layer. In Chapter 4, a SnO₂ layer grown by spatial atomic layer deposition is introduced as the interconnecting contact for tandem solar cells. The SnO₂ layer provides fast electron transport and improves the thermal stability of the underlying perovskite film. More importantly, the compact SnO₂ layer is compatible with the solution processes used by the multi-layers on top. Through optimization, a combination of interconnecting layers based



on $C_{60}/SnO_2/Au/PEDOT:PSS$ allows the fabrication of high potential and low-resistivity tandem solar cells. PCEs of above 19% are achieved in tandem solar cells comprising 1.73 eV and 1.23 eV perovskite absorber layers. Next, in Chapter 5, two-step solution-processed 1.73 eV, 1.57 eV, and 1.23 eV perovskite absorbers are integrated into a monolithic, all-perovskite triple-junction solar cell. The same interconnecting layers provide fast charge recombination, which results in a promising PCE of 16.8% with a low potential energy drop and low resistivity loss. Simulation data suggest that reducing the optical losses in the 1.23 eV sub-cell and developing highly efficient and stable 2.0 eV wide-bandgap perovskite absorber are necessary to enhance the performance of all-perovskite triple-junction solar cells.

The choice of charge transport materials has a significant impact on the performance and stability of PSCs. Despite its poor stability, poly(3,4-ethylenedioxythiophene):polystyrene sulfonate (PEDOT:PSS) is the most used hole transport layers (HTLs) for highly efficient narrow-bandgap PSCs. Potentially, the parasitic absorption of PEDOT:PSS layer in the near-infrared also limit the maximum attainable short-circuit current density (J_{sc}) of a multijunction solar cell. In Chapter 6, two pyrene-based small molecules are introduced as the HTLs for the narrow-bandgap PSCs. The more robust 1,6-pyrenedi-7-azaindole (PyDAI) features two nitrogen atoms from the pyridine rings and two NH– from the pyrrole rings, leading to hydrogen-bond-directed self-assembly. The use of such ultrathin HTLs shows a negligible impact on the quality of the narrow-bandgap perovskite films. It is found that the new HTLs improve device stability while displaying similar hole transport properties as PEDOT:PSS. In addition, the use of a thinner HTL can effectively reduce optical losses caused by a thick PEDOT:PSS layer, thus leading to an improved J_{sc} in the narrow-bandgap solar cell.

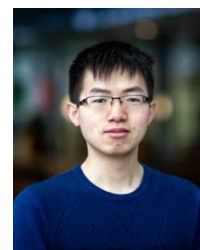


In summary, the thesis presents some new insights into the role of interfaces for perovskite photovoltaics. It attains a deeper understanding of the film formation kinetics and is correlated with the device efficiencies. A simple and reproducible method is developed to fabricate all-perovskite based multijunction solar cells, and strategies to achieve higher efficiencies are discussed.

Summary

Curriculum Vitae

Junke Wang was born on December 10th, 1991, in Shaoyang, China. After finishing high school in 2009 at the No.2 Middle School in Shaoyang, he studied Materials Science and Engineering at the Central South University in Changsha, China. There he finished his final project on fluorite-type thermal sensitive ceramics in the group of prof. Zhicheng Li, before graduating with honors in 2013. One year later, he was admitted to Amandus H. Lundqvist Scholarship Program at the Eindhoven University of Technology. He started to work on the topic of perovskite photovoltaics for eight months during his graduation project under the supervision of dr.ir. Bardo Bruijnaers and prof.dr.ir. René Janssen at the university and worked as a trainee for five months at Solliance Solar Research, Eindhoven. In 2016 he received his master's degree (with great appreciation) in Chemical Engineering. He then started his PhD research at the Eindhoven University of Technology in the group of Molecular Materials and Nanosystems under the supervision of prof.dr.ir. René Janssen. The results obtained during his PhD research are presented in this dissertation.



List of Publications

16.8% Monolithic all-perovskite triple-junction solar cells via a universal two-step solution process. Nature Communications, 2020, 11, 5254.

Wang J., Zardetto V., Datta K., Zhang D., Wienk M.M., Janssen R.A.J.

Understanding the Film Formation Kinetics of Sequential Deposited Narrow-Bandgap Pb–Sn Hybrid Perovskite Films. Advanced Energy Materials, 2020, 10, 2000566.

Wang J., Datta K., Li J., Verheijen M.A., Zhang D., Wienk M.M., Janssen R.A.J.

Insights into Fullerene Passivation of SnO₂ Electron Transport Layers in Perovskite Solar Cells. Advanced Functional Materials, 2019, 29, 1905883.

Wang J., Datta K., Weijtens C.H.L., Wienk M.M., Janssen R.A.J.

Highly Efficient Perovskite Solar Cells Using Non-Toxic Industry Compatible Solvent System. Solar RRL, 2017, 1, 1700091.

Wang J., Di Giacomo F., Brüls J., Gortler H., Katsouras I., Groen P., Janssen R.A.J., Andriessen R., Galagan Y.

Light-Driven Electrochemical Carbon Dioxide Reduction to Carbon Monoxide and Methane Using Perovskite Photovoltaics. Cell Reports Physical Science, 2020, 1, 100058.

Esiner S., **Wang J.**, Janssen R.A.J.

A Self-Assembled Small Molecule-Based Hole Transporting Material for Inverted Perovskite Solar Cells. Chemistry – A European Journal, 2020, 26, 10276.

Más-Montoya M., Gómez P., Curiel D., Da Silva I., **Wang J.**, Janssen R.A.J.

Carboxylate-Substituted Polythiophenes for Efficient Fullerene-Free Polymer Solar Cells: The Effect of Chlorination on Their Properties. Macromolecules, 2019, 52, 4464.

Wang Q., Li M., Zhang X., Qin Y., **Wang J.**, Zhang J., Hou J., Janssen R.A.J., Geng Y.

Air-Stable and Oriented Mixed Lead Halide Perovskite (FA/MA) by the One-Step Deposition Method Using Zinc Iodide and an Alkylammonium Additive. ACS Applied Materials & Interfaces, 2019, 11, 17555.

Muscarella L.A., Petrova D., Jorge Cervasio R., Farawar A., Lugier O., McLure C., Slaman M.J., **Wang J.**, Ehrler B., Von Hauff E., Williams R.M.

High-performance all-polymer solar cells based on fluorinated naphthalene diimide acceptor polymers with fine-tuned crystallinity and enhanced dielectric constants. Nano Energy, 2018, 45, 368.

Xu X., Li Z., **Wang J.**, Lin B., Ma W., Xia Y., Andersson M.R., Janssen R.A.J., Wang E.

The Impact of Device Polarity on the Performance of Polymer–Fullerene Solar Cells. Advanced Energy Materials, 2018, 8, 1800550.

Li M., Li J., Di Carlo Rasi D., Colberts F.J.M, **Wang J.**, Heintges G.H.L., Wienk M.M., Janssen R.A.J.

Acknowledgments

After about 1,500 long days and (sometimes sleepless) nights, my time as a PhD student is finally coming to an end. Writing the acknowledgments page is certainly the biggest challenge to me in finalizing this thesis. It is quite hard to find words to express my gratitude to so many people, without whom this thesis would never have been possible.

I would like to thank my supervisor René Janssen, for always placing your trust and confidence in me. I consider myself one of the lucky ones who get to work in such a wonderful research group and have a tremendous amount of freedom to explore independently. Every week, I have the luxury of discussing my puzzles with you in our group and personal meetings, and you can always help me find a way out. The valuable guidance you provided kept me on the right path to the success of this work. Your immense knowledge, productive work, and big personality are truly inspirational to me.

At the same time, I would like to express my sincere gratitude to my co-supervisor, Martijn Wienk, for your guidance, support, and encouragement throughout my PhD study. With a sharp eye, you can quickly pinpoint the problem in my data and see an interesting trend from another perspective. I have certainly learned a lot from the many brilliant ideas generated from your broad and deep knowledge during our discussions.

I would like to thank Prof. Henry Snaith, Prof. Maria Loi, Prof. Erwin Kessels, and Prof. Erik Garnett for kindly agreeing to participate in my PhD defense committee and their recommendations on the thesis. Also, thanks to Prof. Fausto Gallucci for chairing the PhD defense.

This work has received great help from many colleagues and collaborators. I would like to thank Kunal Datta for performing the XRD and in-situ absorption measurements and developing the wide-bandgap perovskites. My sincere gratitude to Valerio Zardetto (TNO, Solliance) for preparing the precious SALD layers and Dong Zhang (TNO, Solliance) for the optical simulations for the tandem and triple-junction solar cells. I appreciate the help from Christ Weijtens in measuring and analyzing the UPS data. Thanks to Beatriz Barcones (NanoLab) for preparing the cross-sectional TEM sample and Marcel Verheijen (PMP & Philips) for acquiring the TEM/EDX images in the evening and further discussions on the processing of these images. I would like to thank Junyu Li (DSM) for spending long hours measuring GIWAX for my samples and Haijun Bin for taking the AFM images. For Chapter 6,

Acknowledgments

I am grateful to our former colleague Miriam Más-Montoya (now at the University of Murcia) for providing me with the hole transport materials, Riccardo Ollearo for the transient photocurrent measurements, Bas van Gorkom for the sub-gap EQE, and Tom van der Pol for the optical simulations. Furthermore, I would like to thank Stefan Meskers for the help with the PL setup. I sincerely appreciate Ingeborg Schreur-Piet (SEM, SPC) and Tiny Verhoeven (XPS, IMC) for giving me training and access to their lab equipment, which greatly benefit the research of our group.

Living and undertaking research in a country that is 9,000 km from home has never been easy for me. I want to express my sincere gratitude to Margot. You really take good care of us, both physically and mentally. I will always remember that you drove me across Eindhoven to find an emergency dentist in the late evening with just one phone call. You are always there whenever someone needs a conversation. My life in Eindhoven is certainly much easier with your kind help.

I would also like to take the opportunity to thank all the M2N talents for helping me and creating a cheerful working environment. I enjoyed the 1st year of my PhD with Ruurd, Fallon, and Bart in the office STO 4.31. The rest of my time was with Mike (Qiang), Koen, Anna, and Alessandro (the only master student during my PhD) at STW 4.28. I want to thank Wijnand and Martijn for your diligent work in running the device lab so smoothly that all these nice works can be done. Many thanks to Bardo for your great patience in teaching me how to make the first perovskite solar cell (during my master's project) and your pioneer work (on perovskite) in the group, which really makes our life much easier. I want to thank Benjamin for your help in the lab since the day we met during the master study at the Solliance. I enjoyed our many chats, and together we made a good team for the OGO projects. Miriam, thanks for your help in some device characterizations and for providing me with these organic compounds. Together we have made several nice manuscripts for publication. Kunal, you really have helped me a lot in my projects during the past few years. I have learned a lot from your creative thinking and new ideas. Obviously, everyone in the group enjoys the interesting discussions with you during the coffee breaks, and I as well. You are the guy to whom I can send Whatsapp messages at midnight when I see some new Nature Energy papers from competitors, and I appreciate your constant Twitter updates on the perovskite worlds. Beyond that, I am grateful that you agree to be my paranymph. Of course, to Dario, Gaël, Bas, Tom, Nicolas, Serkan, Robin, Olivera, Simone, Pieter, Matt, Willemjin, Wietse, Riccardo, Aart, and other colleagues on the physics

part at Spectrum, thank you all for being great colleagues. I wish you lots of success in your research and future careers.

Here I would like to give my special thanks to some (former) Chinese colleagues that I had the pleasure to meet in Eindhoven: Chunhui, Qiang (Mike), Mengmeng, Feilong, Haijun, Miaomiao, Dong, and Junyu, all are very talented and hard-working researchers. You are like big brothers and sisters to me, and I have learned many things from you in conducting research. Thanks to the company of Mengmeng, Haijun, Chunhui, and Xiao, my long days in the device lab had been much more delightful. To Xiao, I wish you all the best in completing your PhD studies.

I would also like to thank our collaborator from Solliance: Valerio, Dong, Veronique, Herbert, and Francesco. It was the many Solliance–M2N meetings that made the all-perovskite multijunction project possible. To Valerio and Dong, it has been a great pleasure to work with the both of you, and thanks a lot for carrying the precious samples back and forth between the TU/e and high-tech campus.

I would like to thank some friends that I have met in Eindhoven. Yizhou, thank you for the company in the last few years. I share many good memories with you, from the long-night cruise trip (with Jiadong) from Stockholm to Helsinki on the 1st day of the new year, to watching the Europa League Final (with Yu) in the Grand Stade de Lyon. I wish you all the best in the future (either in the Netherlands or in China). Jiadong, we have been studying mates since day one of our master's program at TUE (with Yichu, Rong, and Cheng, can't believe it was six years ago). You helped me a lot to survive the first year because I do not have a chemistry background. After our graduation ceremony (with Cheng) in September 2016, we both started our PhD projects in October (you at IMC, me at M2N). Since 2017 we became housemates (now also with Jin, of course), and both of us are going to defend our PhD theses in December 2020. Although we are mostly busy with our own stuff nowadays, I want to thank you for your support and being there throughout those important moments of my life (and also being my paranymp).

Last but not least, I would like to thank my family. To my wife Yixuan, you are the greatest thing that ever happened to me. Thank you for keeping our love alive for the last 12 years, even though we have been mostly separated from each other since college. I guess distance and time zone never separate two hearts that really care. I hope I can come back to you soon, and together we will enjoy many more beautiful years to come. 感谢爸爸和妈妈在过去

Acknowledgments

29 年里给予我的无限支持，让我能自由地去探寻一个更好的自己。也感谢众多亲友们一直以来对我的关心，你们的鼓励是我不断前进的动力。

Wang Junke

王竣可

2020 年 11 月，Eindhoven